Star formation rate and dynamical state of galaxy clusters

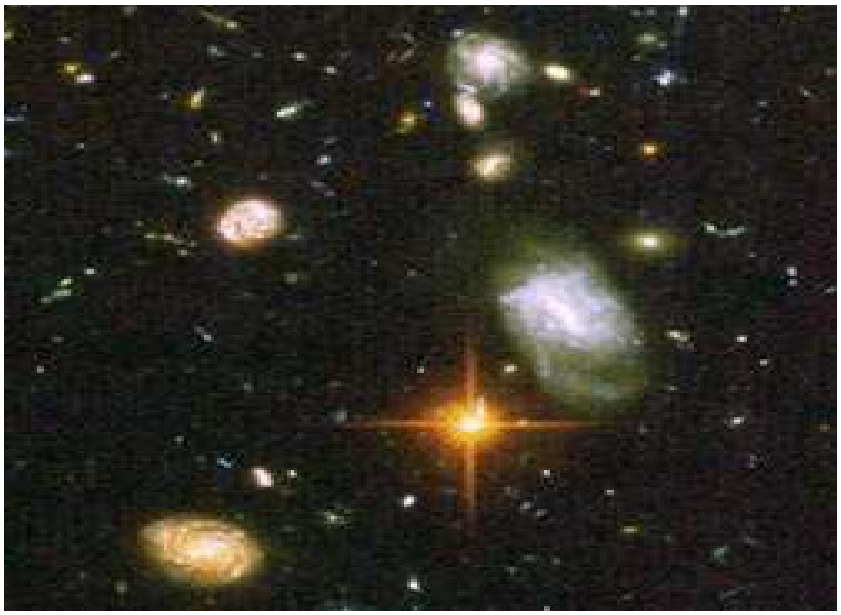

Master of Science Thesis by
Ine Skorbakk

Institute of Theoretical Astrophysics
University of Oslo

June 2010

Acknowledgements

First I would like to thank my supervisor, Håkon Dahle, for introducing me to the exciting world of observational astronomy and for giving me the opportunity to observe with the Nordic Optical Telescope at La Palma. Thank you for guiding me through this project and for all of your constructive feedback.

I also want to thank all of my friends and family for believing in me and always being there. A special thanks to my mom, Sigrun Aamodt, for proof reading, even though you may not have understood half of what you read. I really appreciate it!

Contents

1 Introduction **1**
- 1.1 Motivation and goals . . . 2
- 1.2 Thesis Outline . . . 2
- 1.3 A brief introduction to cosmology . . . 3
- 1.4 Galaxy clusters . . . 7
- 1.5 Morphology of galaxies . . . 11
- 1.6 Luminosity function . . . 13
- 1.7 Evolution of galaxies and star formation . . . 18
  - 1.7.1 Ram pressure stripping . . . 22
  - 1.7.2 Galaxy interactions . . . 22
  - 1.7.3 Galactic starvation . . . 24

2 Observations **25**
- 2.1 The data . . . 26
  - 2.1.1 Image quality . . . 33
  - 2.1.2 Limiting magnitude . . . 33

3 Photometry **35**
- 3.1 Magnitude scale . . . 35
- 3.2 Photometric systems . . . 36
- 3.3 Photometric calibration . . . 37
  - 3.3.1 Finding the coefficients . . . 40
  - 3.3.2 Calibration of the calibration exposures . . . 47
  - 3.3.3 Calibration of the long exposures . . . 47
  - 3.3.4 Calibration of the HDF-images . . . 49

4 Selection of the cluster galaxies **51**
- 4.1 Finding the galactic dust extinction, A . . . 51
- 4.2 Finding the photometric redshifts with ANNz . . . 52
- 4.3 Finding the photometric redshifts with ZEBRA . . . 64
- 4.4 Selecting the cluster members . . . 81

5 Luminosity functions and star formation rates **83**

5.1 The luminosity distance for a ΛCDM-universe 84
5.2 Converting apparent magnitudes into absolute magnitudes . . 85
5.3 Estimating the volume and selection radius, R 88
5.4 Completeness limit 91
5.5 Estimating the schechter function, $\phi(M)$ 92
5.6 Estimating the star forming activity 98

6 Results and discussion **105**
6.1 Luminosity function 106
6.1.1 RSLF in the rest-frame B-band 106
6.1.2 LF in the rest-frame B-band 117
6.1.3 LF in the rest-frame $U_{\mathbf{2800}}$-band 125
6.1.4 Studying the faint-end slope 132
6.2 Star formation and dynamical state 136
6.3 Summary and future prospects 142

A Details of the photometric calibration **145**
A.1 Finding a_2: 145
A.2 Finding a_0 and a_1: 146
A.3 Estimating the aperture sizes 150
A.4 Special cases in the calibration process 150

B Colour-magnitude diagrams **153**

Bibliography **172**

Chapter 1

Introduction

Astronomy is one of the most ancient of sciences. However, a revolution for observational astronomy came with Galileo Galilei ($1564-1642$). In 1609 he was the first person to point a telescope towards the sky. Galileo's telescopic observations led to the first fundamentally new astronomical data in almost 2000 years. Amongst others, he found evidence for Copernicus's heliocentric (Sun-centered) model, that all the planets revolve about the Sun. In 1610 Galileo turned his telescope on the Milky Way and observed that instead of beeing made up by a luminous celestial fluid, it could actually be resolved into a huge number of faint stars. In the mid-eighteenth century Immanuel Kant suggested that there might exist other star systems such as the Milky Way, and that some of the faint nebulae seen in the sky might have similar structures. A catalogue of nearly 5000 such nebulae was made in the late eighteenth century by William Herschel along with his sister Caroline and son John. As the telescopes got more advanced during the nineteenth century, large improvements were made in observational astronomy. In 1914, the American astronomer Vesto Melvin Slipher ($1875-1969$) discovered that the characteristic lines in the spectrum of almost all galaxies are systematically shifted towards the red. The realization that these galaxies were not only moving away from Earth but also away from each other, made astronomers talk about these galactic motions as an expansion. Edwin Hubble (1926) was the first to classify galaxies, sorting them by content, distance, shape and brightness. Just as most stars are found within galaxies, most galaxies are located in groups and clusters. Clusters of galaxies are the largest virialised structures, and because of their size, their mass content reflects that of the Universe. These unique cosmological laboratories can be tracers of cosmic evolution and of galaxy formation and evolution. In order to understand the evolution of galaxies, it is essential to determine both the rate and efficiency of the star formation, that is, the transmutation of gas into stars. This is in part because the process of converting gas into stars can lead to dramatic

changes in a galaxy, both energetic and chemical. The physical mechanisms responsible for the rate and efficiency of the star formation are also of great importance for understanding the evolution of galaxies. Some candidates that will be discussed in the end of this chapter are *ram pressure stripping*, *galaxy interactions* and *galactic starvation*.

1.1 Motivation and goals

It is important to understand the physics behind the evolution of galaxies as a function of cosmic time and environment. First of all we want to understand the main physical processes responsible for forming the galaxies we observe today. In addition, galaxies are used in statistical studies of the evolution of large-scale structures with time. Cosmological studies with high precision depend on a good understanding of the correlation between star formation (which decides the observed morphology and spectral energy distribution of galaxies) and the underlying density distribution of dark and diffuse baryonic matter.

Several physical mechanisms may be responsible for the evolution of the star formation rate in a galaxy cluster, and the environments where these mechanisms are most efficient, differ. The correlation between star formation and the dynamical state of galaxy clusters can provide clues to which physical cluster-related processes are responsible for the quenching of star formation in high-density environments.

The aim of this thesis is to decide the correlation between star formation and dynamical state of a statistical well defined selection of galaxy clusters. From simulations and theory it is expected strong correlations between the dynamical state of a galaxy cluster and the history of how its matter has gathered, and the present and prior star formation rate in the cluster.

1.2 Thesis Outline

The thesis contains six chapters, as well as two appendices and bibliography.

- **Chapter 1** presents the background theory. It starts out by giving a brief introduction to cosmology, followed by the properties of galaxies and clusters of galaxies, and ends with a description of the main topics in this thesis: *the luminosity function* and *evolution of galaxies and star formation*.

- **Chapter 2** presents the data used in this thesis. The data set consists of images of 35 galaxy clusters in UV taken with the Nordic Optical Telescope (NOT) at la Palma. In addition, corresponding photometry in other wavelength regions (from previous imaging in the V- and I-bands with NOT and the 2.2 m University of Hawaii telescope) are used, primarily to estimate the photometric redshift of each galaxy, and hence decide which galaxies are in fact cluster members (chapter 4).

- **Chapter 3** first gives a short introduction to the magnitude system and the photometric system used, then presenting the numerous steps in the photometric calibration process of the data. Accurate photometry is needed to separate the cluster members from the foreground and background galaxies (chapter 4), estimate the luminosity function for each cluster (chapter 5), and estimate the star formation rates for each cluster galaxy (chapter 5).

- **Chapter 4** presents the photometric redshift estimations for each galaxy. Accurate photometric redshifts are needed to calculate the luminosities of the galaxies, and to separate the cluster members from the foreground and background galaxies.

- **Chapter 5** first presents the calculation of the luminosity functions. The photometric redshifts found in chapter 4, are used to calculate the absolute magnitudes and luminosities from the calibrated apparent magnitudes. Based on the luminosities in UV, the star formation rate for each cluster galaxy can be calculated.

- **Chapter 6** presents the results of this thesis, and will be discussed based on the theory from chapter 1. The main topics discussed are the different luminosity functions for each of the 35 galaxy clusters, and the fraction of star forming galaxies in each cluster. The distribution of X-ray luminous gas is a good measurement of the degree of dynamical equilibrium in a galaxy cluster. Existing X-ray measurements are used to classify the galaxy clusters according to their dynamical state, which again is compared with the calculated star formation activity. The results will be put in a wider context, discussing which physical cluster-related processes may be responsible for the observed (or not observed) trends.

1.3 A brief introduction to cosmology

Cosmologists have for a long time been trying to find out what kind of Universe we live in. Since light reaching us today from some distant galaxies

was sent out billions of years ago, we are able to look back in time and follow the evolution of the Universe up till the present epoch. By varying different cosmological parameters, cosmologists search for the best fit to the Universe we observe. After being inspired by Einstein's theory of general relativity, Alexander Friedmann introduced a set of differential equations describing the dynamic evolution of the Universe. The Friedmann equations are based on assumpions of an isotropic and homogeneous universe ("the cosmological principle"), which is a good approximation to our Universe on scales larger than $\sim$ 100Mpc. By using the Friedmann equations we are able to calculate distances and time intervals for different Universe models. Friedmann's first equation can be written as:

$$\dot{a}^2 + kc^2 = \frac{8\pi G}{3}\rho a^2 + \frac{\Lambda}{3}a^2, \tag{1.1}$$

and the second

$$\ddot{a} = -\frac{4\pi G}{3}\left(\rho + \frac{3p}{c^2}\right)a + \frac{\Lambda}{3}a, \tag{1.2}$$

where:

- a is the scale factor describing the expansion of the universe, and is a function of time. The present day value of the expansion factor is $a(t_0) = a_0 = 1$.
- $\dot{} = \frac{d}{dt}$ and $\ddot{} = \frac{d^2}{dt^2}$.
- G is the gravitational constant.
- c is the speed of light in vacuum.
- k is the spatial curvature parameter. $k = -1$ for a negatively curved (open) Universe, $k = 0$ for a flat Universe, and $k = +1$ for a positively curved (closed) Universe.
- ρ represents the *density* of the Universe.
- p represents the *pressure* of the Universe.
- Λ is *the cosmological constant.*

The cosmological constant was first introduced by Einstein in 1916 to allow a static solution of the Universe. He looked at the cosmological constant as a contribution to the curvature of space-time. We now know that a static solution is not valid, which have given the cosmological constant a whole new meaning. It is now considered to be directly linked with the energy density of empty space; the vacuum energy. *Dark energy* is the most general class of models which include vacuum energy. For a positive cosmological constant (which fits current observations), the dark energy has negative pressure. Thus, with a Newtonian interpretation of Λ in terms of gravitational

forces instead of spacetime geometry, Λ gives rise to a repulsive contribution to the gravitational force.

The Hubble parameter is defined as

$$H \equiv \frac{\dot{a}}{a}, \tag{1.3}$$

where the present day value, H_0, is given by $H_0 = 100h\text{kms}^{-1}\text{Mpc}^{-1}$. The seven year Wilkinson Microwave Anisotropy Probe (WMAP7) observations imply that the dimension less quantity $h = 0.710 \pm 0.025$ today (Larson et al. 2010). Inserting the present value, H_0, in the first Friedmann equation and rearranging, gives the critical density today

$$\rho_{c0} \equiv \frac{3H_0^2}{8\pi G} = 1.88 \times 10^{-26} h^2 \text{kg m}^{-3}, \tag{1.4}$$

ρ_{c0} is defined to be the density a universe containing matter only ($\Lambda = 0$) would have today if it was flat ($k = 0$). This universe would then continue to expand forever, but the expansion velocity, v, would get closer and closer to zero in the distant future. In this case, if ρ_0 exceeds the critical density, then there is sufficient mass in the universe for its gravitational influence to stop the expansion, followed by a contraction that eventually would end in a "big crunch". On the other hand, if ρ_0 is less than ρ_c there is not enough mass to halt the expansion, and the universe will expand forever.

It is common to measure densities in units of the critical density. The cosmic density parameter is defined as

$$\Omega_0 \equiv \frac{\rho_0}{\rho_{c0}} = \frac{8\pi G\rho_0}{3H_0^2}, \tag{1.5}$$

where $\Omega_0 = \Omega_{m0} + \Omega_{\Lambda 0}$. Furthermore, one can also introduce a "curvature density parameter"

$$\Omega_{k0} = -\frac{kc^2}{a_0^2 H_0^2}. \tag{1.6}$$

This means that we can write

$$\Omega_0 + \Omega_{k0} = 1, \tag{1.7}$$

There is strong evidence that the spatial geometry of the Universe is flat, so that $\Omega_{m0} + \Omega_{\Lambda 0}$ is very close to unity. In terms of the density parameters, the Friedmann equations take the form

$$\left(\frac{\dot{a}}{a}\right)^2 = H^2(t) = H_0^2 \left[\Omega_{m0}\left(\frac{a_0}{a(t)}\right)^3 + \Omega_{\Lambda 0}\right], \tag{1.8}$$

and

$$\frac{\ddot{a}}{a} = -\frac{1}{2}H_0^2\left[\Omega_{m0}\left(\frac{a_0}{a(t)}\right)^3 - 2\Omega_{\Lambda 0}\right]. \tag{1.9}$$

In the above equations $\rho_\Lambda = \rho_{\Lambda 0} = constant$ have been used (the vacuum energy density remains constant as space expands). Observations point in the direction of a flat universe model dominated by dark energy, Λ, and cold dark matter. This ΛCDM-model is frequently referred to as the *standard model* of big bang cosmology. Throughout this thesis the values $\Omega_{m0} = 0.3$ and $\Omega_{\Lambda 0} = 1 - \Omega_{m0} = 0.7$ will be used. These are close to the best-fit values from the WMAP7 observations (Larson et al. 2010).

Cosmological redshift: By observing distant galaxies, one actually looks back in time. Current observations using the most sensitive telescopes can view galaxies as they appeared over ten billion years ago. These studies are allowing astronomers to learn about the formation and evolution of galaxies during the history of the Universe. However, to be able to gain any valuable information from astronomical objects, it is critical to know their distances. The distance out to a galaxy cluster is almost always referred to in terms of redshift. The redshift of a cosmological object can be obtained by comparing the wavelengths of its spectral lines. In mechanics redshift is normally a consequence of the Doppler effect, a shift in the frequency when the source of the waves is moving relative to the observer. The cosmic redshift, however, is not a consequence of the Doppler effect, but rather a result of space itself stretching. It is usually measured by the parameter z defined by

$$1 + z = \frac{\lambda_0}{\lambda_e} = \frac{a(t_0)}{a(t_e)}, \tag{1.10}$$

where λ_0 is the wavelength measured by the observer and λ_e is the emitted wavelength. The scale factor describing the expansion of the universe, $a(t)$, is a function of time, where t_0 is today (the time of the observeration) and t_e is the time of emission.

1.4 Galaxy clusters

The cosmological principle states that on the largest scales the universe is both homogeneous and isotropic. However, when looking at smaller scales, this assumption breaks down. Galaxies are not scattered randomly across the universe but are found in groups and clusters of different sizes. The structure of galaxies consists of rich and poor clusters, connected by filaments and sheets, with regions largely devoid of galaxies (voids) in between. Clusters constantly accretes galaxies and galaxy groups along these filaments or directly from the field, and various studies suggest that the key sites of galaxy transformation are within these infalling structures rather than the cluster core (e.g. Balogh et al. 2004; Moran et al. 2005; Fadda et al. 2008). The sheets and voids create a foam-like structure sometimes called the "cosmic web" (Bond et al. 1996). The titanic sheets can be more than 100 Mpc long and several megaparsecs thick, and are the largest structures known in the Universe. Groups of galaxy clusters (superclusters) appears as occasional relatively dense nodes in these sheets. A typical supercluster contains dozens of individual clusters spread over a region of space up to 45 Mpc across. However, clusters of galaxies are the largest and most massive objects in our known Universe that have had time to undergo gravitational collapse. Their diameters are typically between 2 and 10 Mpc, and their masses vary from $10^{13} M_{\odot}$ to over $10^{15} M_{\odot}$. A cluster consisting of few galaxies is said to be *poor*, whereas a *rich* cluster may contain several thousand galaxies. A cluster with less than 50 galaxies is often called a *group*. Our own Milky Way galaxy belong to the Local Group, which includes a few dozen smaller systems within a radius of 1-2 Mpc. The first really comprehensive cluster catalogues were made in the 1950s. From 1961 to 1968 Fritz Zwicky and his colleagues published a comprehensive six volume *Catalogue of Galaxies and Clusters of Galaxies*, but the catalogue with the greatest long-term impact was that produced by George Abell in 1958. Abell's 2712 clusters were selected by eye from photographic plates, seeking those areas where more galaxies than average were found at approximately the same distance from us. The catalogue was later extended to the southern hemisphere by Abell, Corwin and Olowin (Abell et al. 1989), with a total sample consisting of 4073 rich galaxy clusters.

Galaxy clusters are further classified as *regular* and *irregular*. Regular clusters are usually rich, and are characterized by their spherical symmetrical appearance and concentrated central core. The brightest galaxy is usually located in the center and is typically a large elliptical galaxy (cD). The vast majority of the galaxies in a rich, regular cluster are ellipticals and lenticulars (S0's). Irregular clusters are more disorganized in appearance, and there is no concentrated central core. Their range of sizes is similar to that of the

regular clusters, but their content is usually somewhat poorer. Although they are made up of all types of galaxies, the majority are spirals. For both regular and irregular clusters, ellipticals become increasingly common as one moves towards the center of the cluster.

The cluster galaxies are held together by gravity, which means that there must be enough matter in the cluster to prevent the galaxies from drifting away. The four principal constituents of clusters ensuring this are:

Galaxies: Groups and clusters may contain from ten to thousands of galaxies. The stars in each galaxy make up the visible part of a galaxy cluster. A typical bright galaxy may contain as much as several 100 billion stars. However, measurements made of the line-of-sight speeds of galaxies within nearby clusters (such as the Coma cluster) show that these velocities are far too large for the galaxies to remain gravitationally bound by their mutual attraction if the visible galaxies constitute the only matter component in the clusters. The solution is either the presence of an additional invisible mass component, or modification to the theory of how gravity works on large scales. Such a modification came with Milgrom's paradigm of modified Newtonian dynamics (MOND) (Milgrom 1983). He suggested that Newton's gravitational law may not hold for extremely low accelerations, and that acceleration is not linearly proportional to force at these low values. Thus, if Milgrom's paradigm applies, there is no need to assume large amounts of hidden mass in galaxy systems. Bekenstein (2004) have proposed a relativistic generalization of Milgrom's MOND where gravity is mediated by a tensor, a vector, and a scalar field, thus called TeVeS (tensor-vector-scalar).

Intracluster stars: During galaxy interactions and mergers, tidal forces often eject stars from their parent galaxies into intergalactic space. These intracluster stars can provide informations about the former interaction. Intracluster starlight can be a unique and powerful tool for studying galaxy clusters, but due to its low surface brightness, observations of this intracluster light (ICL) component are difficult. Several numerical simulations of the ICL phenomenon have been made. Focusing on 117 clusters with masses between $10^{14} M_{\odot}$ and $10^{15} M_{\odot}$, Murante et al. (2004) suggest that between 10% and 50% of a system's stars may be unattached to any galaxy. Simulations of Virgo-like and Coma-like clusters predict that the fraction of intracluster stars lie between 20% and 40% (Sommer-Larsen et al. 2005). Since Virgo is the nearest system to have a significant intracluster population (Ciardullo et al. 2004), numerous surveys have been made of the cluster's intracluster planetary nebulae (Arnaboldi et al. 1996, 2002; Feldmeier et al. 2004). Puchwein et al. (2010) show that intracluster stars preferentially are

stripped in a cluster's densest region from massive galaxies falling into the cluster at $z > 1$. Another interesting result is the finding that some of the intracluster stars also form in the intracluster medium inside cold gas clouds that are stripped out of infalling galaxies.

Hot gas: In the late 1970s X-ray studies revealed the presence of large amounts of hot intracluster gas known as the intracluster medium (ICM). The ICM is heated to temperatures as large as $10^7 - 10^8$ by the gravitational energy released by the formation of the cluster from smaller structures. The high temperature ensures that the elements present in the ICM are ionised. Light elements in the ICM have all the electrons removed from their nuclei. Above 10^7K, recombination of electrons onto atomic nuclei are extremely rare, and the ICM therefore mainly emits thermal Bremsstrahlung. This is electromagnetic radiation produced by the acceleration of a charged particle, such as an electron, when deflected by another charged particle, such as an atomic nucleus. One of the puzzles in astrophysics has been to explain why the ICM remains so hot when it is such a strong X-ray emitter. Mechanisms responsible for heating the ICM are believed to be due to both gravitational processes, such as gravitational accretion shocks emerging from collapsing regions and the dynamical friction which occurs when galaxies move through the ICM, and nongravitational processes, such as heating by central active galactic nuclei (AGNs), galactic winds and massive supernova bursts (Pen 1999; Roychowdhury et al. 2004). The ICM contains most of the baryonic material in the cluster, and consists mainly of ionised hydrogen and helium. The hot ICM, stars and gas in galaxies, and intergalactic photo-ionized gas make up at most half of the baryons that are expected to be present in the Universe. The majority of baryons are still missing and are expected to be found in the intergalactic medium (IGM) in a temperature range $10^5 - 10^7$ K, where they have been difficult to detect (Cen and Ostriker 1999; Davé et al. 2001; Cen and Ostriker 2006). This warm hot intergalactic medium (WHIM) is primarily heated by gravitational accretion shocks emerging from collapsing regions during large-scale structure formation. Even though the total mass of all the intracluster gas in a typical rich cluster can exceed the total stellar mass in that same cluster, it still only acounts for about 10% of the invisible mass. This means that most of the mass in a galaxy cluster must be in the form of non-luminous *dark matter*. Both galaxies and hot gas are sitting in a common dark-matter potential, and the distribution of the X-ray emitting gas can be regarded as a powerful tool when deciding the amount of matter present and the dynamical state of a cluster. This will be used in section 5.6

Dark matter: The Swiss-American astrophysicist Fritz Zwicky was the first person to find observational evidence for the existence of dark matter (1933). The fluctuations observed in the cosmic microwave background (CMB) are believed to be the initial seed for the large scale structure observed in our present-day Universe. These observations indicate that matter has clumped on very small scales, and that the dark matter therefore must be *cold* instead of hot. If most of the matter were in the form of *hot* dark matter, the structure formation would have occured the other way around. Fast moving (hot) particles cannot clump together on such small scales and, in fact, suppress the clumping of other matter. The structure formation would then have occured from fragmention of very large regions into smaller regions. Even though the Cold Dark Matter model now is the preferred explanation for galaxy and structure formation, some hot dark matter is still present in the form of massive neutrinos. The composition of dark matter is a hot topic amongst scientists, and some candidates are:

- Baryonic dark matter: *brown dwarfs* and *black holes*. Big Bang nucleosynthesis sets constraints on the amount of baryonic matter present in the Universe. The cosmic baryon density is recently measured to be $\Omega_{b0} = 0.0449 \pm 0.0028$, while the total mass density is $\Omega_{m0} = 0.266 \pm 0.029$ (WMAP7). Thus, there must be some sort of non-baryonic matter present.

- Non-baryonic dark matter: *axions*, *neutrinos* and *WIMPs* (weakly interacting massive particles).

One way of measuring the amount of dark matter present in a galaxy cluster is by using *gravitational lensing*. This phenomenon is based on the gravitational bending of light rays, and is one of the predictions from Albert Einstein's general theory of relativity (1916). Any massive object (such as a galaxy cluster) placed in front of a bright source may act as a gravitational lens. It is currently believed that the dark matter makes up as much as 85%-90% of the total mass in the Universe. This prediction is based on observation of galaxy rotation curves, gravitational lensing, structure formation, and the fraction of baryons in clusters combined with independent evidence for the baryon density. "Non-baryonic dark matter" does not interact through the electromagnetic or strong nuclear force, and the only evidence for its existence comes from gravitational effects on visible matter. The true nature of the dark matter remains a mystery, but it appears to make up most of the mass in our Universe.

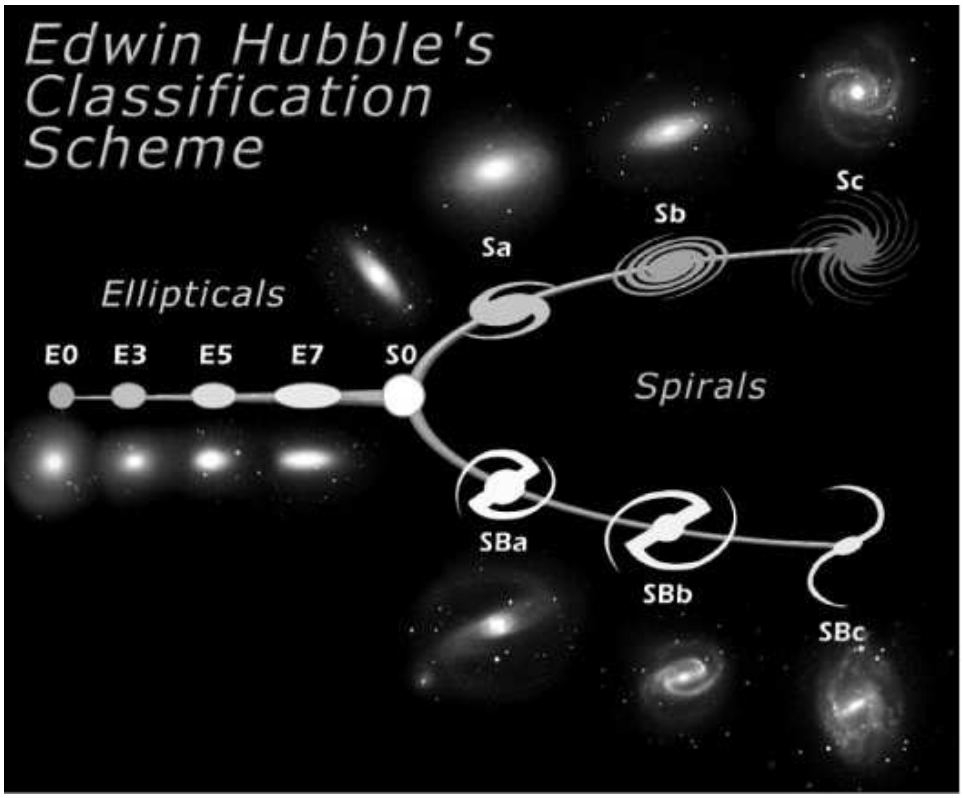

Figure 1.1: Hubble "Tuning Fork" classification of galaxies (NASA).

1.5 Morphology of galaxies

Galaxy morphological classification divides galaxies into groups based on their visual appearance. Edwin Hubble (1926) divided the galaxies into three main groups: ellipticals (E's), spirals and irregulars (Irr's). The spirals are further subdivided into normal spirals (S's) and barred spirals (SB's). Ten years after formulating his classification system, Hubble introduced an extra group between the ellipticals and spirals; *lenticulars* (S0's). These galaxies can either be normal (S's) or barred (SB's). Hubble's classification scheme is known as the Hubble tuning-fork diagram and can be seen in figure 1.1. Hubble placed all galaxies that did not fit into his other categories in the *irregular* class. These galaxies are not shown in figure 1.1. The ellipticals and lenticulars on the far left are conventionally referred to as *early-type galaxies*, while the spirals towards the right are referred to as *late-type galaxies*. This has its basis in Hubble's idea of an evolutionary sequence of galaxies. Although we now know that spirals did not start as ellipticals, the terms are still common. The vast majority of present-day galaxies can be placed in one of Hubble's categories, but it is important to keep in mind

that other types of galaxies with special characteristics also exist. Examples are Seyfert galaxies, radio galaxies, starburst galaxies, Sd galaxies (which are part of the extended Hubble diagram), Sm galaxies, cD galaxies, and different kinds of dwarf-galaxies. The different galaxy-types do not only differ in their appearance, but also in the processes taking place inside them.

Elliptical galaxies: The brightest galaxies in the universe are ellipticals, but so also are the dimmest. Ellipticals predominate in rich clusters of galaxies, and the largest of them, the *cD galaxies*, are found in the densest parts of those clusters. The very faintest ellipticals are subdivided into several groups: the rare compact ellipticals, the faint diffuse dwarf elliptical (dE) galaxies, and the even fainter dwarph spheroidals (dSph). Elliptical galaxies are characterized by a smooth, ellipsoidal light distribution, showing no evidence of spiral arms or disks. They are further divided into seven groups (E1-E7) based on how round or flat they look. Their ellipticity is given by $\epsilon \equiv 1 - b/a$, where a and b are the observed major and minor axis of the ellipse, respectively. The number after E is given by $10 \times \epsilon$, which means that E0 galaxies are circular, while E7 galaxies have the most extreme ellipticity with $\epsilon = 0.7$. Galaxies flatter than E7 are called *lenticulars* (S0's). Ellipticals are some of the most evolved systems observed. Because they are virtually devoid of cold interstellar gas and dust, there is little material from which stars could have recently formed. Ellipticals therefore mainly consist of old, Population II stars. However, ellipticals are not simple systems. They cover a huge range of luminosity and of light concentration. Some ellipticals rotate fast, others hardly at all. Some appear to be oblate, while others have triaxial shape with three unequal axes. The stars of elliptical galaxies follow randomized motion, and ellipticals have little net angular momentum. The more luminous ellipticals have a higher velocity dispersion.

Lenticular galaxies: Lenticular galaxies (S0s) form a transition class between ellipticals and spirals. S0s show a rotating disk in addition to the central elliptical bulge, but unlike spiral galaxies, the disk lacks any spiral arms or extensive dust lanes.

Spiral galaxies: The spiral galaxies are named after their bright spiral arms. Some characteristics of these galaxies are:
- a flat, rotating disk containing stars, gas and dust.
- a central concentration of stars known as the bulge.
- a halo of stars surrounding the bulge and disk. These stars are much older and of lower metallicity than the ones in the disc.
- spiral arms with ongoing star formation. Because of these young, hot stars, the spiral arms appear brighter than the surrounding disk in visible light.

- many bulges are believed to have a supermassive black hole in their center. Spiral galaxies are further subdivided into Sa, Sb, Sc and Sd (similar for the barred spirals) based on the prominence and structure of the spiral arms and the relative size of the central bulge. Sd galaxies are placed after the Sc galaxies in the Hubble diagram. Sa galaxies have smooth, tightly wound spiral arms and a large central bulge, Sb galaxies have moderately well-defined spiral arms and a moderate sized central bulge, while Sc- and Sd galaxies have loosely wound, well-defined spiral arms and a small central bulge. A greater portion of the mass of a Sc- or Sd galaxy is involved in star formation than for Sa and Sb galaxies. Because these classifications are subjective, astronomers often use intermediate designations of Sab, Sbc or Scd. In contrast to elliptical galaxies, the stars in the disk of a large spiral galaxy follow nearly circular orbits. Most of the disk's kinetic energy is in rotation, while only a fraction is in random motion.

Barred spirals: About half of all spiral and lenticular galaxies have a *bar* running through the galaxy's nucleus. The spiral arms originate from the end of this bar rather than from the nucleus itself. As for the normal spiral galaxies, the barred spirals are subdivided into SBa's, SBc's, SBc's and SBd's according to the texture of the spiral arms and the relative size of the central bulge.

Irregular galaxies: Irregulars are galaxies which do not fit in the scheme of ellipticals, spirals and barred spirals. Generally they contain a lot of interstellar gas and dust, and have both young and old stars. Irregulars are further divided into Irr I and Irr II, where Irr I show at least some sign of organized structure such as spiral arms, while Irr II are the most extremely disorganized galaxies. Examples of sub-classes of Irr I galaxies are Sm and Im.

1.6 Luminosity function

The luminosity function (LF) of galaxies is a powerful tool in the study of galaxy formation and evolution. It is often written as $\phi(L)$, and it describes how the relative number density of galaxies (in practice measured per Mpc^3) varies with their luminosity L. $\phi(L)dL$ is then the number density of galaxies with luminosities between L and $L + dL$ per Mpc^3. In general the *Schechter function* (Schechter 1976) is a good approximation of the observed galaxy LF. The Schechter function originates from the calculated mass distribution of clumps emerging from the young universe (Press and Schechter 1974). In 1976 Paul Schechter applied this function to fit the luminosity distribution

of galaxies in Abell clusters. The fit turned out to be excellent. Thus, the galaxy LF is directly related to the galaxy mass function. The Schechter function is defined as:

$$\phi(L)dL = \phi^* \left(\frac{L}{L^*}\right)^{\alpha} exp\left(-\frac{L}{L^*}\right)\frac{dL}{L^*}. \quad (1.11)$$

Equivalently it can be written in terms of the absolute magnitudes, M, of the galaxies:

$$\phi(M)dM = (0.4\ln 10)\phi^* 10^{0.4(\alpha+1)(M^*-M)} exp(-10^{0.4(M^*-M)})dM, \quad (1.12)$$

where

- L^* is the luminosity which characterizes the *break* in the LF. Above this luminosity the number of galaxies falls sharply.
- M^* is the absolute magnitude corresponding to L^*. The absolute magnitude M and the luminosity L are related by the expression

$$log\left(\frac{L}{L^*}\right) = -0.4(M - M^*). \quad (1.13)$$

- ϕ^* is a normalisation factor.
- α sets the slope of the LF at the faint end.

These parameters are chosen to fit the observations. The LF can be divided into two parts:
1) a power law ($\phi \propto L^{\alpha}$) which dominates at low luminosities ($L \ll L^*$).
2) an exponential cutoff ($\phi \propto e^{-L}$) which dominates at high luminosities ($L > L^*$). Thus, very luminous galaxies are also very rare.

The universal Schechter function does not take morphological types into consideration. Thus, it suppresses information about the change of type as the absolute magnitude varies. An illustration of this is made by Binggeli (1987) (see figure 1.2). Here the details of galaxy-type is hidden under Paul Schechter's foot. The existence of a "universal" Schechter function has been suggested (Lugger 1986; Colless 1989; Trentham 1998). However, the mass function, star formation process, and morphological characteristics of galaxies are affected by their environment and evolve with time (will be discussed in the next section). The galaxy LF is therefore also expected to change with time and to vary with galaxy characteristics and density environments. Many studies have been made of the galaxy LF's dependence on morphological type (Wolf et al. 2003; Cole et al. 2005; Croton et al. 2005), redshift (Lilly et al. 1995; Ellis et al. 1996; Wolf et al. 2003; Loveday 2004), and on environment (Molinari et al. 1998; Moretti et al. 1999; Mercurio et al. 2003; Haines et al. 2004; Croton et al. 2005; Hoyle et al. 2005; Cole et al. 2005). These studies show:

Figure 1.2: Binggeli's (1987) cartoon of Paul Schechter suppressing the details of the "general" luminosity function under his foot. Cartoon found in Binggeli 1987.

- there is a clear difference in the LFs of red and blue selected galaxies, where "red" and "blue" correspond to early and late-type galaxies respectively in the Hubble sequence.
- there is evidence that the LF of galaxies in rich clusters differs from that of galaxies in underdense regions of the universe, the void regions. In particular, Croton et al. (2005) find that the LF measured in all density environments, from voids to clusters, can be approximated with Schechter functions with parameters that vary smoothly with local density, but in a fashion that differs strikingly for early- and late-type galaxies.
- the shape of the LF changes with redshift.

Binggeli et al. (1988) have estimated the specific LFs of different morphological types (see figure 1.3). The bottom figure shows type specific LFs for

each of the major Hubble types for the Virgo cluster. The total LF (also plotted) is the composition of the type specific LFs. As can be seen from the figure, the spirals and S0 galaxies have a Gaussian LF, the ellipticals have a skewed Gaussian LF, the dwarf ellipticals (dE+dSph) follow a Schechter function with steep slope, while the irregulars follow a Schechter function with shallower slope. In addition figure 1.3 shows the LFs for the local field sample from the 500 km s^{-1} distance limited catalogue (updated) of Kraan-Korteweg and Tammann (1979) (top figure). These two figures also point out that there is a difference between the LFs in cluster environments and the LFs of field galaxies. Thus, the total LF depends on the proportions of spirals, S0, E, dE, and dIrr galaxies (Binggeli et al. 1988). Since the relative frequencies of the Hubble types depend strongly on the environmental density, it is clear that the total LF must also differ between such regions. Hence, there cannot be such a thing as the universal luminosity function.

The question that remains is which physical processes are responsible for these variations as a function of redshift and environment. This will be discussed in the next section.

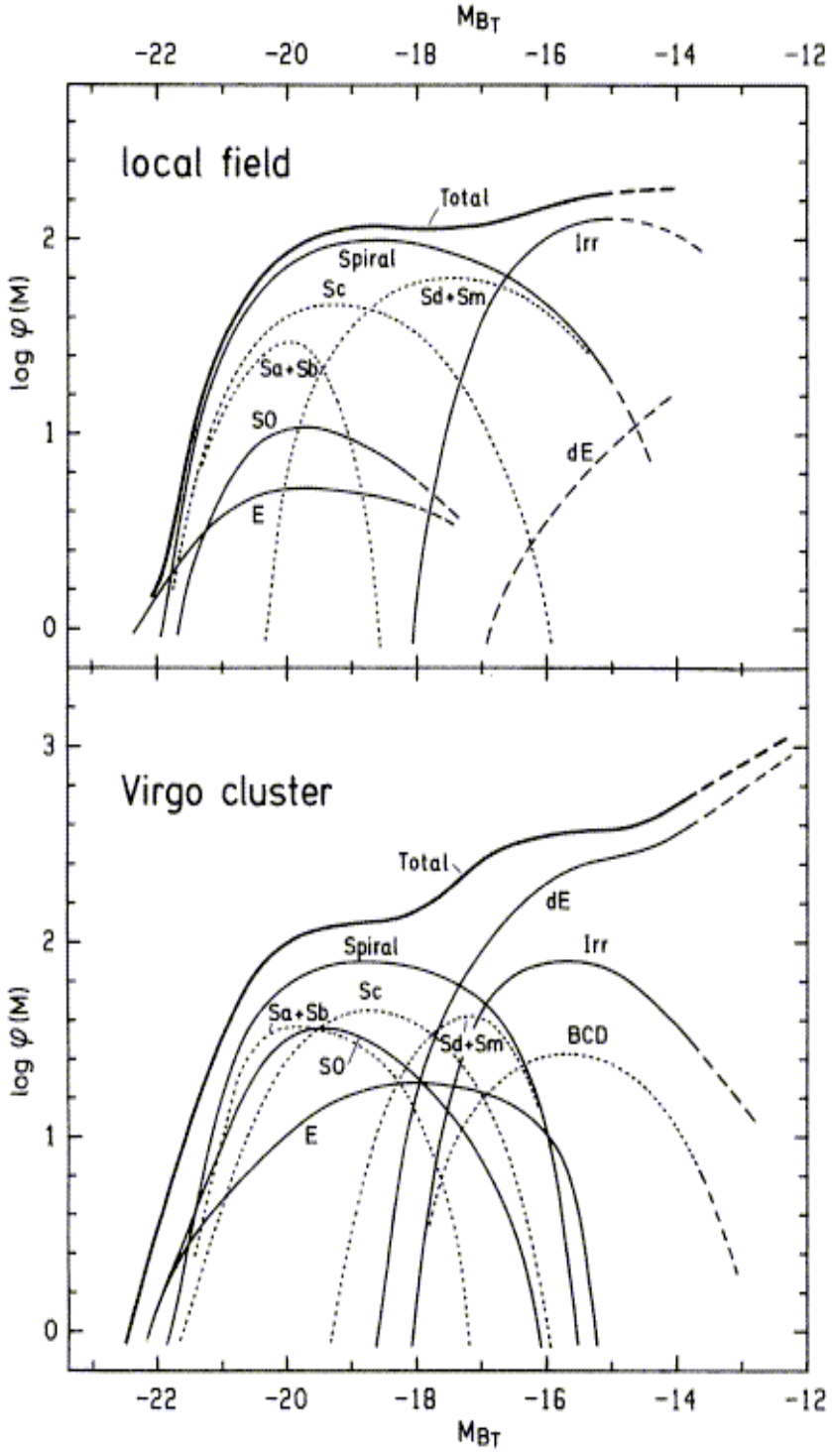

Figure 1.3: The LF of field galaxies (top) and Virgo cluster members (bottom). The zero point of $log\phi(M)$ is arbitrary. The LFs for individual galaxy types are shown. Extrapolations are marked by dashed lines. In addition to the LF for all spirals, the LFs of the subtypes Sa+Sb, Sc, and Sd+Sm are also shown as dotted curves. The LF of Irr galaxies comprises the Im and BCD galaxies; in the case of the Virgo cluster, the BCDs are also shown separately. The classes dS0 and "dE or Im" are not illustrated. They are, however, included in the total LF over all types (heavy line). (From Binggeli, Sandage, and Tammann 1988).

1.7 Evolution of galaxies and star formation

The visible Universe of galaxies is highly inhomogenous, consisting of structures from the scale of isolated galaxies, through groups and clusters of galaxies to superclusters and giant voids in the distribution of galaxies. In the standard ΛCDM-model, these large-scale structures are formed as a consequence of the growth of the primordial density fluctuations in the early universe. In this scenario, the amplitude of the initial density fluctuations decreases with increasing scale. The result is a universe where structure is built up hierarchically, that is, low-mass objects form first and then merge together to form more massive objects. Protogalaxies begin to form from the collapse of rare, highly overdense regions of the universe. As they evolve, they continually accrete mass from the surrounding regions. Clusters are then formed relatively recently between 10 billion years ago and now. Clusters are not just places where galaxies are more densely packed. The cluster environment is different from that of the field. The morphology-density relation (Dressler 1980; Dressler et al. 1997) shows how various morphological types differ between high and low density regions, that is, the shape of galaxies depend strongly on the local density. In particular, the most massive and least star-forming galaxies are found in the highest density environments. Before going deeper into the different mechanisms responsible for galaxy evolution, a short review of star formation is useful. Star formation is in fact galaxy evolution caught in the act.

Star formation: Although space is very empty and the stars in a galaxy are very far apart, the space between the stars contains a very diffuse medium of gas and dust astronomers call the interstellar medium (ISM). This medium consists of neutral hydrogen gas (HI), molecular gas (mostly H_2), ionized gas (HII), and dust grains. Molecular clouds are formed from high density regions of the ISM. If a cloud is massive enough that the gas pressure is insufficient to support it, the cloud will undergo gravitational collapse. This triggers star formation in the cloud's densest regions. As soon as massive O and B stars form, they emit ultraviolet (UV) light that ionizes the surrounding hydrogen. The new HII region has a temperature T$\sim$10 000K, and it produces an emission-line spectrum. An example of such a HII region is the Orion Nebula, which is the closest region of massive star formation to Earth. There are several characteristics of a star forming region, and it can therefore also be detected in different ways:

- *H_α line*: The H_α line is visible in the red part of the electromagnetic spectrum. H_α has a wavelength of 6563 Å and is a result from the transition between the energy levels n=3 and n=2 in hydrogen. After a hydrogen atom has been ionized, the electron and proton recombine

to form a new hydrogen atom. The electron may then begin in any energy-level before finally ending in the ground state (n=1). Approximately half the time, these transitions include the $n = 3$ to $n = 2$ transition, wich leads to a H_α emission-line. Thus, H_α is a good tracer for the ionized hydrogen content of gas clouds, and it is related to the presence of short-lived massive stars (Gallego et al. 1995; Kennicutt et al. 1995; Bechtold et al. 1997). A disadvantage of using the H_α line is that it requires spectroscopi or H_α narrowband plus H_α broadband photometry. Since the Balmer radiation is emitted in the red part of the optical spectrum, it is much less affected by dust extinction than the UV radiation. However, some extinction is still present, and to correct for this, the H_β line should be included.

- *Far-infrared (FIR) continuum*: Because of dust in the star forming regions of galaxies, much of the UV radiation coming from a newly formed star may be obscured. Instead of directly escaping the star forming region, the light is absorbed by the dust surrounding the stars, causing the dust to warm up and radiate in the thermal infrared (IR). The absorption cross section is strongly peaked in the blue and UV as the wavelength comes closer to the characteristic dust grain sizes. Secondly, when heavy elements are formed in a young star, a significant fraction of its radiation is radiated in FIR wavelengths. FIR emission can therefore be a strong tracer of the young stellar population and star formation (Devereux & Young 1990; Devereux & Hameed 1997; Rowan-Robinson et al. 1997; Kennicutt 1998). In particular, FIR luminosity is the ultimate tracer for star formation in regions where the radiation field throughout the UV is dominated by young stars, and where dust opacity is high everywhere. In this scenario the dust is effectively warmed up by the young stars, and the FIR luminosity is a measure of the bolometric luminosity of the starburst. A disadvantage of using the FIR continuum is that it is observational expensive in terms of observational time (less galaxies are observed than in the UV), and it should preferably be observed from space.

- *Ultraviolet (UV) continuum*: The mass-lifetime relation for stars[1] give that stars which are bright in UV (even brighter than the hot evolved stars in ellipticals), must be quite young. Thus, in young stellar clusters the UV continuum is dominated by massive, young stars, and is therefore a good tracer for star formation (Donas et al. 1987; Madau et al. 1998; Dahlen et al. 2007). An advantage of using the UV con-

[1]The brightness of Main-Sequence stars varies as $L \simeq M^{3.5}$, where L is the luminosity and M is the mass of the star. Since the rate at which a star burns its fuel is proportional to L, brighter stars have shorter lifes than the fainter ones. Thus, although the amount of fuel the star has does increase with mass, the rate at which it uses this fuel increases even faster.

tinuum instead of the H_α line and the FIR continuum is that it is least observational expensive in terms of observational time. It is easier to build up a large data sample with many clusters and a large number of galaxies in each cluster. Also, in contrast to the FIR continuum, the UV continuum do not have to be observed from space. One drawback in only using the UV luminosity is its sensibility to extinction. In this thesis, UV luminosities will be used to estimate the star formation rates in each galaxy cluster (see section 5.6).

Other tracers of star formation are for example radio continuum emission and CO molecular-line studies, but these will not be discussed here.

The star formation rate (SFR) strongly affects the evolution of a galaxy. This can be seen by looking at the two most distinct galaxy types; ellipticals and spirals. Whereas ellipticals have no ongoing star formation today, spirals have a lot. The explanation for their different appearances and present SFR lies in the rate of their star formation when they were formed:

- The initial SFR of spirals was relatively slow. The gas surrounding the stars then had time to settle by collisions, and because of conservation of angular momentum, a flattened disk was formed. Star formation continues in spirals because the disk contains an ample amount of hydrogen from which stars can form. Ongoing star formation is the reason for the spiral arms, which are dominated by very luminous O and B stars and HII regions. Spiral arms are waves of compression that move around the galaxy. An encounter between a spiral arm and a cold, dark gas cloud will make the cloud contract under the pull of gravity, triggering star formation. Many of the newly formed stars will be faint, red main sequence stars which will continue to drift through the region. However, some of the stars will also be bright, blue O and B stars. Since the lifetimes of these massive O and B stars are short compared to the characteristic rotation period of a galaxy, they will never be far from the spiral arm where they were born.
- The initial SFR of ellipticals was rapid, and almost all of the available gas was used up to make stars before a disk could form. The ellipticals therefore have a smooth, round appearance.

The composition of stars in a galaxy is also related to the initial SFR. The composition of a protogalaxy is thought to be almost exclusively hydrogen and helium gas. The first stars were therefore Population II stars with hardly any metals. When stars die and form planetary nebulae or supernovae, they eject gases enriched in metals into the interstellar medium. Since spirals have ongoing star formation, these heavier elements are incorporated in the formation of metal-rich Population I stars. Ellipticals on the other hand, have rapid star formation when they are young. After this star formation

ceases, and ellipticals therefore only contain metal-poor Population II stars.

The evolution of the total SFR of the Universe has been a well studied topic. Madau et al. (1996) combined the results from the ultraviolet surveys of Lilly et al. (1996) with the information from the Hubble Deep Field to give an estimate of the star formation history from $z = 0$ to $z \sim 4$. They found that the SFR had a peak around $z \sim 1$, dropping steeply at $z > 2$. Springel and Hernquist (2003) have studied the history of the cosmic star formation from the "dark ages" at $z \sim 20$ to the present by using hydrodynamic simulations of structure formation in a ΛCDM universe. They found that the SFR gradually rises by about a factor of 10 from the present epoch to a peak at $z \sim 5-6$. Their model also predicts that as much as 50% of the stars have formed by redshift $z = 2.14$, and are thus older than 10.4 Gyr, while only 25% form at redshifts lower than $z \simeq 1$. The mean stellar age at $z = 0$ is by their model predicted to be 9 Gyr.

Butcher and Oemler (1978, 1984) was the first to show that populations of galaxies at higher redshifts (up to $z \sim 0.5$ in their original study), particularly in rich clusters, contained many more gas-rich, star-forming galaxies than similar populations today. It was also found that the colours of spiral galaxies in the cores of nearby clusters tend to be redder than those of spirals in the field (Butcher and Oemler 1984). The increase of blue galaxies with redshift is known as the *Butcher-Oemler effect* (BO-effect), and it is believed to be due to a much higher fraction of spirals at the expense of S0s in the higher z-clusters. It seems that over the past few Gyr most late-type cluster galaxies have turned into early-type galaxies because their star formation has ended. Recent observations in the infrared with the Infrared Space Observatory (ISO) and the Spitzer Space Telescope give a similar picture as the BO-effect, indicating that the star-forming activity increases with redshift (Coia et al. 2005; Geach et al. 2006).

Clusters are evolving systems, and there is strong evidence that much of their growth is due to the accretion of galaxies along filaments from the surrounding, low density field environment (Gott & Gunn 1972; Zabludoff and Zaritsky 1995; Tormen 1998). The dense environments of clusters may have strong effects on their galaxy members, and it is therefore expected that cluster galaxy populations will evolve more rapidly than those elsewhere (Oemler et al. 1997). For example, galaxies within galaxy clusters tend to be forming stars at a lower rate compared to field galaxies. Since star formation is fueled by gas, this leads to the conclusion that galaxies in clusters tend to have less gas from which to form stars than their counterparts in less dense environments (Butcher & Oemler 1978). Several physical mechanisms may be responsible for transforming a star-forming field galaxy into a passively evolving cluster member, including ram-pressure stripping, galaxy encoun-

ters and galaxy starvation. These will be described below, and a further discussion will also be done in chapter 6.

1.7.1 Ram pressure stripping

As a galaxy moves through a cluster, it experiences a wind due to its motion relative to the ICM. This drag force is called *ram pressure*, and it is capable of stripping the galaxy of much of its interstellar gas (Gott & Gunn 1978; Abadi et al. 1999; Fujita & Nagashima 1999). The strength of the interaction depends crucially on the orbit of the galaxy. A radial orbit allows the galaxy to go deeper into the cluster potential, where its velocity increases considerably and where the galaxy density and the density of the ICM is substantially higher. The rapid motion of the galaxy causes a pressure front to develop at the boundary between the galaxy's gas and the ICM. If the binding energy of the galaxy's own interstellar medium is not large enough, the ram pressure will remove some or all of it. The stars and dark matter are unaffected, so the gas can be left behind while the rest of the galaxy continues its journey through the cluster. The galaxy's star formation is quenched, but the basic disk structure is left intact and largely unperturbed. On the other hand, if the binding energy of the galaxy's own interstellar medium is large enough, the ICM will move together with the galaxy. Although this gas stripping occurs primarily in the central region ($r < 1$Mpc), it is an important mechanism out to the virial radius of the cluster. As a disk galaxy approaches the centre of a cluster, the ram pressure compresses the molecular gas within the galaxy. A result may be a burst of star formation that consumes gas that has not been stripped.

If ram pressure stripping is the main mechanism, the quenching of star formation is expected to be most efficient near the centres of massive clusters in dynamical equilibrium. A difference in the galaxy population between galaxies in dynamical equilibrium and those that are not, is then expected.

1.7.2 Galaxy interactions

Interacting galaxies (colliding galaxies) are of fundamental importance for the evolution of galaxies, clusters of galaxies and the intergalactic medium. These are not collisions in the normal sense of the word, but rather gravitational interaction. The simulations of Toomre & Toomre (1972) first demonstrated that gravitational interactions between galaxies cause stars and interstellar gas and dust to form bridges between the two galaxies and can also form tails. This is a result from the tidal gravitational force both galaxies feel from the other galaxy. The interactions may cause galaxies to merge

into one enormous elliptical or lenticular galaxy, the galaxies may become elongated, or spiral galaxies may have their arms ripped away. Matter falling in from a merging galaxy will interact with material from the other galaxy. As a result, the gas supply may be used up in a short and intense flash of star formation.

A merger occurs when the colliding galaxies do not have enough momentum to continue traveling after the collision, and it is the most violent type of galaxy interaction. When two galaxies of about the same size merge, their stellar disks are destroyed. If cool gas is present, however, a new disk can be formed. Rapid change in the gravitational forces will then drive gas inward to form a central disk and trigger star formation. On the other hand, if no cool gas is present, no new star formation is possible, and the remnant will consist of mainly old and middle-aged stars. When the two colliding galaxies consist of a small galaxy and a much larger one, the larger galaxy will look much the same while the smaller galaxy will be stripped apart and become part of the larger galaxy. This is often referred to as galactic *cannibalism*, and it usually involves giant or supergiant ellipticals in the centres of rich clusters.

Direct galaxy mergers are extremely rare (Oemler et al. 1997), and the merger frequency has decreased up to the present (Le Fèvre et al. 2000). However, once per Gyr, every galaxy is expected to experience a high speed close encounter with a bright galaxy (Moore et al. 1996). If the relative velocity of two galaxies passing each other is too high, the strength of the dynamical friction between them will not be large enough to slow them down and cause them to merge. However, as they pass each other, both galaxies will feel a tidal gravitational force from the other galaxy. The shape of a spiral galaxy within a galaxy cluster is likely to change after each such encounter, and the outer most weakly bound stars can get stripped away. These frequent high speed galaxy encounters within clusters are called *galaxy harassment*. One effect of galaxy harassment is the intracluster stars observed floating around inside of the cluster, unattached to any particular galaxy.

Tidal encounters are more efficient in structures smaller than massive clusters, such as groups of galaxies. In groups, the relative velocities between galaxies are smaller than those in massive clusters, and the effect of close encounters between galaxies is therefore stronger. If tidal encounters between galaxies are the main mechanism to quench star formation, almost all star formation will end before the galaxies have time to join a larger cluster. The galaxies will go through these interactions while they are still in smaller groups, long before they become a part of a larger cluster. A difference in the galaxy population between galaxies in dynamical equilibrium and those that are not, is then not expected.

1.7.3 Galactic starvation

In a typical $\sim L^*$ spiral galaxy (where L^* is the characteristic luminosity from the galaxy cluster's luminosity function) the time-scale for which the spiral consumes its gas reservoir through star formation is just ~ 3 Gyr. This means that star formation will deplete the gas in most spirals in a fraction of the Hubble time. Larson et al. (1980) therefore proposed that the gas in spirals is continuously replenished from their extended halos, allowing star formation to continue. But what if the accretion of fresh gas from the halo stopped? This is what happens in *galactic starvation* where the galaxy's surrounding halo is removed by the ICM (Larson et al. 1980; Balogh et al. 2000). With no transfer of matter between a galaxy and its surroundings, star formation will eventually use up the gas, and a gas-poor passively evolving galaxy will remain.

If starvation is the main mechanism for ending star formation in galaxies, the quenching of star formation will happen gradually as a function of time and environment.

Chapter 2

Observations

This chapter presents the data of the 35 galaxy clusters used in this thesis. When observing astronomical objects with a telescope, radiation is gathered, usually passing through special optical filters. The energy is then recordered by using a photosensitive instrument. One of the most efficient and accurate detectors in use today, is the charge-coupled device (CCD). This semiconductor detector has revolutionized the way in which photons are counted. A CCD consists of an array of small cells (or pixels) made of silicon. If a photon striking a pixel has the right wavelength (3000 to 11000Å), it is easily absorbed. The photon's energy sets free one or more electron hole pairs. The charges are collected and amplified. An output signal is then produced which should be linearly proportional to the number of photons absorbed. CCDs are analogue detectors. The amplified current is converted into a digital number (DN) in an analog-to-digital converter (A/D). One of the reasons for the CCD's popularity is its large quantum efficiency (QE). The QE is a measurement of how many percent of the incoming photons hitting the detector that are actually detected. Whereas the human eye has a QE of approximately 1%, the QE of an excellent CCD detector can peak above 90%.

The quality of the observations made with a CCD can be found by calculating the signal-to-noise ratio (S/N). As already mentioned, the flux in a CCD image is measured by counting the number of electrons released by the incident photons. This is called the *signal* (S). The *noise* (N) expresses the uncertainty in the measurements. The higher the S/N, the more reliable the measurement is. Merline and Howell (1995) defines the S/N-equation within a measuring aperture as:

$$\frac{S}{N} = \frac{N_\star}{\sqrt{N_\star + n_{pix}\left(1 + \frac{n_{pix}}{n_b}\right)(N_B + N_D + N_R^2 + g^2\sigma_f^2)}}. \qquad (2.1)$$

This equation is also called the CCD equation. The parameters are:

$N_\star$ = total number of photons (signal) collected from the source.
n_{pix} = total number of pixels considered in the S/N calculation
n_b = total number of background pixels considered when estimating the mean background level.
N_B = total number of photons per pixel from the background.
N_D = total number of dark current electrons per pixel.
N_R = total number of electrons per pixel resulting from the readout noise.
g = the gain of the CCD expressed in units of electrons/ADU, where ADU is analog to digital units. Thus, the gain of the device is given by the amount of voltage needed to produce 1 ADU.
σ_f^2 = an estimate of the variance introduced within the analog-to-digital-converter.

All of the released electrons follow Poisson statistics, whether they are released due to incident photons or other processes in the CCD chip. For the faintest galaxies detected by the CCD in this thesis, $N_B >> N_D, N_R^2, g^2\sigma_f^2, N_\star$. This makes the S/N background-limited.

2.1 The data

This thesis deals with the study of 35 galaxy clusters. To gather the best possible data for each cluster, optical imaging data taken from several different sites were used. The data which hereafter will be referred to as the *MOSCA data*, is taken with the 2048^2 MOSaic CAmera (MOSCA) at the 2.56 m Nordic Optical Telescope (NOT) on La Palma. The UT times of these observations are 2006 January 28-30, 2006 February 2, 2006 May 24-25 and 27-30, 2007 May 13-15, and 2007 September 7-8 (in total 16 nights). Thus, the MOSCS data is taken from four different runs, where one run is defined as a serie of subsequent nights.

run 1 = 2006 January 28-30 and February 2,
run 2 = 2006 May 24-25 and 27-30,
run 3 = 2007 May 13-15,
run 4 = 2007 September 7-8.

Table 2.1: Information about the 35 images.

Cluster name	Filter	Exposure time (seconds)	Image quality (arcseconds)	Limiting magnitude (5σ)	Detector name(s)
A2204	U	5400	0.82	25.6	MOSCA
	V	6300	0.90	26.0	ALFOSC
	I	6300	0.80	24.2	ALFOSC
RX J1720.1+2638	U	9000	0.88	26.4	MOSCA
	V	7200	0.90	26.0	ALFOSC
	I	7200	0.70	25.0	ALFOSC
A586	U	9000	0.95	26.2	MOSCA
	V	5400	1.00	25.4	ALFOSC
	I	5400	0.80	25.1	ALFOSC
A1914	U	3600	0.77	25.8	MOSCA
	V	7200	1.10	25.9	ALFOSC
	I	7200	1.00	25.4	ALFOSC
A665	U	9000	0.97	26.4	MOSCA
	V	5400	0.90	26.0	ALFOSC
	I	5400	0.70	24.3	ALFOSC
A115	U	9000	0.78	26.4	MOSCA
	V	5400	0.80	25.9	ALFOSC
	I	6300	0.70	25.0	ALFOSC
A520	U	9000	0.99	26.2	MOSCA
	V	5400	0.80	25.8	Tek
	I	16200	0.90	24.5	UH8K
A963	U	9000	0.96	26.5	MOSCA
	V	5400	1.00	24.1	UH8K
	I	8100	1.00	24.0	UH8K
A1423	U	8100	0.81	26.5	MOSCA
	V	4500	1.00	26.0	ALFOSC
	I	8100	0.80	25.4	ALFOSC
A773	U	9000	0.82	26.4	MOSCA
	V	6300	1.10	26.0	ALFOSC
	I	5400	1.10	25.2	ALFOSC
A2261	U	5400	1.51	26.3	MOSCA
	V	5400	1.00	25.6	ALFOSC
	I	5400	0.90	24.8	ALFOSC
A267	U	7200	0.94	25.7	MOSCA
	V	5400	0.70	25.9	Tek

Continued on next page

Table 2.1 – continued from previous page

Cluster name	Filter	Exposure time (seconds)	Image quality (arcseconds)	Limiting magnitude (5σ)	Detector name(s)
	I	10800	0.80	24.3	UH8K
A1682	U	9000	0.82	26.0	MOSCA
	V	9000	1.00	26.3	ALFOSC
	I	8100	0.90	25.3	ALFOSC
A1763	U	9000	0.87	26.4	MOSCA
	V	4500	1.10	25.9	ALFOSC
	I	4500	0.80	24.7	ALFOSC
A2111	U	3600	0.82	25.6	MOSCA
	V	5400	0.70	26.5	ALFOSC
	I	5400	0.60	24.8	ALFOSC
A2219	U	9000	0.78	26.3	MOSCA
	V	4500	1.00	25.5	ALFOSC
	I	5400	1.00	24.6	ALFOSC
A2390	U	7200	0.93	25.8	MOSCA
	V	7100	0.70	26.2	MOSCA
	I	3600	0.95	25.6	ALFOSC
Zw 5247	U	9000	0.93	26.5	MOSCA
	V	6300	0.70	26.6	ALFOSC
	I	5400	0.70	25.2	ALFOSC
RX J2129.6+0005	U	9000	0.91	26.0	MOSCA
	V	1800	0.90	25.2	ALFOSC
	I	2700	1.00	23.8	ALFOSC
RX J0439.0+0715	U	10800	0.90	26.7	MOSCA
	V	2800	0.75	25.3	MOSCA
	I	3600	0.79	25.2	ALFOSC
Zw 2089	U	10800	1.04	26.5	MOSCA
	V	1800	0.89	26.5	ALFOSC
	I	10800	0.91	24.9	ALFOSC
A1835	U	5400	0.95	25.8	MOSCA
	V	7200	0.90	25.9	Tek
	I	7200	0.70	25.0	Tek
A68	U	5400	0.76	25.5	MOSCA
	V	3600	0.60	25.4	Tek
	I	3500	0.60	25.2	MOSCA
Zw 7160	U	9000	0.80	26.3	MOSCA
	V	5400	0.80	26.2	ALFOSC

Continued on next page

Table 2.1 – continued from previous page

Cluster name	Filter	Exposure time (seconds)	Image quality (arcseconds)	Limiting magnitude (5σ)	Detector name(s)
	I	5400	0.70	24.9	ALFOSC
Zw 5768	U	5400	0.91	25.9	MOSCA
	V	5400	0.91	25.5	ALFOSC
	I	10800	0.84	25.4	ALFOSC
A697	U	9000	0.89	26.4	MOSCA
	V	3600	0.80	25.0	ALFOSC
	I	5400	0.90	24.1	Tek
A1758N	U	7200	0.77	26.2	MOSCA
	V	6300	1.10	25.6	ALFOSC
	I	6300	0.80	24.9	ALFOSC
A2631	U	9000	0.85	26.3	MOSCA
	V	6300	1.08	26.1	ALFOSC
	I	3600	0.70	25.2	ALFOSC
A611	U	9000	0.89	26.2	MOSCA
	V	2700	1.10	25.8	ALFOSC
	I	5400	0.84	25.3	ALFOSC
RX J0437.1+0043	U	7200	1.15	26.6	MOSCA
	V	1800	1.56	25.3	MOSCA
	I	4500	0.74	25.1	ALFOSC
Zw 3146	U	9000	0.92	26.3	MOSCA
	V	2700	1.20	25.9	ALFOSC
	I	4500	0.77	25.0	ALFOSC
Zw 7215	U	5400	0.81	26.2	MOSCA
	V	5400	0.77	26.7	ALFOSC
	I	5400	0.66	25.3	ALFOSC
A781	U	9000	0.92	26.2	MOSCA
	V	4500	0.97	26.4	ALFOSC
	I	3600	0.73	25.1	ALFOSC
A1576	U	7200	0.87	26.1	MOSCA
	V	10800	0.80	26.8	UH8K
	I	14400	0.90	26.2	UH8K
A2552	U	9000	0.90	26.3	MOSCA
	V	3600	0.73	26.7	ALFOSC
	I	5400	0.87	25.3	ALFOSC
HDF	U	9000	0.88	26.2	MOSCA
	V	3600	0.69	27.1	MOSCA

Continued on next page

Table 2.1 – continued from previous page

Cluster name	Filter	Exposure time (seconds)	Image quality (arcseconds)	Limiting magnitude (5σ)	Detector name(s)
	R	3600	0.65	26.7	MOSCA
	I	3600	0.63	25.5	MOSCA

A list of the cluster sample and different properties of the observations. I have used data taken from different observation runs at different telescopes. MOSCA is an abbreviation for the 2048^2 MOSaic CAmera at the 2.56 m Nordic Optical Telescope (NOT) on La Palma, ALFOSC is an abbreviation for the 2048^2 Andalucia Faint Object Spectrograph and Camera at the NOT, "Tek" is an abbreviation for the 2048^2 Tektronix CCD at the University of Hawaii (UH) 2.24 m Telescope, and finally, "UH8K" is an abbreviation for the 8192^2 CCD mosaic at the UH 2.24 m Telescope.

The data listed in table 2.1 will in the following be referred to as the *long exposures*. During photometric conditions, shorter exposures have been taken of the same fields. These exposures are part of the MOSCA data and will be used in the calibration of the long exposures. In the following they will therefore be referred to as the *calibration exposures*. The only two galaxy clusters which lack calibration exposures are A697 and Zw2089. Differences between the calibration exposures and the long exposures are the exposure times, the time of the observations, and in some cases the detector used for the observations. It is important to point out that the calibration exposures are taken the same night as observations of a few standard stars. These standard stars will be used later when calibrating the instrumental magnitudes onto a standard system (see chapter 3). The calibrated calibration exposures will then make it possible to transform the long exposures onto the standard system. The exposure time for the calibration exposures are typically 200 seconds (some are 300 seconds), while for the long exposures they are typically 900 seconds (some are even 1800 seconds). Usually several images (~ 4 or more) of the same field are combined to create a deeper image. The total exposure times listed in table 2.1 are then the sum of the exposure times for each of the combined images. For example, the V-image of A781 is created from 5 images, each with an exposure time of 900 seconds. The total exposure time listed in table 2.1 is therefore 4500 seconds. The calibration exposures used in this thesis are not combined.

The advantage of longer exposure times is that more light is gathered and hence more objects are detected. Calibration exposures of the clusters are available in the V, R -and I-bands. In addition the MOSCA data contain

long exposures of all of the galaxy clusters in the U-band, four long exposures in the V- and I-bands, and long exposures of the Hubble Deep Field (HDF) in the passbands U, V, R and I. HDF denotes a well-studied area of the Universe with large numbers of spectroscopic redshifts down to faint magnitudes. A deep image of the area has been made on the basis of a series of observations taken with the Hubble Space Telescope. In addition to many galaxies at higher redshifts, the HDF also contains many galaxies with similar redshifts as the 35 galaxy clusters studied in this thesis. Thus, the HDF-galaxies will come in hand later when estimating the photometric redshift (z_{phot}) out to each galaxy (see chapter 4).

Long exposure from other detectors are available in the V -and I-bands for the remaining galaxy clusters (in total 66 images). These images are taken at the 2.56 m Nordic Optical Telescope (NOT) in the periods 1997 March 7-10, 1998 April 22-25, 1998 July 20-24, 1999 May 7-13, 2001 February 24-28, 2001 August 17-21, and 2005 August 14-15, and at the 2.24 m University of Hawaii telescope at Mauna Kea Observatory in the periods 1997 April 29-May 1, 1998 February 19-23, 1998 October 20-23, 1999 January 20, 1999 March 5, 1999 May 14-16, and 2000 March 8-11 (Dahle et al. 2002; Dahle 2006). From 47 of these images catalogues with calibrated magnitudes were already created. These data are published by Dahle et al. (2002) and Dahle et al. (2006). The remaining 21 images were received in the Flexible Image Transport System (FITS) format, that is, they had not already been calibrated. The calibration process will be described in chapter 3.

Before being able to use data taken with a CCD detector, the images need to go through a series of reduction steps to remove the background- and instrumental noise. This was already done for the images used in this thesis. Still, a short review of these steps are appropriate:

- Bias-subtraction: To avoid negative counts in the output image, the CCD electronics adds a positive value to each pixel. If this is not done, the pixels will have mean values ~ 0 ADU, with fluctuations on both sides of this value. To decide this *bias level*, bias-frames (or zero-frames) are needed. These are 0 second exposures where the shutter remains closed. Because of statistical reasons, several single images (~ 10) should be combined to a master-image. The bias-frame is then subtracted from the other CCD-images, pixel by pixel.

- Dark-subtraction: Dark current is due to thermaly excited electrons in the silicon layer and cosmic rays. The dark current increases proportional to the exposure time, and only long exposures need corrections. Dark-frames are also taken with the shutter closed and usually over the same time as the exposure time for the object. The dark current was significant for MOSCA and UH8K, but negligible for the other

detectors.

- Flat-fielding: In a CCD, each pixel has a slightly different gain or quantum efficiency (QE) as compared to neighboring pixels. In addition, dust and other effects in the telescope and camera can give uneven illumination over the CCD-array. Flat-field images are meant to correct for these differences between each pixel by dividing the gain variations out of an image. The ideal flat field image is one where all of the pixels are uniformly illuminated. Examples are exposures during twilight, or illuminating the inside of the telescope dome and taking short exposures. This procedure should be carried out at the beginning and at the end of each night. Several single images should be combined to a master-flat-image to remove distortions in the optical path, like stars.
- Final master image: The order of the reduction steps above is to first bias/dark-correct the raw images, and then divide by the flat-image:

  Final master image $= \frac{raw-bias-dark}{flat}$, where the flat-image already has been bias-subtracted.
- Remove bad pixels: In any CCD, one can find bad pixels. These pixels, which sometimes can make up an entire column or row, return values that are misrepresentative of the light falling on them. By applying mask-images, these bad pixels were flagged.

The different detectors used, along with image quality, exposure time and limiting magnitude, are listed in table 2.1. The significance of the different parameters will be described below. First a short description of the different detectors:

MOSCA: MOSCA (MOSaic CAmera) is a mosaic camera at the 2.56 m Nordic Optical Telescope (NOT) on La Palma. This camera is equipped with four 2048^2 thinned Loral-Lesser CCDs. Each pixel in a CCD-chip correspond to 0.217 arcseconds. This means that in imaging mode, MOSCA has a field of view of 7.4×7.4 arcminutes.

ALFOSC: ALFOSC (Andalucia Faint Object Spectrograph and Camera) is another detector at the NOT. This camera is equipped with a thinned Loral 2048^2 CCD, where each pixel in a CCD-chip correspond to 0.189 arcseconds. This means that in imaging mode, ALFOSC has a field of view of 6.4×6.4 arcminutes.

Tek: Tek (Tektronix) is a thinned 2048^2 CCD detector at the UH 2.24 m Telescope. Each pixel in a CCD-chip correspond to 0.22 arcseconds, which

means that Tek has a field of view of 7.5×7.5 arcminutes in imaging mode.

UH8K: UH8K (University of Hawaii 8 Kilo-pixel camera) is a 8 chip mosaic camera on the UH (University of Hawaii) 2.24 m Telescope. The reduced images I use from UH8K have a re-binned pixelsize of 0.6 arcseconds.

The final two parameters listed in table 2.1 are described below:

2.1.1 Image quality

The image quality listed in table 2.1 is equivalent to the astronomical *seeing*. When observing through a telescope, the seeing condition is a measure of how much the Earth's atmosphere perturbs the images of stars. It is usually given as the full width half maximum (FWHM) of the point spread function (PSF). The PSF is a two-dimensional function which describes the spreading and blurring of the light from a point source (such as a star) due to the Earth's atmosphere, the optics of the telescope, guiding/tracking errors and instrumentation. The seeing conditions vary from place to place and from night to night. Sometimes it can even vary on a time scale of minutes. Some of the best conditions are found at high-altitude observatories on small islands such as Mauna Kea and La Palma. Here the seeing conditions can be as good as ~ 0.4 arcseconds.

2.1.2 Limiting magnitude

The limiting magnitude of a given instrument is the faintest apparent magnitude detectable of an astronomical object. To measure the limiting magnitude for each image, the 5-σ detection limit method was used. This limit corresponds to a signal to noise ratio (S/N) of 5 for the smallest sources (point sources).

A photometric uncertainty of 0.198 mag corresponds to the 5-σ detection limit. One way of finding the limiting magnitude is therefore to plot the estimated magnitude error of each source against its calibrated magnitude (the calibration process is explained in the next chapter). One such plot can be seen in figure 2.1. The horizontal line lies at 0.198 magnitudes. The vertical line intersects the horizontal line in the position of the faintest object with a magnitude error less than 0.198 mag. The limiting magnitudes are listed in table 2.1.

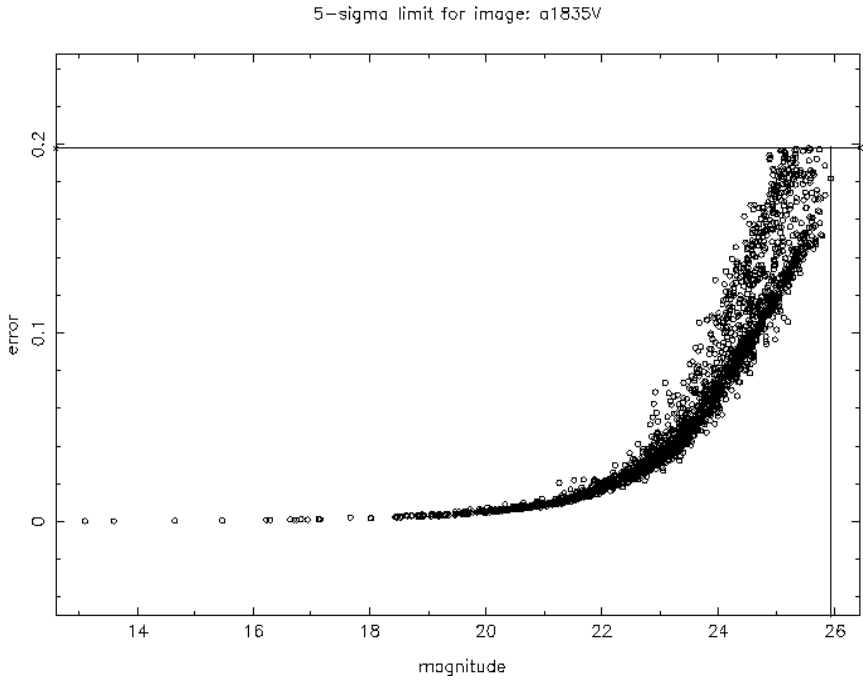

Figure 2.1: Illustration of the 5-σ detection limit method for estimating the limiting magnitudes of the images. This example shows errors in the magnitudes plotted against the magnitudes for the image of A1835 in the V-band.

Chapter 3

Photometry

Photometry is the measurement of the brightness of an astronomical object's electromagnetic radiation. This chapter first gives a short introduction to the magnitude system and the photometric system used, then presenting the numerous steps in the photometric calibration process of the data.

3.1 Magnitude scale

In the second century the Greek astronomer Hipparchus introduced a numerical scale to describe how bright each star appears in the sky seen from Earth. He assigned an apparent magnitude $m = 1$ to the brightest stars in the sky, and he gave the dimmest stars visible to the naked eye an apparent magnitude of $m = 6$. Since Hipparchus's time the magnitude scale has been extended in both directions. Examples are $m = -26.83$ for the Sun to approximately $m = 30$ for the faintest object detectable by sensitive detectors. In the nineteenth century, astronomers developed better techniques for measuring the light energy arriving from a star. By the modern definition, the magnitude scale is a logarithmic scale, and it is given by:

$$m_x = -2.5 log_{10} \left(\frac{F_x}{F_x^0} \right), \tag{3.1}$$

where m_x is the apparent magnitude for the astronomical object in the passband x, F_x is the observed flux in x, and F_x^0 is a reference flux in x (e.g. the flux of Vega).

3.2 Photometric systems

A standard photometric system is defined as a set of passbands (filters) with a known sensitivity to incident radiation as function of wavelength. A set of standard stars with known colours and magnitudes in the standard system is provided for each system. The classification of the photometric systems is usually based on the widths of their passbands:

- *broadband*: filter widths $\sim 500 - 2000$ Å
- *intermediate-band*: filter widths $\sim 100 - 500$ Å
- *narrow-band*: filter widths $\sim 0.5 - 100$ Å

Which system to be used depends on the detector and which objects and physical processes one wishes to study. Whereas narrow-band filters only let through a small range of wavelengths, broadband filters isolate a large range of wavelengths of light.

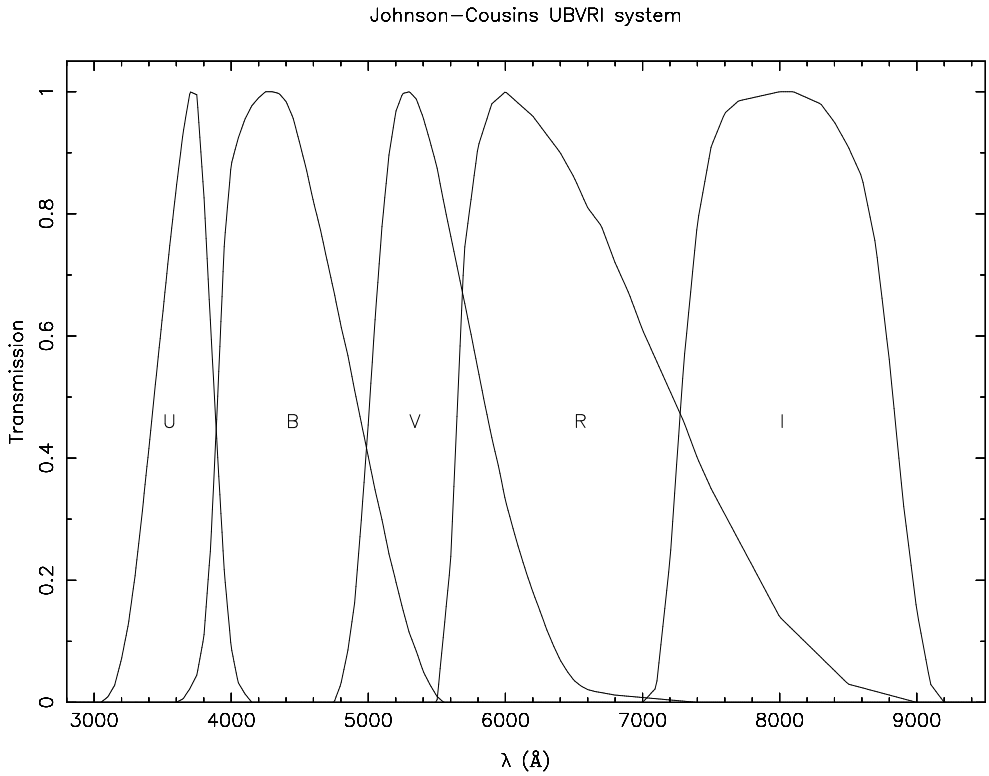

Figure 3.1: Transmission curves for the Johnson-Cousins UBVRI-system.

Filter	λ_{eff}(Å)	$\Delta\lambda$(Å)
U	3663	650
B	4361	890
V	5448	840
R	6407	1580
I	7980	1540

Table 3.1: The Johnson-Cousins UBVRI-system. λ_{eff} is the effective wavelength and $\Delta\lambda$ is the width of the passband.

The photometric system used in this thesis is the *broadband* system UBVRI (Johnson-Cousins). The transmission curves are shown in figure 3.1, while table 3.1 lists the effective wavelength, λ_{eff}, and filter-width, $\Delta\lambda$, of each passband. This widely used set was first described in the 1950s by Harold Johnson and modified a few decades later by A.W.J. Cousins. One advantage of broadband filters is that they transmit a lot of light. It is then possible to detect faint objects with short exposure times and small telescopes. However, it is important to note that there is always a difference between the standard Johnson-Cousins system and the effective passbands of the actual observations. These differences are due to difference in filters, transmission of optics as function of wavelength (λ), sensitivity of detectors as function of λ, and transmission of atmosphere as function of λ. Except from the Johnson-Cousins system, there are today more than 200 photometric systems.

3.3 Photometric calibration

Even after the background- and instrumental noise are removed from the CCD image, the instrumental magnitudes obtained are still not the true magnitudes of the galaxies. Because of extinction in the Earth's atmosphere and differences between the response of the instrumental system and the standard system as a function of wavelength, further corrections are needed. This is done by transforming the instrumental magnitudes onto a standard system, which requires observations of a few standard stars on the same nights as the observations of the galaxies. In this thesis, 148 images of standard stars have been analyzed. The observations used are taken in the the four filters U, V, R and I. Thus, four transformation-equations (one for each filter) are needed. As an example, the equation for the R-band could look like:

$$R_{std} = R_{inst} + a_0 + a_1(V-R)_{std} + a_2X + a_3X(V-R)_{std} + \ldots \qquad (3.2)$$

(Da Costa 1992). Other terms could be added, but because of uncertainties in the calculations of the extra terms, only the minimum number of coefficients needed to get a satisfactory fit should be used. The parameters used in the equation above are:

- R_{std} and V_{std}: standard magnitudes in the R- and V-bands, respectively.
- R_{inst}: instrumental magnitude in the R-band. Since the different observations have different exposure times, corrections were needed in the observed magnitude. The instrumental magnitude used in the equation above is therefore:

$$R_{inst} = R_{obs} + 2.5 \times log_{10}(t_{exp}), \tag{3.3}$$

  where R_{obs} is the magnitude found from the observations in the R-band, and t_{exp} is the exposure time.
- a_0: *the zero point*. This is a measure of the sensitivity of the CCD-system in the bandpass in question.
- a_1: *the colour term*. This is a measure of how well the instrumental system fits the standard system. a_1 should in most circumstances have a value on the order of 0.1 or less.
- $V - R$: the colour of the star (here the difference between the standard V- and the R-magnitude). For the R- and I-bands, the colours (V-R) and (R-I) were used, respectively.
- a_2: *the first order extinction coefficient* for the filter in question. a_2 depends on atmospheric transmission. It therefore varies from site to site and often from night to night. Rayleigh scattering by air molecules, molecular absorption and aerosol scattering are the three main contributions to extinction by the Earth's atmosphere. Rayleigh scattering (Lord Rayleigh, 1871) is the elastic scattering of light by air molecules much smaller than the wavelength of light, and is proportional to $\frac{1}{\lambda^4}$. Short wavelengths are more efficiently scattered because they are more comparable to the size of these small molecules than the longer wavelengths. Aerosols are small scattering particles ("dust" or droplets of salt water) suspended in air. They are usually a bit bigger than the wavelength of light, which means that all wavelengths are approximately equally scattered.
- X: the airmass for the observation. The Earth's atmosphere generally affects the light from a distant source in two ways. One is the amount of atmosphere the light has to travel through, and the other is how the atmosphere affects the different wavelengths. When calculating the airmass the simplyfying assumption of a plan-parallell atmosphere

is made. Let z be the angle of the object from the observer's zenith, then, for $z < 60\,\mathrm{deg}$, $X = sec(z)$. There is minimum absorbation at zenith.

- a_3: *the second order extinction coefficient* for the filter in question. A second order extinction coefficient is usually necessary for bandpasses from B and bluer. This is a combined effect from the rapid variation of extinction across the bandpasses, and the variation in effective extinction with spectral type.

If the same CCD and filters are used, the zero-points and colour-terms for the same objects are expected to remain nearly constant during a single run, provided that the conditions remain photometric.

The 148 standard stars observed have known standard magnitudes in the U-, B-, V-, R- and I-bands. In addition, their instrumental magnitudes in U, V, R and I can be found from the detection images (the B-band will not be used in this thesis). The only unknown parameters in equation 3.2 are therefore the coefficients $a_0 - a_3$. The whole process of source detection, computation of their basic photometric parameters and star-galaxy classification was performed using the 2.0.21 version of the SExtractor package (Bertin & Arnouts 1996). SExtractor (*Source Extractor*) creates object catalogues from astronomical images and is optimized for accurate photometry. Among its characteristics is the ability to separate blended sources and to estimate the probability of an object of being a star or an extended source. However, both processes need to be fine-tuned by input parameters that are fixed for each image. SExtractor also has a parameter file containing a list of the parameters that will be listed in the output catalogue for every detection. When dealing with the standard stars, *MAG_APER* was used as a measure of the magnitudes. This is an estimate of the flux above the background within a fixed, circular aperture. For the standard stars, an aperture diameter of 46 pixels was used. For MOSCA this corresponds to ~ 10 arcseconds. The output catalogues also contained the coordinates of each detection in the images.

SExtractor also gives four different measures of total magnitude which is necessary when dealing with the magnitudes of galaxies. *MAG_ISO* is the integrated light above the detection threshold. *MAG_ISOCOR* is an attempt to correct for the light lost in the wings of the objects making use of a Gaussian model approximation. *MAG_AUTO* uses an adaptive aperture algorithm inspired by Kron's "first moment" algorithm (1980). The Kron (1980) aperture corresponds to a scaling of the intensity-weighted first moment radius, r_1, and was designed to robustly measure the integrated flux

of a galaxy. The first moment of an image is defined as

$$r_1 = \frac{\int_1^{r_{up}} r g(r)}{\int_1^{r_{up}} g(r)}, \tag{3.4}$$

(Kron 1980) where $g(r) = 2\pi I(r)$ is the total amount of light in an annuli of constant width. $I(r)$ is the intensity at radius r in an image, and r_{up} is the upper limit of integration. r_{up} should ideally be at a very large distance from the centroid of the image, but in order to save computational time, three ways of choosing r_{up} are:
- use a fixed isophotal level where $g(r)$ is a certain fraction of the sky.
- use a fixed radius for all images.
- use a fixed treshold above the sky level.
For stars and galaxy profiles convolved with gaussian seeing, an almost constant fraction of the flux is expected to lie within a circular aperture of radius kr_1, independently of their magnitude (Kron 1980, Infante 1987). Kron (1980) claimes that r_1 is approximately equal to the radius within which half of the light from a galaxy is contained. He therefore used an aperture-radius equal to $2r_1$ (1980). Finally, SExtractor includes another total magnitude called *MAG_BEST*. This corresponds to the adaptive aperture method (MAG_AUTO), except if a neighbour is suspected to bias the magnitude by more than 0.1 mag. In crowded fields, the corrected isophotal magnitude (MAG_ISOCOR) is chosen.

3.3.1 Finding the coefficients

For the V-, R- and I-bands, the coefficients included in the calibration equations were a_0, a_1 and a_2. For the U-band, the inclusion of an extra a_3-term was also tried.

Finding a_2: The Carlsberg Meridian Telescope provides nightly values of atmospheric extinction in r' (SDSS) for La Palma. By looking up in tables given by Evans & Argyle (2009), values of atmospheric extinction in r' for the nights in question were found. *La Palma Technical Note No 31* (King 1985) was then used to convert values of extinction at r', to U, V, R and I. By using the two latter references, a differential extinction between r' and the passband of interest was found as follows:

The first step was to find the observed mean extinction coefficient in r', $a_2(r')$, for each night given by the Carlsberg Meridian telescope. $a_2(r')$ is a combination of an extinction coefficient due to Rayleigh scattering and molecular absorbtion, $A(\lambda)$, and an extinction coefficient due to aerosol scattering, A_{aer}, thus

$$a_2(\lambda) = A(\lambda) + A_{aer}. \tag{3.5}$$

RUN	NIGHT	$a_2(U)$	$a_2(V)$	$a_2(R)$	$a_2(I)$
1	28.01.2006	0.4465	0.1192	0.0804	0.0340
1	29.01.2006	0.4535	0.1262	0.0874	0.0410
1	30.01.2006	0.4595	0.1322	0.0934	0.0470
1	02.02.2006	0.4585	0.1312	0.0924	0.0460
2	24.05.2006	0.4365	0.1092	0.0704	0.0240
2	25.05.2006	0.4305	0.1032	0.0644	0.0180
2	27.05.2006	0.4785	0.1512	0.1124	0.0660
2	28.05.2006	0.4925	0.1652	0.1264	0.0800
2	29.05.2006	0.4805	0.1532	0.1144	0.0680
2	30.05.2006	0.4725	0.1452	0.1064	0.0600
3	13.05.2007	0.4615	0.1342	0.0954	0.0490
3	14.05.2007	0.4585	0.1312	0.0924	0.0460
3	15.05.2007	0.4585	0.1312	0.0924	0.0460
4	07.09.2007	0.4485	0.1212	0.0824	0.0340
4	08.09.2007	0.4425	0.1152	0.0764	0.0300

Table 3.2: a_2-values for each night and filter.

Three nights (02.02.2006, 14.05.2007 and 15.05.2007) lacked information about the mean extinction coefficient $a_2(r')$. For these nights an average of the $a_2(r')$-value for the remainig 12 nights was used. By looking up the effective wavelength for r'(6250 Å), King (1985) provided the theoretical extinction coefficient, $A(r')$. Thus, $A(6250\ \text{Å}) = 0.0734$. $A(\lambda)$ is calculated for the location of MOSCA (Roque de los Muchachos, La Palma), and is a mean value over the different nights. The aerosol extinction coefficient for each night is independent of wavelength and can be found by looking at the values tabulated for r'. The final a_2-equations for each of the four passbands are:

$$a_2(U) = A_{aer}(night) + 0.4299. \tag{3.6}$$

$$a_2(V) = A_{aer}(night) + 0.1026. \tag{3.7}$$

$$a_2(R) = A_{aer}(night) + 0.0638. \tag{3.8}$$

$$a_2(I) = A_{aer}(night) + 0.0174. \tag{3.9}$$

The intermediate calculations are shown in appendix A. The final a_2-values for each night and filter are listed in table 3.2. This table also shows the dates corresponding to the different runs. As expected, the extinction is larger for the shorter wavelengths.

Finding a_0 and a_1: The CCD instrument is divided into four chips, and a_0 and a_1 had to be found for each of these chips. This was done by looking

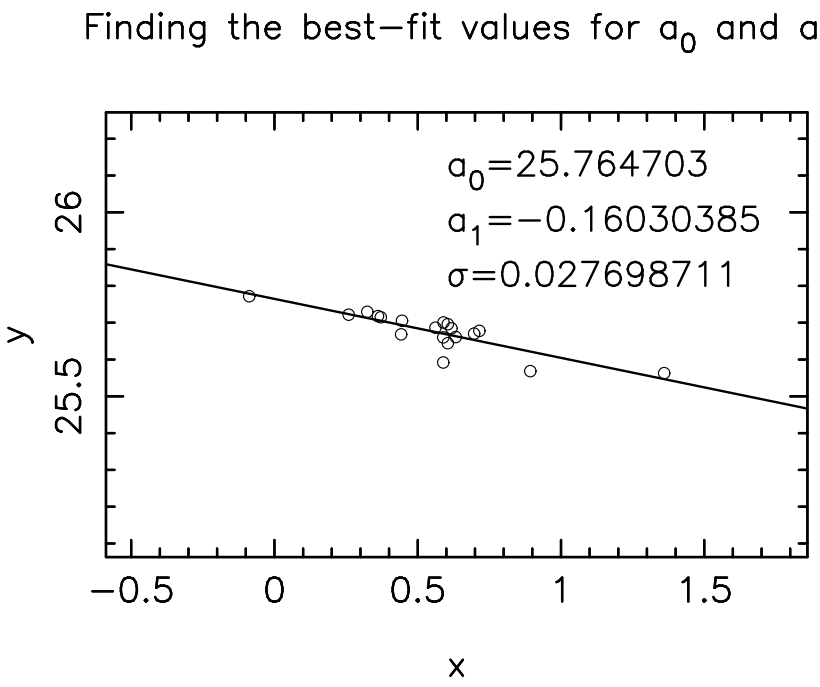

Figure 3.2: Plot of the (x,y)-points for run 4, passband V and chip 1 together with the best-fit line $y = a_0 + a_1 x$. σ is the scatter around the best-fit line.

at the best-fit values to the parameters already known.

Landolt (1992) lists a large set of standard stars for the broadband photometric system UBVRI. By comparing the images under study with those given by Landolt (1992), the standard stars in each image could be identified. Standard magnitudes in all of the passbands U, B, V, R and I could then be found. Without the a_3-term, the calibration equation (with the R-band as an example) takes the form:

$$R_{std} = R_{inst} + a_0 + a_1(V - R)_{std} + a_2 X. \tag{3.10}$$

Here the only unknown parameters are a_0 and a_1. Equation 3.10 was then rearranged to look like a first order polynomial, that is

$$y = mag_{std} - mag_{instr} + a_2 X. \tag{3.11}$$

where mag_{std} and mag_{instr} are the standard and instrumental magnitudes, respectively. This means that

$$y = a_0 + a_1 x, \tag{3.12}$$

where x is the colour of the star (for example $V - R$). y is now a first order polynomial with a_0 and a_1 as the unknown coefficients. The a_0- and a_1-values

are the same for all stars observed in the same run, the same filter and in the same chip. With the expectation that a_1 in most circumstances should have a value on the order of 0.1 or less, it was possible to recognize points that should not have been a part of the determination of a_0 and a_1. Reasons for these outliers can be cosmetic defects in the CCD, cosmic rays, or that the point was located on the edge of the chip. The outliers were removed, and the best-fitted line between the remaining points was found. Figure 3.2 shows the (x,y)-points for run 4, passband V and chip 1, together with the best-fitted line $y = a_0 + a_1 x$. As can be seen, the (x,y)-points lie very close to the fitted line. a_0 is the point where the line meets the y-axis, and a_1 is the slope. More thorough calculations of a_0 and a_1 are shown in appendix A.

The results for the U-band displayed a higher scatter than the other three passbands. An extra a_3-term was therefore added to the calibration equation.

Finding a_3: a_3 was assumed to be the same for all of the datapoints in the U-band. This way the high uncertainty that follows from few datapoints was not a problem. Thus the equation for the U-band looks like:

$$U_{std} = U_{inst} + a_0 + a_1(U - V) + a_2 X + a_3 X(U - V). \tag{3.13}$$

The goal was to decrease the residuals of the (x,y)-points around the fitted line, $y = a_0 + a_1 x$. In other words, to find the a_3-value that gave the least spread. y is now defined as:

$$y = U_{std} - U_{instr} + a_2 X - a_3 X(U - V). \tag{3.14}$$

and

$$y = a_0 + a_1 \times x, \tag{3.15}$$

where $x = U - V$. By looking at the other parameters in the a_3-term, a_3 was expected to lie somewhere in between -0.3 and 0.3. Thus, with a steplength of 0.01, all a_3-values in the interval $a_3 \in [-0.3, 0.3]$ was tried out. The least spread around the fitted line $y = a_0 + a_1 x$ was found for $a_3 = 0.02$. Since the a_3-term appears to be small compared with the other terms, it was dropped from the equation. Thus, the estimation of a_0 and a_1 were done in the same fashion as for the other passbands, without the extra a_3-term.

The final calibration equations used to calibrate the magnitudes of the galaxies are:

$$U_{std} = U_{inst} + a_0 + a_1(U_{std} - V_{std}) - a_2 X. \tag{3.16}$$

$$V_{std} = V_{inst} + a_0 + a_1(V_{std} - R_{std}) - a_2 X. \tag{3.17}$$

$$R_{std} = R_{inst} + a_0 + a_1(V_{std} - R_{std}) - a_2 X. \tag{3.18}$$

$$I_{std} = I_{inst} + a_0 + a_1(R_{std} - I_{std}) - a_2 X. \tag{3.19}$$

The final a_0- and a_1-values for the passbands U, V, R and I, are listed

U-BAND

RUN	CHIP	a_0	a_1	σ	NUMBER OF STARS
1	1	24.412255	-0.14187352	0.038488285	13
1	2	24.349779	0.023988441	0.082445396	35
1	3	24.491395	-0.12134199	0.033532056	10
1	4	24.389180	0.065810148	0.056590501	7
2	1	24.450154	0.028739920	0.083552892	15
2	2	24.419525	0.022458920	0.092185884	13
2	3	24.502352	-0.17823529	0.055811346	19
2	4	24.338334	0.061236639	0.083180935	34
3	1	24.216421	0.057431186	0	Calculated
3	2	24.324988	0.042861081	0.08817343	6
3	3	24.411103	0.027639938	0.041304654	6
3	4	24.289651	0.069990350	0.050400361	17
4	1	24.163830	0.057431186	0.069224323	14
4	2	24.247673	0.063347937	0.074926674	10
4	3	24.359753	0.043377242	0.040512143	15
4	4	24.260544	0.040283409	0.053421875	15

Table 3.3: a_0 and a_1 calculated for each chip in different runs for the U-band. Chip 1 from run 3 did not give adequate results. I therefore had to find the values for a_0 and a_1 using run 4.

in table 3.3, 3.4, 3.5 and 3.6, respectively. The standard deviation, σ, for each calculation is also listed, along with the number of standard stars used. Some of the calculated values for a_0 and a_1 did not give adequate results. These were mostly calculations made from chips consisting of few standard stars. A better fit for the a_0- and a_1-values were found by using relations between the different runs and chips within the same passband. A thorough review of these calculations are found in Appendix A. In the tables, the σ-value of these calculations are set to zero, and the number of stars reads "CALCULATED". The total number of standard star measurements to find all of the a_0- and a_1-values was 575.

V-BAND

RUN	CHIP	a_0	a_1	σ	NUMBER OF STARS
2	1	25.717204	-0.122178160	0.029361288	5
2	2	25.726593	-0.160980550	0.028252094	11
2	3	25.846891	-0.148355610	0.031496924	19
2	4	25.720261	-0.188080970	0.026640955	15
4	1	25.764703	-0.160303850	0.027698711	19
4	2	25.638409	-0.113510300	0.044104453	15
4	3	25.787782	-0.159751220	0.033007411	19
4	4	25.642244	-0.138388820	0.025511786	17

Table 3.4: a_0 and a_1 calculated for each chip in different runs for the V-band.

R-BAND

RUN	CHIP	a_0	a_1	σ	NUMBER OF STARS
2	1	25.529241	-0.130170670	0.031659763	7
2	2	25.488494	-0.088974514	0.024783283	6
2	3	25.666228	-0.081412402	0.038052735	23
2	4	25.489373	-0.036094437	0.046398827	26
3	1	24.971134	-0.063740108	0	Calculated
3	2	25.507161	-0.105272190	0	Calculated
3	3	25.594258	-0.082325403	0	Calculated
3	4	25.483050	-0.089318383	0	Calculated
3	1	25.530826	-0.063740108	0.017618037	16
3	2	25.460742	-0.105272190	0.013718417	9
3	3	25.547839	-0.082325403	0.045081827	13
3	4	25.436631	-0.089318383	0.018449351	9

Table 3.5: a_0 and a_1 calculated for each chip in different runs for the R-band. Run 3 had very few stars, hence values from run 4 have been used for both a_0 and a_1.

I-BAND

RUN	CHIP	a_0	a_1	σ	NUMBER OF STARS
2	1	24.998657	-0.079720975	0.041733874	6
2	2	24.892544	-0.037070484	0	Calculated
2	3	25.075852	-0.017972359	0.050779297	18
2	4	24.90062	-0.013518118	0.054515052	13
4	1	24.924715	0.066380683	0.033763883	17
4	2	24.836795	0.103069110	0.029507213	9
4	3	24.991919	0.063915670	0.014322588	12
4	4	24.873055	0.052019077	0.035513377	15

Table 3.6: a_0 and a_1 calculated for each chip in different runs for the I-band. Chip 2 from run 2 did not give adequate results. I therefor had to find the values for a_0 and a_1 using run 4.

3.3.2 Calibration of the calibration exposures

With the calibration equations in hand (equation 3.17, 3.18 and 3.19), the calibration exposures taken together with the images of the standard stars could be calibrated. Since the exposures taken in the U-band are *long exposures*, they will be described later. The first step was to create object catalogues from every image by running SExtractor. While the SExtractor-magnitude *MAG_APER* is a good estimate of the total magnitude of a star, *MAG_BEST* gives the most precise estimate of the total magnitude for galaxies. After retrieving the total magnitudes of each object detected, the calibration process could begin. However, there was one complication when calibrating the short exposures. It was not possible to find V_{std} by using V_{std} in the colour-term, and the same applied to R_{std} and I_{std}. The standard magnitudes were therefore found iterative. The procedure was as follows:

- A first estimate of the standard magnitudes were calculated without using the colour-term. Thus, with the V-band as an example:

$$V_{est1} = V_{inst} + a_0 - a_2 X, \tag{3.20}$$

  where V_{est1} means the first estimate of the standard magnitude.

- A second estimate of the standard magnitudes were calculated using the first estimate of V_{std} and the first estimate of R_{std} in the colour-term, that is:

$$V_{est2} = V_{inst} + a_0 + a_1(V_{est1} - R_{est1}) - a_2 X, \tag{3.21}$$

  etc.

After four iterations, the results converged. The difference in the third and fourth estimate was < 0.0005 mag. The same procedure was followed by all the four bandpasses.

3.3.3 Calibration of the long exposures

The calibration equations found earlier (equation 3.16, 3.17, 3.18 and 3.19) only apply to the *MOSCA data*, that is, the observations taken with MOSCA during 2006 and 2007. As mentioned in chapter 2, longer exposures are generally preferred, since more objects then are detected in each image. Most of the long exposures in the V- and I-bands were obtained earlier, using other instruments. They are taken with different detectors at different time periods, and some were even received as catalogues with already calibrated magnitudes (Dahle et al. 2002). This made the calibration process of most of the long exposures a bit more complicated. However, since the calibration exposures and long exposures are of the same areas, many of the same objects

were detected in both cases. By using the Imcat [1] command *mergecats*[2], the objects detected in both the calibration exposures and long exposures could be identified and matched. Transformation equations could then be found onto the standard system.

As before, MAG_BEST from SExtractor was used as an estimate of the total magnitudes of the galaxies. The SExtractor-magnitude MAG_APER was also of interest. The main difference between MAG_BEST and MAG_APER is the size of the aperture. When using MAG_BEST, the aperture size can differ for the different filters depending on the galaxy's light profile in that filter. With MAG_APER on the other hand, the aperture diameter is given by the user before running SExtractor. One can therefore choose to keep a constant aperture diameter for all of the different filters. When calculating the colour of a galaxy, for example $U - V$, it is important that the aperture used is of the same size for both U and V. It is then much more convenient to use MAG_APER. The size of the aperture depends on the point spread function (PSF). Capac et al. (2006) show that with a PSF with $fwhm \approx 1''$, the PSF matching is optimized with a $3''$ aperture. Since the data used in this thesis also have a PSF with $fwhm \approx 1''$, the $3''$ aperture was adopted. 1 pixel corresponds to a different physical size for each of the detectors used (MOSCA, ALFOSC, UH8K and Tek). The different apertures were therefore scaled properly to all obtain a physical diameter of $3''$ (see appendix A for the calculations). These aperture diameters were also used on the long exposures from Dahle et. al. (2002).

For the objects detected in both the calibration exposures and the long exposures, calibrated magnitudes from the calibration exposures and instrumnental or calibrated magnitudes (both MAG_BEST and MAG_APER) from the long exposures were now available. By using these objects, transformation equations onto the standard system could be found. Even though the magnitudes in 45 of the V -and I-catalogues were already calibrated, they were still transformed onto the standard system with the same equations as for the rest. This was done to minimize the importance of systematic errors in the calibration process. The transformation equations used are:

$$V_{std} = V_{long} + b_0 + b_1(V_{std} - I_{std}), \tag{3.22}$$

and

$$I_{std} = I_{long} + b_0 + b_1(V_{std} - I_{std}). \tag{3.23}$$

[1] imcat - image and catalogue manipulation software. The 'imcat' software was developed by Nick Kaiser initially to do faint galaxy photometry for weak lensing studies, and provides a fairly complete set of tools for this kind of work. It is available at: http://www.ifa.hawaii.edu/ kaiser/imcat/

[2] 'mergecats' reads N catalogues of objects and outputs a single merged catalogue of objects whose positions match to within tolerance d.

where V_{long} and I_{long} are the instrumental or calibrated magnitudes from the long exposures. Since the SExtractor-magnitude MAG_BEST was used when calibrating the short exposures, the same magnitude was used when finding the transformation equations. The same equations could later be used for the SExtractor-magnitude MAG_APER. As before, the two coefficients (now b_0 and b_1) had to be found. b_0 is the zero-point, and b_1 is the coefficient in the colour-term. The last term, a_2X, in the previous calibration equations falls under b_0 and b_1. These equations only apply to the V -and I-bands. There were no long exposures available in the R-band, and since the long exposures in the U-band fall under the MOSCA data, the U-magnitudes could be calibrated using equation 3.16. In the calculations below the calibrated magnitudes from the calibration exposures are referred to as V_{cal} and I_{cal}. I defined

$$y_V = V_{cal} - V_{long}, \tag{3.24}$$

and

$$y_I = I_{cal} - I_{long}. \tag{3.25}$$

I also defined the colour

$$x = V_{cal} - I_{cal}, \tag{3.26}$$

which leaves two polynomials of first degree:

$$y_V = b_{0,V} + b_{1,V}x, \tag{3.27}$$

and

$$y_I = b_{0,I} + b_{1,I}x. \tag{3.28}$$

The procedure in finding b_0 and b_1 was exactly the same as when finding a_0 and a_1. Further explanations are therefore skipped. With known b_0 and b_1, equation 3.22 and 3.23 were applied to all of the long exposures in the V -an I-bands.

The next step was then to calibrate the U-data with equation 3.16. The imcat command *mergecats* was again used, this time to find a match between the objects detected in the V- and U-bands. The colour-term in equation 3.16 consists of the colour $(U_{std} - V_{std})$. U_{std} therefore had to be calculated iterative. The procedure was the same as for the short exposures. After four iterations the results converged. The difference in the third and fourth estimate was < 0.0005 mag. The calibration of the two special cases A697 and Zw2089 (which lack calibration exposures) are described in appendix A.

3.3.4 Calibration of the HDF-images

In addition to images of the 35 galaxy clusters, images of the Hubble Deep Field (HDF) in the passbands U, V, R and I were also used. These images

are part of the MOSCA-data, which makes the calibration equations 3.16, 3.17, 3.18 and 3.19 valid.

Final note: All of the calibrated long exposures will be corrected for systematic errors in chapter 4.

Chapter 4

Selection of the cluster galaxies

This chapter will give a description of how the cluster members were isolated from the foreground and background galaxies. The photometric redshift, z_{phot}, of each galaxy in the cluster images first had to be determined. A photometric redshift is an estimate of the distance of a galaxy (or AGN, quasar) by using medium or broad band photometry instead of spectroscopy. Two different methods were tried out in the photometric redshift estimations. In both methods the calibrated magnitudes in the U-, V- and I-bands were given as input. It is important to keep in mind that the calibrated magnitudes from chapter 3 are the observed magnitudes. The calibration process only accounted for defects in the instrumental system. When calculating the redshift out to an astronomical object, Galactic dust extinction also has to be taken into consideration.

4.1 Finding the galactic dust extinction, *A*

Interstellar space contains dust that absorbs or scatters light from distant stars. Like the stars themselves, interstellar dust is concentrated in the plane of the Galaxy. As a result, it obscures our view within the plane and make distant objects appear dim, an effect called *Galactic dust extinction*. While interstellar dust in the plane of our Galaxy hides the extragalactic sky covered by the Milky Way, we have an almost unobscured view perpendicular to the plane. $A > 0$ represents the number of magnitudes of Galactic dust extinction present along the line of sight. Galactic dust affects the colour of objects. Red light (longer wavelengths) passes more easily than blue light (shorter wavelengths). This means that if the extinction is high (large A), an object looks redder.

To find the galactic dust extinction for each object within the different clusters, dust maps created by David J. Schlegel, Douglas P. Finkbeiner and Marc Davis (1998) were used for each photometric passband. These maps are composites of the COBE/DIRBE and IRAS/ISSA maps, with the zodiacal foreground and confirmed point sources removed.

4.2 Finding the photometric redshifts with ANNz

In the first attempt here to determine the photometric redshifts of the galaxies, the artificial neural network ANNz.[1] was used. This decision was made on the basis of the positive results found by Collister and Lahav (2008). They compared ANNz to HYPERZ (Bolzonella, Miralles, & Pelló 2000), which is a template-based photometric redshift package. ANNz proved to produce very competitive results.

An artificial neural network (hereafter ANN) is a computing system that can learn on its own. It consists of many simple processors (neurons) each containing a small amount of local memory. The connections between the neurons carry numeric data, and the neurons only operate on their local data and on the inputs they receive via these connections. Each neuron then produces one single output-signal based on an internal weighting system. Typically, this output is sent as an input to another neuron. The starting weights for the different neurons are randomized which means that the ANN must be trained to solve the specific problem.

The network architecture of the ANN consists of a set of input nodes, one or more output nodes, and one or more hidden layers each consisting of a set of nodes (see figure 4.1 for an example). A particular network architecture can be denoted

$$N_{in} : N_1 : N_2 : ... : N_{out}, \tag{4.1}$$

where N_{in} is the number of input nodes, N_1 is the number of nodes in the first hidden layer, and so on, and N_{out} is the number of output nodes. For example, 4:8:8:1 takes 4 inputs, has 2 hidden layers each with 8 nodes, and gives a single output.

When analyzing experimental data, a self-organizing ANN is often used. After beeing exposed to large amounts of data, this ANN tends to discover patterns and relationships in that data. The weights of connections are then adjusted after these patterns. Firth, Lahav & Sommerville (2003) demonstrated that ANNs were well suited for estimating photometric redshifts.

[1] "ANNz: Estimating photometric redshifts using Artificial Neural Networks", Collister and Lahav (2004).

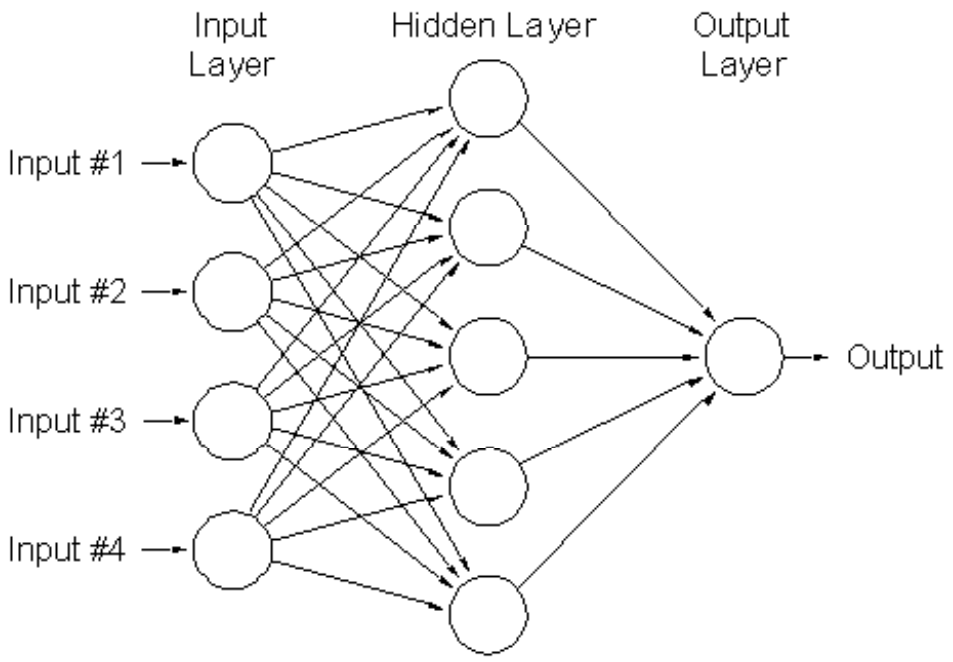

Figure 4.1: Example of an artificial neural network (ANN). This ANN consists of four input nodes, one hidden layer with five nodes and one output node.

The same method was later applied to the Hubble Deep Fields by Vanzella et al. (2003). The software package ANNz derives a parametrization for the redshift as a function of the photometric parameters given as input. To do this it requires a suitable large and representative training set of galaxies where both photometry and spectroscopic redshift are known. This training set should contain photometry, m, in the same filters as the target sample, and it should also cover the same redshift interval. The ideal training set is a representative subset of the actual photometric target sample. ANNz is then trained by minimizing the *cost function*

$$E = \sum_k (z_{phot}(w, m_k) - z_{spec,k})^2, \tag{4.2}$$

with respect to the weights, w. Here $z_{phot}(w, m_k)$ is the network output for the given input and weight vectors, and $z_{spec,k}$ is the spectroscopic redshift given as input for each galaxy k. The sum is over all the galaxies in the training set. To perform this minimization, ANNz uses an iterative quasi-Newton method. After each iteration, the cost function is also evaluated on a separate *validation* set. The number of training iterations is chosen by the user. The final weights chosen for the trained network are those which minimized the cost function on the validation set.

In this study there is only one output node, z_{phot}. The input nodes are the apparent magnitudes, m, of a galaxy in a number of filters. The first challenge was to find a large enough training set for ANNz.

Creating a trainingset for ANNz: After the calibration process described in chapter 3, 32519 galaxies with known calibrated magnitudes in the passbands U, V and I were available from the cluster catalogues. These magnitudes originates from the fixed aperture magnitudes (MAG_APER) from SExtractor (see section 3.3). The next step was to find the spectroscopic redshift for as many of these galaxies as possible in order to create a representative training set for ANNz. The NASA/IPAC Extragalactic Database (NED) was used for this purpose. After searching for objects in the same areas as the 35 galaxy clusters and matching these *NED-objects* with known z_{spec} to the galaxies with known U, V -and I-magnitudes, the training set had been reduced to only 498 objects. To increase the size of this poor training set, galaxies from the Hubble Deep Field (HDF) were added. A total of 1598 HDF-galaxies with known calibrated U, V, R -and I-magnitudes were availabe (section 3.3.4). Again, NED was used to find the spectroscopic redshift for as many of these galaxies as possible, which resulted in 1183 HDF-galaxies with known z_{spec}. However, after matching the NED-objects with known z_{spec} with the galaxies from the photometric catalogue with calibrated U, V, R -and I-magnitudes, only 650 galaxies remained. Thus, the total training set ended up with 1148 galaxies. SExtractor also provides all of the magnitudes with a corresponding estimate of the error. These errors were also given as input to ANNz.

To get a more accurate estimate of the true redshift of any galaxy, it is recommended to train a group of networks (a *committee*) to be used on the target data instead of a single one. A committee is made by varying the initial seed when training the network, that is the starting weight of the neurons. When the training is completed, the target sample is used as input. These galaxies have magnitudes in the same filters as the trained network, but unknown redshifts. ANNz then estimates the photometric redshift of each galaxy.

The network training was carried out as follows:

- A portion of the available training data (originating from the cluster-catalogues and not from the HDF) was first removed. The purpose of this *evaluation-set* was to use it as a mock target sample to improve the performance of ANNz.
- The remaining data was further separated into a *training-set* and a

validation-set. These were the inputs when training the different networks to be used on the target-data later. The difference between the created networks was only the seed given as input when creating them.

- Committees consisting of different compounds of networks were tested on the evaluation-set. The committee which gave the best result was one consisting of four different networks. The network-architecture used was "arch.3.6.6.1.net". "arch.3.8.8.1.net" and "arch.3.5.5.1.net" were also tried out, but "arch.3.6.6.1.net" gave the best results. As mentioned before, "3.6.6.1" means that the network architecture consists of 3 input nodes (the magnitudes in U, V and I), 2 hidden layers each consisting of 6 nodes, and one output node (the photometric redshift z_{phot}).
- After deciding the composition of the committee (that is, how many networks are used and the seeds given as input when creating them) and the network-architecture, the evaluation-set had served its purpose. It was therefore divided between the training-set and the validation-set. These enlarged training- and validation-sets were used to create a new committee with the same composition as mentioned above. A larger trainingset increases the performance of ANNz.
- The trained ANNz was then used on the target data. The resulting catalogues for the 35 galaxy clusters consist of the estimated photometric redshifts of each galaxy with a corresponding error.

To check the credibility of the estimated redshifts, several plots were created. These plots (which will be described below) show whether the estimated redshifts are reliable or not.

In addition to cluster members, a CCD image of a galaxy cluster contains both foreground- and background galaxies. However, the number density of galaxies in a cluster environment is much larger than the number density of field galaxies. It was therefore expected to find more galaxies with an estimated redshift near the tabulated redshift of each galaxy cluster (hereafter $z_{cluster}$). The first plot made for each galaxy cluster was therefore a histogram with the estimated photometric redshift, z_{phot}, along the x-axis and the number of galaxies, N, along the y-axis. 35 such histograms (one for each galaxy cluster) are shown in figure 4.2. These histograms were made by first dividing the estimated redshifts into bins with widths $\Delta z_{phot} = 0.05$, and then counting how many galaxies were estimated to lie in each bin. In addition each plot contains a vertical line at the position of $z_{cluster}$. If ANNz has worked properly, there should be a peak in each histogram at $z_{phot} = z_{cluster}$. Unfortunately these histograms give unsatisfactory results. Instead of, or in addition to, having peaks around $z_{cluster}$, most of the histograms peak around $z_{phot} \sim 1$. Examples of some of the worst cases are A267, A1423,

A1576, A1682, Zw5247, Zw7160 and Zw7215. These histograms have large peaks far from the redshifts of the galaxy clusters (around $z_{phot} \sim 1$). The images used in this thesis contain more than just cluster members, but there is no doubt that the cluster members by far outnumber the field galaxies in intervals located at $z_{cluster}$. Having the main peak at any other place than at $z_{cluster}$ therefore indicates wrong photometric redshift estimates. A reason for these poor redshift estimations is that the data used when training ANNz were not representative of the target data. Most of the training set consisted HDF members, and the rest were members of A2219 ($z_{cluster} = 0.23$), A773 ($z_{cluster} = 0.22$), A665 ($z_{cluster} = 0.18$) and A697 ($z_{cluster} = 0.28$). Another reason is that the training set was too small. A larger and more representative training set, containing more cluster members and more colours, would probably have given much better results. From the 35 histograms alone, it is therefore easy to see that ANNz did not work well on these target data. A histogram of the HDF-galaxies is shown in figure 4.3. Also this histogram peaks around $z_{phot} \sim 1$.

The next plot made was z_{spec} versus z_{phot}. Even though the two are calculated differently, they are still a measure of the same distance. With z_{spec} along the x-axis and z_{phot} along the y-axis, the plotted points were therefore expected to stay close to the line $y = x$. To be able to make this plot, the training set had to be used as target data when running the trained ANNz. This is because the training set was the only data available with known spectroscopic redshift. It is not optimal to use the training set as the target data, but it should give an idea about how successful the training process has been. Four z_{phot} versus z_{spec} plots were made. Figure 4.4 shows a plot of all of the 35 galaxy clusters together with HDF. The error bars show the uncertainty in each z_{phot}-estimate. The lines $y = x$ and $y = a_0 + a_1 x$ are also plotted in the same figure. Here $y = a_0 + a_1 x$ is the first order polynomial to best fit the plotted objects. Ideally it should be close to the line $y = x$. As can be seen from figure 4.4, there are no objects from the cluster catalogues with $z_{spec} > 1.5$. It was therefore convenient to make a similar plot, only this time focusing on objects with $z_{spec} < 1.5$ and $z_{phot} < 1.5$. This plot is shown in figure 4.5. The fitted line $y = a_0 + a_1 x$ is now made only on the basis of the objects with $z_{spec} < 1.5$ and $z_{phot} < 1.5$. Figure 4.5 show that there are far more HDF members at higher redshifts than there are objects from the cluster catalogues. There is a large amount of objects around $z_{spec} \in [0.15, 0.3]$. Most of these objects are expected to be cluster members. To have a better look, an additional plot was made where only objects with $z_{spec} < 0.5$ and $z_{phot} < 0.5$ were plotted (see figure 4.6). Again, the fitted line $y = a_0 + a_1 x$ in this figure is only made on the basis of the objects with $z_{spec} < 0.5$ and $z_{phot} < 0.5$. The same plot, but now without the HDF-members, is shown in figure 4.7. By comparing figure 4.6 and figure 4.7 it can be ascertain that most of the galaxies with $z_{spec} < 0.5$ and

$z_{phot} < 0.5$ are indeed from the cluster catalogues. The dotted line plotted in figure 4.7 is the same one as plotted in figure 4.6. It can also be ascertain that the objects from the cluster catalogues do not follow the relation $y = x$, that is $z_{phot} = z_{spec}$.

Thus, with the data set used in this thesis, ANNz is not a good method to use when estimating the photometric redshifts. The training set was simply too small for ANNz. In addition, a large part of the trainingset consists of HDF-galaxies. Many of these galaxies are at higher redshifts than the target galaxies used as input. If a target galaxy has similar colours as one of these HDF galaxies, it could then be estimated to be at a higher redshift than is the case. This is probably what has happened for many of the target galaxies. Thus, these catastrophic errors could have been avoided with a larger and more representative training set or more colours. Also, in contrast to ZEBRA (the second method that will be used to determine the photometric redshifts in this thesis, and will be discussed in the next section), ANNz does not have a photometry-check. Correct photometry is very important when estimating z_{phot}.

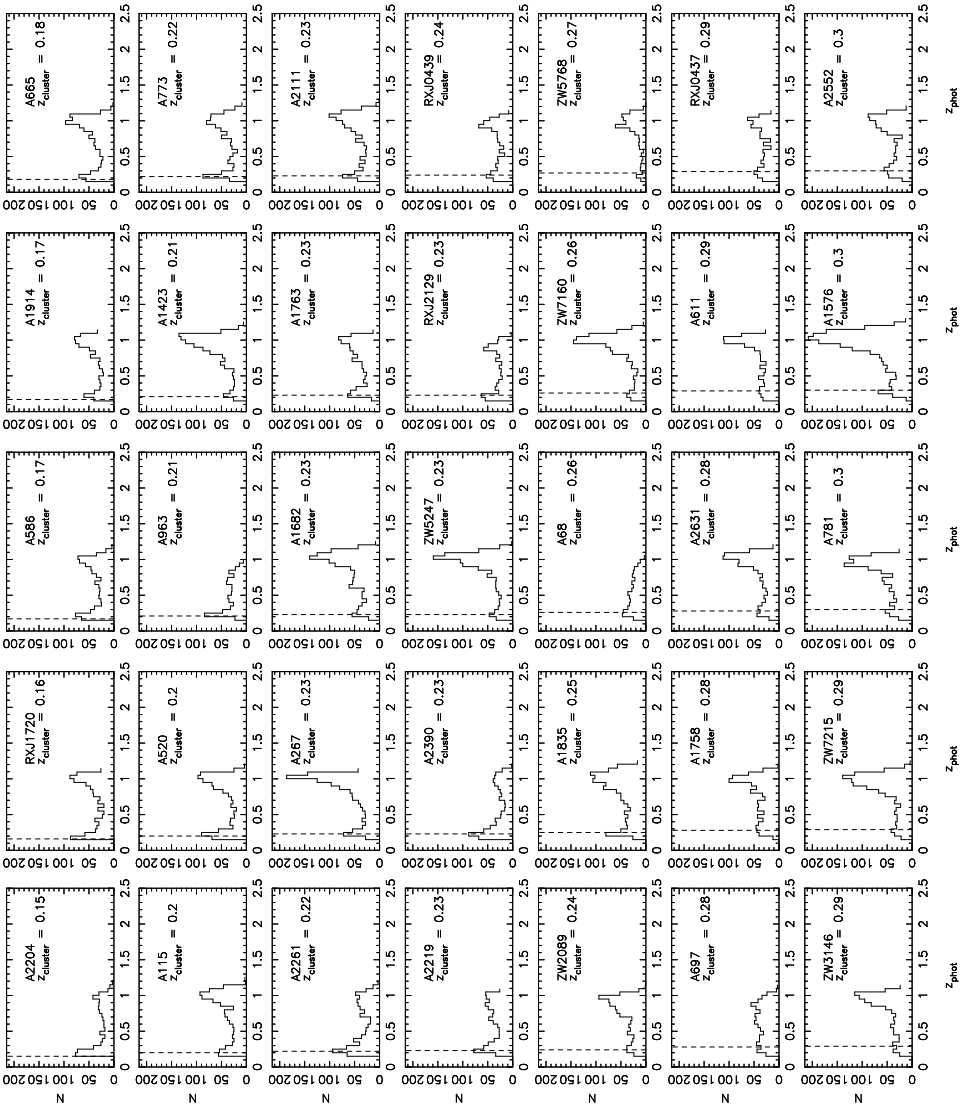

Figure 4.2: Results from ANNz: Histograms of the 35 galaxy clusters where the estimated photometric redshift, z_{phot}, is plotted along the x-axis and the number of galaxies in each redshift interval ($\Delta z_{phot} = 0.05$) is plotted along the y-axis. The true redshift of each cluster is plotted as a dashed, vertical line.

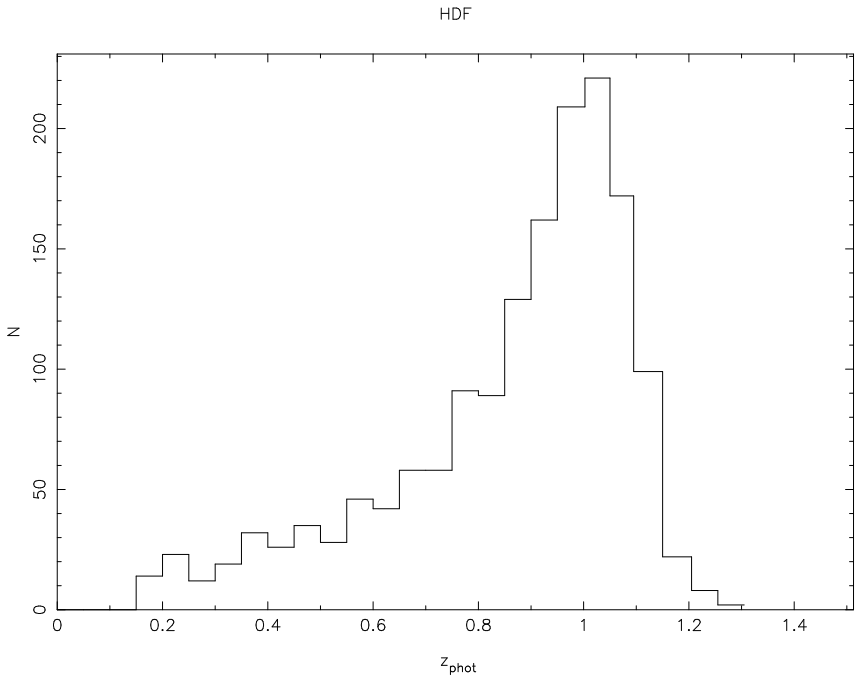

Figure 4.3: Result from ANNz: Histogram of HDF where the estimated photometric redshift, z_{phot} is plotted along the x-axis and the number of galaxies in each redshift interval ($\Delta z_{phot} = 0.05$) is plotted along the y-axis.

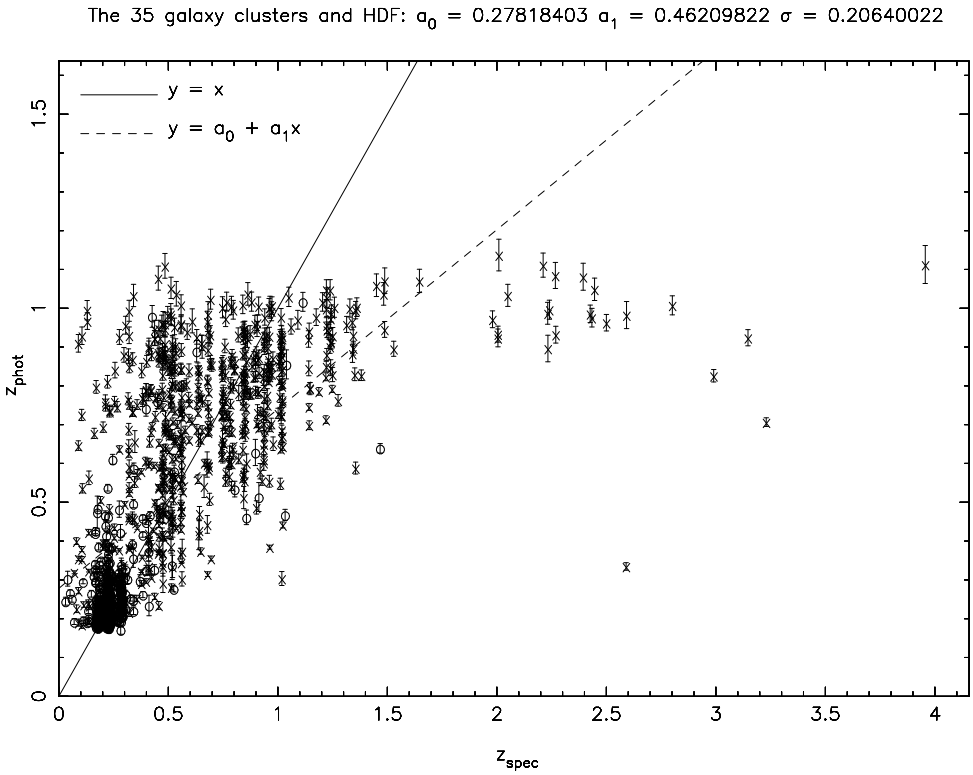

Figure 4.4: Results from ANNz: Plot of the 35 galaxy clusters and HDF where z_{spec} is plotted along the x-axis and z_{phot} is plotted along the y-axis. Objects from the cluster catalogues are plotted with open circles, while objects from the HDF catalogue are plotted with crosses. The error-bars for the z_{phot}-estimations are plotted as vertical lines around each point. In addition, the best fitted line between the points ($y = a_0 + a_1 x$), and the line $y = x$ are plotted. The closer the points are to the line $y = x$, the better the results. σ is the spread around the best fitted line.

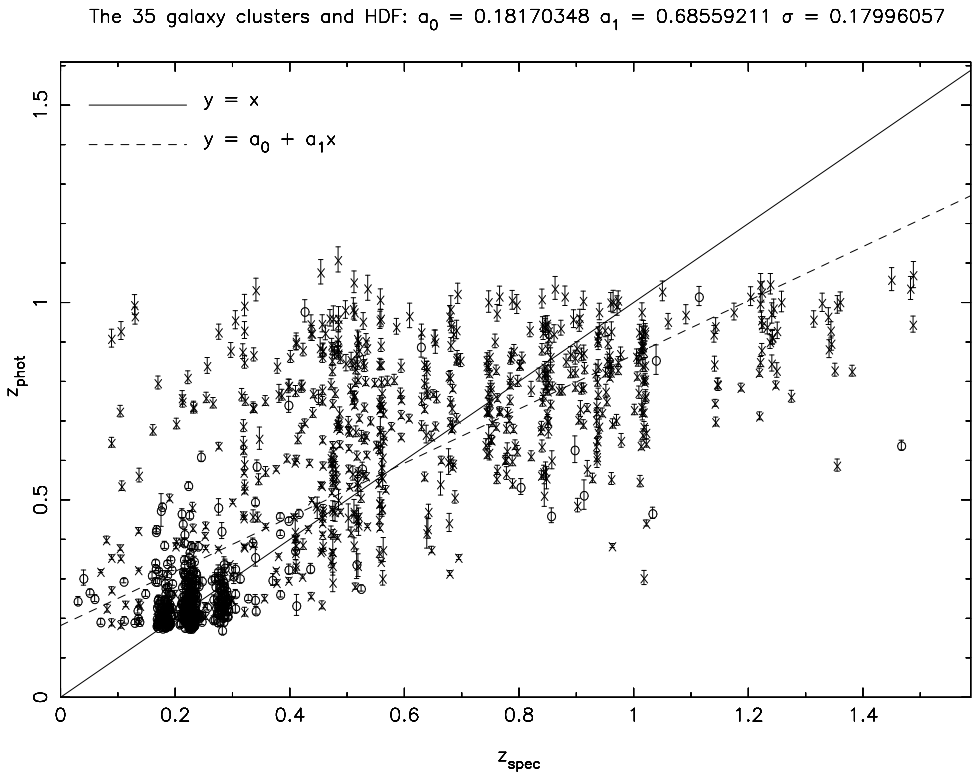

Figure 4.5: Results from ANNz: The same plot as in figure 4.4, but showing only galaxies with $z_{spec} < 1.5$ and $z_{phot} < 1.5$. Objects from the cluster catalogues are plotted with open circles, while objects from the HDF catalogue are plotted with crosses. The error-bars for the z_{phot}-estimations are plotted as vertical lines around each point. The best fitted line $y = a_0 + a_1 x$ is now found only considering these points. Again, the closer the points are to the line $y = x$, the better the results. σ is the spread around the best fitted line.

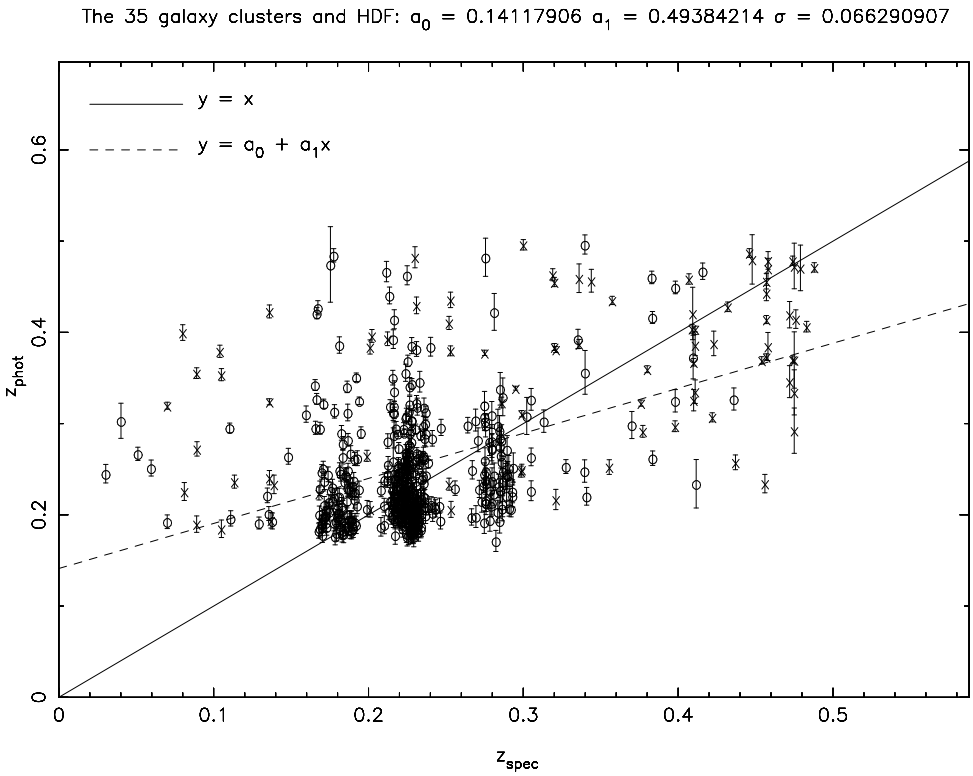

Figure 4.6: Results from ANNz: The same plot as in figure 4.4 and figure 4.5, but showing only galaxies with $z_{spec} < 0.5$ and $z_{phot} < 0.5$. Objects from the cluster catalogues are plotted with open circles, while objects from the HDF catalogue are plotted with crosses. The error-bars for the z_{phot}-estimations are plotted as vertical lines around each point. The best fitted line $y = a_0 + a_1 x$ is now found only considering these points. Again, the closer the points are to the line $y = x$, the better the results. σ is the spread around the best fitted line.

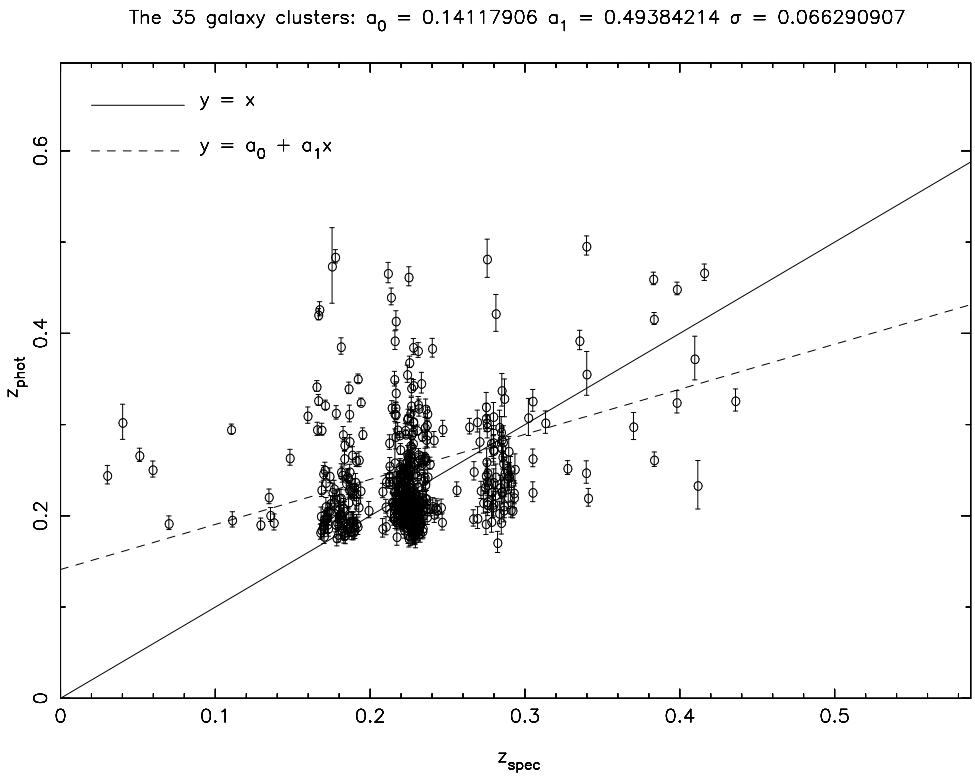

Figure 4.7: Results from ANNz: The same plot as in figure 4.4, 4.5 and 4.6, but showing only galaxies from the 35 cluster catalogues with $z_{spec} < 0.5$ and $z_{phot} < 0.5$. The error-bars for the z_{phot}-estimations are plotted as vertical lines around each point. The best fitted line $y = a_0 + a_1 x$ is now found only considering these points. Again, the closer the points are to the line $y = x$, the better the results. σ is the spread around the best fitted line.

4.3 Finding the photometric redshifts with ZEBRA

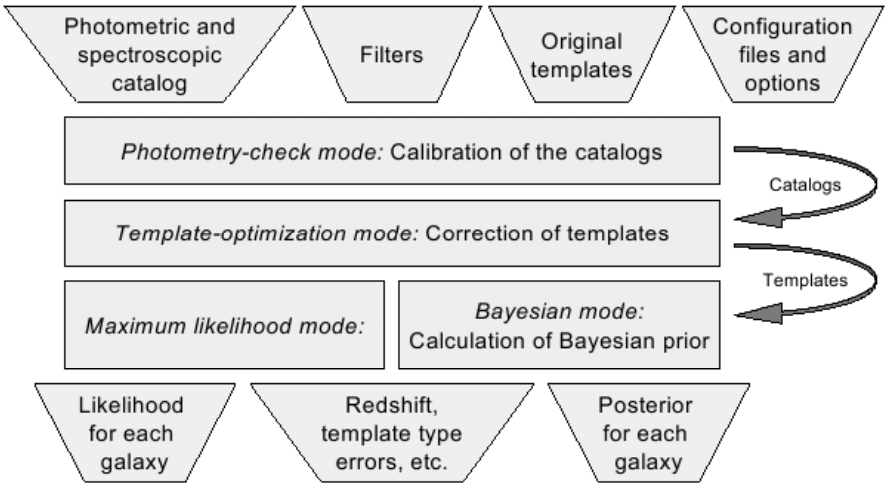

Figure 4.8: The design of ZEBRA. The different operation modi are explained in the text. This figure is taken from Feldmann et al. (2006).

Because of the unsatisfactory results from ANNz, another method had to be looked at when estimating the photometric redshifts of the galaxies. In the second attempt The Zurich Extragalactic Bayesian Redshift Analyzer (ZEBRA) [2] was used. This decision was made on the basis of the positive results found by Feldmann et al. (2006). Like ANNz, ZEBRA also takes medium- and broad-band photometric data as input and gives the photometric redshift, z_{phot}, as output. Since ZEBRA is based on the fitting of the Spectral Energy Distribution (SED) of a model-galaxy, and not just a trained ANN, it was expected that it might provide better results than ANNz. The model galaxy SED will in the following be referred to as a *template*. Without an artificial neural network (ANN) as the main method, there was no dependence on a large training set with accurately known spectroscopic redshifts, z_{spec}. When using the template-fitting approach to estimate z_{phot}, a potential source of error is mismatches between real galaxies and the available templates. However, ZEBRA also uses an ANN, but this is primarily to reduce the error in the estimated z_{phot}. Figure 4.8 shows the design of ZEBRA. ZEBRA uses several steps to get accurate z_{phot}-estimations. These are:

- *Photometry-check* mode:
  First ZEBRA corrects the photometric input catalogue for any systematic calibration errors. This is an important step to obtain an accurate

[2] *The Zurich Extragalactic Bayesian Redshift Analyzer (ZEBRA) and its* 1^{st} *application: COSMOS*, Feldmann et al. (2006).

z_{phot}-estimation. One can either use the full photometric catalogue as input, or a small training set with known spectroscopic redshifts. The latter approach clearly gives the best results since the correct template is more easily identified when the known redshift is kept fixed.

- *Template-optimization* mode:
  The ZEBRA package provides four templates from Coleman et al. (1980) (E, Sbc, Scd and Im) and two templates of star burst galaxies from Kinney et al. (1996). These will in the following be referred to as *the basic templates*. However, these templates are inadequate to reproduce the SEDs of real galaxies at all redshifts. By using a trainingset of galaxies in the redshift interval of interest, the template-optimization mode uses a χ^2-minimization approach to improve the templates. The user can choose different redshift intervals for which the templates should be optimized. The more redshift intervals that are specified, the more corrected templates are created.

- *The Maximum-Likelihood* mode:
  When run in the Maximum-Likelihood mode (hereafter ML mode), ZEBRA returns the best fit template type and redshift together with their confidence limits. Additional information, like the luminosity distance (d_L), is also provided in the output catalogue.

- *The Bayesian* mode:
  When run in the Bayesian mode, ZEBRA calculates the 2D-prior in redshift and template space in an iterative fashion. The final prior and posterior are given as output.

I refer to Feldmann et al. (2006) for a more thourough description of how ZEBRA works.

The first thing ZEBRA requires is that the magnitudes in the photometric input-catalogue are AB-magnitudes. The AB magnitude system is defined such that, when monochromatic flux f is measured in erg s^{-1} cm^{-2} Hz^{-1}, the AB magnitude, m_{AB}, is given by

$$m_{AB} = -2.5log(f) - 48.60, \tag{4.3}$$

where the value of the constant is selected to define m_{AB}=V for a flat-spectrum source. An object with constant flux per unit frequency interval, has zero colour in the AB system (Oke 1974). The Johnson-Cousins system used in this thesis is defined such that the star Alpha Lyr (Vega) has V=0.03 and all colours equal to zero. Thus, all of the calibrated magnitudes from the photometric catalogues had to be converted onto the AB system before using them as input in ZEBRA. This was easily done by using the equations:

$$U_{AB} = U_{Vega} + 1.000, \tag{4.4}$$

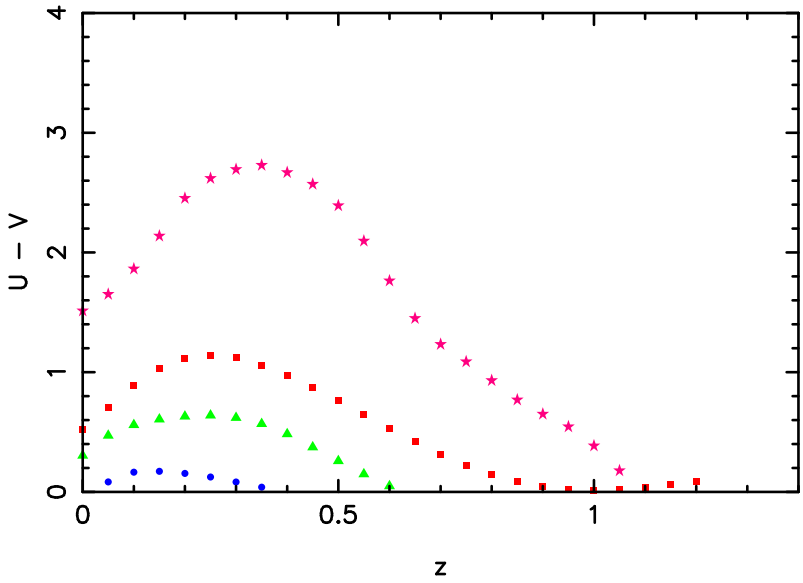

Figure 4.9: The colour $U - V$ plotted against redshift z for four different galaxy-types: ellipticals (pink stars), Sbc spirals (red squares), Scd spirals (green triangles) and irregulars (blue circles).

$$V_{AB} = V_{Vega} - 0.044, \tag{4.5}$$

and

$$I_{AB} = I_{Vega} + 0.309 \tag{4.6}$$

(Frei & Gunn 1994). Systematic calibration errors could then be corrected for by running ZEBRA in the photometry-check mode. This mode works best if the spectroscopic redshift is given as input for each object in the input-catalogue. To obtain the spectroscopic redshift for a larger set of galaxies than the ones already known from NED, more cluster galaxies had to be identified from the photometric catalogues. All galaxy clusters possess a population of galaxies which exhibit a tight colour-magnitude relation. These galaxies are called the *red sequence* (RS), and includes most red early-type galaxies (Visvanathan & Sandage 1977). Figure 4.10 and figure 4.11 show colour-magnitude diagrams of the cluster galaxies and the HDF galaxies respectively. The magnitude V is plotted along the x-axis, and the colour $(U - V)$ is plotted along the y-axis. In figure 4.10 the RS is roughly the galaxies with $(U - V) > 1$. It can be identified as the part where the upper galaxies make a distinct, almost horizontal, line. In contrast to figure 4.10, figure 4.11 does not contain a well defined RS. This is because the RS characterizes galaxy clusters and not the field. Figure 4.9 shows a plot of the colour $U - V$ versus redshift. One can clearly see that the elliptical galaxies (pink stars) create a peak between $z = 0$ and $z = 0.5$. The only galaxy-type above $U - V \sim 1.15$ in this particular redshift interval are ellipticals. The 35

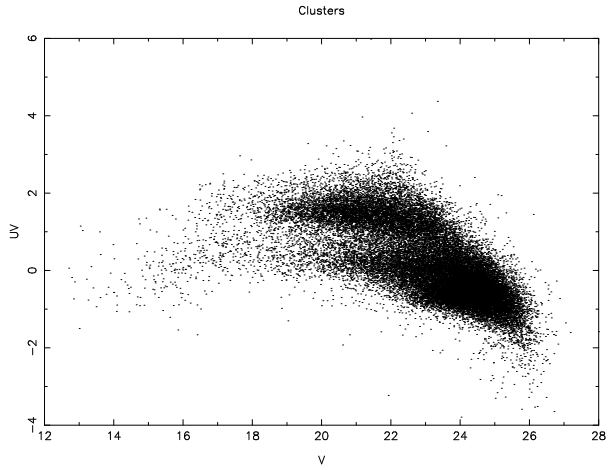

Figure 4.10: Colour-magnitude diagram of the 35 galaxy clusters. The gathering of points that looks like an almost straight line at the top, is defined as the *red sequence*.

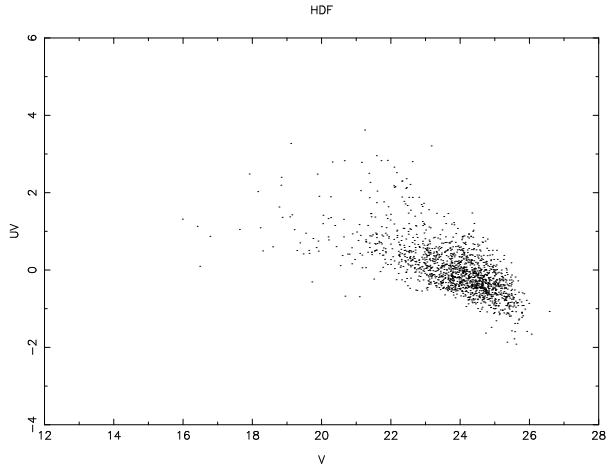

Figure 4.11: Colour-magnitude diagram of the HDF. In contrast to the figure above, this plot does not contain a well defined red sequence. This is because the RS characterizes galaxy clusters and not the field.

galaxy clusters studied in this thesis are found at redshifts between $z = 0.15$ and $z = 0.3$, which is very near the centre of the peak in figure 4.9. One could then naively think that by selecting all galaxies with $U - V > 1.15$, the RS would be obtained. However, some of the reddest galaxies (with the highest $(U - V)$-values) can also be background galaxies which are not part of the galaxy clusters. A more careful selection of the RS was therefore done as follows:

- By using the colour-magnitude diagram (V vs. $U-V$) described above (figure 4.10), all the objects within a drawn rectangular box which at least contained the RS, were picked out for each galaxy cluster. The width and height of this box varied between the clusters depending on the spread in the magnitude and colour of the cluster galaxies. The width was in the interval $\Delta V \in (6, 9)$, while the hight was in the interval $\Delta UV \in (1.5, 2.2)$. The bottom objects chosen in every case were a bit above $U - V = 1$.

- The chosen objects were plotted in a new colour-magnitude diagram, this time with the magnitude V along the x-axis, and the colour $V - I$ along the y-axis. The only objects picked out this time were the ones within ± 0.5 of the median value of the colour $V - I$.

- A straight line was fitted through the remaining points. The final step was then to only pick the objects within $\pm 0.3(V - I)$ of this fitted line. The remaining objects should then with good accuracy be part of the RS, and hence be cluster members. The redshift of the RS galaxies was set equal to the redshift of the cluster in question.

By using the galaxies identified as RS-galaxies (in addition to the galaxies from NED with already known z_{spec}), photometric catalogues were created for each cluster where all of the galaxies had known z_{spec}. An input catalogue consisting of HDF-members *without* z_{spec} and an input catalogue consisting of HDF members *with* z_{spec} were also used. These two catalogues contained the same 650 galaxies, and were the same catalogues used as input to ANNz. The only difference between the two was that the first catalogue did not contain z_{spec} for any of its members. The reason for using this catalogue was mainly to look at the difference it makes to give z_{spec} as an input to ZEBRA. Finally, a catalogue containing all of the galaxies from the 35 cluster-catalogues with known z_{spec}, and a catalogue containing all of the galaxies from the 35 cluster-catalogues pluss the HDF members (with known z_{spec}) were also created.

Table 4.1: Results from the run of ZEBRA in photometry-check mode. U-diff, V-diff and I-diff stand for the difference between the magnitude in the input catalogue and the corrected magnitude in the U-, V- and I-band respectively, that is $mag_{input} - mag_{corr}$. The last column lists the number of objects in each of the cluster-catalogues.

Cluster name	U-diff	V-diff	I-diff	Number of objects
A2204	0.099097	0.090496	-0.158335	172
RX J1720.1+2638	0.322789	0.090954	-0.122843	184
A586	-0.155407	0.120341	-0.058805	256
A1914	0.027046	0.089488	-0.090120	253
A665	-0.186723	0.064986	-0.146384	290
A115	-0.038867	-0.002186	-0.028010	209
A520	-0.075154	-0.032409	-0.011924	247
A963	-0.034222	0.178940	-0.019137	157
A1423	-0.081911	0.060667	-0.073458	182
A773	-0.321687	0.091178	-0.044874	300
A2261	0.177873	0.068895	-0.037694	215
A267	-0.223179	-0.044915	0.009411	168
A1682	-0.150717	0.036115	-0.048945	239
A1763	-0.248249	0.105169	-0.085328	283
A2111	-0.027733	0.032994	-0.069336	241
A2219	-0.206633	0.055556	-0.082407	327
A2390	-0.220765	0.015126	-0.017881	241
Zw 5247	0.033211	0.053778	-0.097801	203
RX J2129.6+0005	-0.011400	-0.011643	-0.014426	146
RX J0439.0+0715	-0.237128	0.012935	-0.030037	169
Zw 2089	0.189281	-0.101657	0.008344	118
A1835	-0.189897	0.019789	-0.057348	243
A68	-0.228281	0.059116	-0.022663	171
Zw 7160	-0.040667	0.076210	-0.081451	133
Zw 5768	-0.550856	-0.127764	0.032238	42
A697	-0.000322	0.191625	-0.048309	268
A1758N	-0.328877	0.116665	-0.066987	268
A2631	-0.146306	0.072492	-0.078412	201
A611	-0.199532	0.069026	-0.078679	172
RX J0437.1+0043	-0.185226	0.057541	-0.032460	168
Zw 3146	-0.138159	0.192438	-0.145190	177
Zw 7215	-0.104099	0.109809	-0.149905	183
A781	-0.227425	0.141501	-0.096358	239
A1576	-0.183774	0.162136	-0.032149	240
A2552	-0.170528	-0.062490	-0.015459	206

Continued on next page

Table 4.1 – continued from previous page

Cluster name	U-diff	V-diff	I-diff	Number of objects
HDF	-0.059730	-0.002223	-0.003363	650
HDF_zspec	0.108420	-0.170993	-0.004187	650
clusters_zspec	0.005056	0.068647	-0.071514	7311
HDF_clusters_zspec	0.004555	0.045127	-0.070768	7961

The results from the photometry-check mode are listed in table 4.1. U-diff, V-diff and I-diff are the differences between the magnitudes in the input-catalogue and the corrected magnitudes in the U-, V- and I-band respectively, that is $mag_{input} - mag_{corr}$. Thus, the corrections that were applied to the full photometric catalogues (without z_{spec}) were U-diff, V-diff and I-diff. The last column in table 4.1 lists the number of objects in each of the clusters with known z_{spec} which were used as input in the photometry-check mode.

The difference in the results for the two HDF catalogues show the importance of including z_{spec} in the input catalogues. As can be observed in table 4.1, the difference in the U-band corrections are 0.16815, the difference in the V-band corrections are 0.173216, while the difference in the I-band corrections are close to zero. Thus, for the U- and V-band there are significant differences in the two results.

The final two rows in table 4.1 show the results obtained when using all of the galaxies from the cluster-catalogues with known z_{spec} as input, and when using all of the galaxies from the cluster- *and* HDF-catalogues with known z_{spec} as input. Because of the variations between the corrections for the 35 galaxy clusters, a total correction factor for all of the 35 clusters was not used.

After correcting all of the photometric catalogues, the next step was to optimize the templates to best fit the spectral energy distributions (SEDs) of the different galaxies at different redshifts. In contrast to the photometry-check mode, the template-optimization mode only had to be run once, that is, the same templates could be used for all the 35 galaxy clusters. As mentioned earlier, it is very favorable to use an input catalogue with known z_{spec} when optimizing the templates. The final input catalogue therefore contained all of the galaxies with known z_{spec} from the 35 galaxy clusters and HDF (in total 7961 galaxies). The magnitudes in this input catalogue were the corrected magnitudes in the U-, V- and I-bands. By using the additional RS galaxies with known z_{spec} as input in ANNz, the results would probably have been

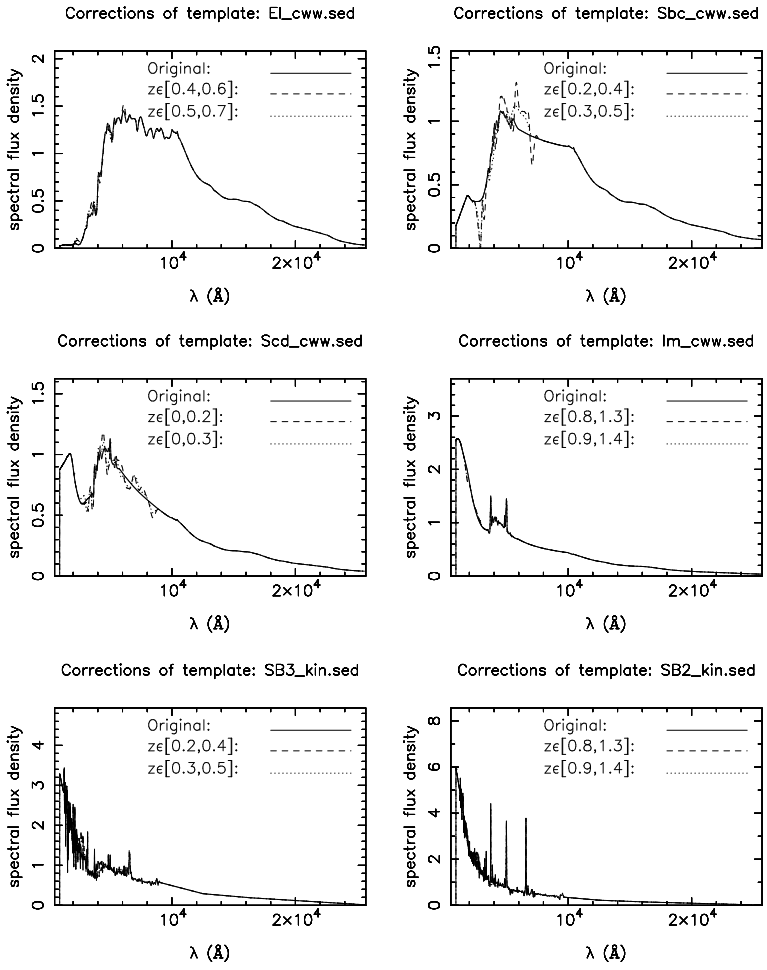

Figure 4.12: Some results from the template-optimization mode. I have chosen one plot from each of the basic templates. The solid line represents the original template to be corrected, the dashed line represents the corrected template optimized in the first redshift interval, while the dotted line represents the corrected template optimized in the second redshift interval. The first and second redshift intervals overlap each other. The final template to be used in the z_{phot}-estimation is a combination of the two corrected templates.

better. However, in addition to having a photometry-check mode, ZEBRA also takes more information (templates) as input than ANNz. Thus, ZEBRA provides much more accurate z_{phot}-estimations for the galaxies under study.

When running ZEBRA in the template-optimization mode, the input catalogue has to be divided into redshift bins. The number and size of these bins are specified by the user. According to the ZEBRA manual, it is recommended to run the template-optimization mode twice with different bin boundaries (ETH 2008). The templates to be optimized were the six basic templates; four templates from Coleman et al. (1980) (E, Sbc, Scd and Im), and two templates of star burst galaxies from Kinney et al. (1996). These templates lack data for the shortest wavelengths when $z_{spec} > 2.5$, that is, far in the UV. Since only 7 of the 7961 galaxies with known redshifts are found at redshifts higher than 2.5, these were removed. Thus, only redshift intervals up to $z = 2.5$ were used. 7 redshift intervals were chosen between 0 and 2.5. These were:
z = 0-0.2; 0.2-0.4; 0.4-0.6; 0.6-0.8; 0.8-1.3; 1.3-1.8; 1.8-2.5 and
z = 0-0.3; 0.3-0.5; 0.5-0.7; 0.7-0.9; 0.9-1.4; 1.4-1.9; 1.9-2.5.
48 templates were made from each run. This comes from the fact that there were 6 basic templates which were optimized in 7 redshift intervals. In addition, ZEBRA printed out the original basic templates. The final templates to be used in the z_{phot}-estimations were found by taking the average template from the two runs for each redshift bin and spectral type. Some examples of corrected templates are shown in figure 4.12. These plots contain the original template, the optimized template from the first run and the optimized template from the second run. Plots were made for all of the redshift intervals, but I have chosen to only show a few. From these plots the corrections in the redshift bins 1.8-2.5 and 1.9-2.5 seem negligible, but there were noticable corrections made for many of the lower redshift bins.

With 42 corrected templates (plus the 6 original templates) and the corrected photometric catalogues (without z_{spec}), ZEBRA was ready to be run in the Maximum-Likelihood mode. Even though the redshift limits were set to $z \in [0 - 2.5]$ when running ZEBRA in the template-optimization mode, they were changed back to $z \in [0 - 4]$ in this last run-mode. This means that for $z \in [2.5 - 4]$, basic templates were used.

To check the credibility of the estimated redshifts, the same plots as for ANNz were created. This also gave an opportunity to compare the two methods. Figure 4.13 shows the histograms of the 35 galaxy clusters. As before, the x-axis represents the estimated photometric redshift, z_{phot}, and the y-axis represents the number of galaxies, N. These histograms, on the other hand, show very satisfactory results. The vertical line representing the true redshift of the clusters, intersects the peak in all of the 35 histograms.

This is exactly what is expected. That there are some smaller peaks at higher redshifts are not a cause for concern, being due to smaller structures along the line of sight. However, Zw5768 shows only a modest peak at the cluster redshift. This does not come as a big surprise since the photometric catalogue for Zw5768 contain very few objects compared to the other cluster-catalogues. Either Zw5768 is a poor cluster, or very few cluster members are detected in the images used of Zw5768. Histograms were also made for the HDF (see figure 4.14). The upper histogram shows the results obtained when z_{spec} was given as input when ZEBRA was run in the ML-mode, while the lower histogram shows the results from when z_{spec} was *not* given as input. Even though the peak in the top histogram is more distinct than the one in the lower histogram, there are clearly similarities between the two. It seems like the bottom histogram is a bit more smeared out. The two histograms also highlight the fact that ANNz did not give good z_{phot}-estimations with such a small training set. This can be seen when comparing figure 4.14 and figure 4.3. The upper histogram in figure 4.14 is believed to be the most correct one out of the three.

The next plot made was z_{phot} versus z_{spec}. With z_{spec} along the x-axis and z_{phot} along the y-axis, the plotted points are supposed to stay close to the line $y = x$. Also this time four z_{phot} versus z_{spec} plots were made. Figure 4.15 shows a plot of all of the 35 galaxy clusters together with HDF. The error bars show the 1σ confidence limits for each z_{phot}-estimate. This plot looks much better than the same plot for the ANNz-results in figure 4.4 from the fact that the fitted line $y = a_0 + a_1 x$ (dashed) now lies closer to the line $y = x$ (solid). Figure 4.16 shows the same plot as the one in figure 4.15, but now only of galaxies with $z_{spec} < 1.5$ and $z_{phot} < 1.5$. The figure clearly shows that galaxies from the HDF galaxies outnumber galaxies from the cluster catalogues at the highest redshifts. In this plot the fitted line $y = a_0 + a_1 x$ is made on the basis of the objects with $z_{spec} < 1.5$ and $z_{phot} < 1.5$, and it turns out to be very close to the line $y = x$. To get a better look at the black cloud formed by all the galaxies around $z_{spec} = 0.2 - 0.3$, a plot containing galaxies with $z_{spec} < 0.5$ and $z_{phot} < 0.5$ was made (see figure 4.17). This time the fitted line $y = a_0 + a_1 x$ is further from the line $y = x$ than it was in figure 4.16. The galaxies creating the vertical lines (same z_{spec}) are the ones identified as the RS-galaxies in the different clusters. Even though z_{spec} was set to $z_{cluster}$ for all of the RS-members, ZEBRA estimated their z_{phot} to be a bit different. It is then important to keep in mind the uncertainties in the z_{phot}-estimations. Later, when deciding which galaxies that are actually part of the clusters, the 2σ confidence limits pluss an extra error term will be used. In the final figure only galaxies from the 35 cluster catalogues with $z_{spec} < 0.5$ and $z_{phot} < 0.5$ are plotted (see figure 4.18). As for the ANNz results, this plot shows that most of the objects at lower redshifts are from the cluster catalogues. In addition to z_{phot}, ZEBRA also gave the best fitted

template as output. This information will come in hand later when information about galaxy-type is needed.

ZEBRA was also run in the *Bayesian* mode. This was primarily to see if the same results were obtained as from the ML-mode. The Bayesian mode takes the same input as the ML-mode; a photometric catalogue, filter and template files, and the standard configuration files which say something about the which templates and filters are used and the structure of the photometric catalogue. The only difference between the ML mode and the Bayesian mode is that the Bayesian mode estimates a prior, $P(d)$, from the input catalogue which is used to calculate the posterior, $P(\beta|d)$ for each galaxy. Here P is a probability, d is the data in the input catalogue, and β stands for the unknown parameters. The posterior provides the parameters β given the data d. The main idea behind *Bayes theorem* is that the posterior can be determined if the prior and the likelihood, $\mathcal{L}(\beta)$, are known, that is:

$$P(\beta|d) = P(\beta)\frac{\mathcal{L}(\beta)}{P(d)}. \tag{4.7}$$

The results from ZEBRA's Bayesian mode were identical with the results from the ML mode, which substantiate the quality of the z_{phot}-estimations.

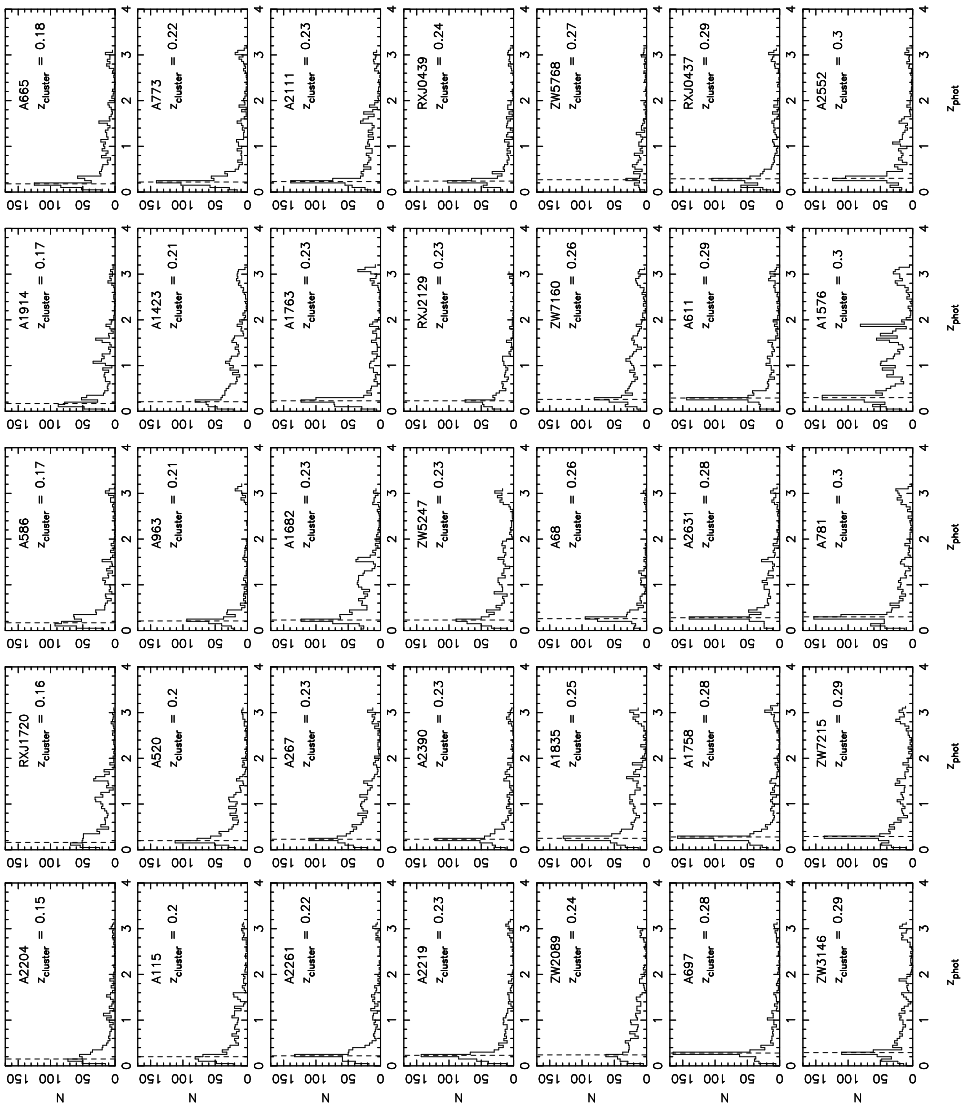

Figure 4.13: Results from ZEBRA: Histograms of the 35 galaxy clusters where the estimated photometric redshift, z_{phot}, is plotted along the x-axis and the number of galaxies in each redshift interval ($\Delta z_{phot} = 0.05$) is plotted along the y-axis. The true redshift of each cluster is plotted as a dashed, vertical line.

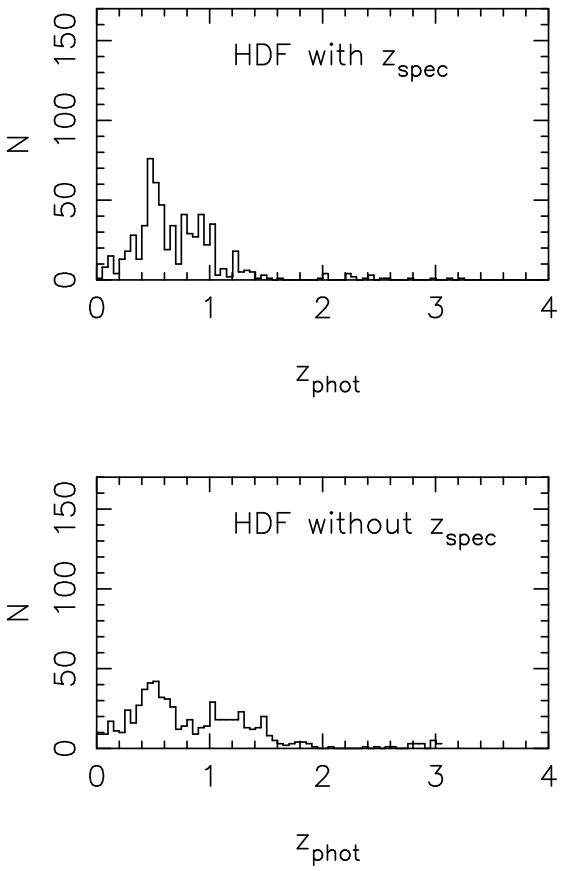

Figure 4.14: Results from ZEBRA: Histograms of HDF where the estimated photometric redshift, z_{phot} is plotted along the x-axis and the number of galaxies in each redshift interval ($\Delta z_{phot} = 0.05$) is plotted along the y-axis. The top histogram shows the result from when z_{spec} was given as input when ZEBRA was run in the ML-mode, while the bottom histogram shows the result from when z_{spec} was *not* given as input.

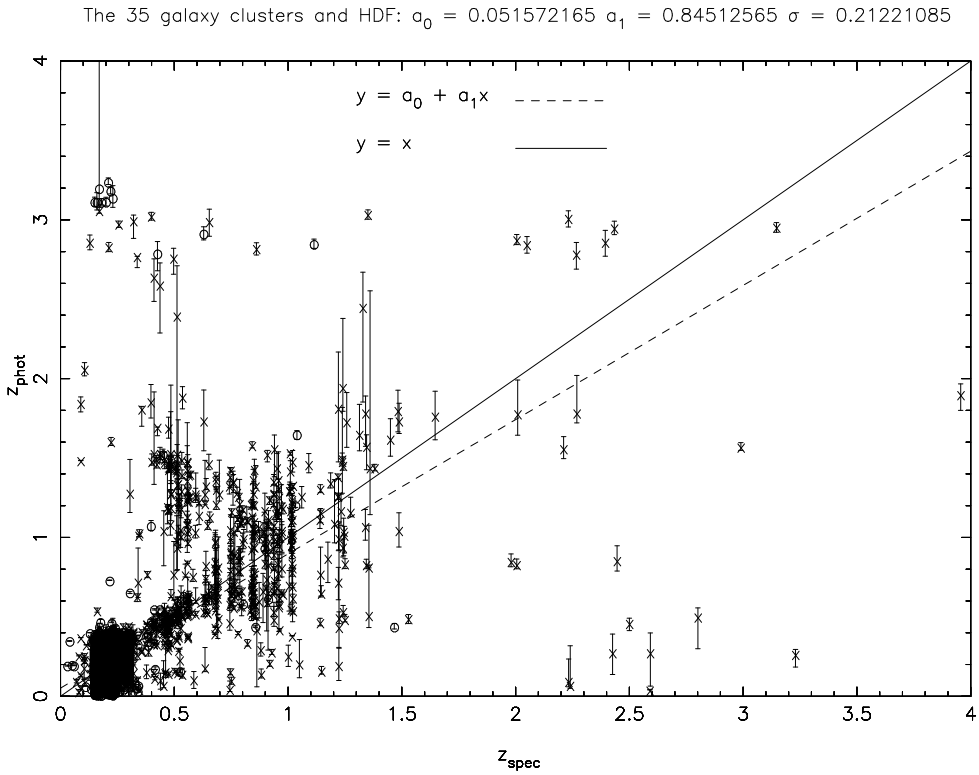

Figure 4.15: Results from ZEBRA: Plot of the 35 galaxy clusters and HDF where z_{spec} is plotted along the x-axis and z_{phot} is plotted along the y-axis. Objects from the cluster catalogues are plotted with open circles, while objects from the HDF catalogue are plotted with crosses. The error-bars for the z_{phot}-estimations are plotted as vertical lines around each point. In addition, the best fitted line between the points ($y = a_0 + a_1 x$), and the line $y = x$ are plotted. The closer the points are to the line $y = x$, the better the results. σ is the spread around the best fitted line.

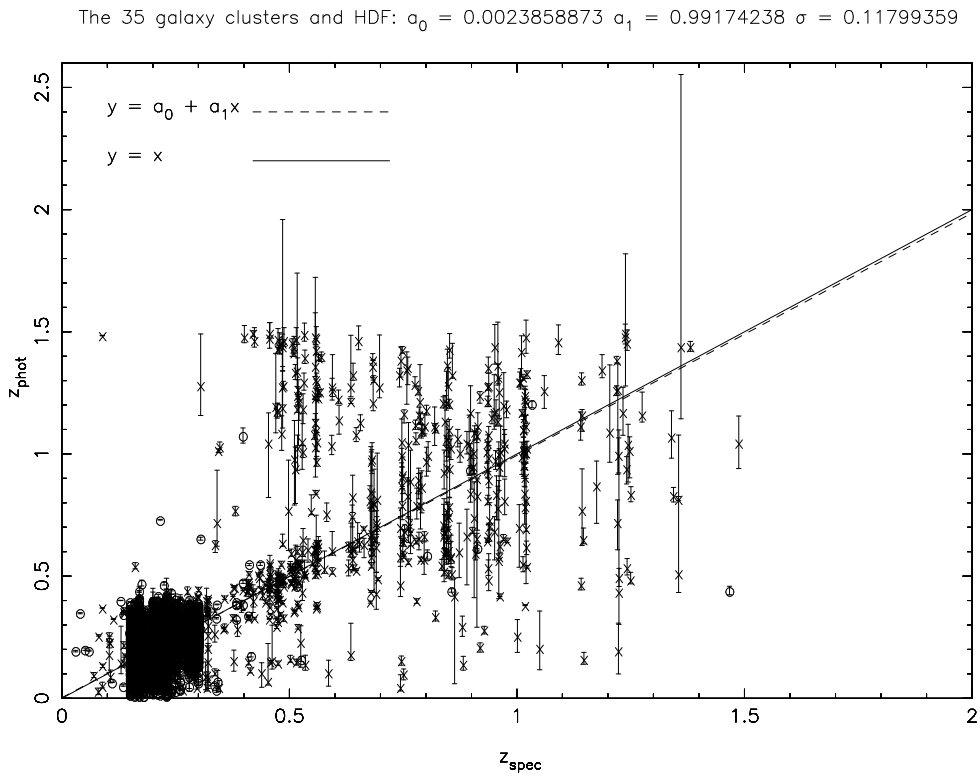

Figure 4.16: Results from ZEBRA: The same plot as in figure 4.15, but showing only galaxies with $z_{spec} < 1.5$ and $z_{phot} < 1.5$. Objects from the cluster catalogues are plotted with open circles, while objects from the HDF catalogue are plotted with crosses. The error-bars for the z_{phot}-estimations are plotted as vertical lines around each point. The best fitted line $y = a_0 + a_1 x$ is now found only considering these points. Again, the closer the points are to the line $y = x$, the better the results. σ is the spread around the best fitted line. σ is the spread around the best fitted line.

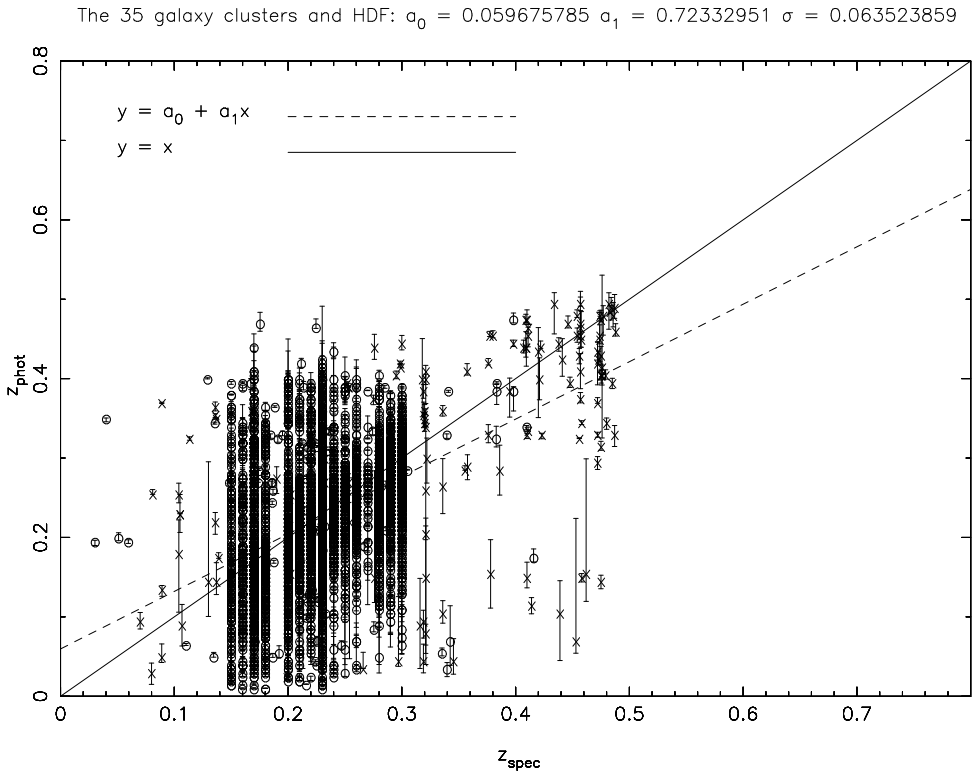

Figure 4.17: Results from ZEBRA: The same plot as in figure 4.15 and 4.16, but showing only galaxies with $z_{spec} < 0.5$ and $z_{phot} < 0.5$. Objects from the cluster catalogues are plotted with open circles, while objects from the HDF catalogue are plotted with crosses. The error-bars for the z_{phot}-estimations are plotted as vertical lines around each point. The best fitted line $y = a_0 + a_1 x$ is now found only considering these points. Again, the closer the points are to the line $y = x$, the better the results. σ is the spread around the best fitted line. σ is the spread around the best fitted line.

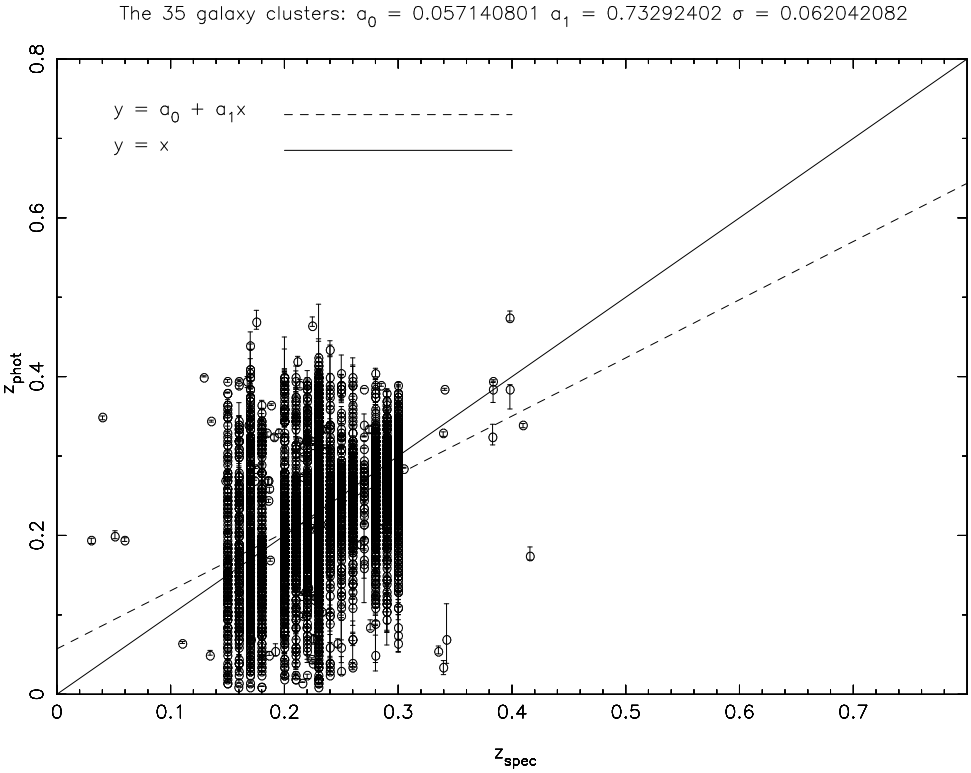

Figure 4.18: Results from ZEBRA: The same plot as in figure 4.15, 4.16 and 4.17, but showing only galaxies from the 35 cluster catalogues with $z_{spec} < 0.5$ and $z_{phot} < 0.5$. The error-bars for the z_{phot}-estimations are plotted as vertical lines around each point. The best fitted line $y = a_0 + a_1 x$ is now found only considering these points. Again, the closer the points are to the line $y = x$, the better the results. σ is the spread around the best fitted line.

4.4 Selecting the cluster members

Using the estimated photometric redshifts for all of the galaxies in the cluster images, the cluster-galaxies could be isolated from the foreground- and background-galaxies. The lower and higher redshift limits (z_L and z_H) of the different clusters were based on the 95% confidence limits for the estimated z_{phot} with an additional error term, S_{extra}. It is important that these limits are small enough that a significant amount of foreground- and background-galaxies are not included, and large enough to include virtually all of the cluster members. The lower error-term, S_L, and the higher error-term, S_H, used are given by:

$$S_L = \sqrt{(z_{phot} - z_{L0.95})^2 + (S_{extra})^2}, \tag{4.8}$$

$$S_H = \sqrt{(z_{H0.95} - z_{phot})^2 + (S_{extra})^2}, \tag{4.9}$$

where $z_{L0.95}$ is the lower redshift in the 95% confidence limit and $z_{H0.95}$ is the upper redshift. Thus, the selection criteria for the cluster members was that the galaxies had to lie in the redshift interval $z_{phot} \in [z_L, z_H]$, where $z_L = z_{phot} - S_L$ and $z_H = z_{phot} + S_H$. The extra error-term was found by looking at the cluster-galaxies with known z_{spec} from NED for the clusters A2219 and A2390. NED provided 94 galaxies from A2219 and 116 galaxies from A2390. These galaxies are for certain part of the clusters, and the aim was therefore to find an extra error-term which included a large amount of these galaxies as cluster-galaxies ($\sim$90%). The extra error-term that accomplished this, turned out to be 0.1. With $S_{extra} = 0.1$, 94% of the cluster members were identified for A2219, while 89% of the cluster members were identified for A2390. When selecting cluster members based on the estimated z_{phot} of the galaxies, there is no guarantee that some of the galaxies identified as cluster members are indeed field galaxies (*fake* cluster member). On the other hand, a cluster galaxy may also have an estimated z_{phot} indicating that the galaxy is not part of the cluster (*lost* cluster member). Figure 4.15 provides information about how many cluster members that are *lost*, and how many *fake* cluster members which are gained. To get an excact number of lost and fake cluster members, cluster boundaries were set to $z = 0.4$ here. Thus, galaxies with $z_{phot} > 0.4$ and $z_{spec} < 0.4$ are lost cluster members, while galaxies with $z_{phot} < 0.4$ and $z_{spec} > 0.4$ are fake, and thus "gained". Only 0.79% of the galaxies estimated to be cluster galaxies ($z_{phot} < 0.4$) were fake ($z_{phot} < 0.4$ and $z_{spec} > 0.4$), while 0.81% of the actual cluster members ($z_{spec} < 0.4$) were lost ($z_{spec} < 0.4$ and $z_{phot} > 0.4$). That these numbers are so small and so equal, indicates that the results from ZEBRA are satisfactory.

Colour-magnitude diagrams of all of the galaxies from the 35 cluster-catalogues are shown in figure B.1 in Appendix B. Here the foreground-, background-

and cluster-galaxies are plotted with different colours (green, blue and red, respectively), while the different galaxy types are plotted with different symbols. The galaxy types are divided into three groups:
group 1 = Elliptical galaxies (E), plotted as open diamonds,
group 2 = Spiral galaxies (Sbc and Scd), plotted as open cross,
group 3 = Irregular galaxies and starburst galaxies (Im, SB2 and SB3), plotted as open stars.
In the second figure in Appendix B (figure B.2) only the galaxies identified as cluster members are plotted. From these figures it is possible to identify the red sequence and blue cloud in each galaxy cluster, where the blue cloud consists mainly of blue late-type galaxies and are located below the red sequence. By comparing figure B.2 with other results from litterature (Bell et al. 2004; Fasano et al. 2006; Simon et al. 2009), it can also serve as a check of how well ZEBRA's template-fitting has worked. Figure B.2 shows very satisfactory results on the basis of the positions of the different galaxy-types in the colour-magnitude diagrams.

Chapter 5

Luminosity functions and star formation rates

An introduction to the luminosity function (LF) was given in section 1.6. The LF describes how the relative number of galaxies varies with their luminosity, and it contains information about galaxy formation and evolution. In this thesis, the most valuable information gained from the LF will be the relation between the bright giant galaxies and the faint dwarf galaxies, given by α. The star formation rate (SFR) of a galaxy was introduced in section . By studying the evolution of the SFR, valuable information about galaxy formation and evolution is gained, like processes that destroy/create galaxies, processes that change one type of galaxy into another (e.g. tidal encounters, ram-pressure stripping, galactic starvation), and processes that transform mass into light.

This chapter first presents three different luminosity functions (LFs) for each galaxy cluster: the red-sequence LF (RSLF) in the rest-frame B-band, the LF in the rest-frame B-band for all galaxy types, and last but not least, the LF based on the rest-frame wavelength $\lambda \approx 2800$ Å. The results will be discussed in chapter 6. In addition, the UV luminosities at $\lambda \approx 2800$ Å will be used to estimate the SFR for each cluster galaxy following a procedure similar to Dahlen et al. (2006).

The LF is fitted by the Schechter function (described in section 1.6), thus

$$\phi(M)dM = (0.4\ln 10)\phi^* 10^{0.4(\alpha+1)(M^*-M)} exp(-10^{0.4(M^*-M)}), \qquad (5.1)$$

In chapter 4 the calibrated magnitudes from chapter 3 were first corrected for Galactic dust extinction, and subsequently corrected for systematic errors by running ZEBRA in the photometry-check mode. However, the magnitudes

needed in equation 5.1 are the absolute magnitudes. With known distance out to each cluster, the absolute magnitudes can easily be calculated. The procedure when finding the LFs is therefore as follows:

- Find the luminosity distance d_L out to each galaxy cluster.
- Use d_L to convert the apparent magnitudes m into absolute magnitudes M.
- Find the three free parameters M^*, ϕ^* and α and their respective uncertainties by using the χ^2 test for goodness of fit.

After this, the absolute magnitudes at rest-frame wavelength 2800 Å can be used to derive the luminosities at that same wavelength. By making assumptions on the past star formation history, a conversion factor relating the UV luminosity and the ongoing SFR was found by Dahlen et al. (2006). This conversion factor will be applied when calculating the SFRs for the galaxies under study in this thesis (see section 5.6).

5.1 The luminosity distance for a ΛCDM-universe

The distance measure to a galaxy is relevant for calculating its absolute magnitude and luminosity. The *luminosity distance*, d_L, is defined as

$$d_L \equiv \sqrt{\frac{L}{4\pi l}}, \tag{5.2}$$

where L is the luminosity of the galaxy (energy per unit time) and l is the flux (energy per unit time and area). In a flat universe, the luminosity distance can be expressed as

$$d_L = c(z+1)\int_0^z \frac{dz'}{H(z')}. \tag{5.3}$$

By inserting the expression for $H(z)$ for a flat ΛCDM-universe (found by inserting $1+z = a^{-1}$ in equation 1.8 in chapter 1, where a is the scale factor at redshift z), we get

$$d_L = \frac{c(z+1)}{H_0}\int_0^z \frac{dz'}{\sqrt{\Omega_{m0}(1+z)^3 + \Omega_{\Lambda 0}}}, \tag{5.4}$$

This integral can not be solved analytically. In order to simplify the computation of difficult numerical integrals, Ue-Li Pen (1999) introduced an analytical fitting formula to this integral:

$$d_L = \frac{c}{H_0}(z+1)\left[\eta(1,\Omega_0) - \eta\left(\frac{1}{1+z},\Omega_0\right)\right], \tag{5.5}$$

where

$$\eta(a,\Omega_0) = 2\sqrt{s^3+1}\left[\frac{1}{a^4} - 0.1540\frac{s}{a^3} + 0.4304\frac{s^2}{a^2} + 0.19097\frac{s^3}{a} + 0.066941s^4\right]^{-1/8}, \tag{5.6}$$

and

$$s^3 = \frac{1-\Omega_0}{\Omega_0}. \tag{5.7}$$

η is the conformal time, $\frac{a_0}{a} = 1+z$, and $a_0 = 1$. The relative error in the fitting formula above is less than 0.4% for $0.2 \leq \Omega_0 \leq 1$ (Ue-Li Pen 1999). For the flat ΛCDM-universe, $\Omega_0 = 0.3$, which means that $s^3 = \frac{7}{3}$. Thus, the luminosity distance out to each cluster was found.

5.2 Converting apparent magnitudes into absolute magnitudes

While the *apparent magnitude*, m, is a measure of an astronomical object's apparent brightness as seen from Earth, the *absolute magnitude*, M, is a measure of its luminosity. It is not a direct measure of the total energy output of an object, but rather the energy in a chosen bandpass. It is defined to be the apparent magnitude an astronomical object *would* have if it was at a distance of 10 parsecs ($1pc \simeq 3.09 \times 10^{13}$km $\simeq 3.26$ly), at rest (that is, not redshifted), and compact.

If space were transparent, with no dust, it would be easy to find an object's absolute magnitude by combining a measurement of its distance with the observed apparent magnitude. But this is not the case. As mentioned in chapter 4, interstellar space contains dust that absorbs or scatters light from distant stars. To convert the observed apparent magnitudes m into absolute magnitudes M, the apparent magnitudes have to be corrected for luminosity distance and Galactic dust extinction. In a given wavelength band centered on λ, we then have

$$M_\lambda = m_\lambda - 5log_{10}\left(\frac{d_L(z)}{10pc}\right) - A_\lambda, \tag{5.8}$$

where d_L is the luminosity distance from the Earth to the object in parsecs, and $A_\lambda > 0$ represents the number of magnitudes of Galactic dust extinction present along the line of sight for the passband in question. However, since most galaxies have measurable redshifts, their spectra will be systematically redshifted. The photons received in the V-band, for example, will have been emitted at shorter wavelengths. This means that the observed apparent magnitude in the V-band, is no longer directly connected to the

value M_V. The *K-correction* is an adjustment made to the magnitudes and colours of distant galaxies, which takes account of the effect of the redshift. A K-correction would not be required if one could measure all the light coming from a galaxy (bolometric flux), but this is not the case. The entire spectral range of galaxies we observe is not covered. An astronomical measurement through a single filter or a single bandpass only shows a fraction of the total spectrum, redshifted into the frame of the observer. The K-correction converts the measurement of an object at distance z to an equivalent measurement in the rest frame of the object. By including the K-correction, the equation for the absolute magnitude becomes:

$$M = m - 5log_{10}\left(\frac{d_L(z)}{10pc}\right) - A - K(z), \tag{5.9}$$

where $K(z)$ is the K-correction.

The K-corrections were calculated using a script which takes galaxy type, redshift, the observed frame spectral energy distribution (SED), and the rest frame SED as input. The equations used are based on those given by Hogg et al. (2002). Below, the rest-frame B-band and the observed frame V-band are used as an example:

$$K_{BV} = -2.5log_{10}\left[[1+z]\frac{\int \frac{d\nu_0}{\nu_0} f_\nu(\nu_0)V(\nu_0)\int \frac{d\nu_e}{\nu_e} g_\nu^B(\nu_e)B(\nu_e)}{\int \frac{d\nu_0}{\nu_0} g_\nu^V(\nu_0)V(\nu_0)\int \frac{d\nu_e}{\nu_e} f_\nu\left(\frac{\nu_e}{1+z}\right)B(\nu_e)}\right]. \tag{5.10}$$

Here K_{BV} is the K-correction from the observed frame V-band to the rest-frame B-band, z is the redshift of the source, ν_0 is the observed frequency of the source, and $\nu_e = [1+z]\nu_0$ is the emitted frequency of the source (hereafter *0* represents observed, while *e* represents emitted). $f_\nu(\nu)$ is its spectral flux density (energy per unit time per unit area per unit frequency), $g_\nu^V(\nu)$ is the spectral flux density for the zero-magnitude, which, for Vega-relative magnitudes, is Vega. Here, $g_\nu^V(\nu) = g_\nu^B(\nu)$. The values of $V(\nu)$ and $B(\nu)$ at each frequency ν are the probabilities that a photon of frequency ν gets counted by the CCD.

The absolute magnitudes of interest in this thesis are the ones in the rest-frame B-band and in the rest-frame U_{2800}-band. Here the U_{2800}-band refers to the UV-band used with $\lambda_{eff} = 2800$ Å. It is simply a blue-shifted version of the Johnson-Cousins U-band. A plot of the transmission curves for U_{2800} together with the Johnson-Cousins UBVRI system is shown in figure 5.1. The galaxy types of the cluster members are known from ZEBRA, the spectroscopic redshift out to each galaxy cluster is known from references in Dahle et al. (2006), and the SEDs for the passbands U_{2800}, U, B, V and I are also known. By using the K-correction it is then possible to relate the absolute magnitudes in the rest-frame bands to the observed frame apparent magnitudes in the U-, V- and I-bands. When finding the absolute

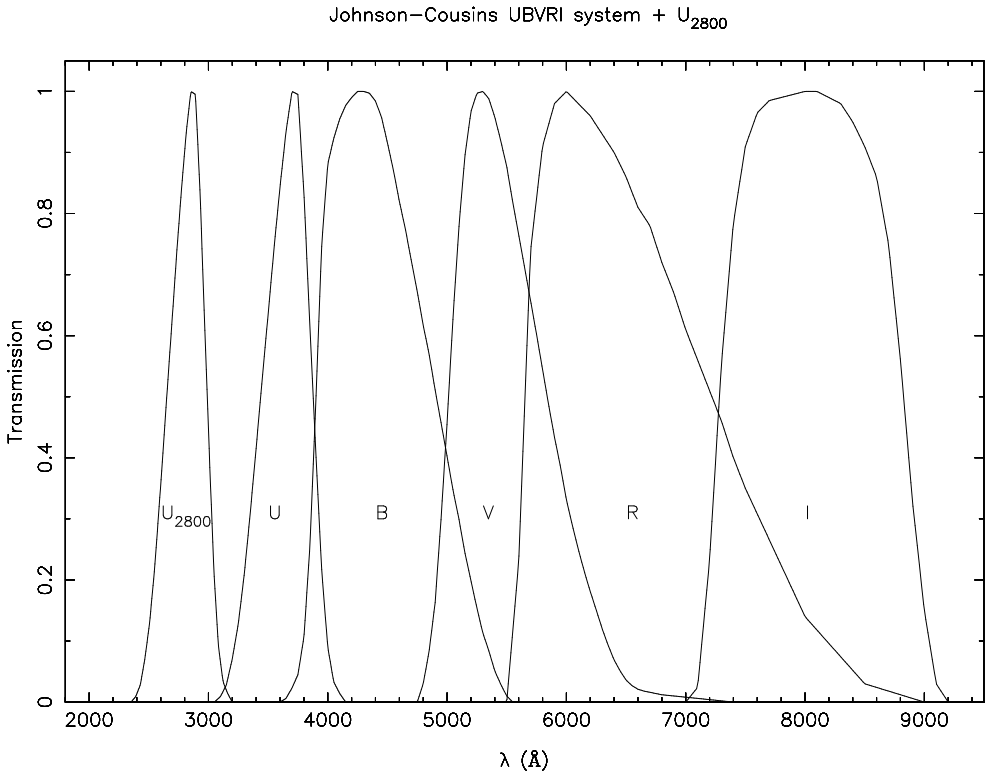

Figure 5.1: Transmission curves for the U_{2800}-band together with the Johnson-Cousins UBVRI-system.

magnitudes in the rest-frame B-band, the V-band observations were used. This makes the calculations the least sensitive to deviations between the assumed and the real SED since the observed V is close to rest frame B for the redshifts considered. For the same reason the apparent magnitudes in the U-band were used when calculating the absolute magnitudes in the rest-frame U_{2800}-band. To summarize, the two equations used were:

$$M_B = m_V - 5log_{10}\left(\frac{d_L(z)}{10pc}\right) - A - K_{BV}(z), \tag{5.11}$$

and

$$M_{U_{2800}} = m_U - 5log_{10}\left(\frac{d_L(z)}{10pc}\right) - A - K_{U_{2800}U}(z). \tag{5.12}$$

where M_B and $M_{U_{2800}}$ are the absolute magnitudes in the rest-frame bands B and U_{2800}, respectively, and m_V and m_U are the apparent magnitudes in the observed frame bands V and U, respectively. An upper limit of -23 was set on the galaxies absolute magnitudes to remove cluster galaxies with unrealistic magnitudes in the further calculations.

5.3 Estimating the volume and selection radius, R

Since the Schechter functions are given as densities, an estimate of the cluster volumes are needed. To be able to compare different LFs, it is also crucial to know the selection radius, R, of each galaxy cluster. The estimated volumes will here only be used as normalization factors when estimating the Schechter functions, and the accuracy of their sizes are therefore not of great importance. However, R needs an accurate estimate. When comparing LFs it is critical to make comparisons within the same selection radius, preferably relative to R_{200} for each cluster (Crawford et al. 2008). R_{200}, which approximates the virial radius in an Einstein-de Sitter univers, is defined to be the radius inside which the average density, $< \rho >$, is 200 times the critical density, ρ_c, at that particular redshift z:

$$200\rho_c(z) = \frac{M_{cluster}}{4/3\pi R_{200}^3} \tag{5.13}$$

A smaller selection radius, which only cover the central region of the cluster, may result in substantial differences in the shape of the LF (Crawford et al. 2008, Lobo et al. 1997, Popesso et al. 2006). This is most likely a result of environmental effects. R_{200} for the 35 galaxy clusters studied in this thesis are known from gravitational lensing mass measurements (Dahle 2006).

The selection radius is based on the size of the field observed. Since the final photometric catalogues consist of objects detected in the U-, V- and I-bands, and the sizes of these three images may differ, the field-size can not be decided using only one these images. Thus, the estimation of each field-size was based on the coordinates of the galaxies in the final photometric catalogue. The first step was to transform the angular size of each field, $\Delta\theta$, into a physical size, D. $\Delta\theta_x$ in the x-direction is the distance (in radians) between the object on the far left and the object on the far right of the image. In the y-direction, $\Delta\theta_y$ is the distance between the top and bottom objects. In a static, Euclidean geometry, a source of known, fixed size D at a large distance d ($d >> D$) covers an angle $\Delta\theta = D/d$ (in radians). The angular diameter distance out to an object is defined to preserve this relation in general case, thus:

$$d_A \equiv \frac{D}{\Delta\theta} \tag{5.14}$$

(S. Dodelson, 2003). The angular diameter distance can also be expressed as:

$$d_A = \frac{d_L}{(1+z)^2} \tag{5.15}$$

(ibid), which gives an equation for the real diameter of the field:

$$D = \frac{d_L}{(1+z)^2}\Delta\theta. \tag{5.16}$$

The parameters d_L, z and $\Delta\theta$ are all known. Since D_x and D_y are diameters, R was estimated in the following way:

$$R = \frac{D_x + D_y}{4}. \tag{5.17}$$

The galaxy clusters are located close to the center of each detection image. The estimated R is therefore assumed to be projected about the cluster-center. R/R_{200} then says something about the fraction of each cluster which is beeing studied. R and R/R_{200} for each cluster are listed in table 5.1. Notice how the R generally increases with increasing z.

Distances and areas

Cluster name	**z**	**d_L (Mpc)**	**d_A (Mpc)**	**Area (Mpc^2)**	**R (Mpc)**	**R/R_{200}**
A2204	0.15	717.84	542.79	0.83	0.46	0.22
RX J1720.1+2638	0.16	770.49	572.60	1.09	0.52	0.32
A586	0.17	823.69	601.72	1.10	0.52	0.17
A1914	0.17	823.69	601.72	1.24	0.56	0.29
A665	0.18	877.44	630.17	1.36	0.58	0.29
A115	0.20	986.57	685.12	1.61	0.63	0.34
A520	0.20	986.57	685.12	2.15	0.73	0.32
A963	0.21	1041.94	711.66	3.02	0.87	0.46
A1423	0.21	1041.94	711.66	1.76	0.66	0.30
A773	0.22	1097.82	737.59	2.97	0.86	0.37
A2261	0.22	1097.82	737.59	1.74	0.66	0.37
A267	0.23	1154.22	762.92	2.54	0.80	0.35
A1682	0.23	1154.22	762.92	2.01	0.71	0.43
A1763	0.23	1154.22	762.92	1.86	0.68	0.34
A2111	0.23	1154.22	762.92	1.99	0.71	0.42
A2219	0.23	1154.22	762.92	2.03	0.71	0.38
A2390	0.23	1154.22	762,92	1.85	0.68	0.30
Zw 5247	0.23	1154.22	762.92	1.97	0.70	0.52
RX J2129.6+0005	0.23	1154.22	762.92	1.97	0.70	0.40
RX J0439.0+0715	0.24	1211.14	787.68	2.10	0.73	0.35
Zw 2089	0.24	1211.14	787.68	2.04	0.71	0.46
A1835	0.25	1268.55	811.87	2.92	0.85	0.43
A68	0.26	1326.46	835.51	2.86	0.85	0.33
Zw 7160	0.26	1326.46	835.51	2.39	0.77	0.36
Zw 5768	0.27	1384.87	858.62	1.25	0.59	0.35
A697	0.28	1443.75	881.20	2.66	0.82	0.31
A1758N	0.28	1443.75	881.20	2.38	0.77	0.29
A2631	0.28	1443.75	881.20	2.62	0.81	0.49
A611	0.29	1503.11	903.26	2.69	0.82	0.49
RX J0437.1+0043	0.29	1503.11	903.26	2.76	0.83	0.55
Zw 3146	0.29	1503.11	903.26	2.78	0.83	0.42
Zw 7215	0.29	1503.11	903.26	2.79	0.83	0.43
A781	0.30	1562.95	924.82	2.91	0.85	0.41
A1576	0.30	1562.95	924.82	4.91	1.11	0.47
A2552	0.30	1562.95	924.82	2.96	0.86	0.58

Table 5.1: Distances out to each galaxy cluster, area of each field, selection radius R, and the fraction of R_{200} this radius represents. The clusters are listed according to their spectroscopic redshift, z, in increasing order. d_L is the luminosity distance and d_A is the angular diameter distance.

To approximate the volume of each cluster, the area of the field ($D_x \times D_y$) and cluster-depth were needed. $z_{cluster} \pm 0.1$ was consequently used as a realistic depth. The higher the redshift of the cluster, the greater this depth is in real size. The same applies to the size of the field since $\Delta\theta$ then covers a larger area. However, in this thesis the main focus is on the two parameters α and M^* from the Schechter function, with the primary scientific emphasis on α. A variation of the volume of each cluster because of the depth chosen, only changes the normalization parameter ϕ^*, which then again changes the value of $\phi(M)$. The two parameters α and M^* remains the same. The redshifts, distances (d_L and d_A), and area of fields (together with R and R/R_{200}) of the 35 galaxy clusters are listed in table 5.1.

5.4 Completeness limit

Before estimating the Schechter functions for each galaxy cluster, the completeness limits for the observations were needed. This limit decides the faintest magnitude to contribute in the estimation of the Schechter function. Here the completeness limit was chosen to be at the 50% detection completeness. The detection completeness, p, is a measure of the fraction of galaxies with a particular brightness, detected as sources. Thus, the 50% detection completeness is found at the magnitude where only half of the objects with this particular brightness are detected.

The detection completeness was found by following much of the same procedure as in Crawford et al. (2008). In this paper they first extract a sample of bright, representative objects of different sizes from each detection image. These objects are dimmed to a chosen brightness and shrunk to smaller sizes, before re-inserted into the image. The detection procedure is then repeated, and the fraction of these "new" objects detected is found.

To calculate the detection-completeness only galaxies identified as part of the RS were used. Since these are the reddest galaxies, and they are detected in all the three filters U, V and I, the detection-completeness is in practice based on the depth of the U-exposures. Thus, these were the detection images used in the calculations. The 5σ limiting magnitudes (mag_{lim}) in each of the three filters U, V and I have already been found (see table 2.1 in section 2.1). These are apparent magnitudes. The limiting magnitude in the U-band, U_{lim}, was used as a starting point for the faintest object detected. The detection completeness was found for 8 magnitude-bins of $\Delta U = 0.5$ between U_{lim} and (U_{lim}-4). This is a large magnitude-range, and brighter magnitude-bins were assumed to be 100% complete. The calculations were as follows:

- A representative sample of galaxies from the bright end of the red sequence was first picked out, together with a corresponding sample from the faint end. The relation between the median value of the full width at half maximum ($fwhm$) of the two was then found: $relation = fwhm_{faint}/fwhm_{bright}$. By using this relation, the objects from the bright end (which are mostly larger) were reduced to the sizes of the faint-end objects.

- The bright, reduced objects were dimmed to the magnitudes corresponding to each of the 8 magnitude-bins. Thus, the same objects were used 8 times, given 8 different magnitudes.

- For each half-magnitude interval, the objects were re-inserted randomly across the original U-image. The detection procedure was repeated, and the number of "new" objects detected as sources was found. The detection completeness for each of the 8 magnitude bins is given by the number of the new objects detected divided by the number of new objects inserted.

After finding the detection completeness for each of the 8 magnitude-bins down to the 5σ limiting magnitude, the next step was to find out which magnitude bin each galaxy in the full photometric catalogues belonged to. As mentioned before, these catalogues contain calibrated magnitudes in the U-, V- and I-bands. Which magnitude bin a galaxy belongs to depends on the deviation between the limiting magnitude in each of the three passbands and the galaxy's apparent magnitude in the same band, that is:
$U_{lim} - U$, $V_{lim} - V$ and $I_{lim} - I$.
The smallest of these three deviations decide which magnitude bin the galaxy belongs to and thus also its detection completeness. All of the galaxies with detection completeness $> 50\%$ were used when estimating the Schechter function parameters (see section 5.5).

5.5 Estimating the schechter function, $\phi(M)$

The only difference when estimating the Schechter function in the rest-frame B-band and the rest-frame U_{2800}-band, was the absolute magnitudes used. However, when estimating the RSLF, only RS-galaxies were used, of course.

The best fit to the parameters M^*, ϕ^* and α was found by using the χ^2 test for goodness of fit. This is given by

$$\chi^2 \equiv \sum_{i=1}^{n} \left[\frac{(n_i - n_{fit,i})^2}{\sigma_i^2} \right], \tag{5.18}$$

where n_i is the number density of galaxies (counts per Mpc^3) in magnitude-bin i, found by dividing the total galaxy-count in bin i (N_i) by the estimated volume of the cluster. $n_{fit,i}$ is the value of the fitted Schechter function in bin i (given by equation 5.1) and σ_i is the uncertainty in n_i. N_i was found by correcting the total *observed* galaxy-counts in bin i, $N_{obs,i}$, down to the 50% completeness limit. This was done by first dividing the galaxies into magnitude-bins of $\Delta M = 0.5$, where M is the absolute magnitude. The average detection completeness, $\bar{p}$, was found for each bin, and the observed galaxy-count in this particular bin was corrected by multiplying the observed count by $\frac{1}{\bar{p}}$. Thus:

$$N_i = N_{obs,i} \times \frac{1}{\bar{p}}. \tag{5.19}$$

The next step was to find the uncertainty in N_i. In general, most counts are distributed according to the Poisson distribution. The uncertainty in each count is then given by the square root of the count itself. However, this does not apply when there are incompleteness in the counts. The uncertainty in bin i is then given by:

$$\sigma_{N,i} = \sqrt{N_{obs}} \times \frac{1}{\bar{p}}. \tag{5.20}$$

Further, the standard deviation of the density n_i is given by:

$$\sigma_i = \frac{\sigma_{N,i}}{V_{cluster}}, \tag{5.21}$$

where $V_{cluster}$ is the estimated volume of each cluster. The best-fit Schechter function was found by varying the three free parameters M^*, ϕ^* and α to find the smallest reduced χ^2. The confidence in the results was found by calculating the uncertainty in each parameter. Gaussian statistics was assumed, which means that the standard deviation, σ, appears in the Gaussian probability density function:

$$p(x;\mu,\sigma) = \frac{1}{\sigma\sqrt{2\pi}} exp\left[-\frac{1}{2}\left(\frac{x-\mu}{\sigma}\right)^2\right]. \tag{5.22}$$

σ determines the width of the distribution, and the probability of an event falling within 1 and 2 standard deviations of the mean, μ, is about 68.3% and 95.4%, respectively. The 1-σ confidence limit for each parameter was found by looking at all combinations of the three parameters with $\Delta\chi^2 < 1$. That is, looking at the range of each parameter where χ^2 was less than 1 higher than the minimum χ^2-value. Table 5.2, 5.3 and 5.4 list the best fit values (ϕ^*, M^* and α) together with the 1-σ uncertainty in each parameter for the RSLF in the rest-frame B-band, the LF for all galaxy-types in the rest-frame B-band, and the LF for all galaxy-types in the rest-frame U_{2800}-band, respectively. The reduced χ^2-values showing how well the Schechter functions fits the observations, are listed in the fifth column in each table.

The reduced χ^2 statistic is simply the χ^2 divided by the number of degrees of freedom:

$$\chi^2_{red} = \frac{\chi^2}{\nu}. \tag{5.23}$$

The number of degrees of freedom, ν, is given by the number of magnitude intervals used when fitting the Schechter function, minus the number of fitted parameters (which in this case is three). The basis for the rule of thumb states that a "good fit" is achieved with a reduced χ^2-value of 1.0. A large χ^2-value indicates that the Schechter function is a poor fit.

Since α and M^* are the two parameters with the most physical significance, the joint confidence limits for these two with the third parameter, ϕ^*, optimized, were also of interest. The 1σ and 2σ confidence limits were found by drawing the contours corresponding to those values of $\Delta\chi^2$ for two degrees of freedom which includes 68.3% and 95.4% of the probability, respectively. χ^2-tables give that $\Delta\chi^2 = 2.30$ corresponds to the 1 standard deviation contour, and $\Delta\chi^2 = 6.14$ corresponds to the 2 standard deviation contour. The Schechter functions and contour-plots will be discussed in chapter 6.

Cluster name	ϕ^* (10^{-3} **Mpc^{-3}**)	$\mathbf{M^*}$	α	χ^2_ν
A2204	66.0^{+16}_{-16}	$-20.4^{+0.3}_{-0.3}$	$-0.84^{+0.10}_{-0.10}$	0.89
RX J1720.1+2638	73.0^{+15}_{-14}	$-20.0^{+0.2}_{-0.2}$	$-0.62^{+0.12}_{-0.12}$	0.85
A586	41.0^{+10}_{-8}	$-20.8^{+0.2}_{-0.2}$	$-1.04^{+0.06}_{-0.06}$	0.95
A1914	73.0^{+15}_{-12}	$-19.9^{+0.3}_{-0.2}$	$-0.70^{+0.10}_{-0.08}$	3.14
A665	54.0^{+14}_{-9}	$-20.2^{+0.2}_{-0.2}$	$-0.94^{+0.10}_{-0.06}$	1.30
A115	13.0^{+7}_{-5}	$-21.7^{+0.6}_{-0.7}$	$-1.20^{+0.10}_{-0.08}$	1.22
A520	36.0^{+10}_{-10}	$-20.4^{+0.3}_{-0.4}$	$-0.92^{+0.10}_{-0.10}$	1.67
A963	46.0^{+7}_{-7}	$-19.9^{+0.2}_{-0.2}$	$-0.24^{+0.24}_{-0.20}$	0.93
A1423	26.0^{+12}_{-10}	$-20.4^{+0.4}_{-0.6}$	$-1.02^{+0.16}_{-0.14}$	1.44
A773	50.0^{+7}_{-12}	$-20.2^{+0.1}_{-0.3}$	$-0.64^{+0.08}_{-0.14}$	2.33
A2261	91.0^{+15}_{-15}	$-19.8^{+0.2}_{-0.2}$	$-0.42^{+0.16}_{-0.14}$	3.41
A267	55.0^{+9}_{-12}	$-19.6^{+0.3}_{-0.3}$	$-0.32^{+0.22}_{-0.22}$	1.19
A1682	58.0^{+19}_{-15}	$-20.2^{+0.3}_{-0.3}$	$-0.76^{+0.20}_{-0.14}$	0.86
A1763	104.0^{+13}_{-18}	$-19.6^{+0.2}_{-0.2}$	$-0.42^{+0.14}_{-0.14}$	1.67
A2111	101.0^{+14}_{-19}	$-19.4^{+0.2}_{-0.3}$	$-0.18^{+0.20}_{-0.24}$	2.93
A2219	46.0^{+17}_{-12}	$-20.5^{+0.3}_{-0.3}$	$-1.04^{+0.12}_{-0.10}$	1.85
A2390	69.0^{+29}_{-27}	$-20.3^{+0.4}_{-0.4}$	$-0.78^{+0.30}_{-0.20}$	2.08
Zw 5247	37.0^{+12}_{-8}	$-20.4^{+0.3}_{-0.2}$	$-0.84^{+0.16}_{-0.10}$	1.10
RX J2129.6+0005	9.0^{+6}_{-4}	$-21.7^{+0.5}_{-0.6}$	$-1.34^{+0.12}_{-0.10}$	0.82
RX J0439.0+0715	45.0^{+25}_{-16}	$-20.0^{+0.5}_{-0.4}$	$-0.92^{+0.30}_{-0.22}$	2.34
Zw 2089	33.0^{+16}_{-12}	$-19.8^{+0.5}_{-0.6}$	$-0.74^{+0.30}_{-0.22}$	1.24
A1835	31.0^{+15}_{-12}	$-20.8^{+0.5}_{-0.6}$	$-0.98^{+0.22}_{-0.16}$	0.98
A68	26.0^{+9}_{-7}	$-20.9^{+0.3}_{-0.3}$	$-0.82^{+0.20}_{-0.18}$	1.49
Zw 7160	29.0^{+10}_{-11}	$-20.5^{+0.3}_{-0.5}$	$-0.76^{+0.20}_{-0.22}$	1.19
Zw 5768	29.0^{+10}_{-13}	$-20.9^{+0.6}_{-1.0}$	$-0.32^{+0.56}_{-0.44}$	0.43
A697	45.0^{+26}_{-17}	$-20.4^{+0.4}_{-0.5}$	$-0.98^{+0.20}_{-0.16}$	1.85
A1758N	87.0^{+16}_{-22}	$-19.9^{+0.2}_{-0.3}$	$-0.66^{+0.14}_{-0.20}$	0.55
A2631	80.0^{+10}_{-14}	$-19.6^{+0.2}_{-0.2}$	$-0.32^{+0.22}_{-0.20}$	0.89
A611	7.0^{+24}_{-4}	$-22.0^{+1.4}_{-1.0}$	$-1.50^{+0.42}_{-0.14}$	1.10
RX J0437.1+0043	66.0^{+13}_{-13}	$-19.9^{+0.4}_{-0.3}$	$-0.28^{+0.42}_{-0.26}$	1.12
Zw 3146	9.0^{+9}_{-5}	$-22.0^{+0.8}_{-1.0}$	$-1.42^{+0.16}_{-0.12}$	0.60
Zw 7215	96.0^{+11}_{-16}	$-19.4^{+0.2}_{-0.2}$	$-0.22^{+0.26}_{-0.26}$	1.23
A781	66.0^{+17}_{-17}	$-20.3^{+0.3}_{-0.3}$	$-0.62^{+0.24}_{-0.20}$	0.80
A1576	51.0^{+6}_{-7}	$-19.8^{+0.2}_{-0.2}$	$-0.18^{+0.28}_{-0.20}$	1.82
A2552	92.0^{+13}_{-17}	$-19.6^{+0.3}_{-0.3}$	$-0.18^{+0.40}_{-0.34}$	1.13

Table 5.2: The best-fitting Schechter function parameters for the *red sequence* (RS) in the B-band. The 1-σ uncertainty in each parameter is also given with the best-fit values.

Cluster name	ϕ^* **(10^{-3} Mpc^{-3})**	**M***	α	χ^2_ν
A2204	171^{+17}_{-20}	$-19.9^{+0.2}_{-0.1}$	$-0.64^{+0.08}_{-0.06}$	1.88
RX J1720.1+2638	86^{+22}_{-17}	$-20.3^{+0.3}_{-0.3}$	$-0.84^{+0.10}_{-0.08}$	3.08
A586	42^{+10}_{-11}	$-21.6^{+0.3}_{-0.5}$	$-1.16^{+0.04}_{-0.04}$	2.48
A1914	139^{+15}_{-14}	$-19.9^{+0.1}_{-0.1}$	$-0.64^{+0.04}_{-0.04}$	3.13
A665	114^{+18}_{-14}	$-20.2^{+0.2}_{-0.1}$	$-0.78^{+0.06}_{-0.06}$	3.40
A115	44^{+11}_{-8}	$-21.0^{+0.3}_{-0.3}$	$-1.06^{+0.06}_{-0.04}$	1.74
A520	88^{+11}_{-12}	$-20.3^{+0.2}_{-0.2}$	$-0.70^{+0.06}_{-0.06}$	4.59
A963	75^{+15}_{-12}	$-20.3^{+0.2}_{-0.2}$	$-0.68^{+0.14}_{-0.12}$	1.76
A1423	80^{+12}_{-12}	$-19.8^{+0.1}_{-0.2}$	$-0.82^{+0.06}_{-0.06}$	2.58
A773	91^{+11}_{-8}	$-20.3^{+0.1}_{-0.1}$	$-0.62^{+0.06}_{-0.04}$	5.15
A2261	129^{+15}_{-21}	$-20.3^{+0.2}_{-0.2}$	$-0.78^{+0.10}_{-0.10}$	4.13
A267	99^{+10}_{-15}	$-19.9^{+0.1}_{-0.2}$	$-0.54^{+0.06}_{-0.10}$	2.29
A1682	159^{+15}_{-18}	$-19.7^{+0.1}_{-0.2}$	$-0.44^{+0.06}_{-0.08}$	2.18
A1763	214^{+22}_{-16}	$-19.5^{+0.1}_{-0.1}$	$-0.36^{+0.08}_{-0.06}$	3.27
A2111	223^{+11}_{-15}	$-18.8^{+0.1}_{-0.1}$	$+0.18^{+0.12}_{-0.12}$	5.80
A2219	150^{+19}_{-18}	$-20.0^{+0.1}_{-0.1}$	$-0.72^{+0.06}_{-0.06}$	2.63
A2390	237^{+14}_{-15}	$-19.4^{+0.1}_{-0.1}$	$+0.04^{+0.10}_{-0.10}$	3.07
Zw 5247	97^{+10}_{-14}	$-20.1^{+0.1}_{-0.2}$	$-0.60^{+0.06}_{-0.08}$	2.99
RX J2129.5+0005	63^{+16}_{-10}	$-20.5^{+0.3}_{-0.2}$	$-0.84^{+0.10}_{-0.06}$	3.37
RX J0439.0+0715	184^{+17}_{-14}	$-19.0^{+0.2}_{-0.1}$	$-0.04^{+0.20}_{-0.12}$	2.98
Zw 2089	69^{+13}_{-16}	$-19.9^{+0.2}_{-0.3}$	$-0.72^{+0.10}_{-0.12}$	1.24
A1835	139^{+17}_{-11}	$-19.8^{+0.2}_{-0.1}$	$-0.40^{+0.10}_{-0.04}$	3.14
A68	35^{+7}_{-7}	$-20.7^{+0.2}_{-0.3}$	$-0.68^{+0.12}_{-0.12}$	2.37
Zw 7160	92^{+13}_{-10}	$-19.9^{+0.2}_{-0.1}$	$-0.42^{+0.12}_{-0.08}$	2.49
Zw 5768	13^{+6}_{-3}	$-22.9^{+0.8}_{-0.1}$	$-1.10^{+0.08}_{-0.06}$	1.52
A697	79^{+20}_{-25}	$-20.6^{+0.2}_{-0.4}$	$-1.10^{+0.08}_{-0.12}$	2.46
A1758N	213^{+21}_{-20}	$-19.8^{+0.1}_{-0.1}$	$-0.50^{+0.06}_{-0.06}$	2.60
A2631	177^{+10}_{-14}	$-19.5^{+0.0}_{-0.1}$	$-0.18^{+0.04}_{-0.08}$	1.75
A611	176^{+8}_{-18}	$-19.5^{+0.0}_{-0.1}$	$-0.20^{+0.04}_{-0.10}$	4.74
RX J0437.1+0043	168^{+9}_{-9}	$-19.3^{+0.2}_{-0.1}$	$+0.34^{+0.22}_{-0.14}$	1.74
Zw 3146	171^{+11}_{-14}	$-19.4^{+0.1}_{-0.1}$	$-0.12^{+0.06}_{-0.06}$	5.30
Zw 7215	179^{+20}_{-12}	$-19.5^{+0.1}_{-0.1}$	$-0.32^{+0.10}_{-0.06}$	4.04
A781	172^{+13}_{-16}	$-20.0^{+0.1}_{-0.1}$	$-0.40^{+0.06}_{-0.06}$	2.73
A1576	104^{+10}_{-9}	$-20.1^{+0.1}_{-0.1}$	$-0.36^{+0.08}_{-0.06}$	3.50
A2552	204^{+10}_{-10}	$-19.2^{+0.1}_{-0.1}$	$+0.30^{+0.14}_{-0.10}$	2.66

Table 5.3: The best-fitting Schechter function parameters for all of the galaxy-types in the B-band. The 1-σ uncertainty in each parameter is also given with the best-fit values.

Cluster name	ϕ^* **(10^{-3} Mpc^{-3})**	$\mathbf{M^*}$	α	χ^2_ν
A2204	215^{+33}_{-23}	$-18.7^{+0.2}_{-0.1}$	$-0.48^{+0.12}_{-0.08}$	3.25
RX J1720.1+2638	133^{+29}_{-27}	$-18.7^{+0.2}_{-0.3}$	$-0.68^{+0.12}_{-0.12}$	2.31
A586	14^{+5}_{-5}	$-22.4^{+0.7}_{-0.6}$	$-1.32^{+0.02}_{-0.04}$	2.14
A1914	72^{+13}_{-17}	$-19.2^{+0.1}_{-0.2}$	$-1.14^{+0.06}_{-0.08}$	2.27
A665	157^{+21}_{-26}	$-18.5^{+0.1}_{-0.2}$	$-0.64^{+0.08}_{-0.10}$	3.04
A115	83^{+20}_{-14}	$-19.0^{+0.2}_{-0.2}$	$-0.94^{+0.10}_{-0.06}$	2.62
A520	48^{+12}_{-13}	$-19.9^{+0.2}_{-0.4}$	$-1.06^{+0.08}_{-0.08}$	1.84
A963	106^{+7}_{-12}	$-18.5^{+0.1}_{-0.2}$	$-0.08^{+0.06}_{-0.14}$	2.63
A1423	219^{+23}_{-24}	$-17.4^{+0.2}_{-0.2}$	$-0.12^{+0.22}_{-0.18}$	3.59
A773	76^{+12}_{-13}	$-19.3^{+0.2}_{-0.2}$	$-0.84^{+0.06}_{-0.08}$	2.29
A2261	52^{+28}_{-21}	$-20.2^{+0.4}_{-0.5}$	$-1.28^{+0.14}_{-0.12}$	1.86
A267	104^{+20}_{-17}	$-18.8^{+0.2}_{-0.2}$	$-0.68^{+0.12}_{-0.12}$	2.43
A1682	164^{+27}_{-27}	$-18.6^{+0.2}_{-0.2}$	$-0.66^{+0.12}_{-0.10}$	2.38
A1763	177^{+38}_{-48}	$-18.3^{+0.2}_{-0.4}$	$-0.66^{+0.16}_{-0.18}$	4.62
A2111	64^{+37}_{-17}	$-19.8^{+0.5}_{-0.3}$	$-1.14^{+0.16}_{-0.10}$	4.42
A2219	163^{+22}_{-32}	$-18.6^{+0.1}_{-0.2}$	$-0.76^{+0.08}_{-0.12}$	2.25
A2390	216^{+39}_{-36}	$-18.7^{+0.2}_{-0.2}$	$-0.54^{+0.18}_{-0.16}$	2.83
Zw 5247	90^{+15}_{-20}	$-19.2^{+0.1}_{-0.3}$	$-0.80^{+0.10}_{-0.12}$	2.14
RX J2129.6+0005	49^{+14}_{-15}	$-19.9^{+0.3}_{-0.4}$	$-1.02^{+0.10}_{-0.12}$	3.18
RX J0439.0+0715	53^{+31}_{-21}	$-19.3^{+0.4}_{-0.4}$	$-1.26^{+0.18}_{-0.16}$	1.94
Zw 2089	57^{+18}_{-16}	$-19.4^{+0.3}_{-0.4}$	$-0.94^{+0.12}_{-0.12}$	2.11
A1835	55^{+18}_{-9}	$-19.7^{+0.2}_{-0.1}$	$-1.26^{+0.12}_{-0.06}$	1.55
A68	42^{+22}_{-22}	$-20.0^{+0.4}_{-0.6}$	$-1.14^{+0.24}_{-0.28}$	2.55
Zw 7160	20^{+31}_{-18}	$-20.4^{+0.9}_{-2.6}$	$-1.38^{+0.30}_{-0.30}$	2.33
Zw 5768	1^{+2}_{-0}	$-23.0^{+1.2}_{-0.0}$	$-1.72^{+0.08}_{-0.12}$	4.73
A697	188^{+26}_{-22}	$-18.6^{+0.1}_{-0.1}$	$-0.68^{+0.12}_{-0.10}$	3.38
A1758N	127^{+35}_{-33}	$-19.1^{+0.2}_{-0.3}$	$-1.04^{+0.12}_{-0.12}$	2.43
A2631	207^{+24}_{-36}	$-18.2^{+0.1}_{-0.2}$	$-0.50^{+0.16}_{-0.22}$	3.26
A611	3^{+2}_{-1}	$-22.5^{+0.5}_{-0.5}$	$-1.78^{+0.04}_{-0.06}$	2.17
RX J0437.1+0043	143^{+20}_{-27}	$-19.0^{+0.1}_{-0.2}$	$-0.68^{+0.16}_{-0.18}$	2.14
Zw 3146	3^{+2}_{-1}	$-22.6^{+0.6}_{-0.4}$	$-1.72^{+0.04}_{-0.04}$	1.80
Zw 7215	163^{+46}_{-63}	$-18.7^{+0.2}_{-0.4}$	$-1.04^{+0.18}_{-0.24}$	2.51
A781	227^{+22}_{-33}	$-18.7^{+0.1}_{-0.2}$	$-0.46^{+0.14}_{-0.18}$	3.11
A1576	36^{+22}_{-16}	$-20.0^{+0.4}_{-0.5}$	$-1.36^{+0.18}_{-0.16}$	2.86
A2552	32^{+24}_{-19}	$-20.2^{+0.4}_{-0.6}$	$-1.66^{+0.18}_{-0.20}$	1.22

Table 5.4: The best-fitting Schechter function parameters for all of the galaxy-types in the U_{2800}-band. The 1-σ uncertainty in each parameter is also given with the best-fit values.

5.6 Estimating the star forming activity

In section 1.7, three different methods of how to detect a star forming region were described. For reasons given in 1.7, the UV continuum will be used to estimate the star formation rate (SFR) for each galaxy, following a procedure similar to Dahlen et al. (2006). In addition, the fraction of star forming galaxies, F_{SF}, in each cluster will be found.

Dahlen et al. (2006) derived a conversion factor k_ν relating the UV luminosity and the ongoing star formation by using results from stellar synthesis codes and assumptions on the past star formation history (PSFH). k_ν was calculated based on two different assumptions on the PSFH; one that assumes a constant SFR(z), and one that assumes an evolving SFR(z). They found that k_ν varies by as much as 30% at 2800 Å, depending on the assumptions on the PSFH. The evolving SFR(z) model is taken from Strolger et al. (2004), who assumed that SFR(t) evolves as

$$\mathrm{SFR}(t) = a(t^b e^{-t/c} + de^{d(t-t_0)/c}), \tag{5.24}$$

where t is the age of the Universe (in Gyr) and $t_0 = 13.47$ Gyr. By fitting the measurements of SFR(z) from several surveys presented in Giavalisco et al. (2004), Strolger et al. (2004) calculated the coefficients to be $a = 0.021$, $b = 2.21$, $c = 1.69$, and $d = 0.207$. In the redshift interval of interest in this thesis ($z \in [0.15, 0.30]$), SFR(z) is an evolving function of redshift (Madau et al. 1996; Springel and Hernquist 2003). Thus, the model from Strolger et al. (2004) is used for the PSFH in this thesis. In addition to the PSFH, Dahlen et al. (2006) used GALEXEV stellar population synthesis models as input, which provide the age-luminosity evolution for a simple stellar population (SSP) at different UV luminosities. For these models they assumed solar metallicity and two different initial mass functions (IMFs); a standard Salpeter IMF (Salpeter 1955) and a Chabrier IMF (Chabrier 2003).[1] In this thesis, the conversion factor used is based on the Salpeter IMF. Finally, by using the PSFH and synthesis models, Dahlen et al. (2006) derived an expression for the conversion factor:

$$k_\nu(t) = \int_{t_{z6}}^{t} \mathrm{SFR}(t') l_\nu(t - t') dt' / \mathrm{SFR}(t), \tag{5.25}$$

where l_ν is the flux at time t' after an istantaneous burst of the SSP, and t_{z6} is the age of the Universe at $z = 6$. The relation between the SFR, the UV

[1] The IMF specifies the distribution in mass of a newly formed stellar population and it is frequently assumed to be a simple power law: $\zeta(M) \propto M^{-\alpha}$, where M is the mass and α is a dimensionless exponent. The Salpeter IMF has $\alpha = 2.35$ in the mass range $M \in [0.1M_\odot, 125M_\odot]$

luminosity, L_ν, and the conversion factor is then given by:

$$L_\nu = k_\nu \frac{\mathrm{SFR}}{M_\odot\ \mathrm{yr}^{-1}} \mathrm{ergs\,s^{-1}\,Hz^{-1}}. \tag{5.26}$$

The procedure when finding the SFR and F_{SF} was as follows:

- Find the conversion factor at 2800 Å for the redshift interval $z \in [0.15, 0.30]$.
- Convert the absolute magnitudes in the rest-frame band U_{2800} to luminosities L_{2800}.
- Estimate the SFR for each cluster galaxy.
- Calculate the F_{SF} for each of the 35 galaxy clusters.

Finding k_{2800}: Fig. 5 in Dahlen et al. (2006) shows the relation between k_{2800} and redshift. As mentioned above, k_{2800} is based on an evolving SFR(z) and the standard Salpeter IMF. In the redshift interval $z \in [0.15, 0.30]$, k_{2800} is nearly constant and has a value $\approx 7.22 \times 10^{27}$. This is the value adopted in this thesis.

Converting M_{2800} to L_{2800}, and calculating SFR: There is a direct relation between an astronomical object's absolute magnitude, M, and its luminosity, L, in a given bandpass

$$\frac{L_\lambda}{L_{\odot,\lambda}} = 10^{0.4(M_{\odot,\lambda} - M_\lambda)} \tag{5.27}$$

Here $L_{\odot,\lambda}$ and $M_{\odot,\lambda}$ are the luminosity and absolute magnitude of the Sun, respectively, while L_λ and M_λ are the luminosity and absolute magnitude of the galaxy. The luminosities are given in units of W nm^{-1}. The bandpass of interest when calculating the SFR is U_{2800} here. The absolute magnitudes, M_{2800}, are known from section 5.2, and $M_{\odot,2800} = 6.76$ (Willmer 2005). Thuillier et al. (1997) provide values of the UV solar spectral irradiance, S_λ, between 200 and 300 nm, where S_λ is given in units of mW m^{-2} nm^{-1}. At $\lambda = 279.89$ nm, $S = 78.62$ mW m^{-2} nm^{-1}, and at $\lambda = 280.22$ nm, $S = 81.59$ mW m^{-2} nm^{-1}. In this thesis an approximate value of $S \approx 80$ mW m^{-2} nm^{-1} was used for $\lambda = 280$ nm. In units of angstroms (which is the wavelength unit used throughout this thesis), $S \approx 8.0$ mW m^{-2} $\mathring{\mathrm{A}}^{-1}$ for $\lambda = 2800$ Å. The solar irradiance is measured on the outer surface of Earth's atmosphere, which roughly has a mean distance of 1AU from the Sun. Thus,

$$L_{\odot,2800} = S_{2800} \times 4\pi r^2, \tag{5.28}$$

where $r = 1\mathrm{AU} = 1.4959787066 \times 10^{11}\mathrm{m}$. Equation 5.27 then provided the the luminosity L_{2800} for each cluster galaxy.

Estimating the SFR for each cluster galaxy: Before using equation 5.26 to calculate the SFR of each galaxy, the luminosities were converted into units ergs s^{-1} Hz^{-1}, where 1 erg= 10^{-7} J. This was done by using the relations $\lambda L_\lambda = \nu L_\nu$, and $\lambda\nu = c$, where ν is the frequency corresponding to λ, and c is the speed of light in vacuum. The biggest uncertainty when using the UV continuum to calculate the SFR, is dust extinction, as newly formed stars which are completely hidden by dust would not contribute to the UV luminosity. Dahlen et al. (2006) estimated the SFR using luminosities from two different rest-frame wavelengths; $\lambda = 1500$ Å and $\lambda = 2800$ Å. They found that the SFR derived from the 2800 Å luminosity was a factor of ~ 1.7 higher compared to the SFR derived from the 1500 Å luminosity. The fact that extinction is more severe at shorter wavelengths, can explain much of the difference. By comparing the two SFR estimations, Dahlen et al. (2006) were able to derive a mean correction factor for dust extinction. At 2800 Å they found that the extinction-corrected SFR was a factor of ~ 3.7 higher than the uncorrected SFR. Similar result were also found by Gallazzi et al. (2009) who explored the amount of obscured star formation as a function of environment. Thus, an extinction-correction factor of 3.7 was applied to the calculated SFRs in this thesis.

Estimating the fraction of star forming galaxies, F_{SF}, in each cluster: To compare the star forming activity between the 35 galaxy clusters, the fraction of star forming galaxies, F_{SF}, was calculated. This was done by classifying the galaxies in each cluster into quiescent and star forming (SF) galaxies. The treshold in SFR was set to $0.6 M_\odot\,yr^{-1}$ based on the observed distribution of SFR amongst the galaxies in each cluster. The main result is not the value of F_{SF} for each individual galaxy cluster, but the relative value compared to the other clusters studied in this thesis. Thus, with a limit of $0.6 M_\odot\,yr^{-1}$ separating the two galaxy classifications, the fraction of star forming galaxies is given by

$$F_{SF} = \frac{N(SFR > 0.6 M_\odot\,yr^{-1})}{N_{TOT}}, \tag{5.29}$$

where $N(SFR > 0.6 M_\odot\,yr^{-1})$ is the number of galaxies with a SFR$> 0.6 M_\odot\,yr^{-1}$, and N_{TOT} is the total number of galaxies used in the F_{SF} estimation for each galaxy cluster. A lower limit on the absolute magnitude in the U_{2800}-band was also imposed, since faint galaxies are more likely to be detected in clusters at lower redshifts. A lower limit was found by looking at the faintest absolute magnitude for the clusters at $z = 0.3$, and it turned out to be $M_{2800} = -15.09$. However, applying this lower magnitude limit

did not change the final F_{SF} estimates. The error of F_{SF} is given by

$$S_{F_{SF}} = \sqrt{\left(\frac{\partial F_{SF}}{\partial N_{SF}}\sqrt{N_{SF}}\right)^2 + \left(\frac{\partial F_{SF}}{\partial N_{TOT}}\sqrt{N_{TOT}}\right)^2}, \qquad (5.30)$$

where $N_{SF} = N(SFR > 0.6\mathrm{M}_{\odot})$ is the number of star forming galaxies in each cluster.

Measurements of the dynamical state of each cluster; centroid shifts: In this thesis, previous measurements of the *centroid shift* of each galaxy cluster (Ben Maughan, private communication) have been used to classify the galaxy clusters into two groups: *relaxed* or *unrelaxed*, or in other words, in dynamical equilibrium or in dynamical disequilibrium. The centroid shift is in principle the displacement of a system's core from the centre of the system, and it can be found by using the distribution of X-ray luminous gas. The centroid shift provides an excellent indicator of how far the system is from virial and hydrostatic equilibrium (Poole et al. 2006). The centroid shift measurements used in this thesis were found following the method of Poole et al. (2006). The centroid of the cluster X-ray emission was determined in a series of circular apertures centered on the cluster X-ray peak. The radii of the apertures were decreased in steps of 5% from R_{500} to $0.05\mathrm{R}_{500}$, where R_{500} is defined to be the radius inside which the average density, $< \rho >$, is 500 times the critical density, ρ_c, at that particular redshift z:

$$500\rho_c(z) = \frac{M_{cluster}}{4/3\pi R_{500}^3}. \qquad (5.31)$$

The centroid shift was defined as the standard deviation of the projected separations between the peak and centroid in units of R_{500}. To increase the sensitivity of this statistic to faint structure, the central 30 kpc was excluded for the centroid (but not the X-ray peak) measurements. Figure 5.2 show the 35 X-ray images used to calculate the centroid shifts used in this thesis. One can clearly see how the clusters go from smooth and round in the upper left corner, to a more disorganized appearance towards the lower right corner. The first six rows contain images of the clusters classified as relaxed, while the last three rows contain images of the clusters classified as unrelaxed. The classification between relaxed and unrelaxed will be done in the next chapter (subsection 6.1.4).

The centroid shift with corresponding error, the total SFR for each cluster, and the F_{SF} with corresponding error are listed in table 5.5. These results will be discussed in the next chapter.

Cluster name	**z**	$\mathbf{M_{200}}$ $(\mathbf{10^{14}\,h^{-1}\ M_\odot})$	**Centroid shift** $(\mathbf{10^{-3}\ R_{500}^{-1}})$	**Total SFR** $(\mathbf{M_\odot\ yr^{-1}})$	$\mathbf{F_{SF}}$
A2204	0.15	$8.06^{+5.40}_{-4.62}$	2.00 ± 0.08	234.8	0.179 ± 0.024
RX J1720.1+2638	0.16	$4.49^{+3.48}_{-3.01}$	3.30 ± 0.19	276.2	0.110 ± 0.017
A586	0.17	$25.85^{+8.17}_{-8.97}$	3.00 ± 1.44	320.7	0.131 ± 0.017
A1914	0.17	$6.92^{+4.46}_{-4.03}$	21.60 ± 1.61	164.9	0.086 ± 0.014
A665	0.18	$7.97^{+4.8}_{-3.64}$	40.10 ± 4.08	171.9	0.066 ± 0.011
A115	0.20	$5.79^{+4.20}_{-3.79}$	67.70 ± 0.79	185.0	0.094 ± 0.014
A520	0.20	$12.56^{+4.87}_{-3.77}$	66.10 ± 3.47	253.7	0.139 ± 0.017
A963	0.21	$6.42^{+6.19}_{-5.02}$	7.40 ± 0.85	181.0	0.219 ± 0.027
A1423	0.21	$11.35^{+5.17}_{-6.26}$	8.30 ± 2.41	104.0	0.055 ± 0.010
A773	0.22	$11.62^{+5.63}_{-4.72}$	10.70 ± 3.32	200.7	0.112 ± 0.014
A2261	0.22	$5.96^{+3.43}_{-3.47}$	9.20 ± 0.89	313.8	0.189 ± 0.021
A267	0.23	$11.34^{+4.51}_{-3.89}$	22.00 ± 7.10	236.9	0.109 ± 0.014
A1682	0.23	$4.21^{+2.77}_{-2.85}$	13.00 ± 4.42	168.9	0.085 ± 0.012
A1763	0.23	$8.02^{+3.84}_{-3.90}$	8.30 ± 7.09	174.5	0.087 ± 0.013
A2111	0.23	$4.69^{+2.88}_{-2.61}$	34.70 ± 17.10	228.1	0.119 ± 0.015
A2219	0.23	$6.28^{+5.04}_{-3.53}$	12.50 ± 6.28	219.4	0.091 ± 0.012
A2390	0.23	$11.53^{+5.08}_{-5.09}$	3.7 ± 0.30	276.9	0.183 ± 0.021
Zw 5247	0.23	$2.43^{+2.09}_{-1.92}$	50.50 ± 12.02	241.0	0.126 ± 0.016
RX J2129.6+0005	0.23	$5.75^{+4.36}_{-3.52}$	3.90 ± 1.26	290.6	0.189 ± 0.025
RX J0439.0+0715	0.24	$9.65^{+4.93}_{-4.88}$	14.70 ± 3.30	217.5	0.104 ± 0.016
Zw 2089	0.24	$3.51^{+3.09}_{-2.79}$	2.40 ± 0.87	134.3	0.135 ± 0.021
A1835	0.25	$8.07^{+4.48}_{-4.04}$	4.70 ± 0.19	277.7	0.133 ± 0.014
A68	0.26	$16.42^{+9.33}_{-7.99}$	10.90 ± 4.58	238.7	0.213 ± 0.025
Zw 7160	0.26	$9.79^{+4.84}_{-4.25}$	6.10 ± 1.13	279.0	0.119 ± 0.016
Zw 5768	0.27	$4.64^{+3.90}_{-3.22}$	52.80 ± 16.00	63.0	0.248 ± 0.044
A697	0.28	$19.64^{+6.93}_{-7.21}$	6.10 ± 6.01	262.9	0.122 ± 0.015
A1758N	0.28	$20.24^{+7.32}_{-6.85}$	61.20 ± 13.01	220.4	0.096 ± 0.012
A2631	0.28	$4.69^{+3.26}_{-3.14}$	11.50 ± 6.53	202.2	0.096 ± 0.013
A611	0.29	$5.00^{+2.85}_{-3.82}$	4.80 ± 0.95	283.9	0.145 ± 0.017
RX J0437.1+0043	0.29	$3.60^{+2.62}_{-2.50}$	3.30 ± 1.47	316.6	0.197 ± 0.022
Zw 3146	0.29	$8.60^{+3.96}_{-4.18}$	10.80 ± 1.10	315.5	0.144 ± 0.017
Zw 7215	0.29	$8.05^{+4.52}_{-4.47}$	12.20 ± 5.40	219.2	0.106 ± 0.013
A781	0.30	$9.63^{+4.66}_{-4.11}$	61.00 ± 18.31	346.2	0.183 ± 0.017
A1576	0.30	$13.95^{+4.54}_{-4.43}$	25.60 ± 8.13	336.7	0.136 ± 0.014
A2552	0.30	$3.56^{+3.19}_{-2.57}$	10.00 ± 3.56	244.7	0.117 ± 0.014

Table 5.5: The centroid shift with corresponding error, the total SFR for each cluster, and the F_{SF} with corresponding error. The clusters are listed in order of increasing redshift, z.

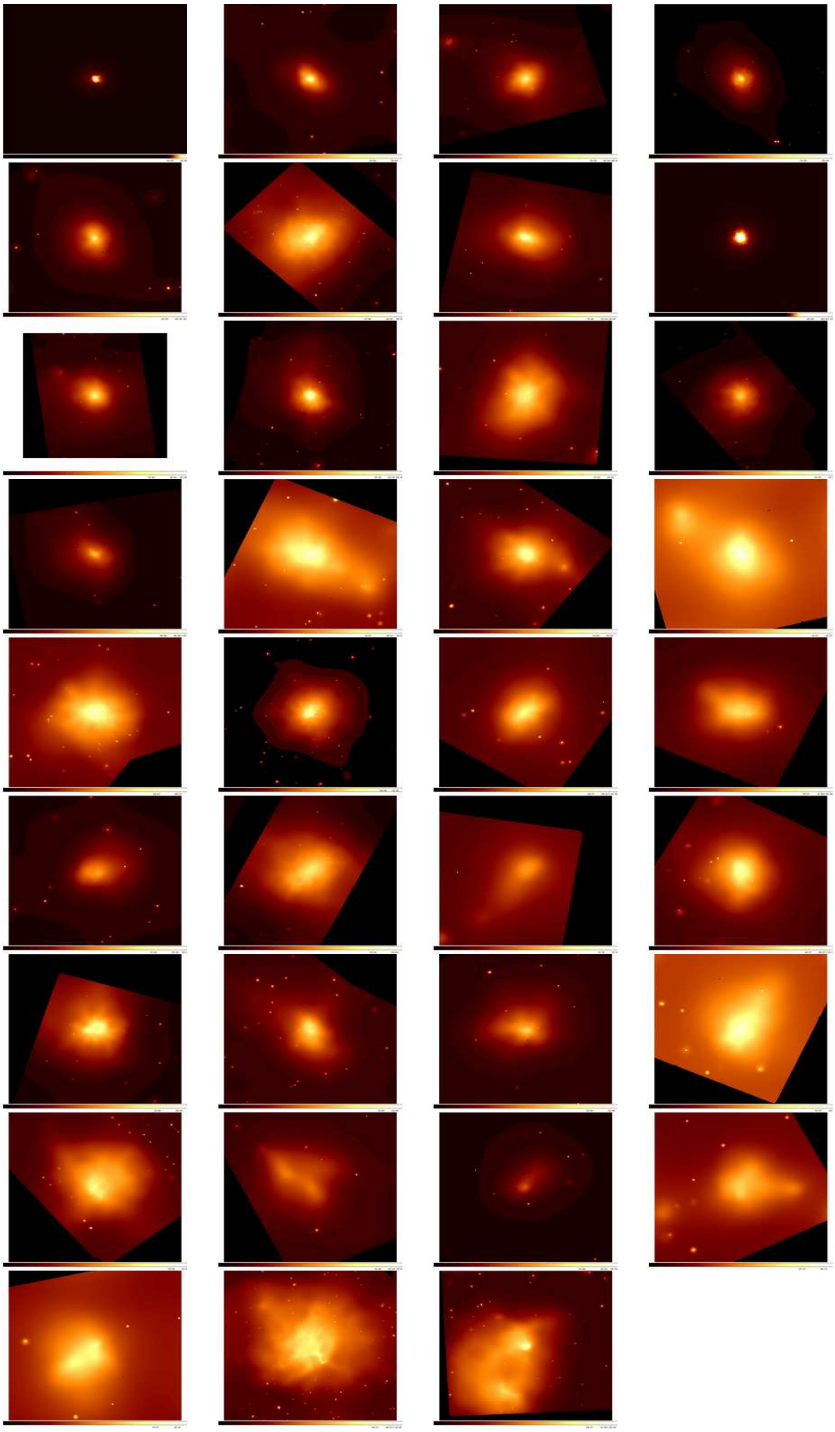

Figure 5.2: X-ray images of the 35 galaxy clusters in order of increasing centroid shift (from left to right) from the *Chandra X-ray Observatory*. The first six rows contain images of the clusters classified as relaxed, while the last three rows contain images of the clusters classified as unrelaxed (see subsection 6.1.4 for classification).

Chapter 6

Results and discussion

Based on the photometric calibration of images in the U-, V, and I-bands (chapter 3), the photometric redshift of each galaxy was estimated, and the cluster members were separated from the foreground and background galaxies (chapter 4). Based on the calibrated photometry, three different luminosity functions (LFs) were calculated for each galaxy cluster (chapter 5). In addition, calibrated luminosities in the UV were used to calculate the star formation rate (SFR) in the cluster galaxies (chapter 5). This chapter presents the main results of this thesis, and it is structured as follows:

- Study the three LFs: the red-sequence LF (RSLF) in the rest-frame B-band, the LF in the rest-frame B-band for all galaxy types, and the LF based on the rest-frame wavelength $\lambda \approx 2800$ Å for all galaxy types. In particular, the RSLF in the rest-frame B-band will be compared with the results from Crawford et al. (2008) who studied the evolution of the faint-end slope with redshift for RSLFs in the rest-frame B-band. In this thesis the primary scientific emphasis is on the parameter α from the fitted Schechter function. α characterizes the faint-end slope of the LF, and is a measure of the relative number of faint to bright galaxies.

- Study the correlation between star formation and the dynamical state of the 35 galaxy clusters. The star formation activity in each cluster is described by the parameter F_{SF} (fraction of star forming galaxies), calculated in section 5.6.

- Discuss the possible physical mechanisms responsible for the observed distribution of star formation rates (SFRs) and relative numbers of faint dwarf galaxies in the galaxy clusters. The three mechanisms that will be discussed were introduced in section 5, and are: ram-pressure stripping, galaxy encounters and galaxy starvation.

6.1 Luminosity function

In chapter 5 three different luminosity functions (LFs) were derived for each galaxy cluster: the red-sequence LF (RSLF) in the rest-frame B-band, the LF in the rest-frame B-band for all galaxy types, and the LF for all galaxy-types based on the rest-frame wavelength $\lambda \approx 2800$ Å. The results are listed in table 5.2, 5.3 and 5.4, respectively. In this section the three LFs will be discussed one by one, starting with the RSLF in the rest-frame B-band, and ending with the LF for all galaxy-types based on the rest-frame wavelength $\lambda \approx 2800$ Å. Since different galaxy-types radiates at different wavelengths, variations are expected between the LFs in different rest-frame bands. The RSLF is also expected to differ from the LF for all morphological types in the same rest-frame band, based on the fact that different morphological types have different specific LFs (see figure 1.3 in section 1.6).

6.1.1 RSLF in the rest-frame B-band

In this subsection the results of the RSLF measurements will be discussed. Further, these results will be compared with measurements found by Crawford et al. (2008) to see if there is an evolution of the RSLF with redshift. Crawford et al. (2008) measured the rest-frame B-band luminosity function of five intermediate-redshift ($0.5 < z < 0.9$), high-mass ($\sigma_v > 950$ km s^{-1}) clusters, where σ_v is the velocity dispersion. The masses of these intermediate-redshift clusters are comparable to the masses of the 35 galaxy clusters studied in this thesis. Crawford et al. (2008) studied the evolution of the faint-end slope by comparing the results at intermediate redshifts with the LFs of 59 low-redshift ($0.035 < z < 0.144$) clusters from Sloan Digital Sky Survey (SDSS), but little evidence was found for such an evolution. With a selection radius of R_{200}, they found an average $\alpha = -0.84 \pm 0.32$ and $M^* = -20.55 \pm 0.56$ for their intermediate-redshift sample. Previous studies have found a deficit of RS galaxies at low luminosities in high-redshift clusters (Nakata et al. 2001; de Lucia et al. 2004; Goto et al. 2005; Tanaka et al. 2005). This deficit might imply that many of the RS galaxies seen today have joined the RS recently, possibly originating from a fading blue population. However, it can also be an effect of the different data sets used and/or different analysis methods. A decline in RSLF at the faint end with increasing redshift, is consistent with the "down-sizing" picture, where star-formation proceeds from the most massive to least massive galaxies as the Universe ages. The question is now whether the results found in this thesis fit with the results found by Crawford et al. (2008), or if there is in fact an observed evolution of α with redshift.

Figure 6.1 shows the RSLFs for the 35 galaxy clusters. Together with the fitted Schechter function, the plots also contain the redshift of the cluster and the reduced χ^2 value describing how well the fitted function fits the data points. As can be seen from figure 6.1, the RSLFs are generally well fitted by a Schechter function. Because of the nature of the volume normalization calculated in section 5.3, the focus will here mainly be on the two parameters α and M^*, not on ϕ^*. Like Crawford et al. (2008), the primary scientific emphasis will be on α which describe the relation between faint dwarf galaxies and bright giant galaxies present in a cluster. The 1σ and 2σ contours for α and M^* are plotted in figure 6.2. These error ellipses are calculated from the χ^2 measurements based on the best fit function (see section 5.5). In the same plots, the best fit values of α and M^* are plotted as crosses. A few of the contour plots show numerical noise (A1423, RX J2129.5+0005, A611 and Zw3146) based on uncertainties in the calculation of the 1σ and 2σ contours.

As shown in table 5.1 in section 5.3, the 35 RSLFs (one for each cluster) are calculated over several different selection radii, R. By studying the results found by Crawford et al. (2008) within different selection radii, it does not seem like a small difference in R affects the results significantly. However, a large variation does (described in section 5.3). The 35 galaxy clusters studied in this thesis have a range of selection radii: R$\in [0.46\,\mathrm{Mpc}, 1.11\,\mathrm{Mpc}]$ with a mean value R$= 0.74$ Mpc, and a corresponding range in units of R_{200}: $\mathrm{R}/\mathrm{R}_{200} \in [0.17, 0.58]$ with a mean value $\mathrm{R}/\mathrm{R}_{200} = 0.38$. Similar to the findings of Crawford et al. (2008), there exists a significant amount of spread in the RSLF parameters α and M^* found in this thesis. α varies between -1.50 and -0.18, while M^* varies between -22.0 and -19.4. Averaging all of the clusters together, gives $\alpha = -0.72 \pm 0.36$ and $M^* = -20.32 \pm 0.68$ at a mean redshift $< z > \approx 0.24$. However, because of the spread in R amongst the 35 clusters, they were divided into three groups depending on their selection radii:

- Group 1: $\mathrm{R}/\mathrm{R}_{200} \in [0.17, 0.30]$. This group consists of 7 clusters, and the average parameter values are $\alpha_1 = -0.85 \pm 0.05$ and $M_1^* = -20.27 \pm 0.11$.
- Group 2: $\mathrm{R}/\mathrm{R}_{200} \in [0.31, 0.44]$. This group consists of 20 clusters, and the average parameter values are $\alpha_2 = -0.75 \pm 0.08$ and $M_2^* = -20.42 \pm 0.16$.
- Group 3: $\mathrm{R}/\mathrm{R}_{200} \in [0.45, 0.58]$. This group consists of 8 clusters, and the average parameter values are $\alpha_3 = -0.54 \pm 0.15$ and $M_3^* = -20.13 \pm 0.26$.

These are the values that will be compared with the results from Crawford et al (2008). The parameter values in the three different groups indicate that there is a difference in the LFs with selection radius.

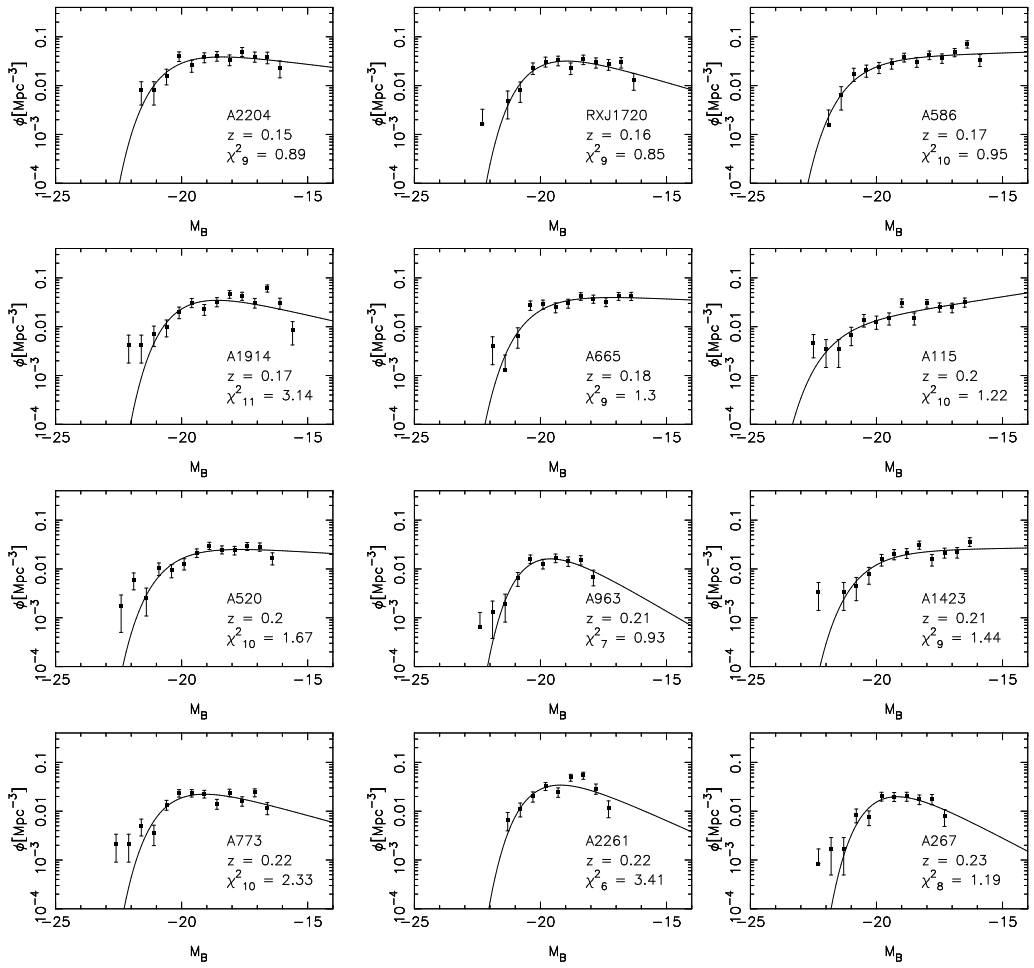

Figure 6.1: The RSLFs in the rest-frame B-band, together with redshift z, and the reduced χ^2 value describing how well the fitted function fits the data points. The number of degrees of freedom is written as subscript. Continued on the next two pages.

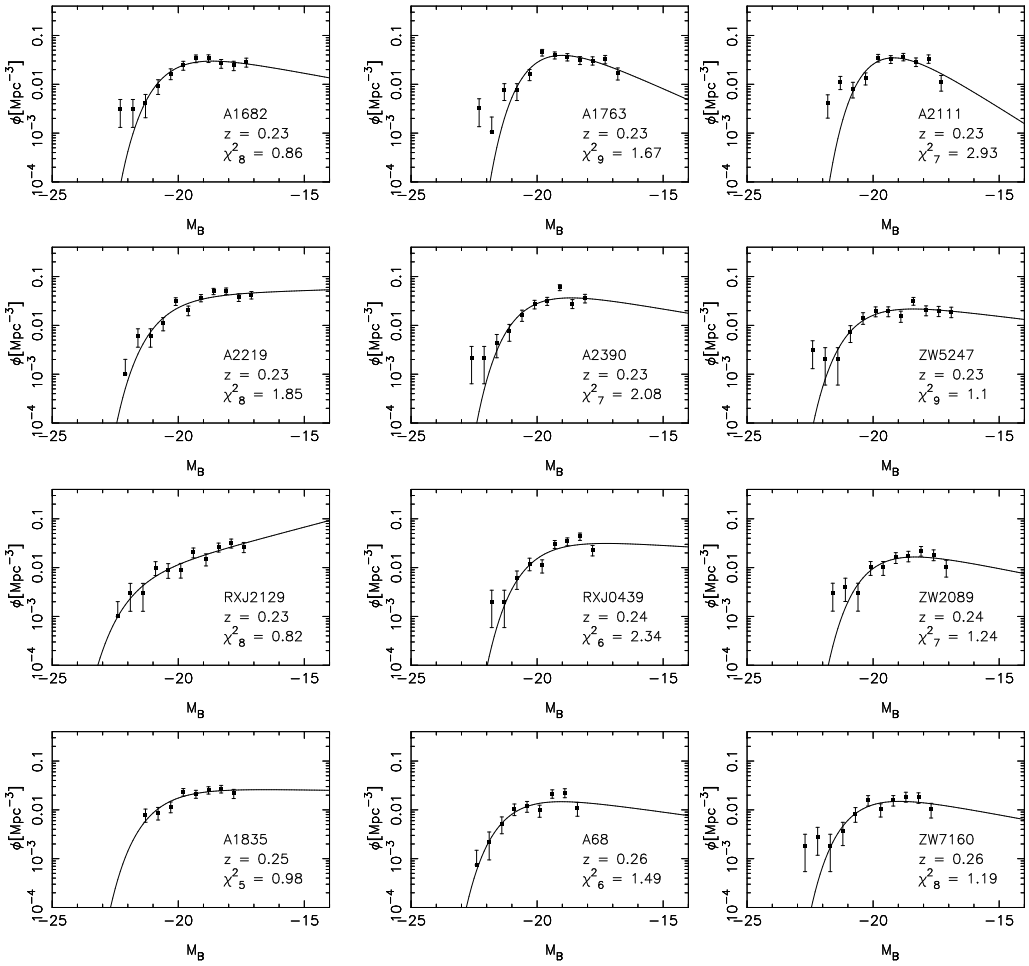

Figure 6.1: Continued from previous page.

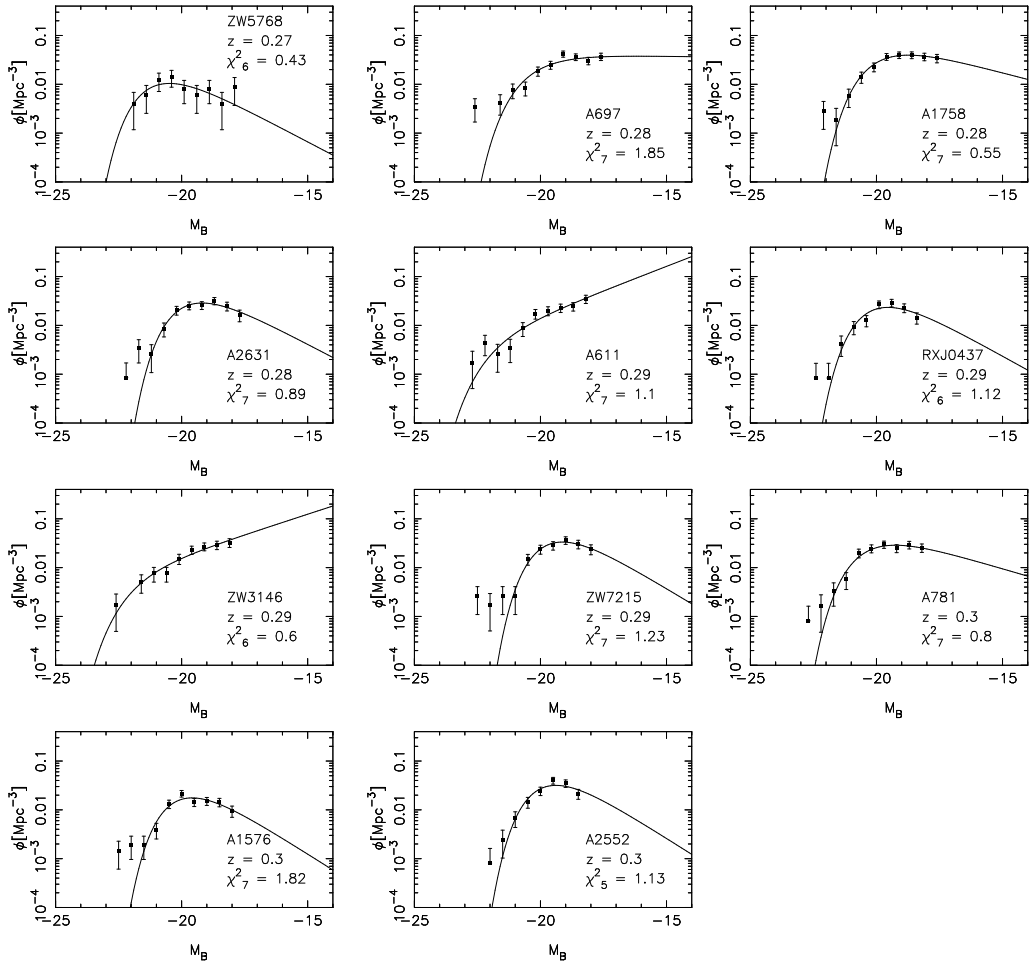

Figure 6.1: Continued from previous page.

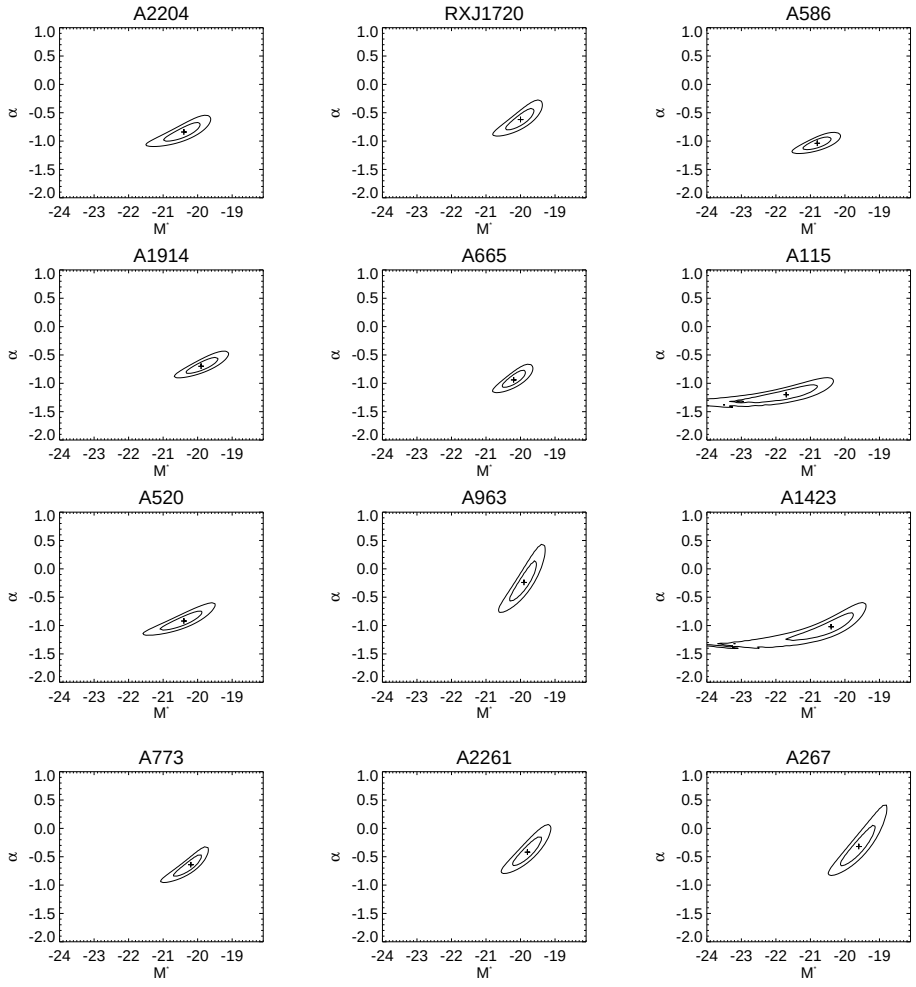

Figure 6.2: The 1σ and 2σ contours for α and M^* from the RSLFs in the rest-frame B-band. The best fit values of α and M^* are plotted as crosses. Continued on the next two pages.

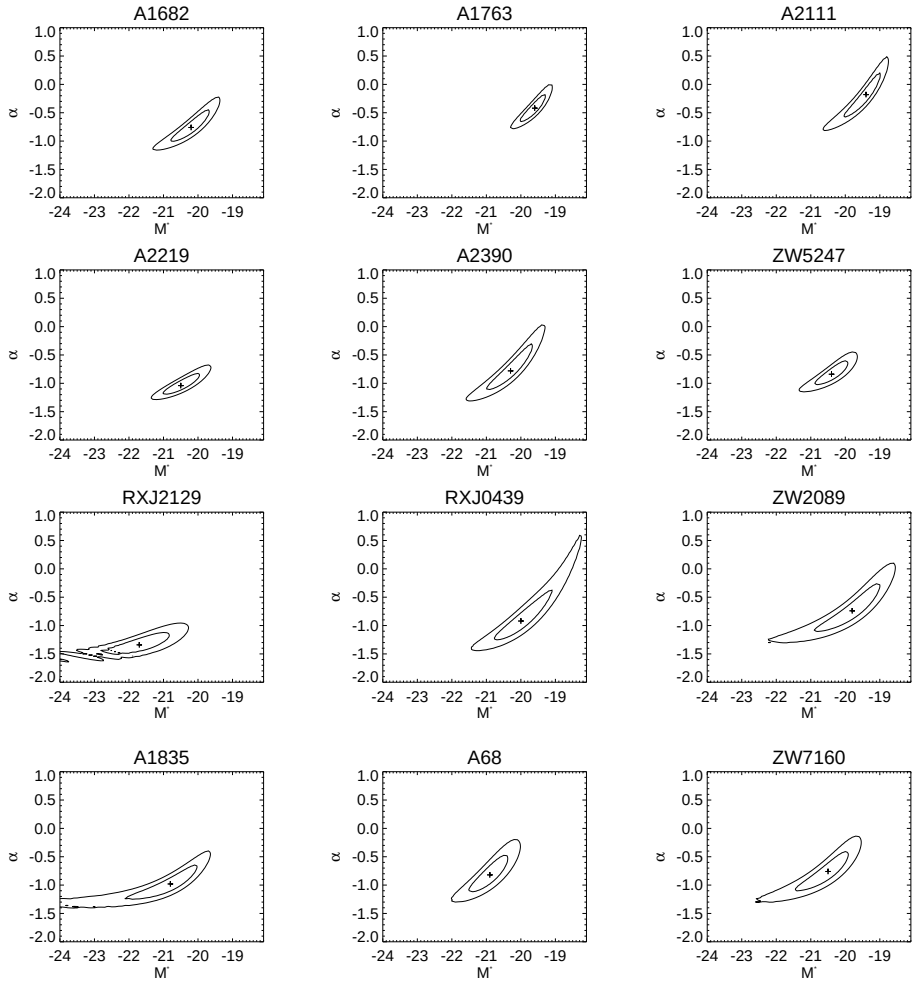

Figure 6.2: Continued from previous page.

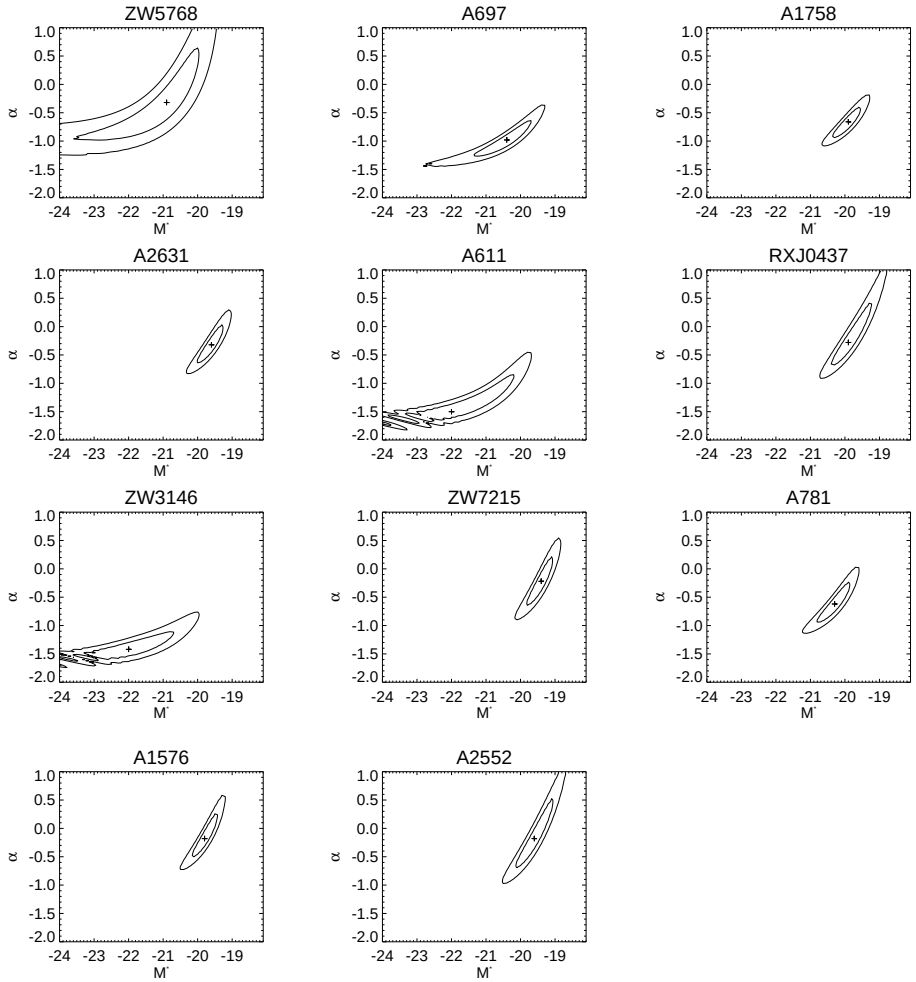

Figure 6.2: Continued from previous page.

Comparison to literature

Even though there are expected different results for different selection radii, the first comparison with Crawford et al. (2008) will be made by using the average parameter values for α and M^* from the 35 galaxy clusters. Crawford et al. (2008) compared five intermediate-redshift ($0.5 < z < 0.9$) clusters with 59 low-redshift ($0.035 < z < 0.144$) clusters. The main idea now is to see if the RSLFs found for the 35 galaxy clusters studied in this thesis fit between the two samples from Crawford et al. (2008). The low-redshift LFs from Crawford et al. (2008) are measured within a selection radius of R = 1 Mpc and R=R_{200}. Within R_{200} the average parameter values are $\alpha = -0.84 \pm 0.32$ and $M^* = -20.55 \pm 0.56$, and within 1 Mpc $\alpha = -0.71 \pm 0.32$ and $M^* = -20.39 \pm 0.48$. Since a selection radius of 1 Mpc is closest to the average selection radius of the sample studied in this thesis (R$\sim$ 0.74 Mpc), the average low-redshift RSLF from Crawford et al. (2008) within 1 Mpc will be compared with the average parameter values from all of the 35 galaxy clusters studied here, that is, $\alpha = -0.72 \pm 0.36$ and $M^* = -20.32 \pm 0.68$. From these results, the RSLF at low redshifts ($z \sim 0.1$) is almost identical with the RSLF at $< z > \sim 0.24$. Within 1 Mpc, the intermediate-redshift clusters at $< z > \sim 0.71$ from Crawford et al. (2008), have average values $\alpha = -0.59 \pm 0.09$ and $M^* = -21.12 \pm 0.30$. These values are not statistically significant different from the lower-redshift values within 1 Mpc. Thus, an evolution of the faint-end slope is not found between $z \sim 0.1$ and ~ 0.71 within a selection radius of ~ 1 Mpc. However, it is important to keep in mind that the comparison is made ignoring the difference in selection radii for the 35 galaxy clusters. This leads to potential uncertainties in this comparison.

By using the results within a cluster radius of 1 Mpc, Crawford et al. (2008) found a function describing the amount of evolution in α with redshift:

$$\alpha = \alpha_0 - 1.47\beta log_{10}(1+z), \tag{6.1}$$

where $\alpha_0 = -0.74$ and $\beta_0 = -0.47$. Inserting the mean redshift for the 35 galaxy clusters studied here ($< z > \approx 0.24$), gives $\alpha \approx 0.68$. This agrees closely to the average estimated α found in this thesis ($\alpha = -0.72 \pm 0.36$), which again support the conclusion found by Crawford et al (2008): no evolution of α with redshift. Crawford et al. (2008) also derived a relation between M^* and redshift. From this relation, a redshift of $z = 0.24$ then corresponds to $M^* \sim -20.5$ which is close to $M^* = -20.32 \pm 0.68$ found in this thesis.

A more accurate comparison of the LF parameters can be made by using the average parameter values of α and M^* calculated for the three groups (with

different selection radii) earlier. For each of the five intermediate-redshift clusters, Crawford et al. (2008) measured the LF within four different selection radii: $0.25R_{200}$, 1 Mpc, $0.5R_{200}$, and R_{200}. Thus, group 1 from the galaxy clusters studied in this thesis will be compared with the values at $0.25R_{200}$ from Crawford et al. (2008), group 2 will be compared with two of the LFs measured within 0.40-$0.44R_{200}$ from Crawford et al. (2008), while group 3 will be compared with the values at $0.5R_{200}$ from Crawford et al. (2008). The values obtained in this thesis and the α- and M^*-values obtained by Crawford et al. (2008) within approximately the same selection radii, are shown in figure 6.3 and 6.4, respectively. Here the α- and M^*-values obtained from this thesis are plotted as open circles, while the values based on the tabulated values from Crawford et al. (2008) are plotted as filled squares. The results of the comparisons are:

- α and M^* from Crawford et al. (2008) have the largest spread within R= $0.25R_{200}$, with values ranging from -0.96 to $+0.42$ for α, and from -23.50 to -19.84 for M^*. Averaging over the five clusters gives $\alpha = -0.36 \pm 0.23$ and $M^* = -21.34 \pm 0.67$. Thus, $\alpha_1 = -0.85 \pm 0.05$ from group 1 (at $z \sim 0.24$), is statistically significant different ($\gtrsim 2\sigma$) from the intermediate-redshift LF within $0.25R_{200}$ (see figure 6.3). However, $M_1^* = -20.27 \pm 0.11$ from group 1 agrees closely to the intermediate-redshift LF within $0.25R_{200}$ (see figure 6.4).

- The average values of the intermediate-redshift LFs within 0.40-$0.44R_{200}$ are $\alpha = -0.40 \pm 0.13$ and $M^* = -20.44 \pm 0.07$. $\alpha_2 = -0.75 \pm 0.08$ from group 2 (at $z \sim 0.24$) is statistically significant different ($\gtrsim 2\sigma$) from the intermediate-redshift LF within 0.40-$0.44R_{200}$ (see figure 6.3). However, $M_2^* = -20.42 \pm 0.16$ from group 2 agrees closely to the intermediate-redshift LF within 0.40-$0.44R_{200}$ (see figure 6.4).

- The average values of the intermediate-redshift LFs within $0.50R_{200}$ are $\alpha = -0.42 \pm 0.09$ and $M^* = -21.08 \pm 0.26$. $\alpha_3 = -0.54 \pm 0.15$ from group 3 (at $z \sim 0.27$) is not statistically significant different from the intermediate-redshift LF within $0.50R_{200}$ (see figure 6.3). However, this time $M_3^* = -20.13 \pm 0.26$ from group 3 is statistically significant different ($\gtrsim 2\sigma$) from the intermediate-redshift LF within $0.50R_{200}$ (see figure 6.4).

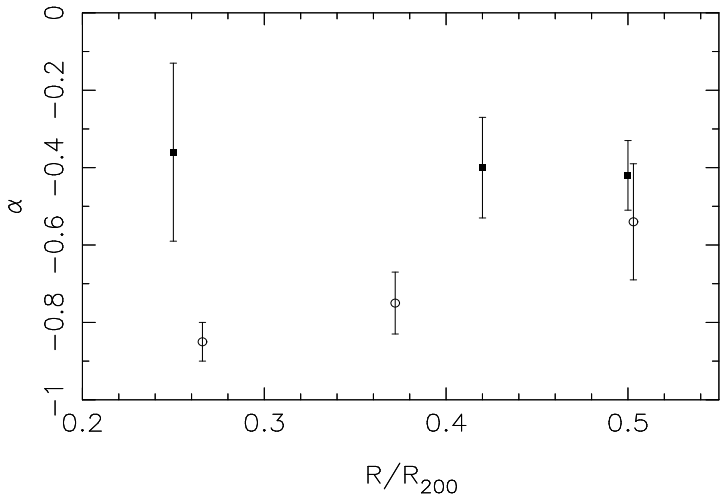

Figure 6.3: Relation between the different selection radii given in units of R_{200} and α. The 35 galaxy clusters are divided into three groups based on their selection radius (R/R_{200}), and the average α-values for each group have been calculated. The same is done for the tabulated values from Crawford et al. (2008) for the intermediate-redshift clusters. The α-values obtained in this thesis are plotted as open circles, while the values based on the tabulated values from Crawford et al. (2008) are plotted as filled squares. Error bars are plotted as vertical lines.

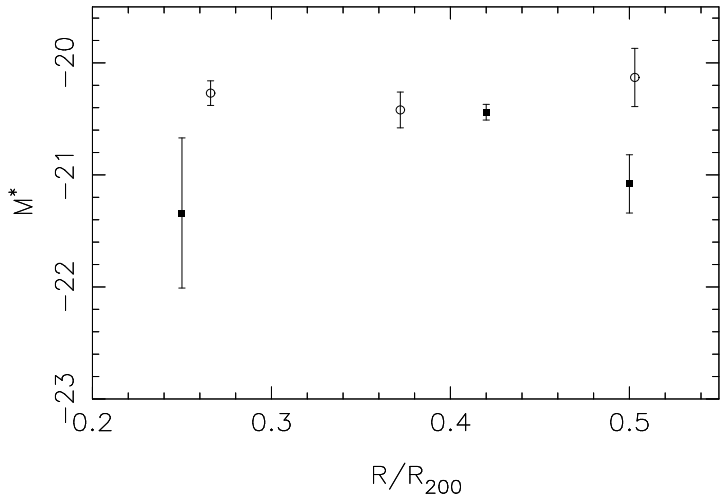

Figure 6.4: Relation between the different selection radii given in units of R_{200} and M^*. The 35 galaxy clusters are divided into three groups based on their selection radius (R/R_{200}), and the average α-values for each group have been calculated. The same is done for the tabulated values from Crawford et al. (2008) for the intermediate-redshift clusters. The M^*-values obtained in this thesis are plotted as open circles, while the values based on the tabulated values from Crawford et al. (2008) are plotted as filled squares. Error bars are plotted as vertical lines.

To conclude this comparison: there are observed differences between the RSLFs found in this thesis and the ones at intermediate redshifts found by Crawford et al. (2008) (see figure 6.3 and 6.4) when the comparisons are made within approximately the same selection radii. Here the α values at lower redshifts (that is, from the 35 galaxy clusters studied in this thesis at $z \in [0.15, 0.30]$) are more negative than the ones at intermediate redshifts ($z \in [0.50, 0.90]$) from Crawford et al (2008). In addition, group 1 and 3 show a decrease in M^* (less negative) compared to the LFs at intermediate redshifts. This is opposite from the findings of Crawford et al. (2008), who found little evidence for an evolution of the faint-end slope (α) with redshift within a selection radius R=R_{200}. The results found in this thesis are based on observations within smaller selection radii ($R < R_{200}$), and the observed areas are therefore of the inner cluster regions. The evolution of α is thus just evident within smaller selection radii. This evolution favour the "down-sizing" picture, where star-formation proceeds from the most massive to least massive galaxies as the Universe ages. From the results obtained here, it seems like faint galaxies in the central regions of the clusters ($R < 0.5R_{200}$) have joined the RS recently because their star formation has ended.

6.1.2 LF for all morphological types in the rest-frame B-band

In this subsection the results of the LF in the rest-frame B-band for all galaxy types, will be discussed. The LFs will be compared with the RSLFs in the same rest-frame band to see if there is a significant difference when all morphological types are considered. Figure 6.5 shows the LFs for the 35 galaxy clusters. Together with the fitted Schechter function, the plots also contain the redshift of the cluster and the reduced χ^2 value describing how well the fitted function fits the data points. As can be seen from figure 6.5 and the χ^2 values, the fit is somewhat poorer than when only RS galaxies were considered. The 1σ and 2σ contours for α and M^* are plotted in figure 6.6. In the same plots, the best fit values of α and M^* are plotted as crosses.

As can be seen in figure 1.3 in section 1.6, the spirals and S0 galaxies have a Gaussian LF, the ellipticals have a skewed Gaussian LF, the dwarf ellipticals (dE+dSph) follow a Schechter function with steep slope, while the irregulars follow a Schechter function with shallower slope. Thus, when all morphological types are considered, the LF is expected to have a shallower faint-end slope. It is important to keep in mind that this applies to low-redshift clusters. At higher redshifts (higher than the ones in this thesis), the type specific LFs may look somewhat different. To compare the results, the 35 clusters are again divided into the three groups mentioned earlier, depending on their selection radius:

- Group 1: $R/R_{200} \in [0.17, 0.30]$. This group consists of 7 clusters, and the average parameter values are $\alpha = -0.64 \pm 0.13$ and $M^* = -20.09 \pm 0.25$. For RSLF the parameter values are $\alpha_{RS} = -0.85 \pm 0.05$ and $M^*_{RS} = -20.27 \pm 0.11$. As expected, the faint-end slope is more shallow (less negative α) than when only RS galaxies were considered.

- Group 2: $R/R_{200} \in [0.31, 0.44]$. This group consists of 20 clusters, and the average parameter values are $\alpha = -0.57 \pm 0.08$ and $M^* = -20.12 \pm 0.19$. For RSLF the parameter values are $\alpha_{RS} = -0.75 \pm 0.08$ and $M^*_{RS} = -20.42 \pm 0.16$. Also group 2 shows a more shallow faint-end slope.

- Group 3: $R/R_{200} \in [0.45, 0.58]$. This group consists of 8 clusters, and the average parameter values are $\alpha = -0.26 \pm 0.14$ and $M^* = -19.74 \pm 0.14$. For RSLF the parameter values are $\alpha_{RS} = -0.54 \pm 0.15$ and $M^*_{RS} = -20.13 \pm 0.26$. Group 3 also shows a more shallow faint-end slope.

The M^* values are a bit lower (less negative) from the values found when only RS galaxies were considered, but they do not differ much. All of the three groups above show a large spread in parameter values with $\alpha \in [-1.16, 0.34]$ and $M^* \in [-22.19, -18.8]$. Averaging over all of the 35 galaxy clusters, gives $\alpha = -0.51 \pm 0.06$ and $M^* = -20.03 \pm 0.12$.

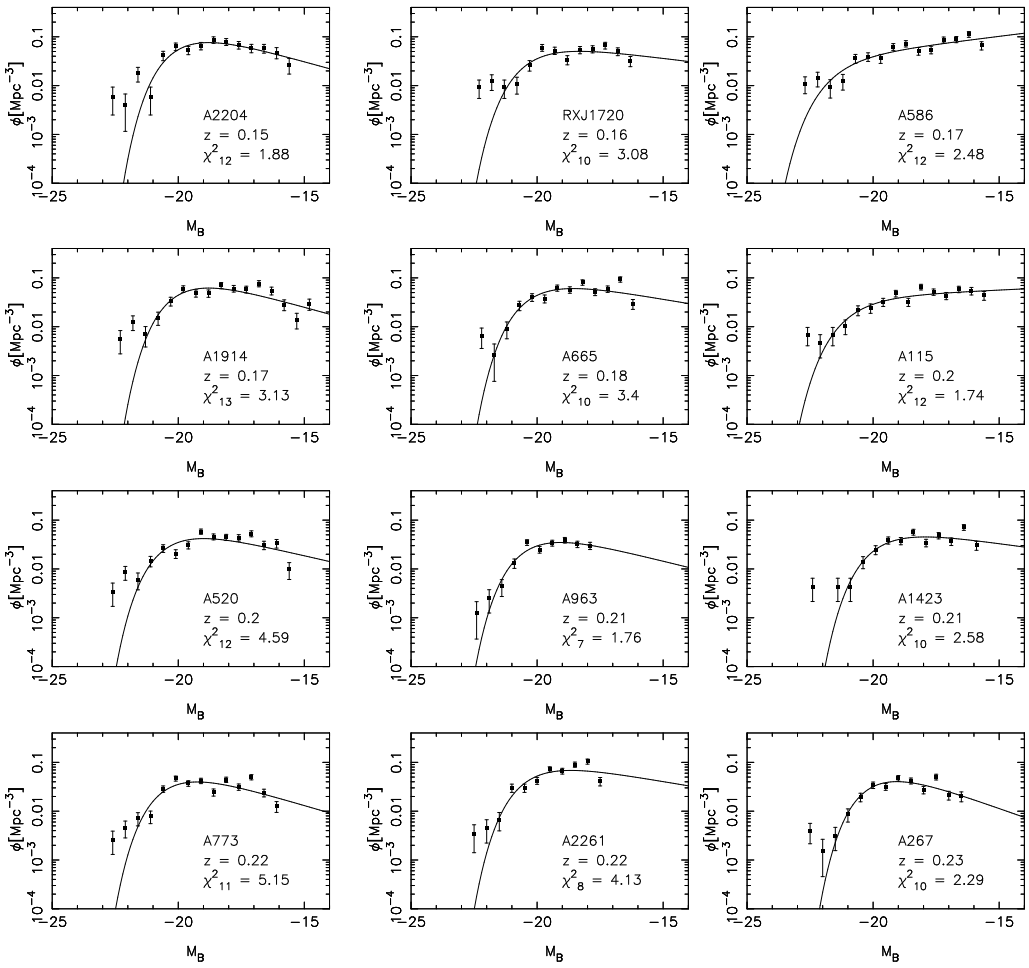

Figure 6.5: The LFs for all morphological types in the rest-frame B-band, together with redshift z, and the reduced χ^2 value describing how well the fitted function fits the data points. The number of degrees of freedom is written as subscript. Continued on the next two pages.

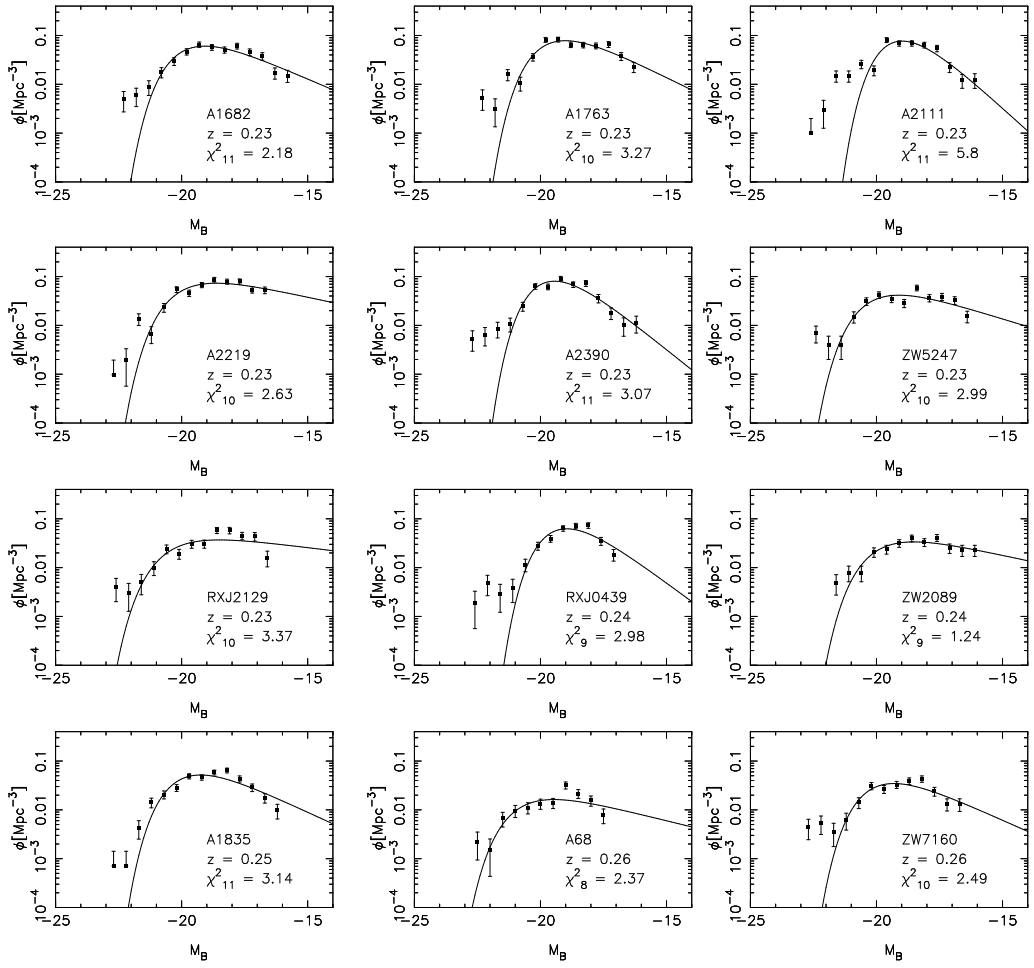

Figure 6.5: Continued from previous page.

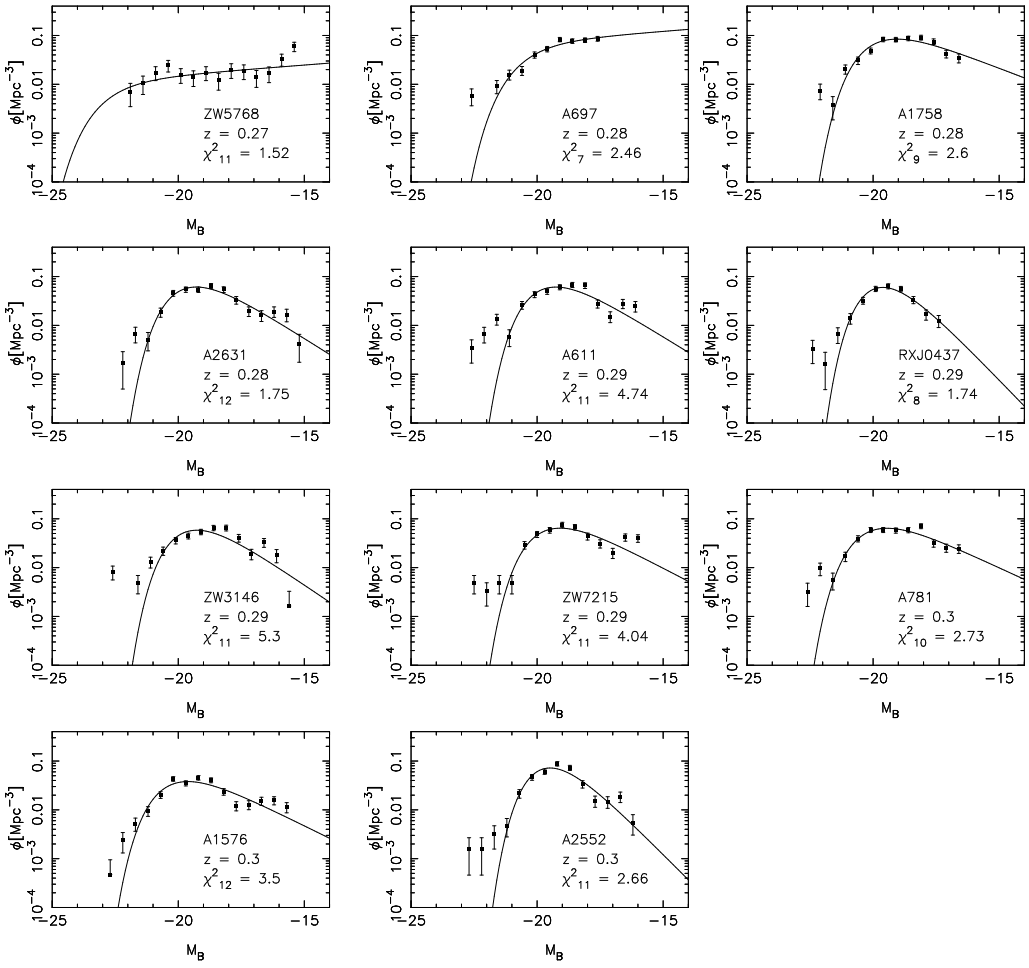

Figure 6.5: Continued from previous page.

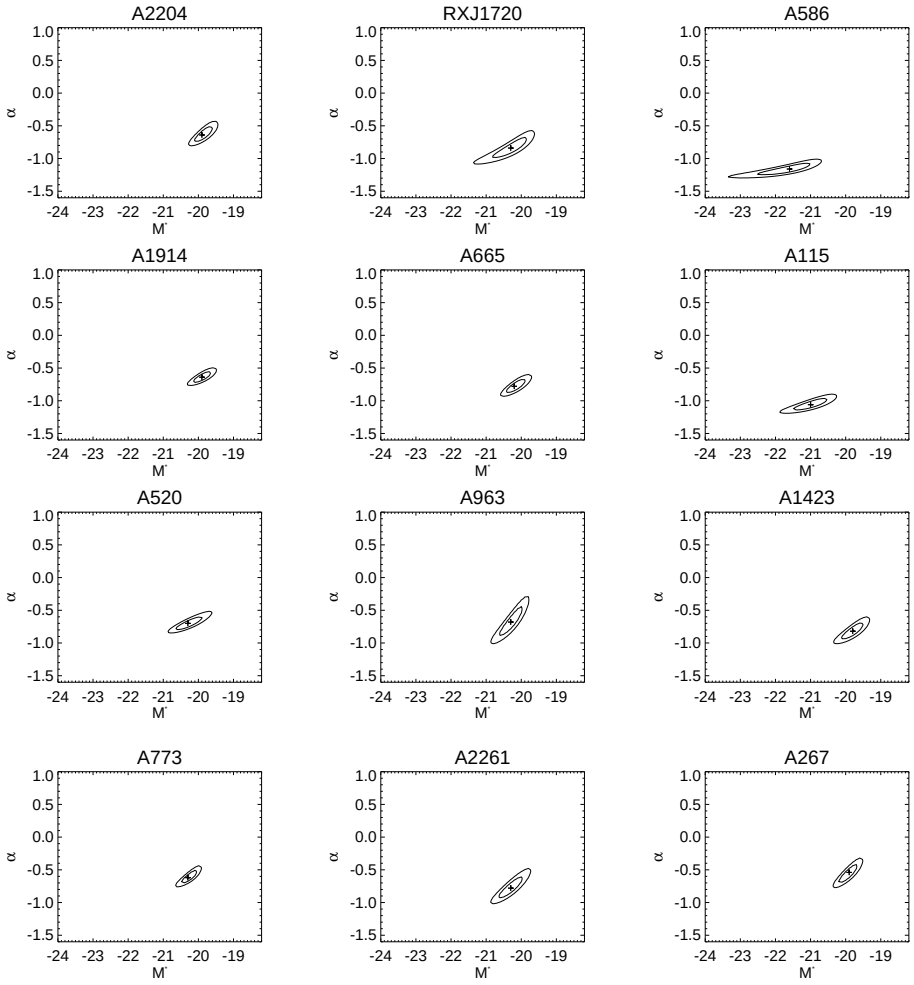

Figure 6.6: The 1σ and 2σ contours for α and M^* from the LFs for all morphological types in the rest-frame B-band. The best fit values of α and M^* are plotted as crosses. Continued on the next two pages.

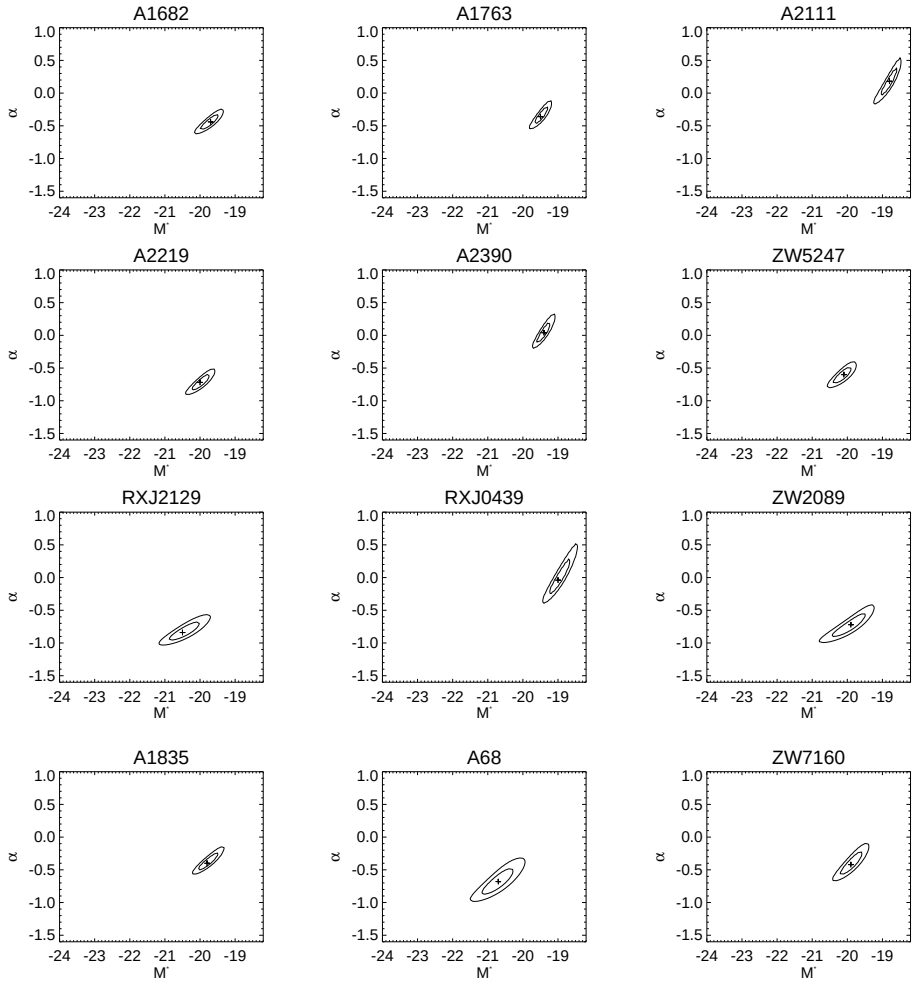

Figure 6.6: Continued from previous page.

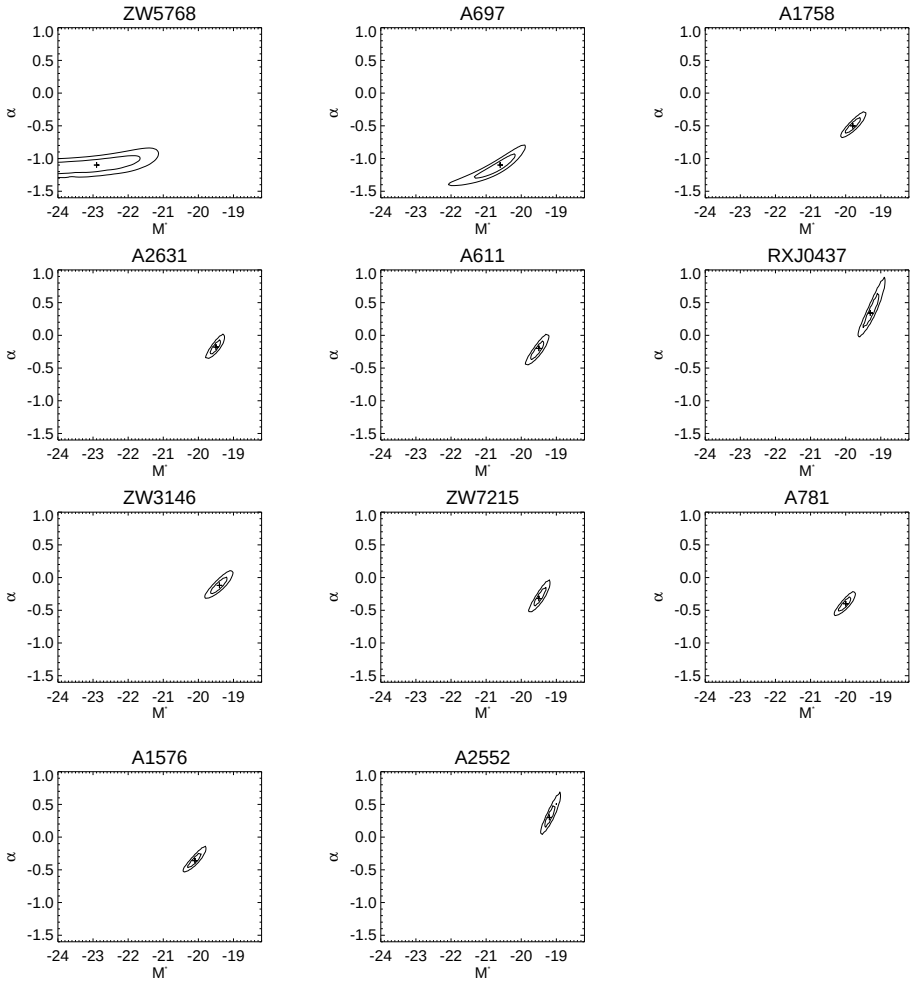

Figure 6.6: Continued from previous page.

6.1.3 LF for all morphological types in the rest-frame U_{2800}-band

In this subsection the results of the LF for all galaxy-types based on the rest-frame wavelength $\lambda \approx 2800$ Å, will be discussed. The LFs will be compared with the LFs in the same rest-frame B-band to see if there is a significant difference between colours. Figure 6.7 shows the LFs for the 35 galaxy clusters. Together with the fitted Schechter function, the plots also contain the redshift of the cluster and the reduced χ^2 value describing how well the fitted function fits the data points. As can be seen from figure 6.7 and the χ^2 values, the goodness of the fit varies between the different clusters. The best fit is found for A2552 with $\chi^2_7 = 1.22$, while the poorest fit is for Zw5768 with $\chi^2_6 = 4.73$. The 1σ and 2σ contours for α and M^* are plotted in figure 6.8. In the same plots, the best fit values of α and M^* are plotted as crosses. A few of the contour plots show numerical noise (A68, Zw7160, Zw5768, A611, Zw3146 and A2552) based on uncertainties in the calculation of the 1σ and 2σ contours.

To compare the results for the U_{2800}-band LFs with the B-band LFs, the clusters are again divided into three groups depending on their selection radius:

- Group 1: $R/R_{200} \in [0.17, 0.30]$. This group consists of 7 clusters, and the average parameter values are $\alpha = -0.75 \pm 0.15$ and $M^* = -19.14 \pm 0.54$. The faint-end slope is steeper (more negative α) than for the B-band LFs, and M^* is smaller (less negative).

- Group 2: $R/R_{200} \in [0.31, 0.44]$. This group consists of 20 clusters, and the average parameter values are $\alpha = -1.02 \pm 0.08$ and $M^* = -19.61 \pm 0.27$. Also group 2 shows a steeper faint-end slope, and a smaller M^*.

- Group 3: $R/R_{200} \in [0.45, 0.58]$. This group consists of 8 clusters, and the average parameter values are $\alpha = -0.98 \pm 0.19$ and $M^* = -19.63 \pm 0.44$. Group 3 also shows a steeper faint-end slope. However, M^* agrees closely to $M^* = -19.74 \pm 0.14$ found for the rest-frame B-band.

All of the three groups above show a large spread in parameter values with $\alpha \in [-1.78, -0.08]$ and $M^* \in [-23.00, -17.4]$. Averaging over all of the 35 galaxy clusters, gives $\alpha = -0.96 \pm 0.07$ and $M^* = -19.52 \pm 0.22$. Thus, the faint-end slope is significantly steeper for the U_{2800}-band LFs than for the B-band LFs, while M^* is fainter. Reasons for these differences lie in the populations of galaxies that are brightest and faintest at the different wavelengths. While the early-type galaxies are characterized by their red

colour, late-type galaxies are bluer. From the results found here, it seems like there are more faint blue galaxies relative to bright blue galaxies than there are faint red galaxies relative to bright red galaxies. This can also be seen by studying figure 1.3 (lower figure) in section 1.6. Figure 1.3 shows the type specific LFs in the rest-frame B-band. The UV flux of ellipticals and lenticulars are lower compared to their flux in the B-band, and their contribution to the total LF is therefore shifted towards the right in figure 1.3. The spirals and irregulars, on the other hand, are bright in the UV. By looking at the type specific LFs for the ellipticals and lenticulars, this means that the faint-end slope should be steeper in the rest-frame U_{2800}-band than in the rest-frame B-band, and this is exactly what is observed.

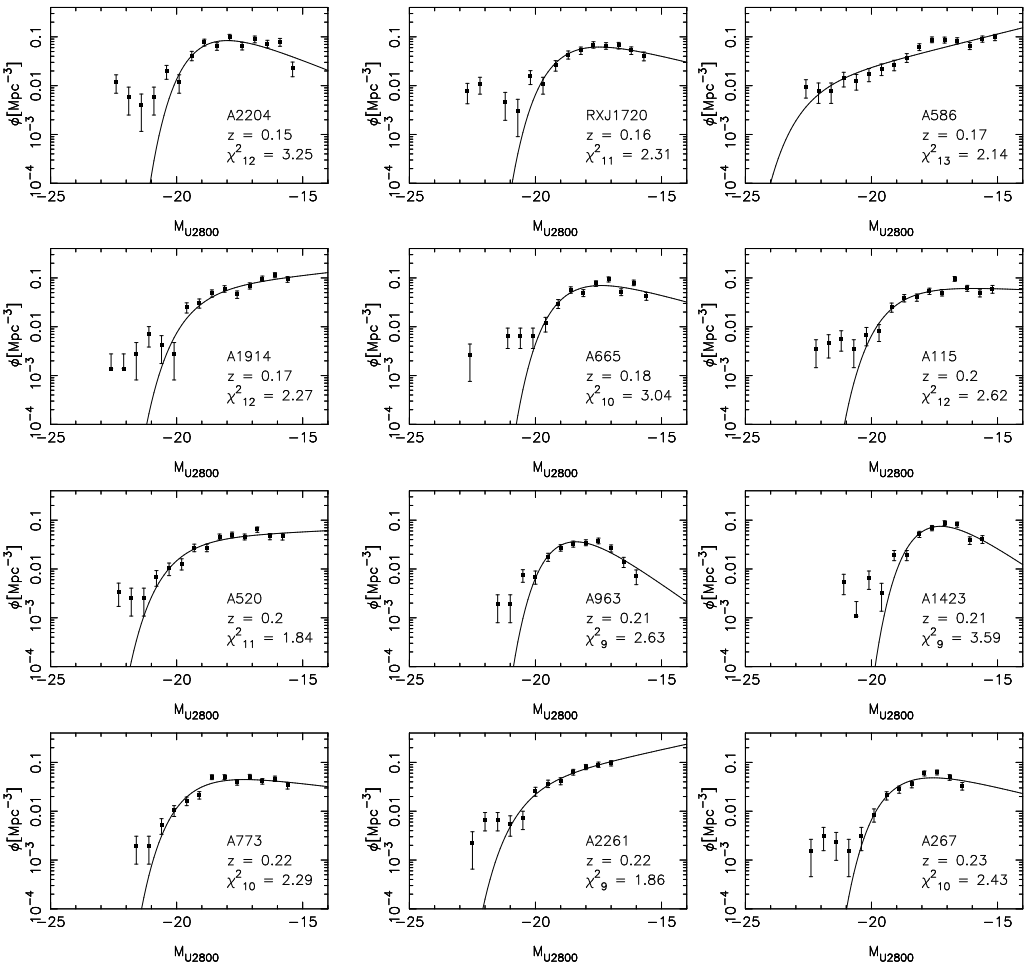

Figure 6.7: The LFs for all morphological types in the rest-frame U_{2800}-band, together with redshift z, and the reduced χ^2 value describing how well the fitted function fits the data points. The number of degrees of freedom is written as subscript.Continued on the next two pages.

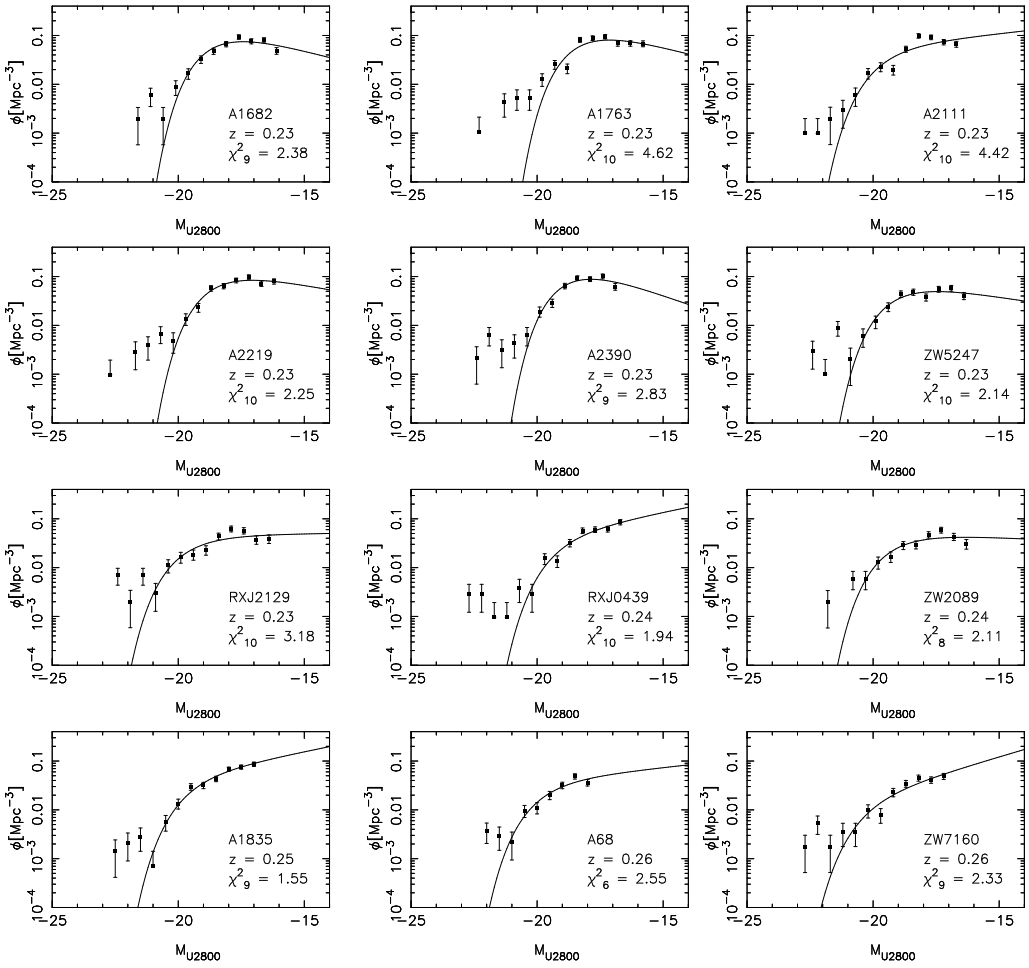

Figure 6.7: Continued from previous page

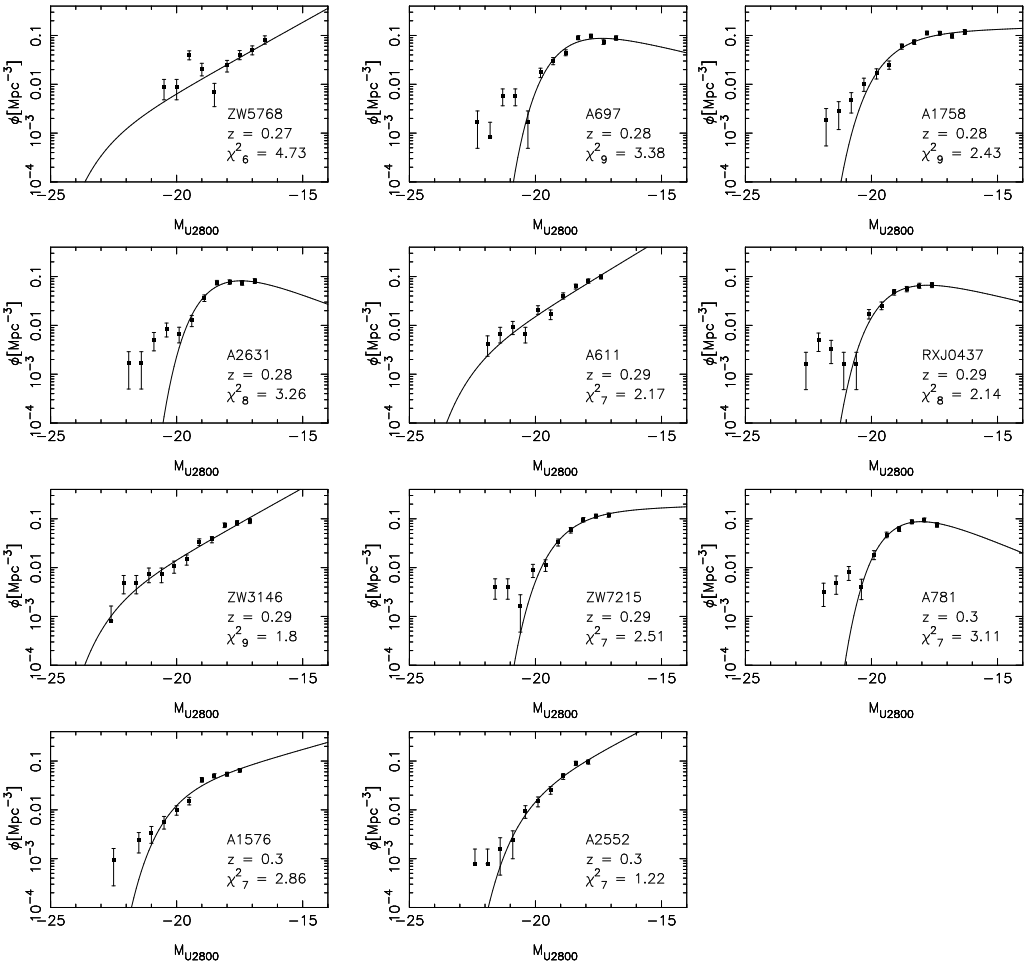

Figure 6.7: Continued from previous page

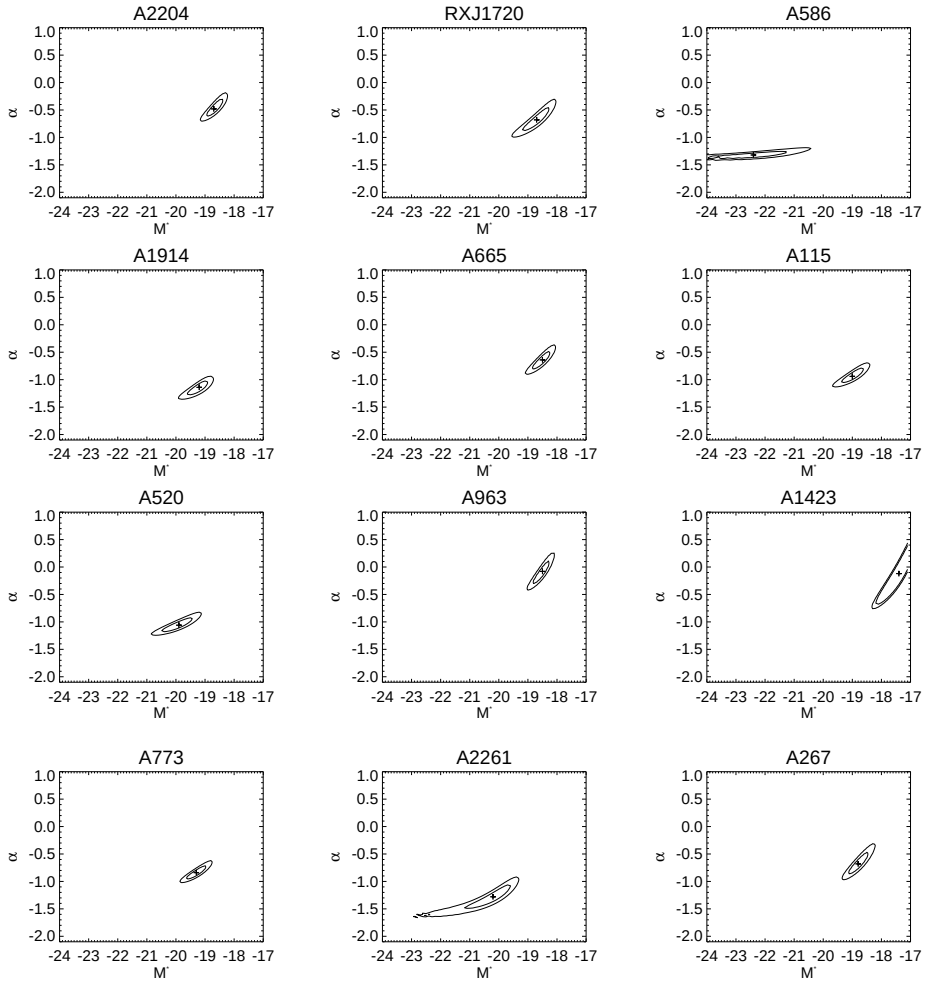

Figure 6.8: The 1σ and 2σ contours for α and M^* from the LFs for all morphological types in the rest-frame U_{2800}-band. The best fit values of α and M^* are plotted as crosses. Continued on the next two pages.

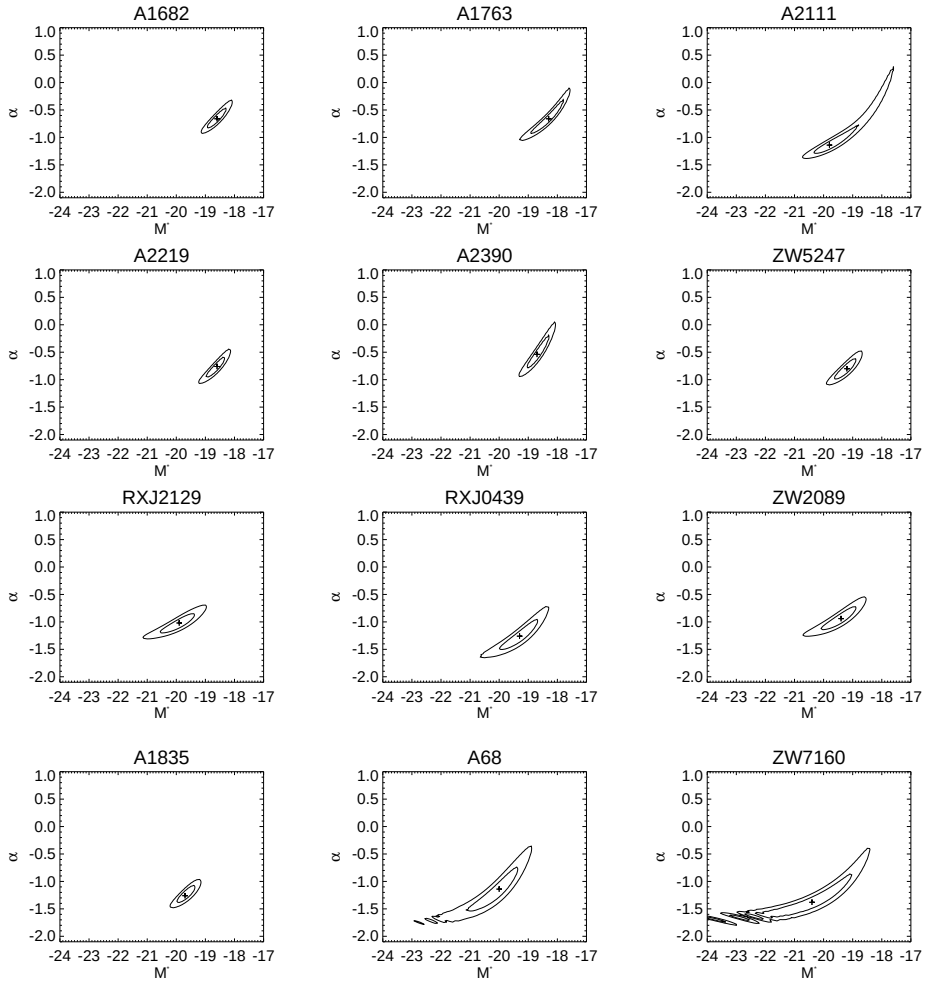

Figure 6.8: Continued from previous page.

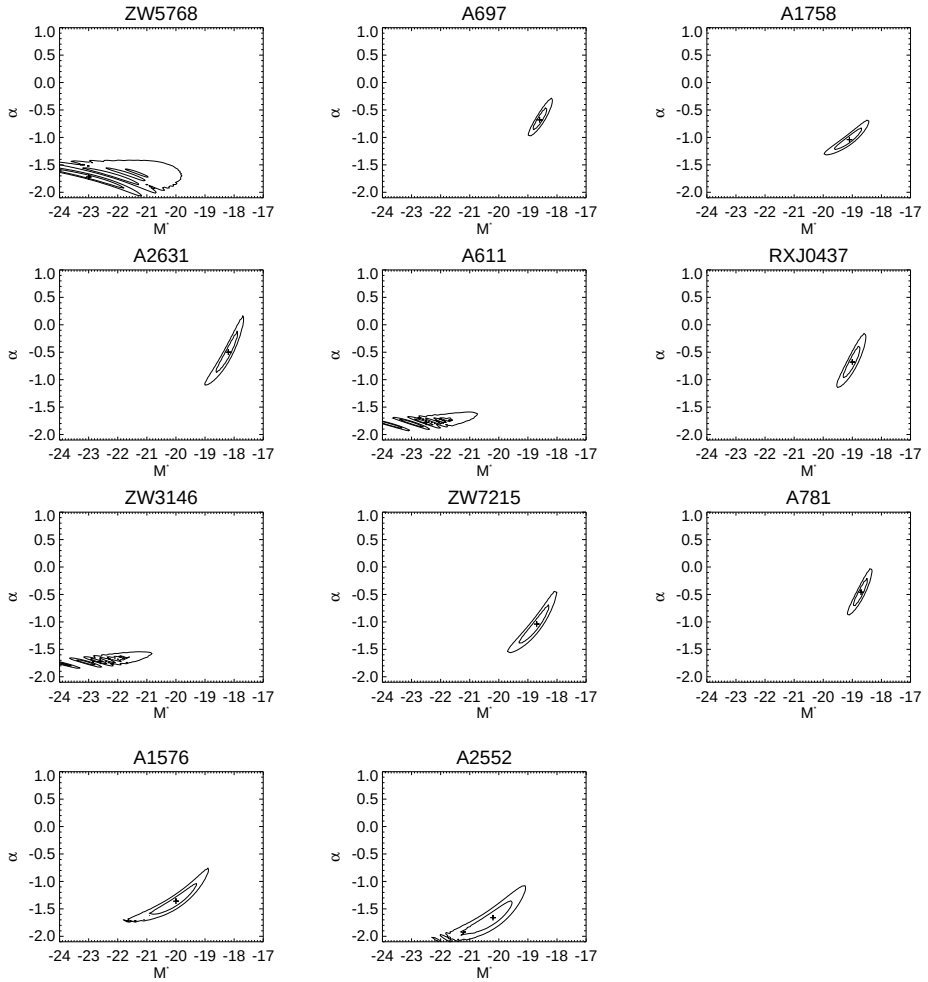

Figure 6.8: Continued from previous page.

6.1.4 Studying the faint-end slope

To further investigate the evolution of the faint-end slope, the relation between α and centroid shift (in units of R_{500}) is plotted in figure 6.9, 6.10 and 6.11 for the RSLFs in the rest-frame B-band, the LFs for all morphological types in the rest-frame B-band, and the LFs for all morphological types in the rest-frame U_{2800}-band, respectively. As mentioned in section 5.6, the centroid shift is a measure of the dynamical state of a cluster. Lower centroid shifts equals more relaxed clusters. By looking at the distribution of centroid shifts in figure 6.9, 6.10 and 6.11, a limit was set at centroid shift= 0.02, separating relaxed clusters from unrelaxed clusters. If α varies between relaxed and unrelaxed clusters, there will be an observable trend in α with centroid shift. In particular, a higher α (more negative) in the unrelaxed clusters implies that there are more faint galaxies in unrelaxed clusters relative to relaxed clusters. Thus, cluster-related processes occuring between the time a cluster goes from unrelaxed to relaxed, are responsible for destroying faint dwarf galaxies. There are far more relaxed clusters (24) than unrelaxed (11), and the spread in α of the former are large. From the three figures alone, it does not seem like there is a trend in α with centroid shift. To further investigate the situation, the average value of α was calculated for each of the two groups (relaxed and unrelaxed):

- **RSLF in the B-band:**
  Averaging over the 24 galaxy clusters in dynamical equilibrium gives $\alpha = -0.76 \pm 0.08$, while the average value of the 11 galaxy clusters in dynamical disequilibrium is $\alpha = -0.63 \pm 0.10$. These values are not statistically significant different ($\gtrsim 2\sigma$).

- **LF for all galaxy types in the B-band:**
  Averaging over the 24 galaxy clusters in dynamical equilibrium gives $\alpha = -0.48 \pm 0.08$, while the average value of the 11 galaxy clusters in dynamical disequilibrium is $\alpha = -0.59 \pm 0.10$. These values are not statistically significant different ($\gtrsim 2\sigma$).

- **LF for all galaxy types in the U_{2800}-band:**
  Averaging over the 24 galaxy clusters in dynamical equilibrium gives $\alpha = -0.94 \pm 0.09$, while the average value of the 11 galaxy clusters in dynamical disequilibrium is $\alpha = -1.00 \pm 0.10$. Neither these values are statistically significant different ($\gtrsim 2\sigma$).

No trend of statistical significance is found in α with centroid shift. Thus, processes responsible for destroying faint dwarf galaxies are most efficient in less dense environments and occur before the galaxies join larger clusters.

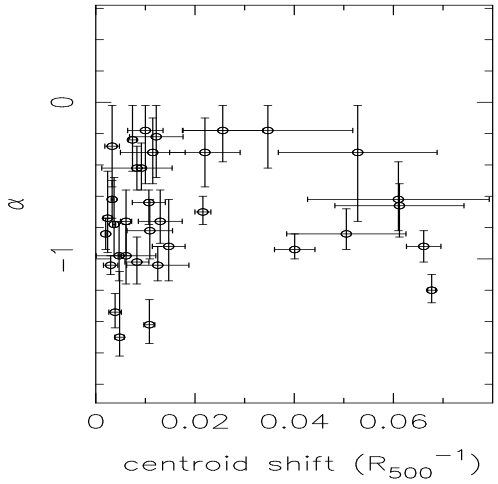

Figure 6.9: Relation between α from the B-band RSLF and the centroid shift in units of R_{500}. Error bars are plotted for both α and centroid shift.

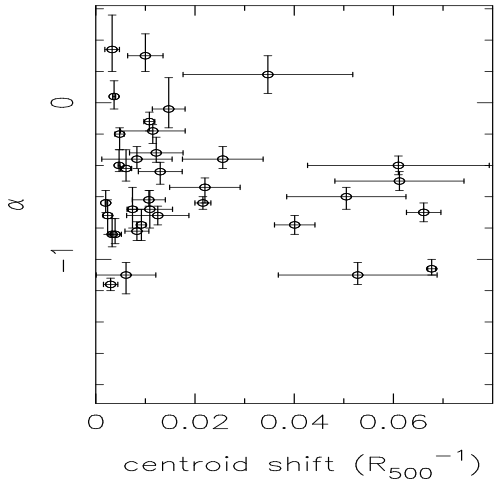

Figure 6.10: Relation between α from the the B-band LF of all galaxy types and the centroid shift in units of R_{500}. Error bars are plotted for both α and centroid shift.

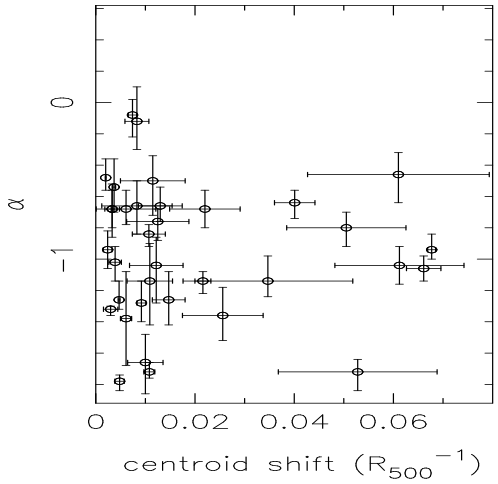

Figure 6.11: Relation between α from the U_{2800}-band LF of all galaxy types and the centroid shift in units of R_{500}. Error bars are plotted for both α and centroid shift.

To further investigate the evolution of the faint-end slope, Crawford et al. (2008) plotted α as a function of the galaxy velocity dispersion within the cluster (σ_v), both within selection radii 1 Mpc and R_{200}. The velocity dispersion increases with cluster mass, and it is therefore often used as a mass estimate. When looking at both the low-redshift and intermediate-redshift clusters studied by Crawford et al. (2008), it does not seem to be a trend with cluster mass. However, when only considering the five intermediate-redshift clusters, α decreases with cluster mass (less negative), implying that there are more faint RS galaxies relative to bright RS galaxies in lower mass clusters. Such a result indicates that processes responsible for the destruction of faint dwarf galaxies are more efficient in high mass clusters. Figure 6.12, 6.13 and 6.14 show similar plots of the 35 galaxy clusters studied in this thesis for the RSLFs in the rest-frame B-band, the LFs for all morphological types in the rest-frame B-band and the LFs for all morphological types in the rest-frame U_{2800}-band, respectively. Here the clusters classified as relaxed are plotted with open circles, while the clusters classified as unrelaxed are plotted with filled squares. None of these three plots show any evolution in α with cluster mass, neither for the relaxed or unrelaxed clusters. It is important to note that the trend found by Crawford et al. (2008) for the intermediate-redshift clusters, was only based on five objects. This trend may not hold for a larger cluster sample.

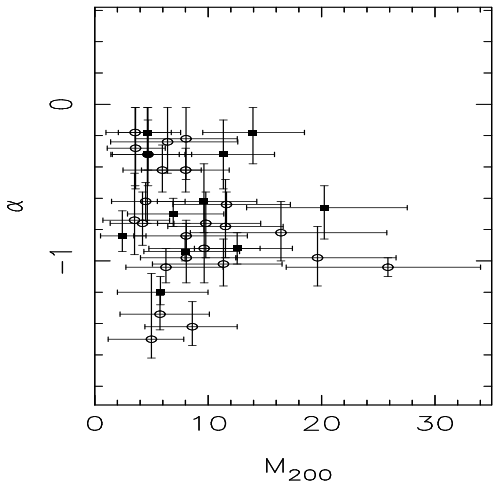

Figure 6.12: Relation between α from the B-band RSLF and M_{200}. Error bars are plotted for both α and M_{200}. Relaxed clusters are plotted with open circles, while unrelaxed clusters are plotted with filled squares (the same applies to figure 6.13 and 6.14).

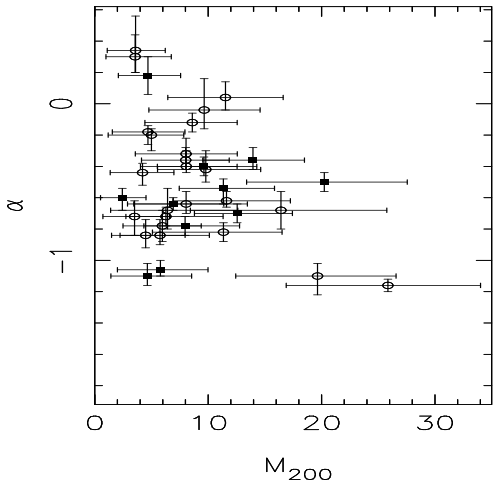

Figure 6.13: Relation between α from the the B-band LF of all galaxy types and M_{200}. Error bars are plotted for both α and M_{200}.

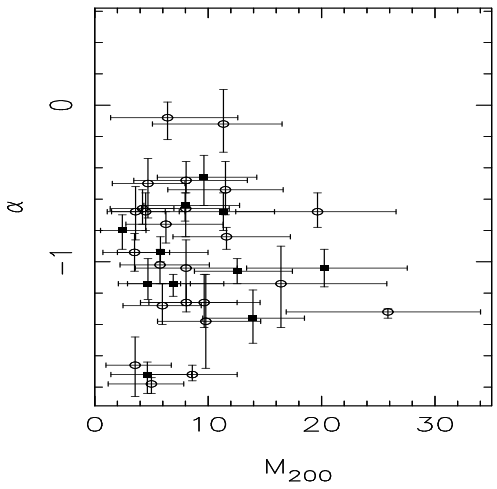

Figure 6.14: Relation between α from the U_{2800}-band LF of all galaxy types and M_{200}. Error bars are plotted for both α and M_{200}.

6.2 Star formation and dynamical state

In this section the correlation between star formation and dynamical state of the 35 galaxy clusters will be studied. In addition, a trend in star formation with redshift (Butcher-Oemler effect) will be investigated. The star formation activity in each cluster is parametrized by F_{SF} (fraction of star forming cluster galaxies), calculated in section 5.6. The limit in centroid shift dividing the relaxed and unrelaxed clusters is, as mentioned earlier, set to 0.02 based on the observed distribution of clusters with centroid shift. If F_{SF} varies between relaxed and unrelaxed clusters, there will be an observable trend in F_{SF} with centroid shift. In particular, a higher F_{SF} in the unrelaxed clusters implies that the quenching of star formation occurs inside the cluster environment, between the time a cluster goes from unrelaxed to relaxed. Several cluster-related processes can affect the star formation rates (SFRs) of galaxies, like ram-pressure stripping, galaxy encounters and galaxy starvation. While ram-pressure stripping and galaxy starvation only affect the gaseous content of a galaxy, galaxy encounters affect both the gaseous and the stellar properties of a galaxy. In this thesis the relation between F_{SF} and dynamical state of the galaxy clusters will be used to reveal which of these processes are dominant (see section 5).

Figure 6.15 shows the relation between F_{SF} and centroid shift in units of R_{500}. This plot does not reveal a significant trend in F_{SF} with centroid shift, which means that an approximate horizontal line can be drawn through the points. Averaging all of the 35 F_{SF}-values places the horizontal line at $F_{SF} = 0.133 \pm 0.008$. However, there is a lot of spread around this line, especially from the relaxed clusters (centroid shift < 0.02). In addition, one of the unrelaxed clusters deviates from the rest with the highest F_{SF}-value of them all. This cluster is identified to be Zw5768 with $F_{SF} = 0.248 \pm 0.044$. Zw5768 has shown deviating results throughout this thesis. However, the results obtained for Zw5768 will generally be treated with the same amount of importance as the rest. The data obtained for Zw5768 indicates a significantly poorer cluster. As can be seen in figure 5.2 (fifth image from the bottom), the X-ray luminosity is significantly lower. The cluster environment is less dense, and the fact that the centroid shift is large (~ 0.053), indicates that it is an object under formation.

Figure 6.15 also reveals some structure between the relaxed clusters. They can be divided into two groups: one around $F_{SF} \sim 0.1$ and one around $F_{SF} \sim 0.2$. The significance of the upper group around $F_{SF} \sim 0.2$ will be discussed later. Ignoring this upper relaxed group around $F_{SF} \sim 0.2$ and Zw5768 with its high F_{SF}-value, an approximate horizontal line can be drawn at $F_{SF} \sim 0.117$ through the lowest relaxed group and the unre-

laxed clusters. This gives a constant relation between F_{SF} and centroid shift with much less spread. But why is there an "upper" relaxed group around $F_{SF} \sim 0.2$? A possible answer may lie in the structure of a galaxy cluster. In hierarchical structure formation scenarios, clusters of galaxies grow by the accretion of outlying galaxies and groups along filaments (see section 1.4). If the line of sight is along one of these filaments, galaxies outside the central region of the cluster will also be imaged. The morphology-density relation for galaxies indicates that early-type galaxies are preferentially located in high density environments, while late-type galaxies are preferentially located in low density environments. More spirals are therefore suspected to be found in the general field and in the outer regions of galaxy clusters. Thus, more star forming spirals are also suspected to be found along the filaments from which the clusters accrete galaxies. In addition, as field galaxies encounter the cluster environment for the first time, new star formation may be triggered, presumably due to gentle processes in the local group environments (Haines et al. 2009). Thus, the upper relaxed group in figure 6.15 may just be due to the line-of-sight being along a filament.

To further investigate the difference between relaxed and unrelaxed clusters, the average value of F_{SF} was calculated for each of the two classified groups: relaxed and unrelaxed.

- **Relaxed:**
  The range of F_{SF} in the relaxed clusters is $F_{SF} \in [0.055, 0.219]$, with a mean value $F_{SF} = 0.136 \pm 0.009$.

- **Unrelaxed:**
  The range of F_{SF} in the unrelaxed clusters is $F_{SF} \in [0.066, 0.248]$, with a mean value $F_{SF} = 0.127 \pm 0.014$.

These two values are not statistical significant different ($\gtrsim 2\sigma$), and I therefore conclude that there is no correlation between star formation and dynamical state of the 35 galaxy clusters studied in this thesis. A similar relation was studied by Haines et al. (2009). Their sample consisted of 30 massive galaxy clusters at $0.02 \leq z \leq 0.40$, and instead of using centroid shifts as an indicator of a clusters dynamical state, they used the offset of the brightest cluster galaxy (BCG) from the peak of X-ray emission. In agreement with the findings in this thesis, no correlation between F_{SF} and dynamical state was found. This indicates that many of the galaxies already have been stripped of their gas when they enter the cluster environment. Thus, from these results alone it does not seem like ram-pressure stripping or galactic starvation are the dominant mechanisms responsible for the quenching of star formation in the cluster galaxies. For instance, ram-pressure stripping is thought to be most efficient close to the clusters core. Galactic starvation is a result from the removal of the galaxy's surrounding halo by the intra-

cluster medium (ICM), and is therefore also a process occuring in the cluster environment. Tidal encounters are therefore more likely to be the dominant mechanism, since these processes are most efficient in structures smaller than massive clusters, such as groups of galaxies (see section 5). Cluster members will therefore already have had their star formation quenched before joining a larger cluster, and no difference between relaxed and unrelaxed clusters is expected.

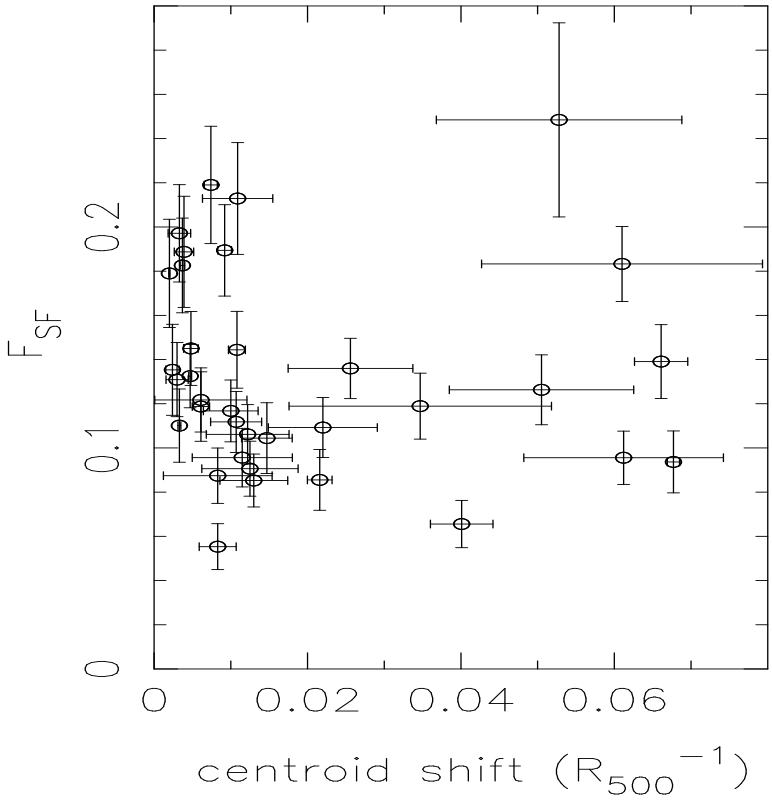

Figure 6.15: Relation between the fraction of star-forming cluster galaxies and the centroid shift in units of R_{500}. Error bars are plotted for both F_{SF} and centroid shift.

Another interesting plot is the relation between α and F_{SF}. A trend in this plot indicates that there is a relation between processes that quench star formation and processes that destroy faint dwarf galaxies. In particular, a decreasing α (less negative) with decreasing F_{SF}, suggests that these processes are closely linked. An opposite trend would suggest that there are less faint dwarf galaxies in clusters with a high fraction of star forming galaxies. The latter would be a less expected result. Figure 6.16, 6.17 and 6.18 show F_{SF} versus α from the RSLFs in the rest-frame B-band, the LFs for all morphological types in the rest-frame B-band and the LFs for all morphological

types in the rest-frame U_{2800}-band, respectively. Here the clusters classified as relaxed are plotted with open circles, while the clusters classified as unrelaxed are plotted with filled squares. None of these three plots show any trend between F_{SF} and α. When studying the relaxed and unrelaxed clusters separately, there is an indication of a trend in figure 6.16 for the unrelaxed clusters. This trend implies that there are less faint RS galaxies with increasing F_{SF}. However, in this case α only accounts for ellipticals and lenticulars. The same plot for all morphological types (figure 6.17) show no such trend. The trend in figure 6.16 is therefore ignored. An opposite trend in figure 6.16 would be the more expected result.

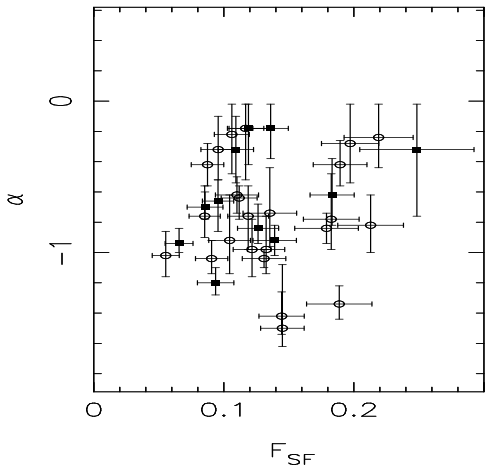

Figure 6.16: Relation between the fraction of star-forming cluster galaxies and α from the B-band RSLF. Error bars are plotted for both F_{SF} and α. Relaxed clusters are plotted with open circles, while unrelaxed clusters are plotted with filled squares (the same applies to figure 6.17 and 6.18).

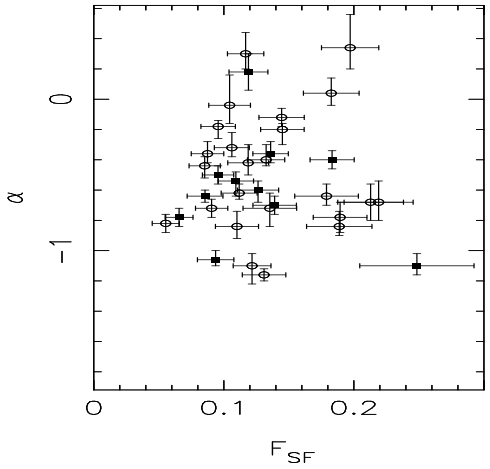

Figure 6.17: Relation between the fraction of star-forming cluster galaxies and α from the the B-band LF of all galaxy types. Error bars are plotted for both F_{SF} and α.

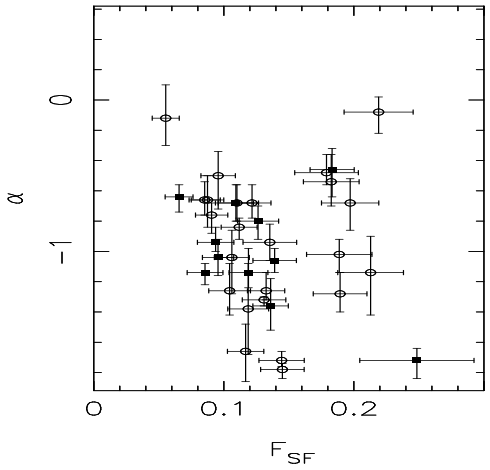

Figure 6.18: Relation between the fraction of star-forming cluster galaxies and α from the U_{2800}-band LF of all galaxy types. Error bars are plotted for both F_{SF} and α.

So far cluster-related processes responsible for evolution of galaxies have been discussed, but the evolution with time has not. As described in section 5, there is a well known increase of blue star-forming galaxies with redshift (the Butcher-Oemler effect). A similar relation was found by Haines et al. (2009) for their 30 massive galaxy clusters at $0.02 \leq z \leq 0.40$. The large sample of 35 clusters in total studied in this thesis, makes it possible to study the F_{SF}-redshift relation to see if the Butcher-Oemler effect is evident. This plot is shown in figure 6.19, and similar to what was expected, the plot shows an increase of star formation with redshift, much similar to the plot made by Haines et al. (2009). Even though there is significant cluster-to-cluster scatter, the Butcher-Oemler effect is very much noticeable in the redshift span $z \in [0.15, 0.30]$. There are no observable differences between relaxed and unrelaxed clusters in figure 6.19.

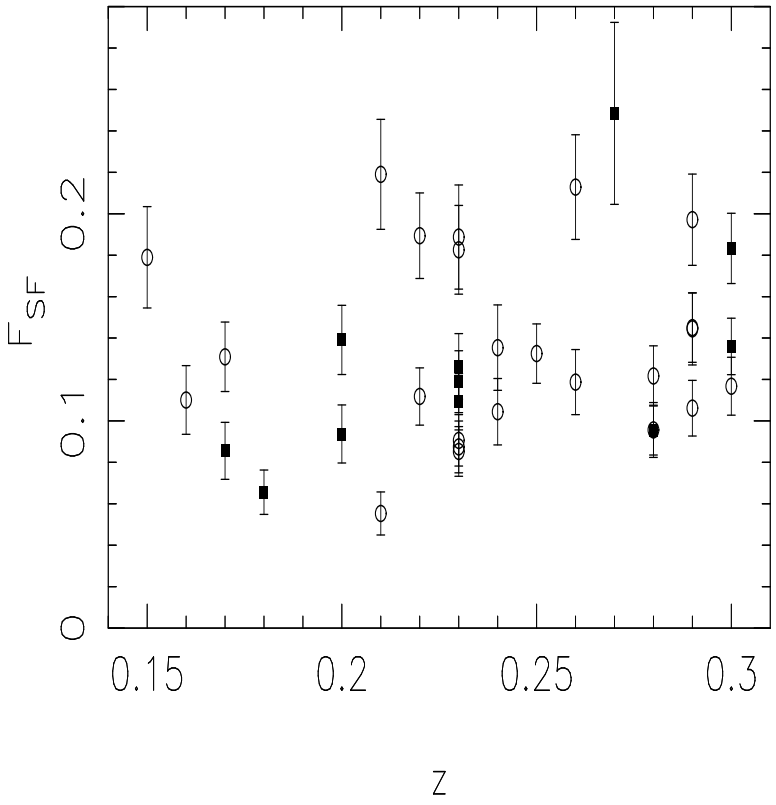

Figure 6.19: Relation between the fraction of star-forming cluster galaxies and redshift. Relaxed clusters are plotted with open circles, while unrelaxed clusters are plotted with filled squares. Error bars are plotted as vertical lines.

6.3 Summary and future prospects

The red-sequence LF (RSLF) in the rest-frame B-band was compared with the results from Crawford et al. (2008). Similar to Crawford et al. (2008), no evolution of the faint-end slope was found within large selection radii. There are uncertainties concerning these results because of the different selection radii used in the comparisons. However, by comparing LFs found within smaller selection radii (the inner regions of the clusters), and by only comparing LFs found within the same selection radii, an evolution of the faint-end slope was found in this thesis. This evolution favour the "downsizing" picture, where star-formation proceeds from the most massive to least massive galaxies as the Universe ages. From the results obtained here, it seems like faint galaxies in the central regions of the clusters ($R < 0.5R_{200}$) have joined the RS recently because their star formation has ended.

A relation between α and the dynamical state of the clusters was studied. No trend of statistical significance was found in α with centroid shift for neither the RSLF in the rest-frame B-band, the LF for all galaxy types in the rest-frame B-band, nor the LF for all galaxy types in the rest-frame U_{2800}-band. Thus, processes responsible for destroying faint dwarf galaxies are most efficient in less dense environments and occur before the galaxies join larger clusters.

α from the three different LFs (the RSLF in the rest-frame B-band, the LF for all galaxy types in the rest-frame B-band, and the LF for all galaxy types in the rest-frame U_{2800}-band) was also plotted against cluster mass. None of these three plots show any evolution in α with cluster mass, neither for the relaxed nor unrelaxed clusters. Thus, the relative number of faint galaxies does not show any dependence on cluster mass.

The relation between the fraction of star forming galaxies, F_{SF}, and centroid shift was investigated, and no correlation was found between star formation and dynamical state of the 35 galaxy clusters studied in this thesis. This indicates that many of the galaxies already have been stripped of their gas when they enter the cluster environment, and the dominant physical mechanism responsible for quenching the star formation in the cluster galaxies are most likely tidal encounters. Tidal encounters are most efficient in structures smaller than massive clusters, such as groups of galaxies. Cluster members will therefore already have had their star formation quenched before joining a larger cluster, and no difference between relaxed and unrelaxed clusters is expected.

To investigate if the dominant physical mechanism responsible for quenching

star formation is the same one responsible for destroying faint dwarf galaxies, F_{SF} was plotted against α from the three different LFs (the RSLF in the rest-frame B-band, the LF for all galaxy types in the rest-frame B-band, and the LF for all galaxy types in the rest-frame U_{2800}-band). A decrease in α (less negative) with decreasing F_{SF}, would indicate that the process responsible for quenching star formation is closely linked to the process responsible for destroying faint galaxies. No correlation was found for either of the three α-values. Thus, the dominant cluster-related process responsible for quenching star formation in the cluster galaxies is found, and the processes responsible for destroying faint galaxies are found to be most efficient before the galaxies join larger clusters.

The 35 galaxy clusters studied in this thesis are selected based on their high masses. Zw5768 is one of the poorest clusters out of the 35. This can be seen from table 5.5 and figure 5.2. In figure 5.2, Zw5768 is the fifth X-ray image from the bottom, and is the cluster with the lowest X-ray luminosity. The fact that Zw5768 is the cluster with the highest F_{SF}, is a motivation to expand the study of F_{SF} to less massive clusters to see if there is a trend with mass. The cluster regions studied in this thesis are very dense. With poorer, less dense clusters, it would be possible to detect processes occuring in less dense environments within the same selection radii as used in this thesis. The study of less dense regions can also be done by extending the selection radii. In this thesis, only selesction radii up to $\sim 0.5R_{200}$ have been used. In the future it would therefore be interesting to extend the study well beyond R_{200}.

In addition to lower mass clusters, it would also be interesting to extend the study of F_{SF} to include clusters at other redshifts, and to use additional indicators of star formation (such as the H_α line and FIR continuum described in section 1.7).

Some of the calculations in this thesis can also be improved. For instance, the accuracy of the photometric redshift estimates would be improved by using photometry in more passbands. In addition, the trends found between the different parameters in this thesis, are based primarily on observations. In the future it would be interesting to performe a more thorough statistical analysis to study the correlations further.

Appendix A

Details of the photometric calibration

This appendix is a supplement to chapter 3. It will start out with some intermediate calculations when estimating the coefficients in the photomretric calibration equations. In addition, some other intermediate calculations are shown.

A.1 Finding a_2:

The aerosol extinction coefficient for each night is independent of wavelength and can be found by looking at the values tabulated for r':

$$A_{aer} = a_2(r') - A(r'). \tag{A.1}$$

The total vertical extinction is given by

$$a_2(\lambda) = A(\lambda) + A_{aer}. \tag{A.2}$$

King (1985) give:

$A(U) = A(3663\text{Å} \approx A(3650\ \text{Å}) = 0.4299$
$A(V) = A(5448\text{Å}) \approx A(5450\text{Å}) = 0.1026$
$A(R) = A(6407\text{Å}) \approx A(6400\ \text{Å}) = 0.0638$
$A(I) = A(7980\text{Å}) \approx A(8000\text{Å}) = 0.0174$

The theoretical extinction coefficient were not tabulated for the wavelengths 3663Å, 5448Å, 6407Å and 7980Å. The nearest table-values for $A(\lambda)$ therefore had to be used for the four passbands.

A.2 Finding a_0 and a_1:

Some of the calculated values for a_0 and a_1 did not give adequate results. These were mostly calculations made from chips consisting of few standard stars. A better fit for the a_0- and a_1-values were found by using relations between the different runs and chips within the same passband. a_1 should not differ too much for the same chip between runs. a_0 can differ significantly between runs and chips, but the difference between the same chip from two different runs should be approximately the same for all of the 4 chips (the filter must be the same, of course). That is,

$$\begin{aligned} chip_1(run_3) - chip_1(run_4) &= chip_2(run_3) - chip_2(run_4) \\ &= chip_3(run_3) - chip_3(run_4) \\ &= chip_4(run_3) - chip_4(run_4) \end{aligned} \tag{A.3}$$

The exception is the difference in chip 1 between the runs 1 & 2 and 3 & 4. Between run 2 and 3 chip 1 was replaced. It therefore makes no sense comparing chip 1 from run 1 or 2 with chip 1 from run 3 or 4.

U-band: The calculated values for a_0 and a_1 gave adequate results for most of the chips in the different runs. The exception is chip 1 from run 3. Since a_1 should not differ too much for the same chip between runs, the a_1-value from chip 1 run 4 was therefore used instead. To find the right a_0-value for chip 1 from run 3, the differences in a_0 for chip 2, 3 and 4 between run 3 and 4 were studied. the average of these differences was then added to the a_0-value of chip 1 from run 4. The calculations are shown below:

$$\begin{aligned} chip_2(run_3) - chip_2(run_4) &= 24.324988 - 24.247673 \\ &= 0.077315 \end{aligned} \tag{A.4}$$

$$\begin{aligned} chip_3(run_3) - chip_3(run_4) &= 24.411103 - 24.359753 \\ &= 0.051350 \end{aligned} \tag{A.5}$$

$$\begin{aligned} chip_4(run_3) - chip_4(run_4) &= 24.289651 - 24.260544 \\ &= 0.029107 \end{aligned} \tag{A.6}$$

$$\frac{0.077315 + 0.05135 + 0.029107}{3} = 0.052591 \tag{A.7}$$

$$\begin{aligned} chip_1(run_3) &= chip_1(run_4) + 0.052591 \\ &= 24.163830 + 0.052591 \\ &= 24.216421 \end{aligned} \tag{A.8}$$

The values used above are found in table A.1.

V-band: The calculated values for a_0 and a_1 gave adequate results for each chip in the different runs.

R-band: Run 3 had very few stars, hence the exact values from run 4 have been used for a_1. The a_0-values were a bit more complicated. The a_0-values from run 3 were first replaced with the a_0-values from run 4. They were then adjusted by adding the difference between chip 4 from run 3 and chip 4 from run 4 ($25.48305 - 25.436631$). The calculations are shown below:

$$\begin{aligned} chip_1(run_3) &= chip_1(run_4) + [chip_4(run_3) - chip_4(run_4)] \\ &= 24.924715 + [25.483050 - 25.436631] \\ &= 24.971134 \end{aligned} \tag{A.9}$$

$$\begin{aligned} chip_2(run_3) &= chip_2(run_4) + [chip_4(run_3) - chip_4(run_4)] \\ &= 25.460742 + [25.483050 - 25.436631] \\ &= 25.507161 \end{aligned} \tag{A.10}$$

$$\begin{aligned} chip_3(run_3) &= chip_3(run_4) + [chip_4(run_3) - chip_4(run_4)] \\ &= 25.547839 + [25.483050 - 25.436631] \\ &= 25.594258 \end{aligned} \tag{A.11}$$

$$\begin{aligned} chip_4(run_3) &= chip_4(run_4) + [chip_4(run_3) - chip_4(run_4)] \\ &= run_3(chip_4) \\ &= 25.483050 \end{aligned} \tag{A.12}$$

I-band: Chip 2 from run 2 did not give adequate results. The a_1-values in the I-band are positive for run 4, and negative in run 2. Because of this, the calculation were not the same as for the U-band. An average value from the other 3 chips in run 2 were used instead:

$$\begin{aligned} \frac{chip_1run_2(run_2) + chip_3(run_2) + chip_4(run_2)}{3} &= \frac{-0.079720975 - 0.017972359 - 0.013518118}{3} \\ &= -0.037070484 \end{aligned} \tag{A.13}$$

See table A.1 for the values used in the equation above. For the I-band there are no observations taken during run 1 (only during run 2 and 4). Thus, the a_0-value was found by looking at differences between run 2 an 4. Between these two runs chip 1 has been replaced and cannot be used in the comparison. The difference in a_0 for chip 3 and 4 between run 2 and 4 was

therefore studied. The calculations were done in the same way as for the U-band, that is:

$$\begin{aligned} chip_3(run_2) - chip_3(run_4) &= 25.075852 - 24.991919 \\ &= 0.083933 \end{aligned} \tag{A.14}$$

$$\begin{aligned} chip_4(run_2) - chip_4(run_4) &= 24.900620 - 24.873055 \\ &= 0.027565 \end{aligned} \tag{A.15}$$

$$\frac{0.083933 + 0.027565}{2} = 0.055749 \tag{A.16}$$

$$\begin{aligned} chip_2(run_2) &= chip_2(run_4) + 0.055749 \\ &= 24.836795 + 0.055749 \\ &= 24.892544 \end{aligned} \tag{A.17}$$

RUN	FILTER	CHIP	a_0	a_1	σ	NUMBER OF STARS
1	U	1	24.412255	-0.14187352	0.038488285	13
1	U	2	24.349779	0.023988441	0.082445396	35
1	U	3	24.491395	-0.12134199	0.033532056	10
1	U	4	24.389180	0.065810148	0.056590501	7
2	I	1	24.998657	-0.079720975	0.041733874	6
2	I	2	24.869870	0.1814938400	0.053335335	7
2	I	3	25.075852	-0.017972359	0.050779297	18
2	I	4	24.90062	-0.013518118	0.054515052	13
2	R	1	25.529241	-0.130170670	0.031659763	7
2	R	2	25.488494	-0.088974514	0.024783283	6
2	R	3	25.666228	-0.081412402	0.038052735	23
2	R	4	25.489373	-0.036094437	0.046398827	26
2	U	1	24.450154	0.028739920	0.083552892	15
2	U	2	24.419525	0.022458920	0.092185884	13
2	U	3	24.502352	-0.17823529	0.055811346	19
2	U	4	24.338334	0.061236639	0.083180935	34
2	V	1	25.717204	-0.122178160	0.029361288	5
2	V	2	25.726593	-0.160980550	0.028252094	11
2	V	3	25.846891	-0.148355610	0.031496924	19
2	V	4	25.720261	-0.188080970	0.026640955	15
3	R	1	-122900.15	355271.37	0	1
3	R	2	24.142636	2.4788261	0.49911927	5
3	R	3	25.576049	-0	0	1
3	R	4	25.48305	-0.027371017	0.019808049	8
3	U	1	21.343389	2.3393729	0	2
3	U	2	24.324988	0.042861081	0.08817343	6
3	U	3	24.411103	0.027639938	0.041304654	6
3	U	4	24.289651	0.069990350	0.050400361	17
4	I	1	24.924715	0.066380683	0.033763883	17
4	I	2	24.836795	0.103069110	0.029507213	9
4	I	3	24.991919	0.063915670	0.014322588	12
4	I	4	24.873055	0.052019077	0.035513377	15
4	R	1	25.530826	-0.063740108	0.017618037	16
4	R	2	25.460742	-0.105272190	0.013718417	9
4	R	3	25.547839	-0.082325403	0.045081827	13
4	R	4	25.436631	-0.089318383	0.018449351	9
4	U	1	24.163830	0.057431186	0.069224323	14
4	U	2	24.247673	0.063347937	0.074926674	10
4	U	3	24.359753	0.043377242	0.040512143	15
4	U	4	24.260544	0.040283409	0.053421875	15
4	V	1	25.764703	-0.160303850	0.027698711	19
4	V	2	25.638409	-0.113510300	0.044104453	15
4	V	3	25.787782	-0.159751220	0.033007411	19
4	V	4	25.642244	-0.138388820	0.025511786	17

Table A.1: Original a_0- and a_1-values for the different runs, passbands and chips.

A.3 Estimating the aperture sizes

The observations used are taken with four different detectors: MOSCA, ALFOSC, UH8K and Tek. It is then important to be consistent with the size of the physical aperture diameter. An aperture diameter of $3''$ is chosen. Since 1 pixel corresponds to a different physical size for each of the detectors (MOSCA, ALFOSC, UH8K and Tek), the images were divided into four groups before running SExtractor. For MOSCA 1 pixel corresponds to $0.217''$, for ALFOSC 1 pixel corresponds to $0.189''$, for UH8K 1 pixel corresponds to $0.6''$ and for TEK 1 pixel corresponds to $0.22''$. This means that when running SExtractor the aperture diameter (PHOT_APERTURES) was set to 13.8249 for the MOSCA-images, 15.8730 for the ALFOSC-images, 5.0000 for the UH8K-images and 13.6364 for the Tek-images. This can be seen from the calculations below:

$$\frac{3''}{0.217''/pixel} = 13.8249 pixels, \tag{A.18}$$

$$\frac{3''}{0.189''/pixel} = 15.8730 pixels, \tag{A.19}$$

$$\frac{3''}{0.6''/pixel} = 5.0000 pixels \tag{A.20}$$

and

$$\frac{3''}{0.22''/pixel} = 13.6364 pixels. \tag{A.21}$$

A.4 Special cases in the calibration process

There were two special cases in the calibration process. These occured for the long exposures in the passbands V and I for the galaxy clusters A697 and Zw2089. The V-image of A697 is taken with ALFOSC, while the I-image is from Tek. The V -and I-images for Zw2089 are both taken with ALFOSC. Thus, the calibration equations 3.16, 3.17, 3.18 and 3.19 could not be used. The transformation equations for the other long exposures were found solely on the basis of calibrated calibration exposures of the same clusters. However, for A697 and Zw2089 there were no available calibration exposures taken with MOSCA during the runs of the main data. For this reason I was not able to find transformation equations onto the "MOSCA-system" for these two special cases. The information about the V -and I-images for A697 were received as calibrated imcat-catalogues. The calibrations should be sactisfactory, but the best would clearly have been to use the same calibration equations on all the images. Then systematic errors would not be of the greatest importance. The long exposures in the V -and I-bands for

Zw2089 were reveived both as calibrated catalogues and as images (both from ALFOSC). The images received were much deeper than the images used to form calibrated catalogues. As for A697 I was not able to transform the magnitudes onto the MOSCA-system. However, a transformation from the uncalibreted magnitudes from the FITS files onto the ALFOSC-system was found. In other words, transformation equations between the uncalibrated magnitudes from the FITS files and the ALFOSC-calibrated catalogues from Dahle et. al. (2002) were found. The procedure was equal as the one used to transform the other long exposures onto the MOSCA-system.

Appendix B

Colour-magnitude diagrams

Figure B.1 and B.2 show colour-magnitude diagrams of the 35 galaxy clusters. The magnitude U is plotted along the x-axis and the colour $U - V$ is plotted along the y-axis. The only difference between the two figures is that only cluster-members are plotted in figure B.2, that is, the foreground- and background-galaxies are removed. Because of the many galaxies plotted in each figure, it can be difficult to distinguish between the different symbols. However, as expected, many of the bluest galaxies in figure B.1 are foreground-galaxies. It is also possible to recognize the red sequence (RS) from the different plots (the gathering of many red open diamonds in the position of the RS). The positions of the different galaxy-types in the colour-magnitude diagrams can better be seen by studying figure B.2. From these plots one can clearly distinguish between the RS and what is often referred to as *the blue cloud*. The blue cloud includes most blue galaxies which are generally spirals. In most of the plots in figure B.2 it can be recognized as the small gathering of open stars and cross a bit under the RS. As expected, the bluest galaxies are the spirals, irregulars and starburst galaxies, while the elliptical galaxies are the reddest.

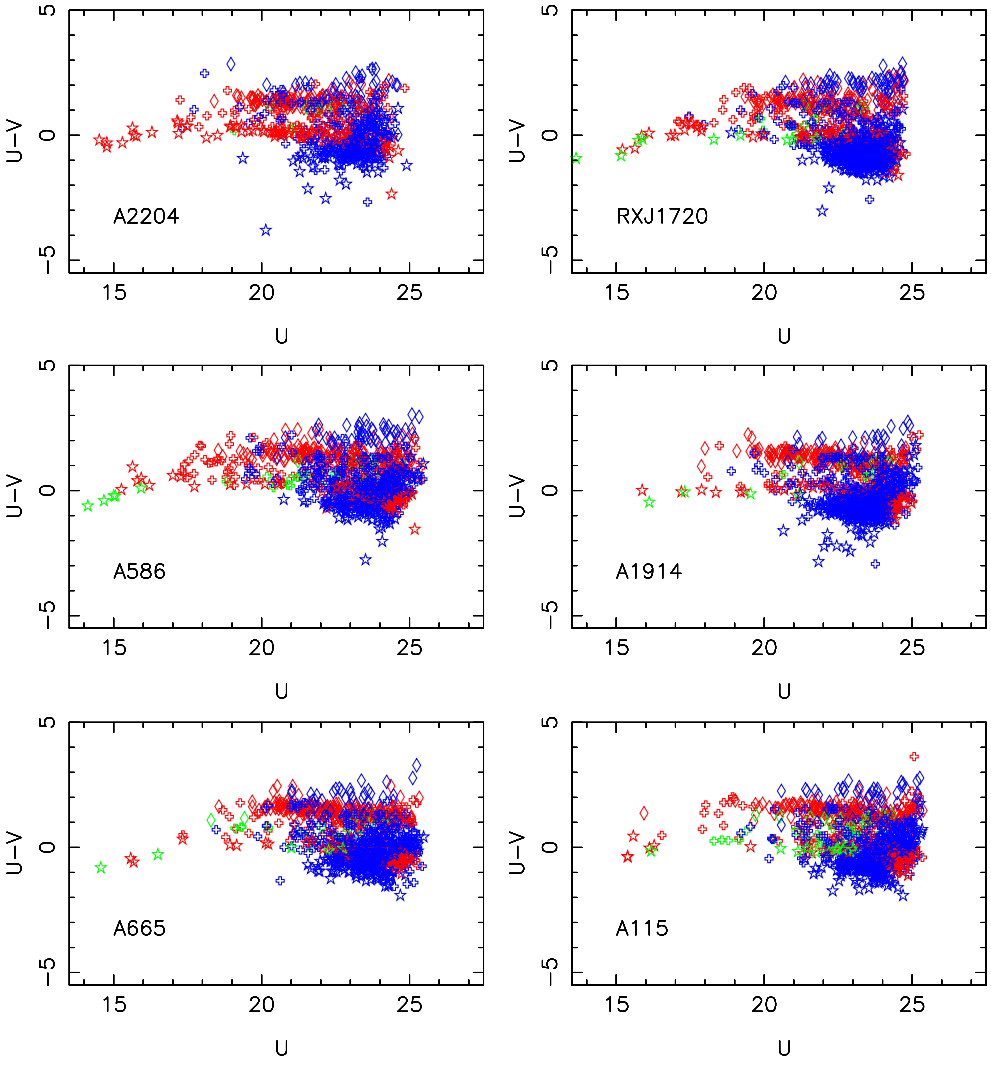

Figure B.1: Colour-magnitude diagrams of the 35 galaxy clusters. The apparent magnitude in the U-band is plotted along the x-axis, while the colour U-V is plotted along the y-axis. Elliptical galaxies (E) are plotted as open diamonds, spiral galaxies (Sbc and Scd) are plotted as open cross, and irregular galaxies and starburst galaxies (Im, SB2 and SB3) are plotted as open stars. In addition, cluster-members are plotted with the colour red, foreground-galaxies are plotted with the colour green, and background-galaxies are plotted with the colour blue. Continued on next page

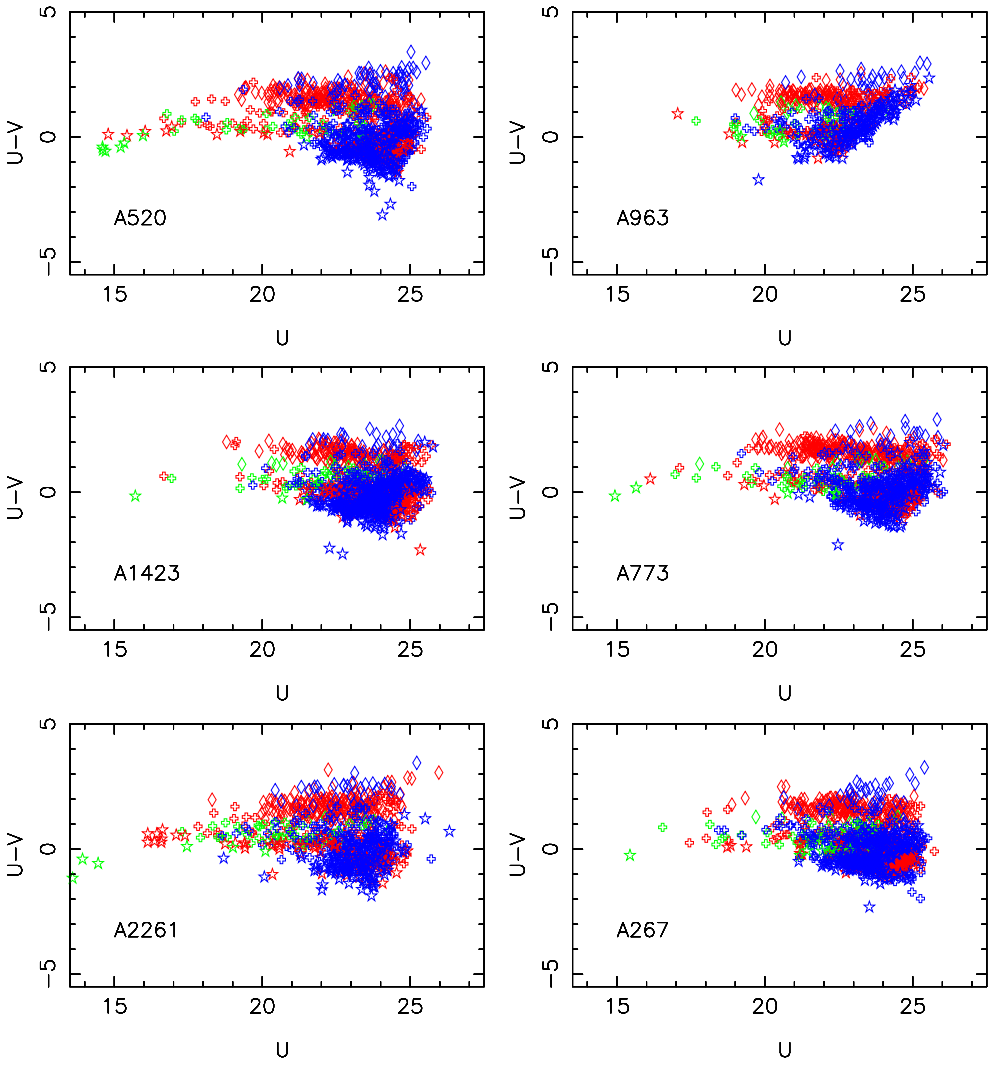

Figure B.1: Continued on next page

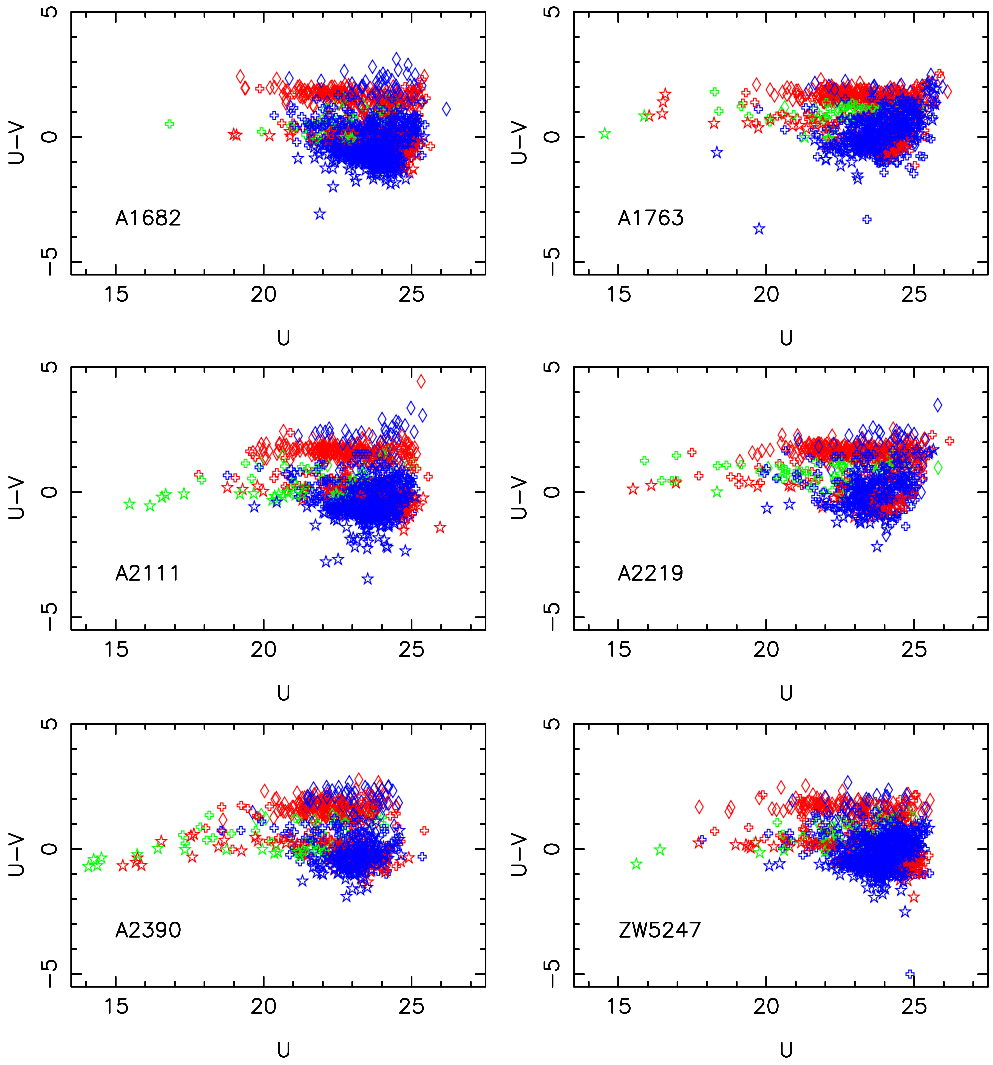

Figure B.1: Continued on next page

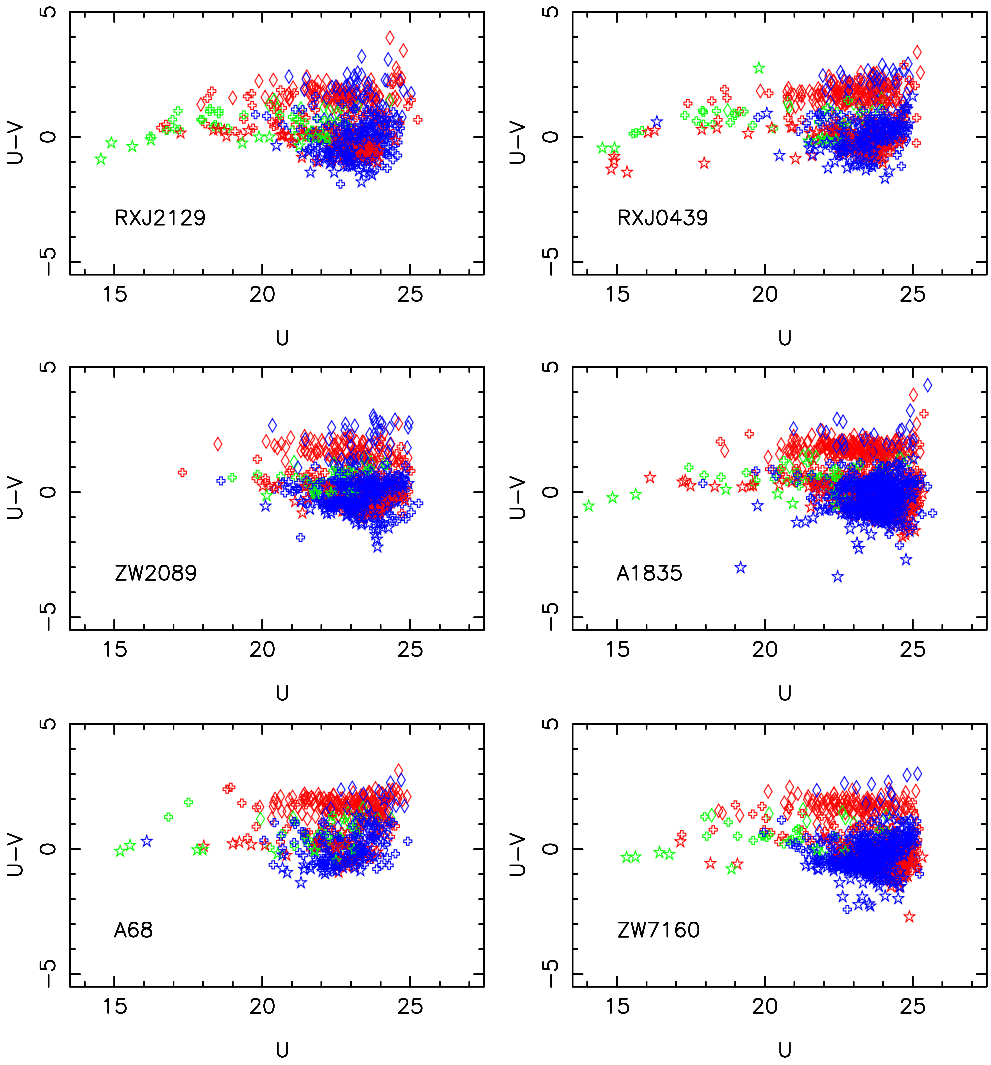

Figure B.1: Continued on next page

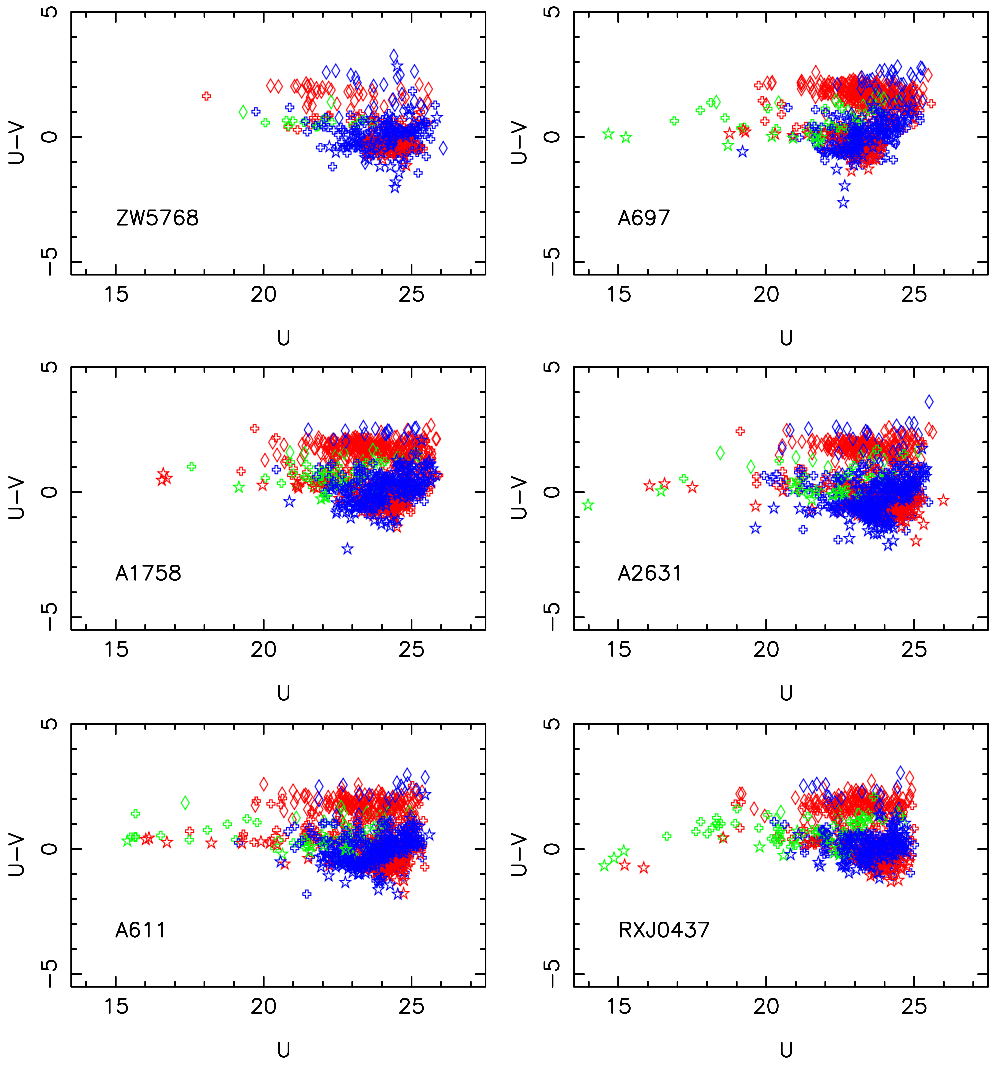

Figure B.1: Continued on next page

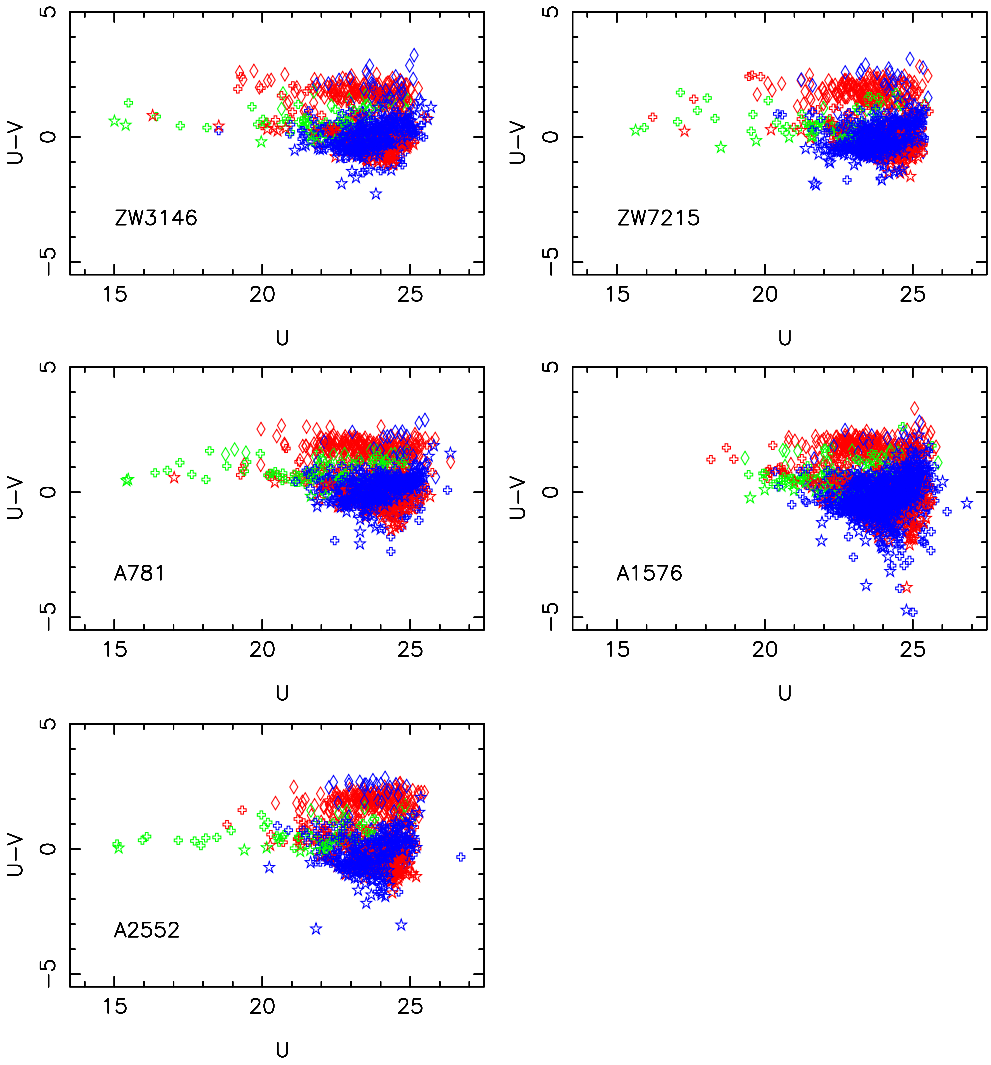

Figure B.1: Continued from previous page

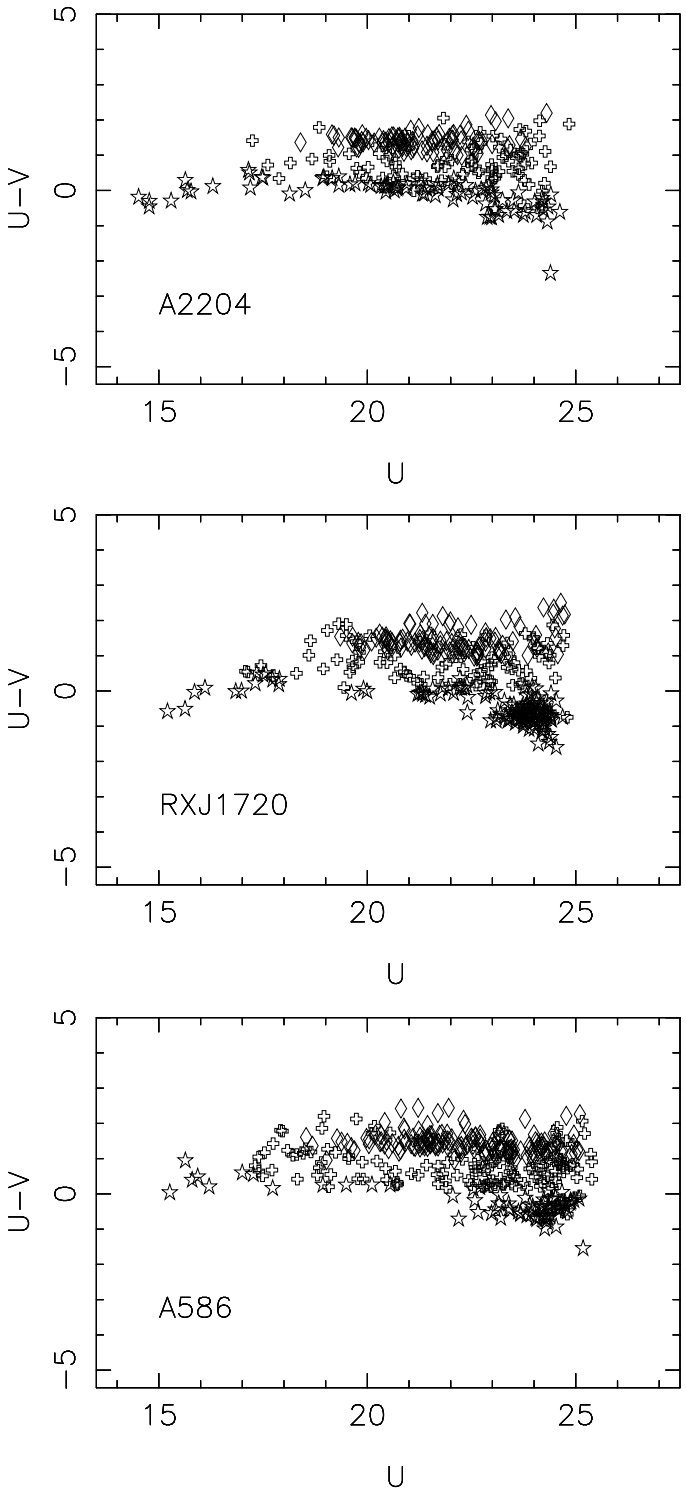

Figure B.2: Colour-magnitude diagrams of the 35 galaxy clusters. The same plots as in figure B.1, but this time only cluster-members have been plotted. Elliptical galaxies (E) are plotted as open diamonds, spiral galaxies (Sbc and Scd) are plotted as open cross, and irregular galaxies and starburst galaxies (Im, SB2 and SB3) are plotted as open stars. Continued on next page

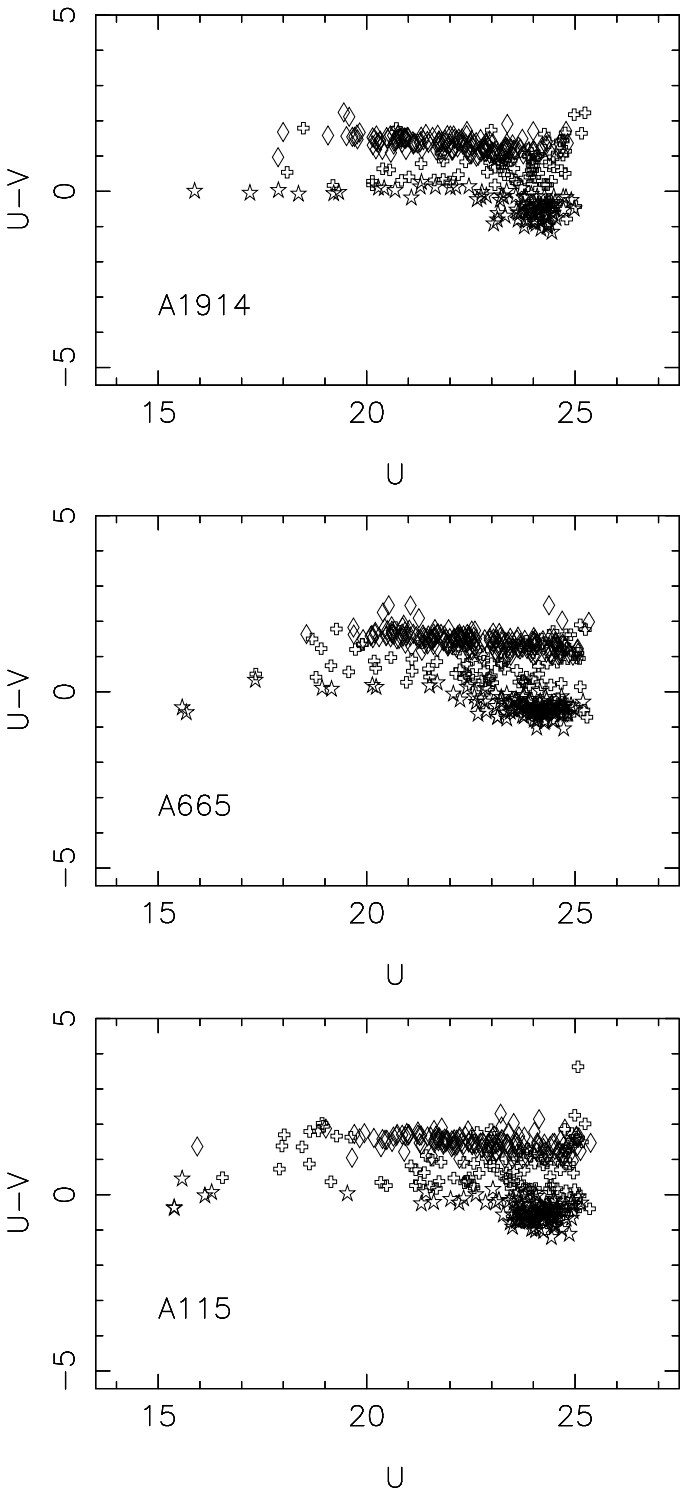

Figure B.2: Continued on next page

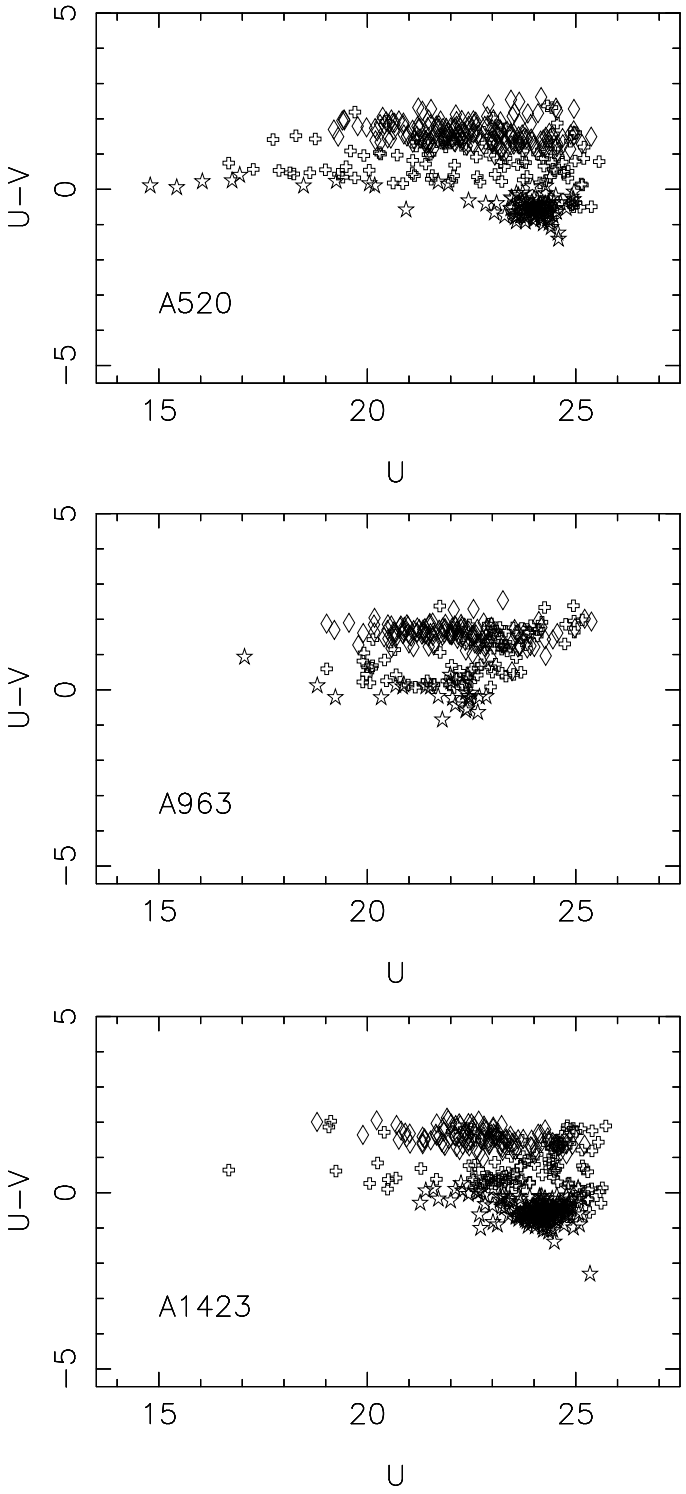

Figure B.2: Continued on next page

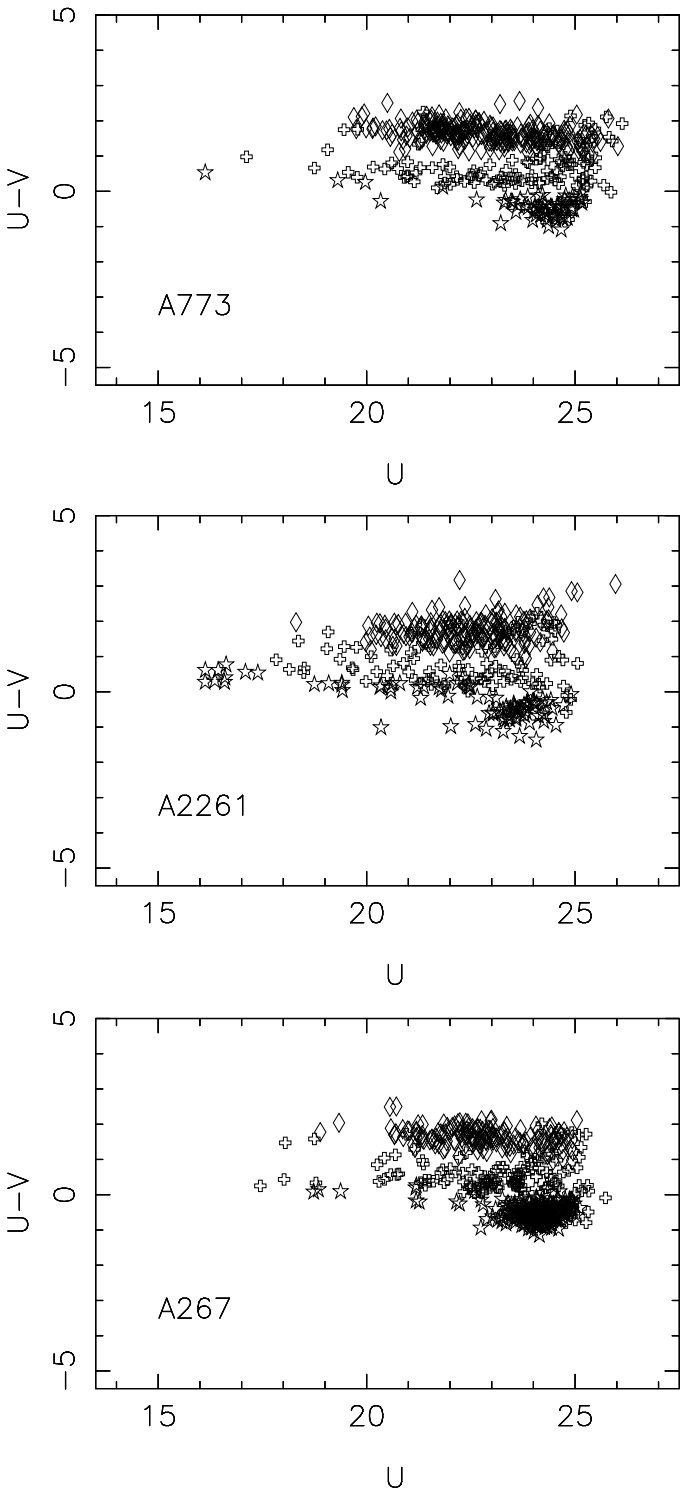

Figure B.2: Continued on next page

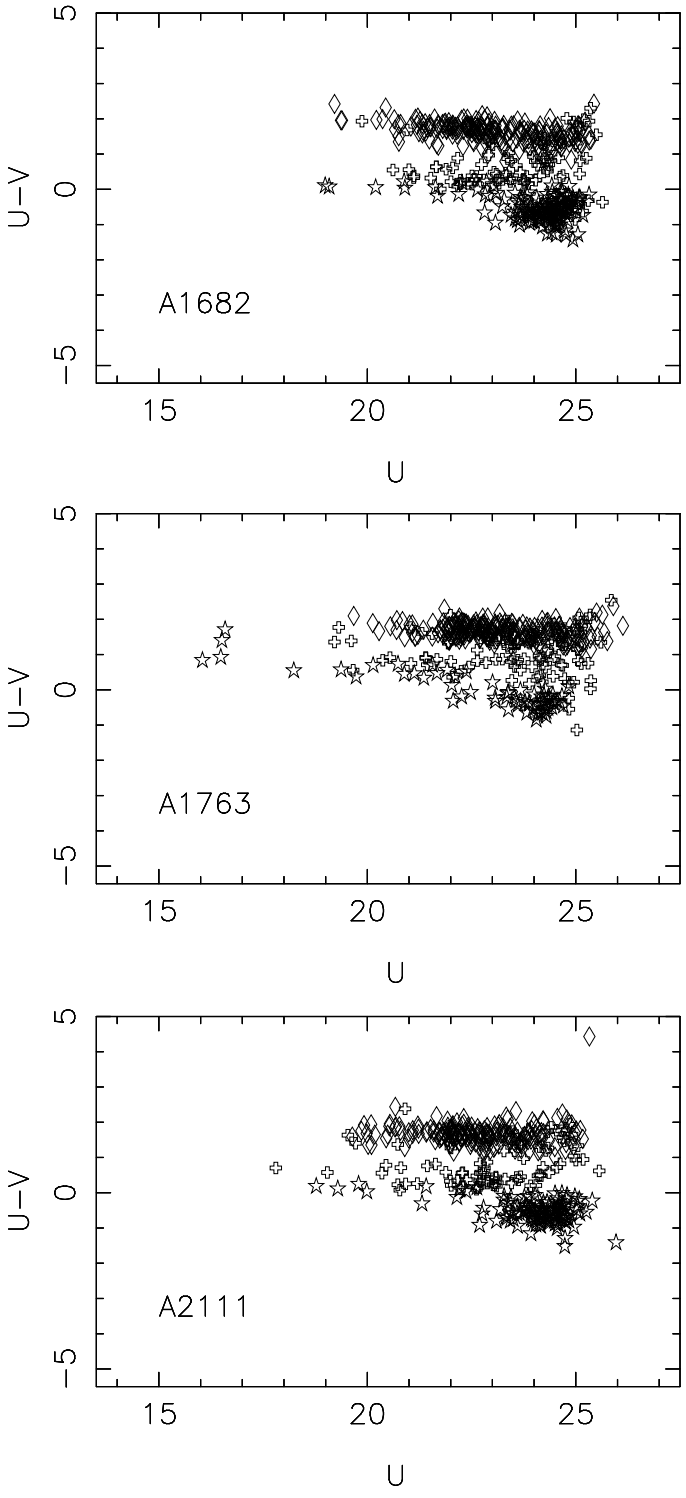

Figure B.2: Continued on next page

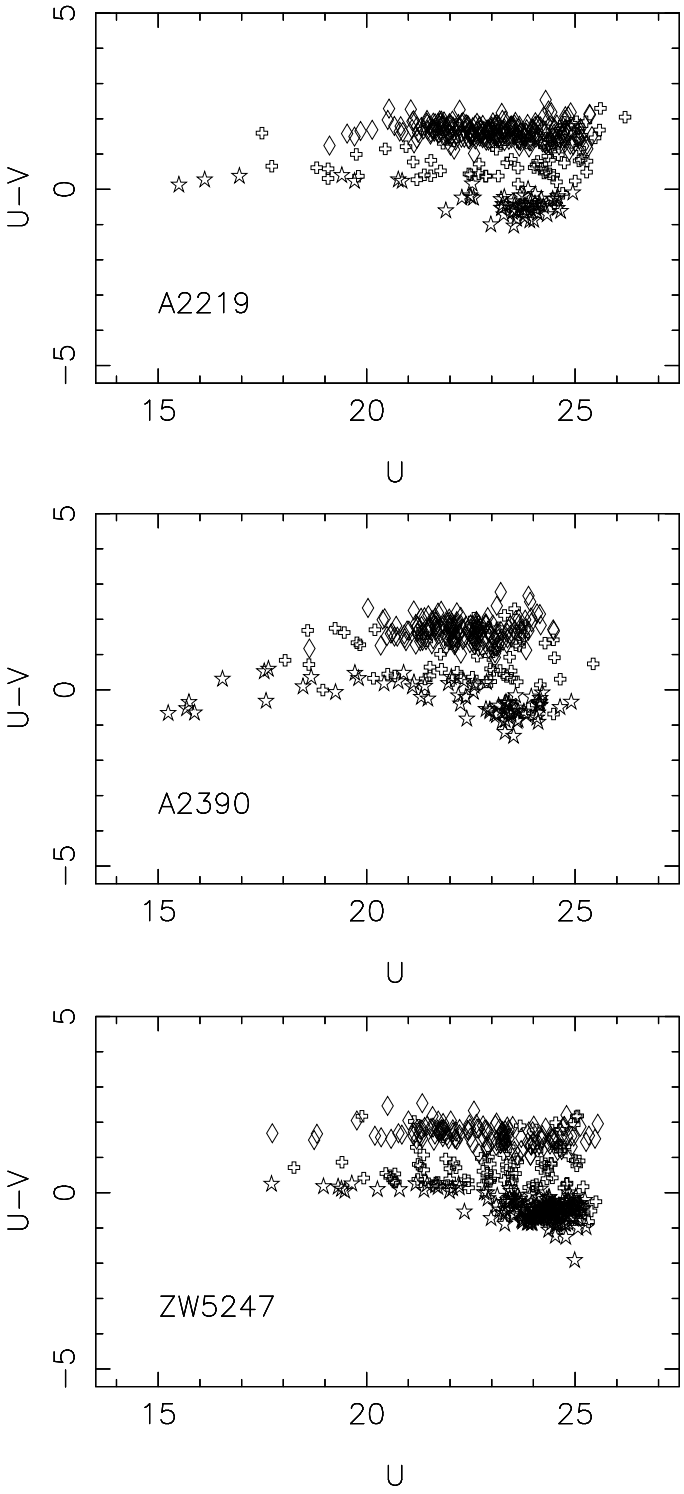

Figure B.2: Continued on next page

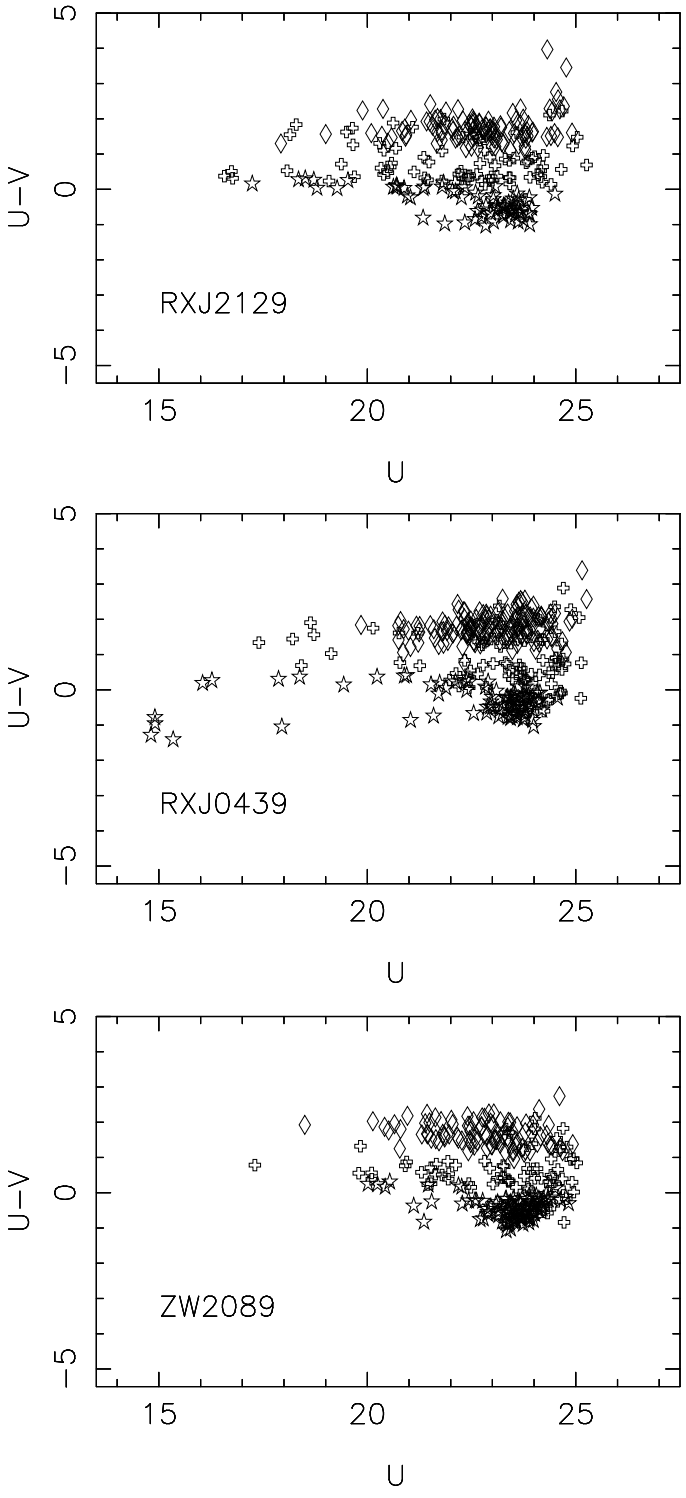

Figure B.2: Continued on next page

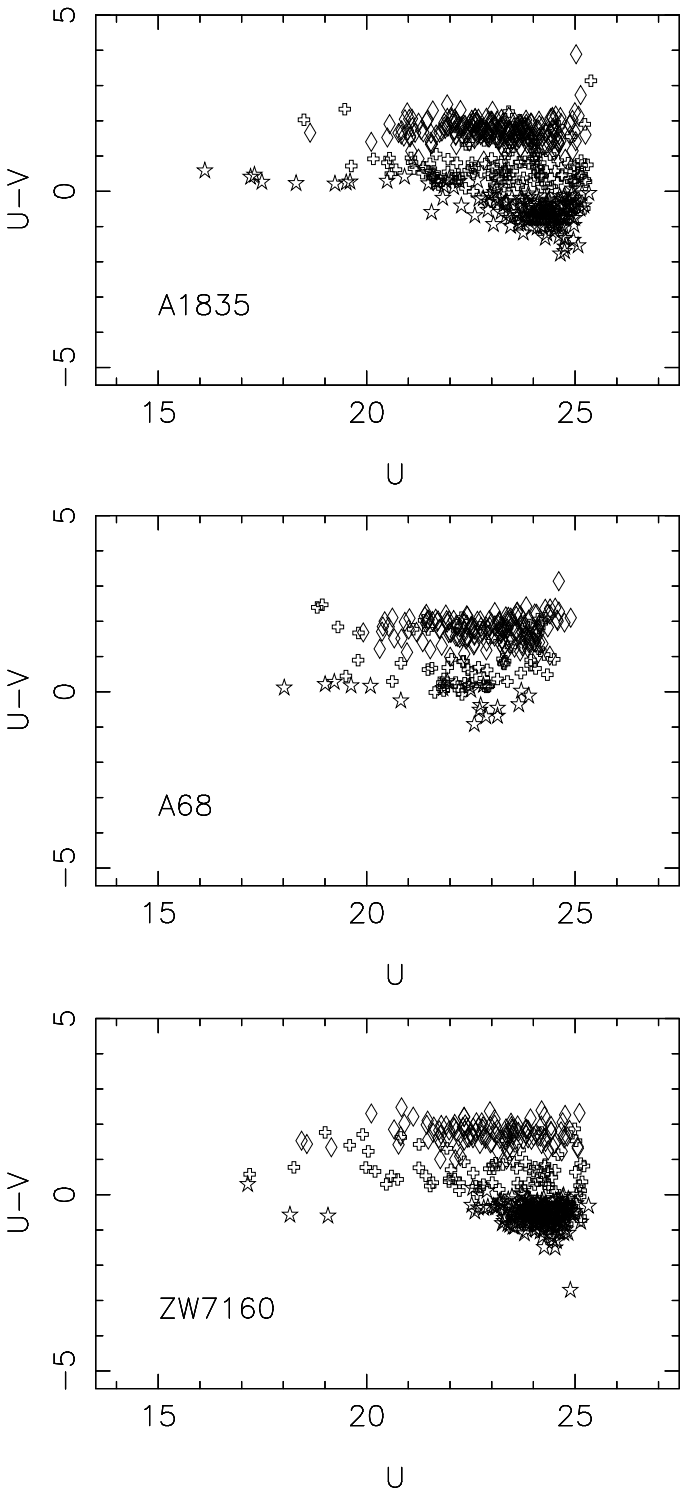

Figure B.2: Continued on next page

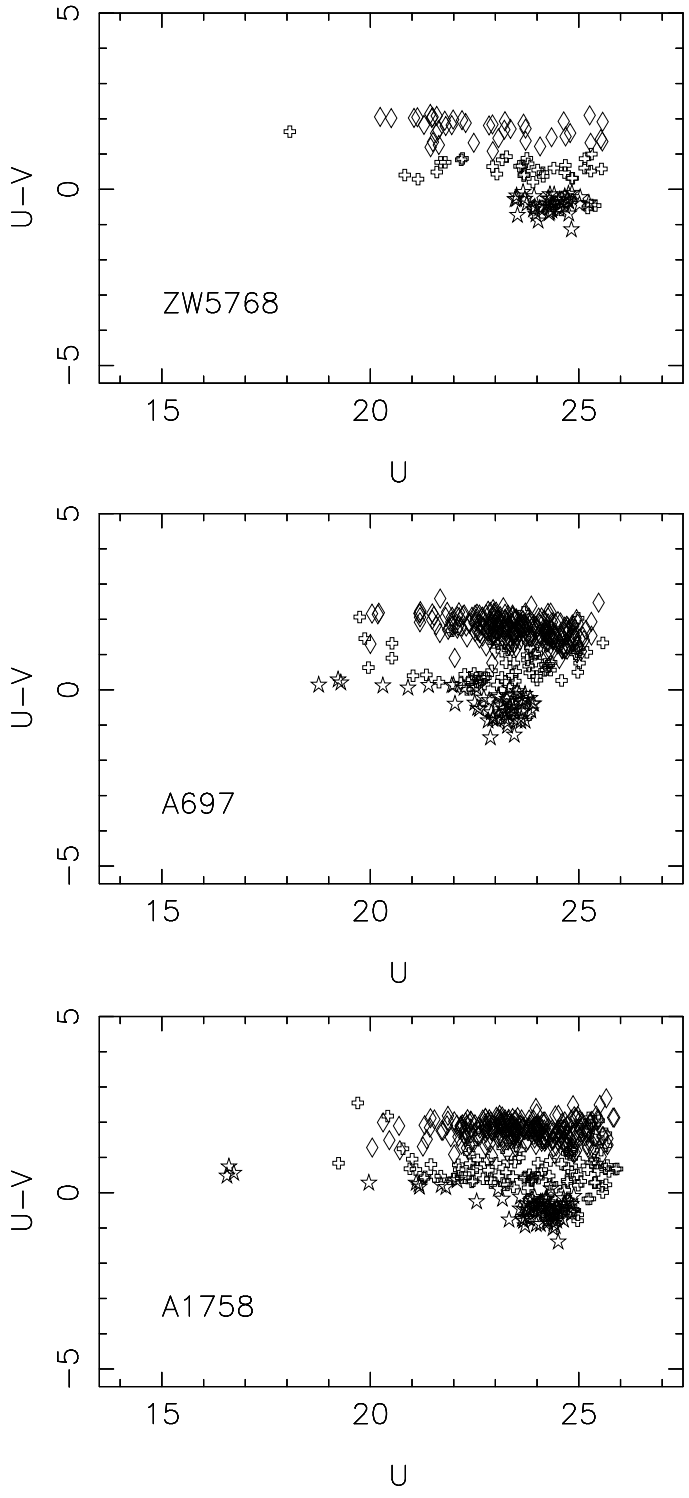

Figure B.2: Continued on next page

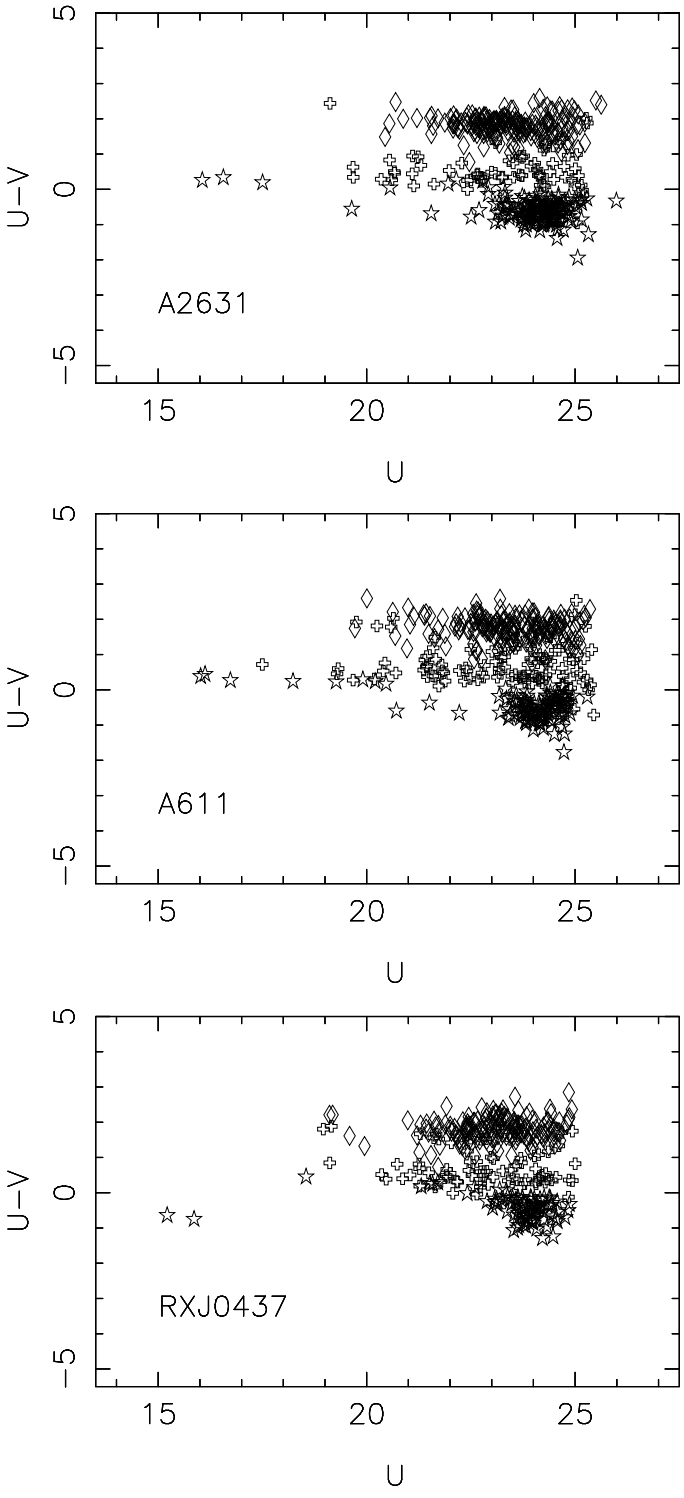

Figure B.2: Continued on next page

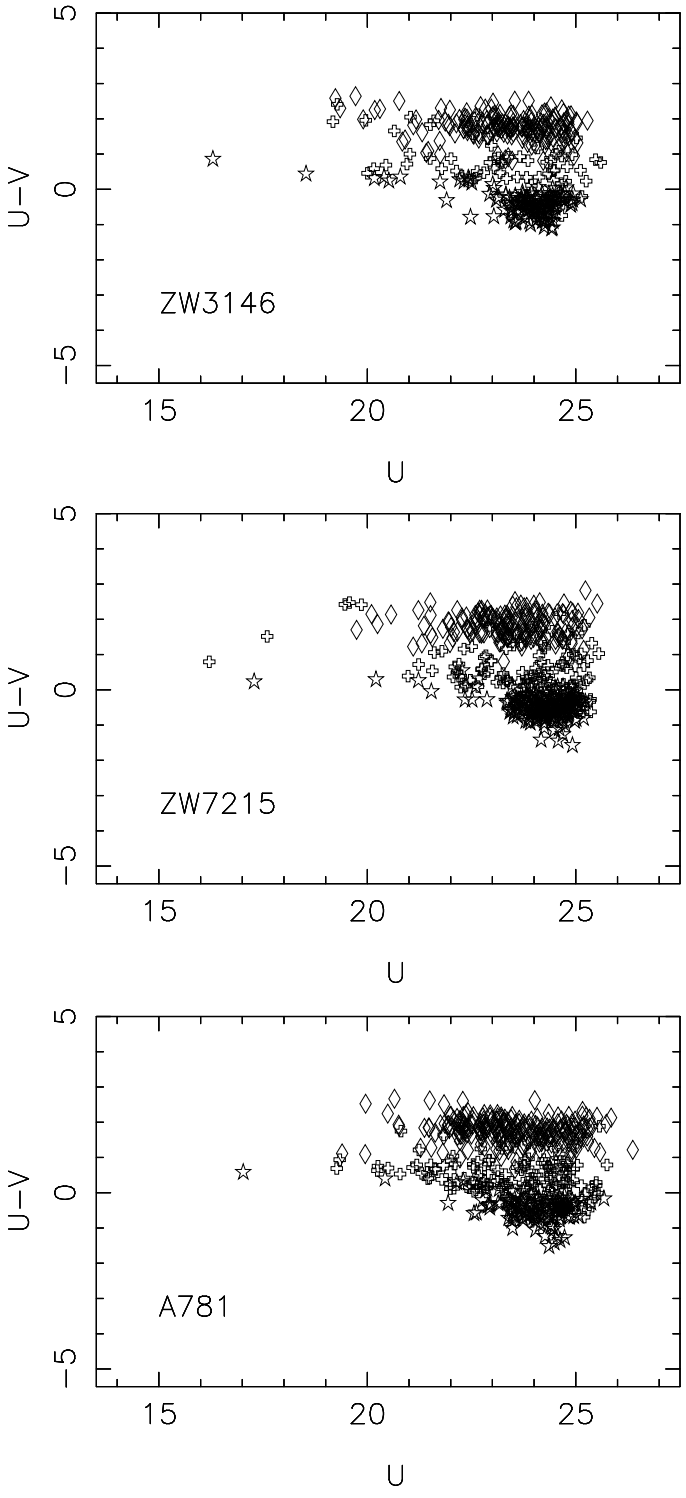

Figure B.2: Continued on next page

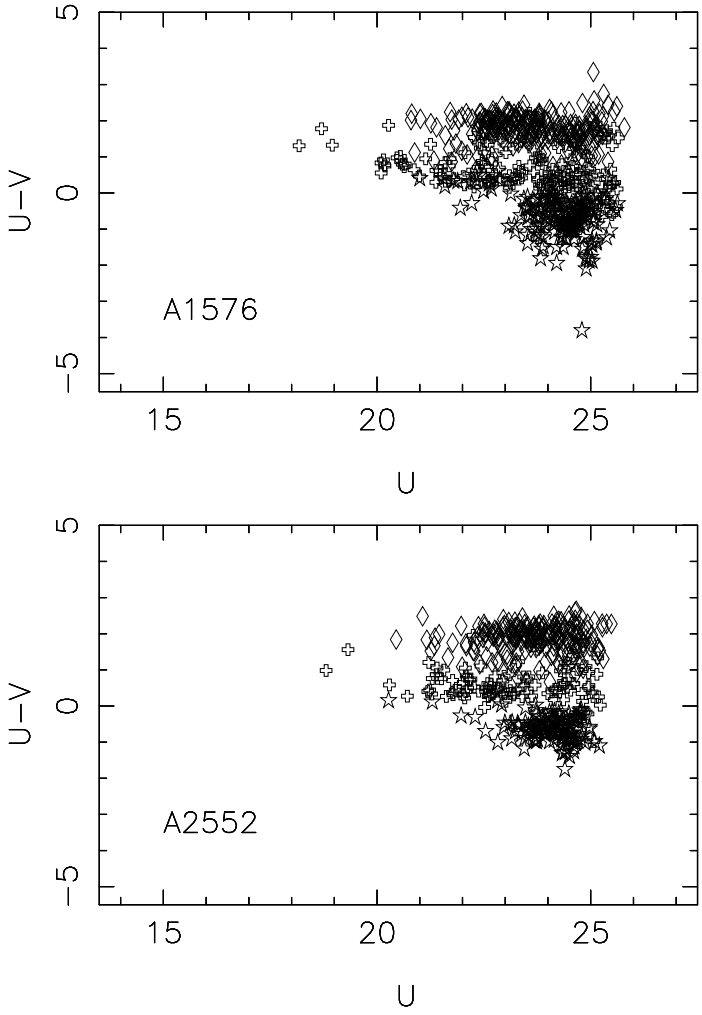

Figure B.2: Continued from previous page

Bibliography

[1] M. G. Abadi, B. Moore, and R. G. Bower. Ram pressure stripping of spiral galaxies in clusters. *MNRAS*, 308:947–954, October 1999.

[2] G. O. Abell, H. G. Corwin, Jr., and R. P. Olowin. A catalog of rich clusters of galaxies. *ApJS*, 70:1–138, May 1989.

[3] M. Arnaboldi, J. A. L. Aguerri, N. R. Napolitano, O. Gerhard, K. C. Freeman, J. Feldmeier, M. Capaccioli, R. P. Kudritzki, and R. H. Méndez. Intracluster Planetary Nebulae in Virgo: Photometric Selection, Spectroscopic Validation, and Cluster Depth. *AJ*, 123:760–771, February 2002.

[4] M. Arnaboldi, K. C. Freeman, R. H. Mendez, M. Capaccioli, R. Ciardullo, H. Ford, O. Gerhard, X. Hui, G. H. Jacoby, R. P. Kudritzki, and P. J. Quinn. The Kinematics of the Planetary Nebulae in the Outer Regions of NGC 4406. *ApJ*, 472:145–+, November 1996.

[5] M. Balogh, V. Eke, C. Miller, I. Lewis, R. Bower, W. Couch, R. Nichol, J. Bland-Hawthorn, I. K. Baldry, C. Baugh, T. Bridges, R. Cannon, S. Cole, M. Colless, C. Collins, N. Cross, G. Dalton, R. de Propris, S. P. Driver, G. Efstathiou, R. S. Ellis, C. S. Frenk, K. Glazebrook, P. Gomez, A. Gray, E. Hawkins, C. Jackson, O. Lahav, S. Lumsden, S. Maddox, D. Madgwick, P. Norberg, J. A. Peacock, W. Percival, B. A. Peterson, W. Sutherland, and K. Taylor. Galaxy ecology: groups and low-density environments in the SDSS and 2dFGRS. *MNRAS*, 348:1355–1372, March 2004.

[6] M. L. Balogh, J. F. Navarro, and S. L. Morris. The Origin of Star Formation Gradients in Rich Galaxy Clusters. *ApJ*, 540:113–121, September 2000.

[7] M. L. Balogh, D. Schade, S. L. Morris, H. K. C. Yee, R. G. Carlberg, and E. Ellingson. The Dependence of Cluster Galaxy Star Formation Rates on the Global Environment. *ApJL*, 504:L75+, September 1998.

[8] J. Bechtold, H. K. C. Yee, R. Elston, and E. Ellingson. H Imaging of the Candidate Protogalaxy MS 1512-cB58. *ApJL*, 477:L29+, March 1997.

[9] J. D. Bekenstein. Relativistic gravitation theory for the modified Newtonian dynamics paradigm. *Physical Review D*, 70(8):083509–+, October 2004.

[10] E. F. Bell, C. Wolf, K. Meisenheimer, H.-W. Rix, A. Borch, S. Dye, M. Kleinheinrich, L. Wisotzki, and D. H. McIntosh. Nearly 5000 Distant Early-Type Galaxies in COMBO-17: A Red Sequence and Its Evolution since z˜1. *ApJ*, 608:752–767, June 2004.

[11] E. Bertin and S. Arnouts. SExtractor: Software for source extraction. *Astron. Astrophys. Suppl.*, 117:393–404, June 1996.

[12] M. S. Bessell. Standard Photometric Systems. *Annu.Rev.Astron.Astrophys*, 43:293–336, September 2005.

[13] B. Binggeli. The luminosity function - Dependence on Hubble type and environment. In S. M. Faber, editor, *Nearly Normal Galaxies. From the Planck Time to the Present*, pages 195–206, 1987.

[14] B. Binggeli, A. Sandage, and G. A. Tammann. The luminosity function of galaxies. *Annu.Rev.Astron.Astrophys.*, 26:509–560, 1988.

[15] James Binney and Michael Merrifield. *Galactic astronomy*. Princeton University Press, 1998.

[16] M. Bolzonella, J.-M. Miralles, and R. Pelló. Photometric redshifts based on standard SED fitting procedures. *Astron. Astrophys.*, 363:476–492, November 2000.

[17] J. R. Bond, L. Kofman, and D. Pogosyan. How filaments of galaxies are woven into the cosmic web. *Nature*, 380:603–606, April 1996.

[18] H. Butcher and A. Oemler, Jr. The evolution of galaxies in clusters. V - A study of populations since Z approximately equal to 0.5. *ApJ*, 285:426–438, October 1984.

[19] Bradley W. Caroll and Dale A. Ostlie. *An introduction to modern astrophysics*. Pearson Education, second edition, 2007.

[20] R. P. Cebula, G. O. Thuillier, M. E. Vanhoosier, E. Hilsenrath, M. Herse, G. E. Brueckner, and P. C. Simon. Observations of the Solar Irradiance in the 200-350 NM Interval During the ATLAS-1 Mission: A Comparison Among Three Sets of Measurements-SSBUV, SOLSPEC and SUSIM. *NASA STI/Recon Technical Report N*, 97:23595–+, August 1996.

[21] R. Cen and J. P. Ostriker. Where Are the Baryons? *ApJ*, 514:1–6, March 1999.

[22] R. Ciardullo, G. H. Jacoby, J. J. Feldmeier, and R. E. Bartlett. The Planetary Nebula Luminosity Function of M87 and the Intracluster Stars of Virgo. *ApJ*, 492:62–+, January 1998.

[23] R. Ciardullo, J. C. Mihos, J. J. Feldmeier, P. R. Durrell, and S. Sigurdsson. The Systematics of Intracluster Starlight. In P.-A. Duc, J. Braine, & E. Brinks, editor, *Recycling Intergalactic and Interstellar Matter*, volume 217 of *IAU Symposium*, pages 88–+, June 2004.

[24] D. Coia, B. McBreen, L. Metcalfe, A. Biviano, B. Altieri, S. Ott, B. Fort, J.-P. Kneib, Y. Mellier, M.-A. Miville-Deschênes, B. O'Halloran, and C. Sanchez-Fernandez. An ISOCAM survey through gravitationally lensing galaxy clusters. IV. Luminous infrared galaxies in Cl 0024+1654 and the dynamical status of clusters. *A&A*, 431:433–449, February 2005.

[25] S. Cole, W. J. Percival, J. A. Peacock, P. Norberg, C. M. Baugh, C. S. Frenk, I. Baldry, J. Bland-Hawthorn, T. Bridges, R. Cannon, M. Colless, C. Collins, W. Couch, N. J. G. Cross, G. Dalton, V. R. Eke, R. De Propris, S. P. Driver, G. Efstathiou, R. S. Ellis, K. Glazebrook, C. Jackson, A. Jenkins, O. Lahav, I. Lewis, S. Lumsden, S. Maddox, D. Madgwick, B. A. Peterson, W. Sutherland, and K. Taylor. The 2dF Galaxy Redshift Survey: power-spectrum analysis of the final data set and cosmological implications. *MNRAS*, 362:505–534, September 2005.

[26] G. D. Coleman, C.-C. Wu, and D. W. Weedman. Colors and magnitudes predicted for high redshift galaxies. *ApJS*, 43:393–416, July 1980.

[27] M. Colless. The dynamics of rich clusters. II - Luminosity functions. *MNRAS*, 237:799–826, April 1989.

[28] Adrian A. Collister. *ANNz User guide*, May 2005.

[29] Adrian A. Collister and Ofer Lahav. Annz: Estimating photometric redshifts using artificial neural networks. August 2009. Draft version.

[30] L. Cortese, G. Gavazzi, and A. Boselli. The ultraviolet luminosity function and star formation rate of the Coma cluster. *MNRAS*, 390:1282–1296, November 2008.

[31] W. J. Couch, A. J. Barger, I. Smail, R. S. Ellis, and R. M. Sharples. Morphological Studies of the Galaxy Populations in Distant "Butcher-Oemler" Clusters with the Hubble Space Telescope. II. AC 103, AC 118, and AC 114 at Z = 0.31. *ApJ*, 497:188–+, April 1998.

[32] S. M. Crawford, M. A. Bershady, and J. G. Hoessel. The Red-Sequence Luminosity Function in Massive Intermediate-Redshift Galaxy Clusters. *ApJ*, 690:1158–1180, January 2009.

[33] D. J. Croton, G. R. Farrar, P. Norberg, M. Colless, J. A. Peacock, I. K. Baldry, C. M. Baugh, J. Bland-Hawthorn, T. Bridges, R. Cannon, S. Cole, C. Collins, W. Couch, G. Dalton, R. De Propris, S. P. Driver, G. Efstathiou, R. S. Ellis, C. S. Frenk, K. Glazebrook, C. Jackson, O. Lahav, I. Lewis, S. Lumsden, S. Maddox, D. Madgwick, B. A. Peterson, W. Sutherland, and K. Taylor. The 2dF Galaxy Redshift Survey: luminosity functions by density environment and galaxy type. *MNRAS*, 356:1155–1167, January 2005.

[34] G. S. Da Costa. Basic Photometry Techniques. In S. B. Howell, editor, *Astronomical CCD Observing and Reduction Techniques*, volume 23 of *Astronomical Society of the Pacific Conference Series*, pages 90–+, 1992.

[35] H. Dahle. The Cluster Mass Function from Weak Gravitational Lensing. *ApJ*, 653:954–962, December 2006.

[36] H. Dahle, N. Kaiser, R. J. Irgens, P. B. Lilje, and S. J. Maddox. Weak Gravitational Lensing by a Sample of X-Ray Luminous Clusters of Galaxies. I. The Data Set. *ApJS*, 139:313–368, April 2002.

[37] T. Dahlen, B. Mobasher, M. Dickinson, H. C. Ferguson, M. Giavalisco, C. Kretchmer, and S. Ravindranath. Evolution of the Luminosity Function, Star Formation Rate, Morphology, and Size of Star-forming Galaxies Selected at Rest-Frame 1500 and 2800 Å. *ApJ*, 654:172–185, January 2007.

[38] R. Davé, R. Cen, J. P. Ostriker, G. L. Bryan, L. Hernquist, N. Katz, D. H. Weinberg, M. L. Norman, and B. O'Shea. Baryons in the Warm-Hot Intergalactic Medium. *ApJ*, 552:473–483, May 2001.

[39] G. De Lucia, B. M. Poggianti, A. Aragón-Salamanca, D. Clowe, C. Halliday, P. Jablonka, B. Milvang-Jensen, R. Pelló, S. Poirier, G. Rudnick, R. Saglia, L. Simard, and S. D. M. White. The Buildup of the Red Sequence in Galaxy Clusters since z ˜ 0.8. *ApJL*, 610:L77–L80, August 2004.

[40] Scott Dodelson. *Modern cosmology*. Academic Press, 2003.

[41] J. Donas, J. M. Deharveng, M. Laget, B. Milliard, and D. Huguenin. Ultraviolet observations and star-formation rate in galaxies. *A&A*, 180:12–26, June 1987.

[42] A. Dressler. Galaxy morphology in rich clusters - Implications for the formation and evolution of galaxies. *ApJ*, 236:351–365, March 1980.

[43] A. Dressler, A. Oemler, Jr., W. J. Couch, I. Smail, R. S. Ellis, A. Barger, H. Butcher, B. M. Poggianti, and R. M. Sharples. Evolution since Z = 0.5 of the Morphology-Density Relation for Clusters of Galaxies. *ApJ*, 490:577–+, December 1997.

[44] R. S. Ellis, M. Colless, T. Broadhurst, J. Heyl, and K. Glazebrook. Autofib Redshift Survey - I. Evolution of the galaxy luminosity function. *MNRAS*, 280:235–251, May 1996.

[45] Dafydd Wyn Evans and Bob Argyle. *Atmospheric Extinction from the CMT*, 2009.

[46] D. Fadda, A. Biviano, F. R. Marleau, L. J. Storrie-Lombardi, and F. Durret. Starburst Galaxies in Cluster-feeding Filaments Unveiled by Spitzer. *ApJL*, 672:L9–L12, January 2008.

[47] G. Fasano, C. Marmo, J. Varela, M. D'Onofrio, B. M. Poggianti, M. Moles, E. Pignatelli, D. Bettoni, P. Kjærgaard, L. Rizzi, W. J. Couch, and A. Dressler. WINGS: a WIde-field Nearby Galaxy-cluster Survey. I. Optical imaging. *A&A*, 445:805–817, January 2006.

[48] R. Feldmann, C. M. Carollo, C. Porciani, S. J. Lilly, P. Capak, Y. Taniguchi, O. Le Fèvre, A. Renzini, N. Scoville, M. Ajiki, H. Aussel, T. Contini, H. McCracken, B. Mobasher, T. Murayama, D. Sanders, S. Sasaki, C. Scarlata, M. Scodeggio, Y. Shioya, J. Silverman, M. Takahashi, D. Thompson, and G. Zamorani. The Zurich Extragalactic Bayesian Redshift Analyzer and its first application: COSMOS. *MNRAS*, 372:565–577, October 2006.

[49] J. J. Feldmeier, R. Ciardullo, G. H. Jacoby, and P. R. Durrell. Intracluster Planetary Nebulae in the Virgo Cluster. III. Luminosity of the Intracluster Light and Tests of the Spatial Distribution. *ApJ*, 615:196–208, November 2004.

[50] R. A. Finn, D. Zaritsky, D. W. McCarthy, Jr., B. Poggianti, G. Rudnick, C. Halliday, B. Milvang-Jensen, R. Pelló, and L. Simard. Hα-derived Star Formation Rates for Three z˜=0.75 EDisCS Galaxy Clusters. *ApJ*, 630:206–227, September 2005.

[51] Z. Frei and J. E. Gunn. Generating colors and K corrections from existing catalog data. *AJ*, 108:1476–1485, October 1994.

[52] A. Gallazzi, E. F. Bell, C. Wolf, M. E. Gray, C. Papovich, M. Barden, C. Y. Peng, K. Meisenheimer, C. Heymans, E. van Kampen, R. Gilmour, M. Balogh, D. H. McIntosh, D. Bacon, F. D. Barazza, A. Böhm, J. A. R. Caldwell, B. Häußler, K. Jahnke, S. Jogee, K. Lane, A. R. Robaina, S. F. Sanchez, A. Taylor, L. Wisotzki, and X. Zheng. Obscured Star Formation in Intermediate-Density Environments: A

Spitzer Study of the Abell 901/902 Supercluster. *ApJ*, 690:1883–1900, January 2009.

[53] J. Gallego, J. Zamorano, A. Aragon-Salamanca, and M. Rego. The Current Star Formation Rate of the Local Universe. *ApJL*, 455:L1+, December 1995.

[54] J. E. Geach, I. Smail, R. S. Ellis, S. M. Moran, G. P. Smith, T. Treu, J.-P. Kneib, A. C. Edge, and T. Kodama. A Panoramic Mid-Infrared Survey of Two Distant Clusters. *ApJ*, 649:661–672, October 2006.

[55] O. Gerhard, M. Arnaboldi, K. C. Freeman, and S. Okamura. Isolated Star Formation: A Compact H II Region in the Virgo Cluster. *ApJL*, 580:L121–L124, December 2002.

[56] M. Giavalisco, M. Dickinson, H. C. Ferguson, S. Ravindranath, C. Kretchmer, L. A. Moustakas, P. Madau, S. M. Fall, J. P. Gardner, M. Livio, C. Papovich, A. Renzini, H. Spinrad, D. Stern, and A. Riess. The Rest-Frame Ultraviolet Luminosity Density of Star-forming Galaxies at Redshifts z>3.5. *ApJL*, 600:L103–L106, January 2004.

[57] T. Goto, M. Postman, N. J. G. Cross, G. D. Illingworth, K. Tran, D. Magee, M. Franx, N. Benítez, R. J. Bouwens, R. Demarco, H. C. Ford, N. L. Homeier, A. R. Martel, F. Menanteau, M. Clampin, G. F. Hartig, D. R. Ardila, F. Bartko, J. P. Blakeslee, L. D. Bradley, T. J. Broadhurst, R. A. Brown, C. J. Burrows, E. S. Cheng, P. D. Feldman, D. A. Golimowski, C. Gronwall, B. Holden, L. Infante, M. J. Jee, J. E. Krist, M. P. Lesser, S. Mei, G. R. Meurer, G. K. Miley, V. Motta, R. Overzier, M. Sirianni, W. B. Sparks, H. D. Tran, Z. I. Tsvetanov, R. L. White, W. Zheng, and A. Zirm. Luminosity Functions of the Galaxy Cluster MS 1054-0321 at z=0.83 based on ACS Photometry. *ApJ*, 621:188–200, March 2005.

[58] J. E. Gunn and J. R. Gott, III. On the Infall of Matter Into Clusters of Galaxies and Some Effects on Their Evolution. *ApJ*, 176:1–+, August 1972.

[59] C. P. Haines, A. Mercurio, P. Merluzzi, F. La Barbera, M. Massarotti, G. Busarello, and M. Girardi. Galaxy evolution in the environment of ABCG 209. *A&A*, 425:783–796, October 2004.

[60] C. P. Haines, G. P. Smith, E. Egami, R. S. Ellis, S. M. Moran, A. J. R. Sanderson, P. Merluzzi, G. Busarello, and R. J. Smith. LOCUSS: The Mid-Infrared Butcher-Oemler Effect. *ApJ*, 704:126–136, October 2009.

[61] M. A. Hausman and J. P. Ostriker. Galactic cannibalism. III - The morphological evolution of galaxies and clusters. *ApJ*, 224:320–336, September 1978.

[62] J. P. Henry and U. G. Briel. An X-ray temperature map of Abell 754: A major merger. *ApJL*, 443:L9–L12, April 1995.

[63] D. W. Hogg, I. K. Baldry, M. R. Blanton, and D. J. Eisenstein. The K correction. eprint arXiv:astro-ph/0210394, October 2002.

[64] D. W. Hogg, M. Masjedi, A. A. Berlind, M. R. Blanton, A. D. Quintero, and J. Brinkmann. What Triggers Galaxy Transformations? The Environments of Poststarburst Galaxies. *ApJ*, 650:763–769, October 2006.

[65] Steve B. Howell. *Handbook of CCD Astronomy*. Cambridge University Press, second edition, 2006.

[66] F. Hoyle, R. R. Rojas, M. S. Vogeley, and J. Brinkmann. The Luminosity Function of Void Galaxies in the Sloan Digital Sky Survey. *ApJ*, 620:618–628, February 2005.

[67] L. Infante. A faint object processing software - Description and testing. *A&A*, 183:177–184, September 1987.

[68] R. C. Kennicutt, Jr. Star Formation in Galaxies Along the Hubble Sequence. *Annu.Rev.Astron.Astrophys*, 36:189–232, 1998.

[69] R. C. Kennicutt, Jr., F. Bresolin, D. J. Bomans, G. D. Bothun, and I. B. Thompson. Large scale structure of the ionized gas in the magellanic clouds. *AJ*, 109:594–604, February 1995.

[70] D. L. King. *Atmospheric Extinction at the Roque de los Muchachos Observatory*, September 1985. RGO/La Palma technical note no 31.

[71] A. L. Kinney, D. Calzetti, R. C. Bohlin, K. McQuade, T. Storchi-Bergmann, and H. R. Schmitt. Template Ultraviolet to Near-Infrared Spectra of Star-forming Galaxies and Their Application to K-Corrections. *ApJ*, 467:38–+, August 1996.

[72] C. R. Kitchin. *Astrophysical Techniques*. CRC Press, fifth edition, 2009.

[73] A. Kravtsov, A. Gonzalez, A. Vikhlinin, D. Marrone, A. Zabludoff, D. Nagai, M. Markevitch, B. Benson, S. Golwala, S. Meyers, M. Gladders, D. Rudd, A. Evrard, C. Conroy, and S. Allen. Towards the 2020 vision of the baryon content of galaxy groups and clusters. In *astro2010: The Astronomy and Astrophysics Decadal Survey*, volume 2010 of *Astronomy*, pages 164–+, 2009.

[74] R. G. Kron. Photometry of a complete sample of faint galaxies. *ApJS*, 43:305–325, June 1980.

[75] A. U. Landolt. UBVRI photometric standard stars in the magnitude range 11.5-16.0 around the celestial equator. *AJ*, 104:340–371,436–491, July 1992.

[76] D. Larson, J. Dunkley, G. Hinshaw, E. Komatsu, M. R. Nolta, C. L. Bennett, B. Gold, M. Halpern, R. S. Hill, N. Jarosik, A. Kogut, M. Limon, S. S. Meyer, N. Odegard, L. Page, K. M. Smith, D. N. Spergel, G. S. Tucker, J. L. Weiland, E. Wollack, and E. L. Wright. Seven-Year Wilkinson Microwave Anisotropy Probe (WMAP) Observations: Power Spectra and WMAP-Derived Parameters. *ArXiv e-prints*, January 2010.

[77] R. B. Larson, B. M. Tinsley, and C. N. Caldwell. The evolution of disk galaxies and the origin of S0 galaxies. *ApJ*, 237:692–707, May 1980.

[78] O. Le Fèvre, R. Abraham, S. J. Lilly, R. S. Ellis, J. Brinchmann, D. Schade, L. Tresse, M. Colless, D. Crampton, K. Glazebrook, F. Hammer, and T. Broadhurst. Hubble Space Telescope imaging of the CFRS and LDSS redshift surveys - IV. Influence of mergers in the evolution of faint field galaxies from z˜1. *MNRAS*, 311:565–575, January 2000.

[79] I. Lewis, M. Balogh, R. De Propris, W. Couch, R. Bower, A. Offer, J. Bland-Hawthorn, I. K. Baldry, C. Baugh, T. Bridges, R. Cannon, S. Cole, M. Colless, C. Collins, N. Cross, G. Dalton, S. P. Driver, G. Efstathiou, R. S. Ellis, C. S. Frenk, K. Glazebrook, E. Hawkins, C. Jackson, O. Lahav, S. Lumsden, S. Maddox, D. Madgwick, P. Norberg, J. A. Peacock, W. Percival, B. A. Peterson, W. Sutherland, and K. Taylor. The 2dF Galaxy Redshift Survey: the environmental dependence of galaxy star formation rates near clusters. *MNRAS*, 334:673–683, August 2002.

[80] S. J. Lilly, O. Le Fevre, F. Hammer, and D. Crampton. The Canada-France Redshift Survey: The Luminosity Density and Star Formation History of the Universe to Z approximately 1. *ApJL*, 460:L1+, March 1996.

[81] S. J. Lilly, L. Tresse, F. Hammer, D. Crampton, and O. Le Fevre. The Canada-France Redshift Survey. VI. Evolution of the Galaxy Luminosity Function to Z approximately 1. *ApJ*, 455:108–+, December 1995.

[82] C. Lobo, A. Biviano, F. Durret, D. Gerbal, O. Le Fevre, A. Mazure, and E. Slezak. Environmental effects on the Coma cluster luminosity function. *A&A*, 317:385–392, January 1997.

[83] Malcolm S. Longair. *Galaxy Formation*. Springer, second edition, 2008.

[84] J. Loveday. Evolution of the galaxy luminosity function at z $<$ 0.3. *MNRAS*, 347:601–606, January 2004.

[85] P. M. Lugger. Luminosity functions for nine Abell clusters. *ApJ*, 303:535–555, April 1986.

[86] P. Madau, H. C. Ferguson, M. E. Dickinson, M. Giavalisco, C. C. Steidel, and A. Fruchter. High-redshift galaxies in the Hubble Deep Field: colour selection and star formation history to z˜4. *MNRAS*, 283:1388–1404, December 1996.

[87] P. Madau, L. Pozzetti, and M. Dickinson. The Star Formation History of Field Galaxies. *ApJ*, 498:106–+, May 1998.

[88] A. Mercurio, M. Massarotti, P. Merluzzi, M. Girardi, F. La Barbera, and G. Busarello. Optical luminosity functions of the Abell galaxy cluster ABCG 209 at z = 0.21. *A&A*, 408:57–65, September 2003.

[89] W. J. Merline and S. B. Howell. A Realistic Model for Point-sources Imaged on Array Detectors: The Model and Initial Results. *Experimental Astronomy*, 6:163–210, January 1995.

[90] M. Milgrom. A modification of the Newtonian dynamics - Implications for galaxies. *ApJ*, 270:371–389, July 1983.

[91] M. Milgrom. A Modification of the Newtonian Dynamics - Implications for Galaxy Systems. *ApJ*, 270:384–+, July 1983.

[92] M. Milgrom. A modification of the Newtonian dynamics as a possible alternative to the hidden mass hypothesis. *ApJ*, 270:365–370, July 1983.

[93] J. J. Mohr, A. E. Evrard, D. G. Fabricant, and M. J. Geller. Cosmological Constraints from Observed Cluster X-Ray Morphologies. *ApJ*, 447:8–+, July 1995.

[94] E. Molinari, G. Chincarini, A. Moretti, and S. de Grandi. The composite luminosity function of A 496. *A&A*, 338:874–880, October 1998.

[95] B. Moore, N. Katz, G. Lake, A. Dressler, and A. Oemler. Galaxy harassment and the evolution of clusters of galaxies. *Nature*, 379:613–616, February 1996.

[96] S. M. Moran, R. S. Ellis, T. Treu, I. Smail, A. Dressler, A. L. Coil, and G. P. Smith. A Wide-Field Hubble Space Telescope Survey of the Cluster Cl 0024+16 at z = 0.4. III. Spectroscopic Signatures of Environmental Evolution in Early-Type Galaxies. *ApJ*, 634:977–1001, December 2005.

[97] A. Moretti, E. Molinari, G. Chincarini, and S. De Grandi. The luminosity function of cluster galaxies. II. Data reduction procedures applied to the cluster Abell 496. *A&AS*, 140:155–170, December 1999.

[98] G. Murante, M. Giovalli, O. Gerhard, M. Arnaboldi, S. Borgani, and K. Dolag. The importance of mergers for the origin of intracluster stars in cosmological simulations of galaxy clusters. *MNRAS*, 377:2–16, May 2007.

[99] F. Nakata, M. Kajisawa, T. Yamada, T. Kodama, K. Shimasaku, I. Tanaka, M. Doi, H. Furusawa, M. Hamabe, M. Iye, M. Kimura, Y. Komiyama, S. Miyazaki, S. Okamura, M. Ouchi, T. Sasaki, M. Sekiguchi, M. Yagi, and N. Yasuda. Galaxy Population in a Cluster of Galaxies around the Radio Galaxy 3C 324 at z=1.2. *PASJ*, 53:1139–1152, December 2001.

[100] A. Oemler, Jr., A. Dressler, and H. R. Butcher. The Morphology of Distant Cluster Galaxies. II. HST Observations of Four Rich Clusters at Z 0.4. *ApJ*, 474:561–+, January 1997.

[101] J. B. Oke. Absolute Spectral Energy Distributions for White Dwarfs. *ApJS*, 27:21–+, February 1974.

[102] U.-L. Pen. Heating of the Intergalactic Medium. *ApJL*, 510:L1–L5, January 1999.

[103] Ue-Li Pen. Analytical Fit to the Luminosity Distance for Flat Cosmologies with a Cosmological Constant. *ApJS*, 120:49–50, January 1999.

[104] Steven Phillips. *The structure and evolution of galaxies*. Wiley, 2005.

[105] G. B. Poole, M. A. Fardal, A. Babul, I. G. McCarthy, T. Quinn, and J. Wadsley. The impact of mergers on relaxed X-ray clusters - I. Dynamical evolution and emergent transient structures. *MNRAS*, 373:881–905, December 2006.

[106] P. Popesso, A. Biviano, H. Böhringer, and M. Romaniello. RASS-SDSS Galaxy cluster survey. IV. A ubiquitous dwarf galaxy population in clusters. *A&A*, 445:29–42, January 2006.

[107] W. H. Press and P. Schechter. Formation of Galaxies and Clusters of Galaxies by Self-Similar Gravitational Condensation. *ApJ*, 187:425–438, February 1974.

[108] E. Puchwein, V. Springel, D. Sijacki, and K. Dolag. Intracluster stars in simulations with AGN feedback. *ArXiv e-prints*, January 2010.

[109] A. Renzini. Stellar Population Diagnostics of Elliptical Galaxy Formation. *Annu.Rev.Astron.Astrophys*, 44:141–192, September 2006.

[110] M. Rowan-Robinson, R. G. Mann, S. J. Oliver, A. Efstathiou, N. Eaton, P. Goldschmidt, B. Mobasher, S. B. G. Serjeant, T. J. Sumner, L. Danese, D. Elbaz, A. Franceschini, E. Egami, M. Kontizas, A. Lawrence, R. McMahon, H. U. Norgaard-Nielsen, I. Perez-Fournon, and J. I. Gonzalez-Serrano. Observations of the Hubble Deep Field with the Infrared Space Observatory - V. Spectral energy distributions, starburst models and star formation history. *MNRAS*, 289:490–496, August 1997.

[111] S. Roychowdhury, M. Ruszkowski, B. B. Nath, and M. C. Begelman. Entropy "Floor" and Effervescent Heating of Intracluster Gas. *ApJ*, 615:681–688, November 2004.

[112] D. J. Schlegel, D. P. Finkbeiner, and M. Davis. Maps of Dust Infrared Emission for Use in Estimation of Reddening and Cosmic Microwave Background Radiation Foregrounds. *ApJ*, 500:525–+, June 1998.

[113] P. Simon, M. Hetterscheidt, C. Wolf, K. Meisenheimer, H. Hildebrandt, P. Schneider, M. Schirmer, and T. Erben. Relative clustering and the joint halo occupation distribution of red sequence and blue-cloud galaxies in COMBO-17. *MNRAS*, 398:807–831, September 2009.

[114] J. Sommer-Larsen, A. D. Romeo, and L. Portinari. Simulating galaxy clusters - III. Properties of the intracluster stars. *MNRAS*, 357:478–488, February 2005.

[115] V. Springel and L. Hernquist. The history of star formation in a Λ cold dark matter universe. *MNRAS*, 339:312–334, February 2003.

[116] L.-G. Strolger, A. G. Riess, T. Dahlen, M. Livio, N. Panagia, P. Challis, J. L. Tonry, A. V. Filippenko, R. Chornock, H. Ferguson, A. Koekemoer, B. Mobasher, M. Dickinson, M. Giavalisco, S. Casertano, R. Hook, S. Blondin, B. Leibundgut, M. Nonino, P. Rosati, H. Spinrad, C. C. Steidel, D. Stern, P. M. Garnavich, T. Matheson, N. Grogin, A. Hornschemeier, C. Kretchmer, V. G. Laidler, K. Lee, R. Lucas, D. de Mello, L. A. Moustakas, S. Ravindranath, M. Richardson, and E. Taylor. The Hubble Higher z Supernova Search: Supernovae to z ˜ 1.6 and Constraints on Type Ia Progenitor Models. *ApJ*, 613:200–223, September 2004.

[117] Swiss Federal Institute of Technology Zurich. *The Zurich Extragalactic Bayesian Redshift Analyzer (ZEBRA), Version 1.0 - User manual*, February 2008.

[118] M. Tanaka, T. Kodama, N. Arimoto, S. Okamura, K. Umetsu, K. Shimasaku, I. Tanaka, and T. Yamada. The build-up of the colour-magnitude relation as a function of environment. *MNRAS*, 362:268–288, September 2005.

[119] G. Thuillier, M. Herse, P. C. Simon, D. Labs, H. Mandel, and D. Gillotay. Observation of the UV Solar Spectral Irradiance Between 200 and 350 NM during the Atlas i Mission by the SOLSPEC Spectrometer. *Solar Physics*, 171:283–302, April 1997.

[120] A. Toomre and J. Toomre. Galactic Bridges and Tails. *ApJ*, 178:623–666, December 1972.

[121] G. Tormen. The assembly of matter in galaxy clusters. *MNRAS*, 297:648–656, June 1998.

[122] N. Trentham. The galaxy luminosity function in clusters and the field. *MNRAS*, 294:193–+, February 1998.

[123] N. Visvanathan and A. Sandage. The color-absolute magnitude relation for E and S0 galaxies. I - Calibration and tests for universality using Virgo and eight other nearby clusters. *ApJ*, 216:214–226, August 1977.

[124] D. H. Weinberg. Mapping the Large Scale Structure of the Universe. eprint arXiv:astro-ph/0510197, October 2005.

[125] C. N. A. Willmer. Absolute Magnitudes of the Sun using synthetic spectra. http://www.ucolick.org/ cnaw/sun.html, November 2005.

[126] C. Wolf, K. Meisenheimer, H.-W. Rix, A. Borch, S. Dye, and M. Kleinheinrich. The COMBO-17 survey: Evolution of the galaxy luminosity function from 25 000 galaxies with $0.2 < z < 1.2$. *A&A*, 401:73–98, April 2003.

[127] A. I. Zabludoff and D. Zaritsky. A Collision of Subclusters in Abell 754. *ApJL*, 447:L21+, July 1995.